Spark Ignition and Flame Propagation in Sprays

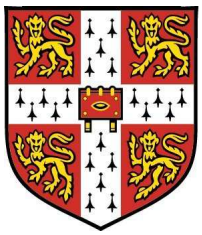

University of Cambridge

Department of Engineering

This dissertation is submitted for the degree of Doctor of Philosophy

by:

Alexandre Neophytou

Fitzwilliam College

Friday, 10th of September, 2010

To Zinonas

Declaration

This dissertation is the result of my own work and includes nothing which is the outcome of work done in collaboration except where specifically indicated in the text. The dissertation contains approximately **55,000** words, **113** figures and **seven** tables.

Alexandre Neophytou

Hopkinson Laboratory, University of Cambridge,
Friday, 10^{th} of September, 2010

Acknowledgements

I am very grateful to many people for their support and their help. First and foremost, I would like to thank my supervisor, Prof. Epaminondas Mastorakos for his genuine interest in my work, his invaluable guidance and his useful suggestions. I would also like to thank him for his continuing availability and his rapid feedback. I believe this helped me to have a smooth and positive PhD experience.

I would like to thank Prof. Stewart Cant for some interesting discussions and his useful advices to carry out Direct Numerical Simulations. I also thank Peter Benie (Cambridge) for his priceless expertise on computing science that benefits all PhD students in Hopkinson Laboratory. For technical help, I thank Dr Hans Ernst (Rotexo-SoftPredict) for his support with the code RUN1DL, Dr Andrew Wandel (University of Southern Queensland) for his help with the code SENGA, Prof. Heinz Pitsch (Stanford) for his help with the n-heptane chemistry, Dr Edward Richardson (Sandia Laboratory) for his contribution to the ignitability model, and Dr Simon Stow (Rolls-Royce plc.) for valuable CFD data and his interest. I also thank Dr Stuart Rankin and Wojciech Turek for technical assistance with the HPC at the University of Cambridge. Financial support has been received from the UK Engineering and Physical Sciences Research Council and Rolls-Royce plc.

I would like to express my gratitude to all my colleagues from the University of Cambridge who created a pleasant atmosphere and helped me during those three years of PhD. In particular, I thank Cheng Tung Chong, Andrea Pastore, Marta de la Cruz-Garcia, Peter Schroll, Antonis Triantafyllidis, Ivan Bahena-Ledezma,

Simon Ayache, Andrea Maffioli, Thibault Pringuey, Camille Letty, Robert Gordon, Theresa Leung, Frank Yuen and Davide Cavaliere. Some of them are now dear to me and I hope to preserve our friendship in the future.

My final thanks go to Carole, who has been here and has believed in me all the way through, and to my parents who have always supported me in my life, my studies and my odd choices such as doing a PhD.

Publications

Journal publications

1. A. Neophytou, E. Mastorakos, Simulations of Laminar Flame Propagation in Droplet Mists. *Combustion and Flame*, 156:1627-1640, 2009.

2. A. Neophytou, E. Mastorakos, R.S. Cant, DNS of Spark Ignition and Edge Flame Propagation in Turbulent Droplet-Laden Mixing Layers. *Combustion and Flame*, 157:1071-1086, 2010.

3. A. Neophytou, E. Mastorakos, R.S. Cant, Complex Chemistry Simulations of Spark Ignition in Turbulent Sprays. *Proceedings of the Combustion Institute*, To Appear.

Conference publications and presentations

1. A. Neophytou, E. Mastorakos, R.S. Cant, DNS of Spark Ignition in Turbulent Droplet-Laden Mixing Layers. *In: 4th European Combustion Meeting, Vienna, Austria, 14-17 April*, 2009.

2. A. Neophytou, E. Mastorakos, R.S. Cant, Spark Ignition Kernels in Sprays: Direct Numerical Simulations with Complex Chemistry. *In: 8th Euromech Fluid Mechanics Conference, Bad Reichenhall, Germany, 13-16 September*, 2010.

Webpage link for videos

http://www.dspace.cam.ac.uk/handle/1810/226367

Abstract

This thesis aims at improving the current knowledge of spark ignition in turbulent sprays that can aid the design of combustion chambers in aviation gas-turbines.

The investigation addresses three fundamental issues: the laminar flame propagation in a uniform spray, the spark ignition in a turbulent spray-air mixing layer with fine droplets and the spark ignition in a turbulent premixed spray with moderate droplet sizes. Moreover, a model that intends to reproduce the flame expansion following ignition in realistic non-premixed flows is presented.

The first issue is studied with a complex chemistry one-dimensional code. The flame speed and the flame structure as a function of various spray and flow parameters are presented. The flame speed is partially correlated with the amount of fuel vapour in the reaction zone. It is shown that the evaporation of the droplets in the post-flame region can result in additional heat release. Flame speeds at atmospheric conditions are shown to be similar to those at high altitude conditions, because of the competitive effect of low pressure and low temperature.

The second issue is studied with a single-step chemistry Direct Numerical Simulation code. Rapid ignition and kernel growth occurs for a spark located at the mixing layer. For a spark on the air side, the long range effect of the spark, i.e. spark size and the heat diffusion, can still lead to successful ignition provided the fuel is volatile. The flame following ignition has a tribrachial structure and its speed is close to the value of a turbulent gaseous edge flame. The edge flame speed is negatively correlated with curvature which can be reduced with a large kernel and

a wide mixing layer. A high turbulence intensity widens the mixing layer on one hand, but distorts the kernel on the other hand. This distortion can lead to high values of the curvature.

The third issue is studied with a complex chemistry Direct Numerical Simulation code. Heat release occurs over a large range of mixture fractions due to the stratified nature of the spray. It can also be finite well below the nominal flammability limit, due to the spark effect and the diffusion of heat and species from vigorously burning regions. Two ignition modes are observed and discussed. With a dispersed spray, the interdroplet spacing is very lean. Localised diffusion flames occur around droplets or groups of droplets. With a dense spray, the interdroplet spacing is flammable. Heat release occurs over a large volume and the flame looks like a gaseous kernel but with extra-wrinkling due to the stratified mixture. The curvature of the reaction zone is high in the first mode and low in the second mode.

Finally, the ignitability model for examining ignition of recirculating flames is based on the ignition of discrete volume elements of the flow by tracking flame particles. The convection by the mean flow, the turbulent random movement and the stochastic mixture fraction of a flame particle are incorporated. The quenching of a flame particle is also included by comparing the local laminar flame speed to the turbulence intensity, but flame propagation by molecular diffusion is not incorporated. The results, including maps of ignition probability, compare favourably with experimental observations. The computational cost of the simulation is low and the model can be applied to industrial combustors.

Contents

Contents viii
List of Figures xiii
List of Tables xxi
Nomenclature xxii

1 Introduction **1**
1.1 The problem of ignition 1
1.2 Gas turbine ignition 2
1.3 Forced ignition in premixed and non-premixed flows 3
1.4 Spray combustion 4
1.5 DNS of spray flames 4
1.6 Objectives of this study 6
1.7 Structure of this thesis 6

2 Literature review **8**
2.1 Forced ignition in a premixed gas 8
2.1.1 Flame kernel growth 8
2.1.2 MIE of premixed gases 11
2.2 Forced ignition in uniform sprays 13
2.2.1 Background on spray combustion 14
2.2.2 Flame propagation in a uniform spray 15
2.2.3 MIE measurements in premixed sprays 19

2.3 Forced ignition in non-premixed gases . . . 21
2.3.1 Kernel generation in a gaseous mixing layer . . . 21
2.3.2 Flame propagation in a gaseous mixing layer . . . 24
2.4 Forced ignition of realistic flows . . . 27
2.4.1 Academic burners . . . 27
2.4.2 Practical combustors . . . 29
2.5 Area of future research . . . 30

3 One dimensional simulation of laminar spray flames 32
3.1 Introduction . . . 32
3.2 Numerical formulation . . . 33
3.2.1 Gas Phase . . . 33
3.2.2 Liquid Phase . . . 35
3.2.3 Chemical Mechanisms . . . 39
3.3 Results . . . 40
3.3.1 Typical spray flame structure . . . 40
3.3.2 n-Heptane flame . . . 41
3.3.3 n-Decane flame: atmospheric conditions . . . 46
3.3.4 n-Decane flame: relight conditions . . . 48
3.4 Discussion . . . 49
3.4.1 Effective equivalence ratio . . . 50
3.4.2 Structure of the flame and influence of chemistry . . . 55
3.4.3 Summary of main findings . . . 64

4 DNS of spark ignition in a droplet laden mixing layer with 1-step chemistry 67
4.1 Introduction . . . 67
4.2 Numerical formulation . . . 68
4.2.1 Gas phase . . . 68

4.2.2 Liquid phase . . . 72
4.2.3 Solver . . . 74
4.2.4 Initial Conditions . . . 74
4.3 Results with classical 1-step chemistry . . . 78
4.3.1 Distribution of fuel . . . 78
4.3.2 General behaviour . . . 80
4.3.3 Flame kernel at the end of spark . . . 88
4.3.4 Flame displacement speed . . . 92
4.3.5 Displacement speed components . . . 96
4.3.6 Influence of parameters on displacement speed components . . 101
4.4 Results with modified 1-step chemistry . . . 104
4.4.1 Distribution of fuel with modified chemistry . . . 105
4.4.2 General behaviour with modified chemistry . . . 105
4.4.3 Flame kernel at the end of spark with modified chemistry . . . 110
4.4.4 Flame displacement speed with modified chemistry . . . 111
4.4.5 Influence of parameters on displacement speed components with modified chemistry . . . 114
4.5 Summary of main findings . . . 117

5 DNS of spark ignition in turbulent sprays with complex chemistry 119
5.1 Introduction . . . 119
5.2 Mathematical modelling . . . 120
5.2.1 Liquid phase . . . 120
5.2.2 Gas phase . . . 121
5.2.3 Numerical procedure and problem parameters . . . 122
5.3 Results . . . 125
5.3.1 Visualisation of flame front . . . 125
5.3.2 Volume averaged quantities . . . 134
5.3.3 Radial distributions . . . 138

5.3.4 Comparison with a laminar 1D premixed flame 151
5.3.5 Distribution in mixture fraction space and comparison with a 1D diffusion flame 152
5.3.6 Scalar dissipation rate 160
5.3.7 Flame propagation in cases A and D 161
5.3.8 Flame propagation in case C 170
5.3.9 Discussion on the two modes of ignition 172
5.3.10 Statistics of the flame curvature 173
5.4 Summary of main findings 177

6 A numerical model for the computation of ignition probability 179
6.1 Introduction 179
6.2 Mathematical modelling 180
6.2.1 Model description: main idea 180
6.2.2 Details of the model 182
6.2.3 Initialisation of the grid cells 184
6.2.4 Flame speed calculation 185
6.3 Methane Bluff-Body 189
6.3.1 Numerical setup 189
6.3.2 Results 192
6.4 Counterflow experiment 201
6.4.1 Numerical setup 201
6.4.2 Results 203
6.5 Industrial combustor 212
6.5.1 Numerical setup 212
6.5.2 Results 214
6.6 Summary of main findings 218

7 Conclusions **220**

7.1 Laminar flame propagation in a uniform spray 220

7.2 Spark ignition in a turbulent spray-air mixing layer 222

7.3 Spark ignition in a turbulent premixed spray 223

7.4 Numerical model for the computation of ignition probability 224

7.5 Guidelines for future studies 226

A Modified single step chemistry **228**

B Implementation of spray in SENGA2 **230**

B.1 Liquid phase equations 230

B.2 Parallel communication of the particles and source terms 232

B.3 Validation of evaporation cases 234

B.4 User guide to set up a simulation 235

C Implementation of detailed chemistry in SENGA2 **237**

Bibliography **240**

List of Figures

2.1 Schematic of the temperature profile across a laminar freely propagating premixed spray flame. 17

3.1 Temperature variation through n-heptane flames with l=5 mm and the indicated equivalence ratio and droplet size. 41
3.2 Heat release through n-heptane flames with l=5 mm and the indicated equivalence ratio and droplet size. 42
3.3 Reactants mass fractions through n-heptane flames with l=5 mm and the indicated equivalence ratio and droplet size. 43
3.4 CO_2 mass fraction through n-heptane flames with l=5 mm and the indicated equivalence ratio and droplet size. 44
3.5 n-Heptane flame speed as a function of the initial droplet diameter for different lengths l. 45
3.6 n-Heptane flame speed as a function of the overall equivalence ratio for different initial droplet diameters and l=5 mm. 46
3.7 Influence of Ω and a_d on n-heptane flame speed. 47
3.8 n-Decane flame speed at various ϕ_0 as a function of the initial droplet diameter for different lengths l. 48
3.9 n-Decane flame speed as a function of the overall equivalence ratio for different initial droplet diameters and l=5 mm. 49

3.10 Comparison between the theoretical curve, experiments with heavy fuel oil ($S_{L,0}$=0.41 m/s) [47] and our results with n-decane at an $\phi_0 = 1$ and l=2 mm. 50
3.11 Flame speed of gaseous n-decane at three different conditions of pressure and initial temperature. 51
3.12 Effective equivalence ratio through n-heptane flames with l=5 mm and the indicated equivalence ratio and droplet size. 52
3.13 Effective equivalence ratio for n-heptane as a function of the initial droplet diameter for different lengths l. 53
3.14 Effective equivalence ratio for n-decane as a function of the initial droplet diameters for different lengths l. 54
3.15 Normalised flame speeds as a function of ϕ_{eff}. 56
3.16 OH mass fraction through n-heptane flames with l=5 mm and the indicated equivalence ratio and droplet size. 57
3.17 Mass fraction of intermediate species through n-heptane flames with l=5 mm and the indicated equivalence ratio and droplet size. 59
3.18 Rates of elementary reactions through n-heptane flames with l=5 mm and the indicated equivalence ratio and droplet size. 60
3.19 Pyrolysis reaction rate through n-heptane flames with l=5 mm and the indicated equivalence ratio and droplet size. 61
3.20 Formation rate of some products of fuel decomposition through n-heptane flames with l=5 mm and the indicated equivalence ratio and droplet size. 62
3.21 Normalised sensitivity coefficient of the velocity on reaction rates. The particular reactions selected have the highest degree of sensitivity. 63
3.22 Rates of the indicated elementary reaction, selected as reactions with high degree of sensitivity through n-heptane flames with l=5 mm and the indicated equivalence ratio and droplet size. 64

4.1 (a) DNS Domain with non-dimensional coordinates. (b) Variation of the normalised number density in x-direction. 75
4.2 Distribution of the normalised mean droplet number density (i.e. $y-z$ plane averaged) along $\hat{x}$. 80
4.3 Distribution of the mean gaseous mixture fraction ξ (i.e. $y-z$ plane averaged) along $\hat{x}$. 81
4.4 $\hat{T}$ field in the plane $\hat{z}$=0.5. 82
4.5 Evolution of the flame kernel in the spray with time. 84
4.6 Non-dimensional reaction rate distribution in the plane $\hat{z}$=0.5. 85
4.7 Maximum temperature in the domain. 86
4.8 Time evolution of (a) Non-dimensional heat release rate in the domain, (b) Kernel volume normalised by δ_r^3. 87
4.9 Scatter plot of c versus mixture fraction at $t = 3t_{sp}$ for case A. 89
4.10 Variation of conditionally-averaged non-dimensional temperature vs. mixture fraction using data in the range $0.5 < c < 1$ at $t = t_{sp}$. 90
4.11 Mixture fraction in burning region ($0.5 < c < 1$) at $t = t_{sp}$. 91
4.12 Variation of conditionally-averaged normalised fuel reaction rate magnitude vs. mixture fraction using data in the range $0.5 < c < 1$. . . . 92
4.13 Probability density function (PDF) of the density weighted displacement speed at different times. 95
4.14 Volume average of the density weighted displacement speed at the triple point normalised by the stoichiometric laminar flame speed. . . 96
4.15 Iso-surface Y_{O_2}=0.12 coloured by normalised mean curvature ($k_m \times \delta_r$) at $t = 3t_{sp}$. 97
4.16 Components of the density-weighted displacement speed conditionally-averaged on the progress variable c, using data for $0.9 \leq \xi/\xi_{st} \leq 1.1$ for case A at $3t_{sp}$. 99
4.17 Scatter plot for case A in region $0.1 \leq c \leq 0.85$ at $t = 3t_{sp}$ of: (a) normalised ∇Y_{O_2} versus normalised mean curvature k_m. 100

4.18 Scatter plot for case A in region $0.1 \leq c \leq 0.85$ at $t = 3t_{sp}$ of: (a) $(S_r^* + S_n^*)$ versus normalised k_m. (b) S_d^* versus normalised k_m. 101
4.19 Data as in Fig. 4.16 but for all cases studied. (a) $\langle S_d^* \rangle$. (b) $\langle S_r^* \rangle$. (c) $\langle S_n^* \rangle$. 103
4.20 $\hat{T}$ field in the plane $\hat{z}$=0.5. 105
4.21 Evolution of the flame kernel in the spray with time. 106
4.22 w_F field in the plane $\hat{z}$=0.5. 107
4.23 Maximum temperature in the domain against time. 108
4.24 Volume of the kernel $\hat{T} \geq 0.5$ against time. 109
4.25 Scatter plot of c versus mixture fraction at $t = 3t_{sp}$ for case A. 110
4.26 Variation of conditionally-averaged normalised temperature vs. mixture fraction using data in the range $0.5 < c < 1$ at $1t_{sp}$. 111
4.27 Probability density function (PDF) of the density weighted displacement speed at different times. 112
4.28 Volume average of the density weighted displacement speed at the triple point normalised by the stoichiometric laminar flame speed at 1, 2, 3, 4 and 5 t_{sp}. 113
4.29 Iso-surface Y_{O_2}=0.12 coloured by curvature k_m at $t = 3t_{sp}$. 114
4.30 Data as in Fig. 4.16 but for all cases studied. 115

5.1 Coloured iso-surfaces of heat release rate in 3D (upper) and contours in a 2D slice passing through the spark centre (lower). Gas case. . . . 126
5.2 Coloured iso-surfaces of heat release rate in 3D (upper) and contours in a 2D slice passing through the spark centre (lower). Case A. 127
5.3 Coloured iso-surfaces of heat release rate in 3D (upper) and contours in a 2D slice passing through the spark centre (lower). Case B. 128
5.4 Coloured iso-surfaces of heat release rate in 3D (upper) and contours in a 2D slice passing through the spark centre (lower). Case C. 129

5.5 Coloured iso-surfaces of heat release rate in 3D (upper) and contours in a 2D slice passing through the spark centre (lower). Case D. 130
5.6 Contours of mixture fraction in a 2D slice passing through the spark centre at $t = 2.5t_{sp}$. 133
5.7 Volume integrated quantities in region $T > 400K$ *vs.* normalised time. 135
5.8 Mean droplet temperature in region $T > 400K$ *vs.* normalised time. . 137
5.9 Temperature averaged over a spherical shell of radius r as a function of normalised r. 139
5.10 Mixture fraction averaged over a spherical shell of radius r as a function of normalised r. 140
5.11 Heat release rate averaged over a spherical shell of radius r as a function of normalised r. 141
5.12 Y_{O_2} averaged over a spherical shell of radius r as a function of normalised r. 142
5.13 Y_{CO_2} averaged over a spherical shell of radius r as a function of normalised r. 143
5.14 Y_{H_2} averaged over a spherical shell of radius r as a function of normalised r. 144
5.15 $Y_{C_2H_4}$ averaged over a spherical shell of radius r as a function of normalised r. 145
5.16 Y_H averaged over a spherical shell of radius r as a function of normalised r. 146
5.17 Y_{OH} averaged over a spherical shell of radius r as a function of normalised r. 147
5.18 Plain lines show averages over a spherical shell of radius r as a function of normalised r for Gas case at $t = 2.5t_{sp}$. Dotted lines show stoichiometric 1D laminar flame profiles. 148
5.19 Scatter plot for case A of heat release rate *vs.* mixture fraction. . . . 153
5.20 Scatter plot for case C of heat release rate *vs.* mixture fraction. . . . 154

5.21 Scatter plot for case B of heat release rate *vs.* mixture fraction. . . . 155
5.22 Scatter plot for case D of heat release rate *vs.* mixture fraction. . . . 156
5.23 Conditional average of heat release rate on mixture fraction in region $T > 400K$ *vs.* mixture fraction at $t = 2.5t_{sp}$. 157
5.24 Scatter plot *vs.* mixture fraction for case A at $t = 2.5t_{sp}$. 158
5.25 Scatter plot *vs.* mixture fraction for case C at $t = 2.5t_{sp}$. 159
5.26 Scatter plot of scalar dissipation rate *vs.* mixture fraction at $t = 2.5t_{sp}$.160
5.27 Scatter plot of Heat release rate *vs.* scalar dissipation rate at $t = 2.5t_{sp}$.161
5.28 Ignition of droplets D1, D2 and D3 for case A. 162
5.29 Focused view of contours of mixture fraction on a plane containing droplets D2 and D3 for case A.. 163
5.30 Profiles along a line passing through droplet D1 ($r/R_{ign} = 0$) and the spark centre ($r/R_{ign} = 1$). 167
5.31 Profiles along a line passing through droplet D2 ($r/R_{ign} = 0$) and the spark centre ($r/R_{ign} = 1.5$). 168
5.32 Profiles along a line passing through droplet D3 ($r/R_{ign} = 0$) and droplet D2. 169
5.33 Scatter plot of heat release rate *vs.* mixture fraction in a sphere centred at droplet D3, with radius R_{ign} at $t = 2.5t_{sp}$. 170
5.34 Contours for case C of mixture fraction on 2D Slice passing through the centre of the domain. 171
5.35 Probability density function of normalised curvature. 175

6.1 Flame speed against ϕ_0 for different initial droplet diameters. 188
6.2 (a) LES mean mixture fraction with spark locations I, II and III, (b) LES Flammability factor [105], (c) Experimental mean mixture fraction for case B of Ref. [103], (d) Experimental flammability factor for case B of Ref. [103], (e) Karlovitz number based on averaged LES quantities. 190

6.3 Time evolution of π_{ign} of each event. 193
6.4 Statistics over 50 events at each spark location at $t = 60$ ms for case A (a) average of π_{ign} , (b) rms of π_{ign}. 194
6.5 Ignition probability maps. 195
6.6 Evolution of particles for a successful event between t=0 ms and t=60 ms for spark location I. 197
6.7 Evolution of particles for a failed event between t=0 ms and t=60 ms for spark location I. 198
6.8 Evolution of particles for a failed event between t=0 ms and t=60 ms for spark location II. 199
6.9 Evolution of particles for a successful event between t=0 ms and t=60 ms for spark location III. 200
6.10 (a) Flammability factor with spark locations I, II and III, (b) Karlovitz number based on averaged quantities. 203
6.11 Time evolution of π_{ign} of each event. 205
6.12 Statistics over 50 events at each spark location at $t = 60$ ms. 206
6.13 Ignition probability maps. 207
6.14 Top view of the evolution of particles for a successful event between t=0 ms and t=60 ms for spark location I. 209
6.15 Top view of the evolution of particles for a successful event between t=0 ms and t=60 ms for spark location II. 210
6.16 Top view of the evolution of particles for a failed event between t=0ms and t=60 ms for spark location III. 211
6.17 Geometry of the industrial combustor [160]. 212
6.18 Time evolution of π_{ign} of each event. 215
6.19 Evolution of particles with Spark I between t=0 ms and t=60 ms. . . 216
6.20 Evolution of particles with Spark II between t=0 ms and t=60 ms. . . 217

A.1 Comparison of normalised flame speed profiles. 229

B.1 Evolution of $< T > /T_0$, $< a_d > /a_{d,0}$, $< a_d^2 > /a_{d,0}^2$, $< a_d^3 > /a_{d,0}^3$. . . . 234
B.2 Evolution of a_d^2 for a single evaporating n-heptane droplet in ambient air (P=1 bar, $T = 741$ K). 235

C.1 Computed time evolution of Temperature and Y_{H_2}. 238
C.2 Comparison of normalised flame speed profiles. 239

List of Tables

3.1 Range of conditions studied. 39

4.1 Parameters for the investigated cases. 78

5.1 Turbulence and spark characteristics for the investigated cases. 122

6.1 Cases studied for the experiment of Ref. [103]. 191
6.2 Cases studied for the experiment of Ref. [84]. 204
6.3 Operating conditions used in the CFD RANS simulation. 213
6.4 Parameters used in the simulations. 214

Nomenclature

Roman letters

$\dot{m}$	droplet evaporation rate (absolute value), [kg/m^3/s]
$\dot{q}$	heat exhange at droplet surface, W/m^3
a_d	droplet diameter, [m]
B	Spalding transfer number
c	progress variable
C_P	specific heat capacity at constant pressure, [J/kg/K]
C_v	specific heat capacity at constant volume, [J/kg/K]
D	mass diffusivity of fuel in air, [m^2/s]
D_i	mass diffusivity of species i in air, [m^2/s]
d_q	quenching distance, [m]
D_{32}	Sauter mean diameter, [m]
E	stagnation internal energy per unit mass, [J/kg]
F	flammability factor
G	Group number

H counterflow inner pipe diameter, [m]

h absolute enthalpy per unit mass, [J/kg]

k_m curvature, [m^{-1}]

Ka Karlovitz number

L length of DNS domain, [m]

l length of primary evaporation zone, [m]

L_v latent heat of evaporation, [J/mol]

L_{11} turbulence integral lengthscale, [m]

Le Lewis number

m_d droplet mass, [kg]

n number density of droplets, [m^{-3}]

Nu Nusselt number

P pressure, [Pa]

P_{ign} successful ignition probability

P_{ker} successful kernel development probability

P_{ref} reference pressure, [Pa]

Pr Prandtl number

q_{sp} spark power, [W/m^3]

R universal gas constant, [J/mol/K]

r droplet radial coordinate, [m]

R_{ign} spark radius, [m]

Re Reynolds number

s mass of oxygen unit per mass of fuel at stoichiometry

S_d displacement speed, [m/s]

s_d interdroplet distance, [m]

S_L laminar flame speed, [m/s]

S_m evaporation component of displacement speed, [m/s]

S_n normal component of displacement speed, [m/s]

S_r reaction component of displacement speed, [m/s]

S_t tangential component of displacement speed, [m/s]

$S_{L,0}$ stoichiometric laminar flame speed, [m/s]

Sc Schmidt number

Sh Sherwood number

T temperature, [K]

t time, [s]

T_{ad} adiabatic flame temperature, [K]

T_{ref} reference temperature, [K]

t_r flame reaction zone timescale, [s]

t_{sp} spark duration, [s]

t_{turb} turbulent timescale, [s]

U velocity, [m/s]

u' turbulence intensity, [m/s]

U_b counterflow air velocity, [m/s]

U_F counterflow fuel velocity, [m/s]

U_r counterflow radial velocity, [m/s]

U_z counterflow axial velocity, [m/s]

V diffusion velocity, [m/s]

W molecular mass, [kg/mol]

X mole fraction

x, y, z spatial coordinates

X_d dilution factor

x_d, y_d, z_d droplet coordinate, [m]

x_{sp}, y_{sp}, z_{sp} spark coordinates, [s]

Y mass fraction

v_d droplet velocity, [m/s]

Greek letters

α thermal diffusivity, [m^2/s]

χ scalar dissipation rate, [s^{-1}]

χ_c cross scalar dissipation rate, [s^{-1}]

Δt time step, [s]

Δx grid size, [m]

δ_{ij} kronecker symbol

δ_M mixing layer thickness, [m]

δ_r flame reaction zone thickness, [m]

δ_{th} flame thermal thickness, [m]

ϵ void volume fraction

Γ liquid source term

γ heat capacity ratio

λ thermal conductivity, [W/m/s]

μ dynamic viscosity, [kg/m/s]

ν kinematic viscosity, [m^2/s]

Ω vapour fraction of fuel

ω chemical reaction rate, [kg/m^3/s]

ϕ equivalence ratio in gas

ϕ_0 overall equivalence ratio

ϕ_{eff} effective equivalence ratio

π_{ign} ignition progress factor

ρ density, [kg/m^3]

τ non-dimensional heat release parameter

τ_d^p droplet diameter relaxation time, [s]

τ_d^T droplet temperature relaxation time, [s]

τ_d^v droplet velocity relaxation time, [s]

τ_{evap} droplet evaporation time, [s]

τ_{ij} viscous stress tensor, [Pa]

ξ mixture fraction

ξ_0 overall mixture fraction

ξ_L nominal lean flammability limit

ξ_R nominal rich flammability limit

ξ_{st} stoichiometric mixture fraction

Subscript indices

0 initial/cold state

b burned

d droplet

F fuel

f droplet thin film

L liquid

M mass

T temperature

u unburned

Superscript indices

g gas

L liquid

s droplet surface

Overbar symbols

$*$ density weighted

$< . >$ volume average

$\bar{.}$ Reynolds average

$\hat{.}$ non-dimensional

$\tilde{.}$ Favre average

Other symbols

l.h.s. Left Hand Side

r.h.s. Right Hand Side

CMC Conditional Moment Closure

CPU Central Processing Unit

DLR-VT Deutsches Zentrum fr Luft- und Raumfahrt (German Aerospace Center)

DNS Direct Numerical Simulation

LES Large Eddy Simulation

MIE Minimum Ignition Energy

SMD Sauter Mean Diameter

Chapter 1

Introduction

1.1 The problem of ignition

In the field of aviation gas turbines, the problem of forced ignition is critical. With the current trend towards lean combustion and pollutant reduction, old empirical rules, developed for the design of ignition units, have become obsolete. Experiments on gas turbines are expensive while computational models used in industry have not been thoroughly validated for this problem. Hence, there is a need to develop industrial tools that provide non-expensive ignition predictions with good accuracy. This thesis provides some new fundamental knowledge that can assist this effort.

Ignition of gas turbines is a transient process that involves complicated phenomena such as spray atomisation, evaporation and combustion, turbulent flows and forced ignition. The subject is very rich from a scientific point of view and has motivated numerous studies. However, there is still a substantial lack of fundamental understanding which makes the modelling for computational tools particularly difficult. In order to create more efficient design tools, further understanding of the phenomena is needed.

This thesis aims to provide such understanding through numerical simulations of spark ignition and flame propagation in sprays.

1.2 Gas turbine ignition

Forced ignition involves an external source of energy that induces rapid exothermic reactions and eventually a propagating flame in an initially cold mixture. The most common type of forced ignition is a spark generated by a breakdown voltage between two electrodes. The surface-spark discharge plug, used in most civil aircraft engines, is based on this principle and is described in Ref. [1]. A major drawback of the system is that only a small portion of the energy supplied to the igniter is actually used to raise the mixture temperature. In addition, in order to extend the ignitor's lifetime, it is desirable to reduce the energy in the spark, which makes ignition challenging. Other methods of forced ignition exist such as laser ignition, plasma jet, torch ignitor and glow plug, and are summarised in [1]. In this thesis, we use the term forced ignition to mean spark ignition.

The forced ignition unit must be adapted to the design of new combustors. Modern regulations on the reduction of the emission of pollutants have pushed manufacturers toward lean combustion. At the same time, they must respect strict safety rules regarding the ignition capabilities over a range of flight conditions, up to 9,000 m (see Fig. 5-30 of Ref. [1]). Those requirements derive from the need to ensure ignition for ground starting and immediate relight after the possible extinction of the flame, for example due to excessive ingestion of water during the flight.

The relight capability is evaluated by carrying a series of test on a combustor test rig with various inlet parameters, such as inlet pressure, temperature, air mass flow rate and air/fuel ratio that represent the different flight conditions [1]. The ignition loop is the range of parameters for which successful ignition has been obtained. Successful ignition is obtained when the flame spreads and stabilises in the entire combustor. This is a particular challenge at high altitude and low Mach number where the inlet pressure and temperature are low. Poor design of the ignition unit may preclude the ignition loop from satisfying the safety requirements. In such a case, the design of the ignition unit must be modified which can prove very costly at

this stage of the development. Research can offer a better understanding of forced ignition and in turn improve the design of the ignition unit.

1.3 Forced ignition in premixed and non-premixed flows

Lefebvre [1] characterises ignition of a combustor according to three distinct phases, kernel development, flame propagation and flame stabilisation. The fulfilment of those three phases is necessary to obtain successful ignition. The success of ignition depends on the flow in which the energy is deposited.

The Minimum Ignition Energy (MIE), that is the necessary energy to generate a growing flame kernel, has been the key parameter to quantify ignition success in premixed flows. Numerous investigations have offered a deep understanding of the development of a flame kernel and the factors controlling the MIE in premixed gases [1, 2]. Similar studies in uniform sprays have successfully evaluated the effect of droplets on the MIE [3].

In turbulent non-premixed gas or turbulent non-premixed spray, the spatial and the temporal variation of the mixture strength results in a highly probabilistic nature of forced ignition. The MIE can no longer characterise the entire problem. Instead, the ignition probability at a fixed spark energy has been adopted [4]. Given a spark energy, this quantity is the probability of igniting a flame at a given location. Generating a field of ignition probabilities has become a subject of interest for academic work and for industrial combustion chambers. In order to quantify the ignition success in a realistic combustor, numerical tools that generate probability maps are appealing. However, investigations of the factors controlling ignition success and studies of the ignition probability are more limited for non-premixed gas and very seldom for non-premixed sprays [4].

In Chapter 2, we give a review of the main findings on the factors controlling the

MIE in premixed flows and the ignition probability in non-premixed flows.

1.4 Spray combustion

Spark ignition in gas turbine implies the presence of two-phase flows. The subject is complicated and involves liquid break-up, atomisation, evaporation and combustion. A common assumption in spray combustion problems is that the liquid has already undergone the break-up phase and is in spherical droplet form. Even at this level, complicated physical phenomena occur because of the interaction between the turbulent gas phase and the liquid phase (exchange of mass, energy and momentum). Moreover, the distribution of droplets generally results in highly stratified mixtures which cannot be restricted to the simple premixed or non-premixed categories but involve features of both. The understanding of the physics of combustion in such flows needs substantial progress while its modelling is often inappropriate [5]. In Chapter 2, we summarise findings on spray combustion and the structure of a spray flame. Additional knowledge on spray ignition can be gained through numerical simulations, in particular Direct Numerical Simulations (DNS).

1.5 DNS of spray flames

The DNS is a numerical tool that solves the exact Navier-Stokes equations without any model for turbulence. This implies that all scales of turbulence must be resolved. To this end, the grid spacing is usually taken smaller than the smallest turbulence scale, the Kolmogorov length scale. As a result, the CPU time scales with $Re^{9/4}$ [6], with Re the Reynolds number, which limits the flows that can be simulated.

In combustion problems, DNS additionally solves transport equations for species and enthalpy, generally assuming the ideal gas law, Ficks law of diffusion and Fourier's law of conduction of heat [6]. Hence, equations for transport are generally not exact but involve some modelling. Moreover, serious considerations must

be given to the treatment of chemistry. Reproducing all the reactions and species involved in chemical reactions is a difficult task. The most reliable chemical models often incorporate hundreds of species and reactions. However, for each species, a new equation is included. Given that the CPU time of a DNS simulation scales with the number of equations, they must be brought to a minimum. The less costly assumption is that of 1-step chemistry were only fuel and oxidiser are considered. But this excludes important chemical phenomena, which can be important in auto-ignition or spark ignition problems. Reduced schemes that involve tens of species are more reliable. With the current computational capabilities, DNS simulations with complex chemistry can be performed. In this thesis, we use the term complex chemistry to mean chemistry which incorporates more than two reactants. The results have the potential for substantial improvement of our knowledge.

Finally, the DNS of flows involving spray combustion generally demands additional assumptions. First, it is assumed that the liquid is in form of spherical droplets. Moreover, it is supposed that evaporation occurs at the surface of the liquid and that equilibrium of the phases holds. Furthermore, it is not attempted to solve the thin layer surrounding droplets where transport of mass, momentum and energy due to evaporation occurs. This would require very fine grids, much smaller than the Kolmogorov length scale, which are extremely costly. In practice, theoretical models combined with experimental correlations are employed and the thin layer is not resolved.

Therefore, DNS of spray combustion gives exact solution only for the fluid mechanics part. In spite of the modelling assumptions for the chemistry and the liquid phase, the simulations remain costly and few 3D DNS simulations deal with spray combustion. However, using the DNS tool, progress can be made for areas such as spark ignition in sprays. In Chapters 4 and 5, we use DNS to analyse the physics associated with spark ignition in sprays.

1.6 Objectives of this study

The scope of this work is to use numerical tools in order to make progress in the understanding of the phenomena controlling spark ignition and flame propagation in sprays, and to develop further the conceptual ignititability model that was one of the outcome of a previous PhD thesis carried out at the University of Cambridge [7].

1.7 Structure of this thesis

Chapter 2 provides a literature review of spark ignition and flame propagation in gas and sprays. In Chapter 3, a parametric study is carried out with an existing one-dimensional code in order to compute the structure and the flame speed of laminar unstrained propagating spray flames. In Chapter 4, an existing DNS code with simple chemistry is used to simulate the growth of a kernel in a spray-air mixing layer. The success and the failure of ignition depending on flow and spray parameters is presented and the flame displacement speed of the growing flames is measured. In Chapter 5, a DNS code that incorporates complex chemistry has been extended to two-phase flows. Simulations of the kernel growth in a uniform spray are presented for various spray parameters and the detailed structure of those flames is analysed. Finally, given the physical insights offered by the simulations, key quantities are implemented in the ignititability model to cover spray ignition with greater accuracy. This model and some results are presented in Chapter 6. In Chapter 7, the findings of the investigation are summarised and guidelines for future research are suggested.

There are three appendices in this thesis. Appendix A deals with the implementation of the single step chemistry used in Chapter 4. Appendix B describes the development and the validation of the DNS code used in Chapter 5 for two-phase flows. Appendix C presents the numerical implementation and validation of the

skeletal chemistry scheme used in the same code.

Chapter 2

Literature review

In this chapter, we present a literature review of forced ignition for different categories of flows. Firstly, we present the physics of the kernel growth and we report factors controlling the MIE in premixed gases. Secondly, after a brief introduction on spray combustion, we summarise findings on spray flames and MIE measurements in uniform sprays. Thirdly, we present measurements of the ignition probability and investigations of flame propagation in non-premixed gases. Finally, we report work done on spark ignition in realistic configurations.

2.1 Forced ignition in a premixed gas

2.1.1 Flame kernel growth

Spark ignition generally involves two electrodes linked to a discharge circuit which produces capacitance sparks [2]. This allows to control the energy and duration of the spark created in the mixture between the electrodes. From an electrical point of view, three different phases will follow the appearance of a spark and are presented here for premixed gas [8]. First, the voltage between the electrodes must reach a threshold, the breakdown voltage, to initiate an electrical current. A very short breakdown phase (1-10 ns) ensues, with very high peak values of voltage (10 kV)

and current between the electrodes. This creates a highly conducting plasma channel with temperatures up to 60,000K. After the establishment of a plasma channel, the voltage between the electrodes becomes much lower and a second phase begins, the arc phase. There, an appreciable fraction of the arc voltage is wasted in the cathode fall [8, 9]. The cathode fall is the voltage fall in a distance of about 1 μm from the cathode. This energy is lost to the electrodes and the plasma temperature falls to 6000K [8]. After a few hundred μs the cathode fall becomes more important and the glow phase begins. In this last phase, the energy lost to the electrodes is significant, of the order of 70 %. The conversion efficiency from electrical to thermal energy is thus low and the temperature in the hot gas is less than 3000K [8]. Although the described phenomena show that the plasma and the electrodes play a role in the actual energy provided to the kernel, few numerical studies have dealt with their computation [10, 11]. Numerical investigations of spark ignition generally assume that the energy provided raises the mixture temperature to about 3000K or 4000K [12–14]. Hence, they ignore phenomena associated with the plasma and focus on the fluid dynamic aspect of the kernel growth.

From the point of view of the kernel growth, three different phases may also be identified in a homogeneous turbulent mixture [15]. In a first phase, the kernel growth is dominated by the pressure wave. Due to the large pressure increase inside the small plasma volume, a shockwave leaves at about 1 μs. This shockwave transports radially a significant part of the spark energy and heats up the surrounding mixture, as observed in several experiments with homogeneous mixtures [15–20]. This results in a fast kernel growth between 1 and 10 μs. If the energy during the breakdown phase is very high, this shockwave can act as an ignition source but for energy of the order of the MIE, this is unlikely [17]. Hence, in the general case, the shockwave can be considered as a loss to the fresh mixture since this energy is not used to increase the kernel temperature [21]. Behind the shockwave, the pressure is high and a rapid expansion occurs to reach atmospheric pressure. This expansion, of the order of 10 μs, results in a rapid kernel growth at decreasing rate [10, 16].

Following this phase, the kernel growth slows down and a second phase begins, the thermal spread supported by the spark energy. This lasts up to about 1ms after the onset of the spark [2, 11, 12, 15, 22, 23]. There, the kernel grows spherically through the diffusion of the spark energy from the hot kernel to the fresh mixture. This can be aided by heat release in the hot gas.

At early times, the kernel is similar to a laminar one because the influence of turbulent eddy diffusivity is very weak owing to the small kernel size and the short timescale [15, 17, 24, 25]. During that period the effect of turbulence is rather to transport the kernel as a body [17]. Between about 50 μs and 300 μs after the breakdown, the kernel growth is dominated by molecular diffusion of energy and reactive species [10, 15, 17, 26]. The turbulent diffusivity is time dependent and it becomes increasingly important around 300 μs after the breakdown [15, 17, 26, 27]. It then enhances the heat diffusion [17]. Ishii et al. [25] showed experimentally that the transformation of a laminar kernel into a turbulent wrinkled kernel occurs earlier as the turbulent intensity increases.

When sufficient heat has been lost to the fresh mixture so that the kernel temperature has dropped near the adiabatic flame temperature T_{ad}, its size will determine if it will become self-propagating [2]. At that stage, the heat release has to overcome the heat lost by the kernel. This happens if the kernel reaches a critical size [2]. A third phase then starts where its growth is controlled only by the heat release and it becomes a self-propagating flame. Its speed increases and approaches the adiabatic flame speed of the homogeneous mixture [2, 19, 22].

Eventually, ignition of the entire combustor will be successful if the flame propagates towards the primary zone of the combustor and is not swept away downstream by the flow. High flame speeds will favour the success of the propagation phase.

2.1.2 MIE of premixed gases

Numerous investigations have focused on the problem of spark ignition in premixed gas theoretically [15, 17, 22], numerically [10, 11, 26, 27] and experimentally [2, 8, 9, 12, 16, 18–21, 23–25, 28–35]. As a result, they have offered a deep understanding of the development of a flame kernel and the factors controlling the MIE. The MIE relates to the total energy delivered by the electrodes. However, one must keep in mind that only a fraction of this energy is used to warm up the flame kernel [2]. The rest of the energy is lost through the initial shockwave propagation, radiation, the electrodes fall and the electrodes quenching effect. In this section, we first introduce the theoretical link between MIE and the critical kernel size. Then we intend to summarize the flow parameters that affect the MIE.

The MIE can be related to the critical size a kernel must reach to become self-propagating. Lewis and von Elbe define the MIE as the energy, which in association with the heat release, warms a sphere with a critical radius to T_{ad} [2]. According to their theory, an ideal spherical kernel is subjected to a high strain rate due to its curvature which increases the heat loss. At the critical radius, the heat release inside the kernel compensates for the large strain rate. This critical radius is of the order of the flame thickness [2, 17, 22]. Glassman [36] gives

$$MIE \sim (D_{th}/S_{L,0})^3 \rho C_p (T_{ad} - T_0) \tag{2.1}$$

where $D_{th}/S_{L,0}$ is a measure of the flame reaction zone thickness. Ballal and Lefebvre [31] suggested that the critical size should be of the order of the quenching distance d_q and they correlated d_q with the MIE. The quenching distance d_q is the lengthscale at which heat release equals heat dissipation and is about 10 times $D_{th}/S_{L,0}$ [31]. Calcote et al. [28] reported the MIE for different fuels and showed $MIE \sim d_q^{2.5}$. Ballal and Lefebvre found a cubic dependence with methane and propane [31]. Finally, since the effect of turbulence is to provide an additional strain rate and to extend the flame thickness, turbulence results in an increase of the critical radius and therefore an increase of the MIE [15, 24].

It is noteworthy that the MIE is well defined as long as the flows are reproducible, i.e. uniform and laminar. However, even in premixed flows, a stochasticity is introduced by turbulence. For the same spark energy, both igniting and quenching flames can be observed. This is presumably due to the randomness of the turbulent strain rate at the kernel location at the moment of the spark, as pointed out by Mastorakos [4]. Many studies reported next measured the MIE as the one which gave 50% ignition probability [17, 24, 25, 32, 35].

Now, we focus on the flow variables which have an impact on the MIE. A higher initial temperature will result in a lower MIE [9]. Moreover, one can expect the MIE to be the lowest close to stoichiometric mixture since the laminar flame speed is maximum there. Lewis and Von Elbe [2] showed that, in quiescent mixtures, the mixture strength which yielded to the lowest MIE ranged from slightly lean for fuel with low carbon number, e.g. methane, to richer than stoichiometry for higher hydrocarbons, e.g. heptane. This is substantiated by similar findings with methane and propane [9, 30]. Lewis and Von Elbe attributed the shift of the equivalence ratio from stoichiometry to preferential diffusion processes across the greatly curved kernel [2]. However, Ballal and Lefebvre [30, 31] showed that in flowing gases the optimum equivalence ratio for MIE maximised the laminar flame speed. They suggested that in flowing gases, the transport processes are accelerated to such an extent that the effects of preferential molecular diffusion rates become much less significant than in quiescent mixtures [30]. Finally, the effect of pressure on the MIE has been investigated and it was noticed that $MIE \sim P^{-n}$ with n between 1 and 2 [2, 9, 30]. The negative exponent comes from the net effect of the reduced flame thickness $D_{th}/S_{L,0}$ with higher pressure and the higher density ρ which implies more mass to heat in the kernel [37]. Ballal and Lefebvre [30] showed that n varied from 2 in stagnant mixture to about 1.25 at high flow velocity.

It is of interest to look at the dependency of the MIE on the turbulence parameters. First, low levels of turbulence promote the flame propagation by wrinkling the flame front which is favourable for the self-sustained propagation of the flame.

Nevertheless, as explained above, turbulence increases the critical kernel size. This detrimental effect is overriding in ignition performance and the MIE has been found to increase with the square of the turbulence intensity u' [9, 30, 31, 35]. In fact, it was found that the increase of the MIE with turbulence intensity is mild in a low turbulence region and large in a region of high turbulence intensity [31, 35]. In the first zone, the turbulence simply wrinkles the external flame surface while in the second eddies penetrate the burning zone. The transition between the two regions is found by Ballal and Lefebvre to occur at $u'/S_{L,0} = 2$ [31]. In addition, it was observed that an increase in turbulence scale caused a reduction of the MIE in the low turbulence region whilst it produces a pronounced increase of the MIE in the high turbulence region [30, 31]. In the transition region, the references indicate that the MIE is independent of the turbulent scale.

Finally, we mention that the MIE is obtained for an optimum electrode gap, equal to the quenching distance [2, 9, 21, 24, 31, 32], and an optimum spark duration [9, 21, 22, 32]. The optimum electrode gap is a compromise between a distance large enough to prevent excessive heat losses to the electrodes [2] and low enough to reduce the air electrical resistance between the electrodes [9]. The optimum spark duration is a trade-off between a duration long enough to minimise the early shockwave losses [21] and short enough to avoid relatively high heat dissipation compared to the spark power [22].

2.2 Forced ignition in uniform sprays

Most of forced ignition investigations with sprays have been carried out with spatially uniform sprays. In this section, we first briefly mention common knowledge on spray combustion. Then, we summarise findings on the canonical problem of flame propagation in a uniform spray. Finally, we present results on the MIE as a function of spray parameters.

2.2.1 Background on spray combustion

Research on spray combustion often refers to single droplet evaporation and combustion. Generally, the surface of a spherical droplet is assumed to be in phase equilibrium and the saturated gaseous properties at the droplet surface can be calculated (e.g. Clausius Clapeyron law). The high value of the saturation fuel vapour pressure compared to the surrounding gas induces an outward convective transport called Stefan flow. This transport occurs over a thin layer around the droplet and causes evaporation. The evaporation rate is controlled by the exchange of heat and mass between the droplet surface and the surrounding gas. The theory of a single evaporating droplet shows the linear decay of the square of the droplet diameter with time. This decay is used often in combustion problems involving droplets. The theory of a single burning droplet considers a droplet surrounded by a diffusion flame fed by the evaporated fuel. The droplet burning rate is controlled by the evaporation rate and a decay law can be derived for the droplet diameter. Reference books provide more detailed description on single droplet evaporation and combustion [5, 38].

The understanding of combustion in a spray is more limited. An interesting approach has been offered by Chiu and Liu [39] who established a classification of different modes of steady-state spray combustion in a spherical cloud of droplets. A dimensionless group number G was used to determine the mode of combustion.

$$G = 3(1 + 0.276\mathrm{Re_d}^{1/2}\mathrm{Sc}^{1/3})\mathrm{LeN}^{2/3}(\mathrm{a_d}/\mathrm{s_d}) \tag{2.2}$$

where $\mathrm{Re_d}$, Sc and Le are respectively the droplet Reynolds number, the Schmidt number and the Lewis number of the cloud. G increases with the total number of droplets N and the initial droplet diameter a_d while it decreases with s_d, the mean spacing between droplets. Four different combustion modes were characterised as G increases. For $G < 10^{-2}$, individual droplet combustion occurs. A diffusion flame surrounds each droplet with low interaction between them. For $10^{-2} < G < 10^{-1}$, internal group combustion occurs. Inside the cloud, a core contains non-burning

evaporating droplets. The core itself is surrounded by a flame. Outside the core, droplets burn individually. As G increases, the size of the core increases and for G higher than unity, a flame surrounds the whole cloud of droplets. This mode is called external group combustion. Inside the cloud, droplets evaporate at different rates. Those at the cloud surface evaporate faster than those near the centre. For $G > 10^2$, only droplets in a thin layer near the flame at the surface of the cloud evaporate fuel. This last mode is called external sheet combustion. This classification is insightful for real applications. It can be used to analyse an established spray flame in a combustor or for auto-ignition problems of droplet clouds. For example, it was used to interpret the autoignition of a spherical cloud of droplets in a convective environment [40]. Aggarwal [3] discussed the different ignition modes following spray auto-ignition. He also suggested that in turbulent sprays, ignition modes could occur locally in the cloud of droplets [3].

Although the Group Combustion Theory offers global physical insight for burning clouds of droplets, it does not describe the physics of an expanding spray flame. A spherical kernel may have some attributes of Group Combustion, but it also has features of a propagating flame. Little is known about the structure of a spark kernel in a spray [41, 42]. With the limited data obtained, no classification of the structure of a spark kernel as a function of droplet parameters can be given. In premixed gases, the early kernel has been likened to a spherical laminar flame [2]. By analogy, the structure of a kernel in a spray should have features of a laminar flame propagating in a uniform spray. This canonical problem is also useful to describe the ensuing propagating flame. It is reviewed in the next section.

2.2.2 Flame propagation in a uniform spray

In a premixed gaseous laminar flame, with a fixed cold temperature and pressure, the flame structure is only function of the fuel-air ratio. With sprays, for the same overall equivalence ratio ϕ_0 (cumulative mass of gaseous fuel and droplets), the flame

speed and the flame structure are different when varying the droplet diameter a_d and the vapour fraction Ω (relative amount of fuel vapour) [43]. Depending on those parameters, the flame can propagate in the interdroplet spacing if there is sufficient fuel vapour there. Moreover, droplet diffusion flames can occur for sufficiently large droplets (typically $a_d > 20\mu$m) if the interdroplet spacing is not rich [43]. Flame propagation in a uniformly-dispersed spray has been widely studied in the past [44–51]. Insight can be gained by examining the structure of a laminar unstrained spray flame. Such flames may be divided in several zones, as shown in Fig. 2.1. With analytical methods, Silverman et al. [49] distinguished five parts. The first three parts are a primary evaporation zone with a length l, a heating zone, and a "homogeneous" reaction zone. The fuel evaporated in the first two zones reacts in the "homogeneous" reaction zone. Behind it, the surviving droplets keep evaporating at a high rate. If oxygen remains, the fuel burns as soon as it evaporates, in the so-called droplet burning zone. Finally, when there is no more oxidiser, droplets, if any, finish evaporating in a secondary evaporation zone.

An interesting area of fundamental studies of spray flames is that of droplet arrays. In this field, an ordered array of several droplets is studied. In early studies [52, 53], theoretical work demonstrated the influence of one droplet on the evaporation or the combustion of its neighbour. More recent studies have focused on the flame spread in arrays of equally spaced droplets [54, 55]. Under conditions where the fuel existed only in a thin layer near the droplet and the interdroplet spacing contained little or no fuel, these studies reported diffusion flames surrounding droplets. Depending on the interdroplet spacing, different modes of spreading of those diffusion flames were observed and described in Ref. [54]. In their mode 1, the interdroplet spacing is relatively small. The diffusion flame created around one droplet rapidly surrounds the next one and accelerates its evaporation. The higher evaporation rate of this droplet pushes the diffusion flame forward and the flame surrounds the next droplet. In their mode 2, the interdroplet spacing is larger, the diffusion flame created around one droplet reaches the fuel layer evaporated around

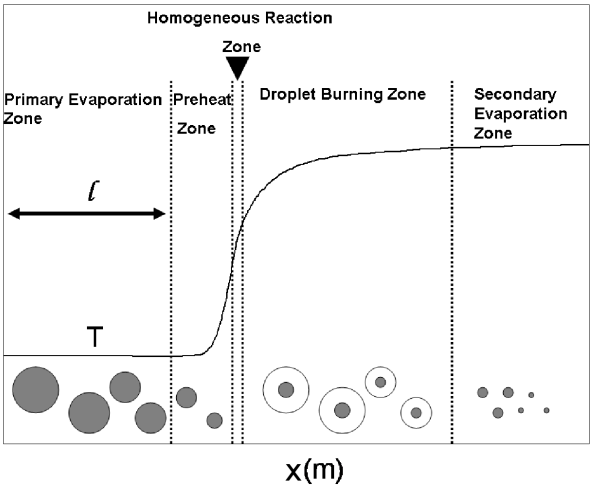

Figure 2.1: Schematic of the temperature profile across a laminar freely propagating premixed spray flame with a large SMD. The post evaporation zone exists in a rich case only. Adapted from Ref. [49].

the next droplet. The fuel layer then ignites and a diffusion flame forms around this droplet. In their mode 3, the interdroplet spacing is even larger. The diffusion flame created around a droplet can only raise the temperature of the next droplet by heat conduction until ignition occurs. Based on this physics, a model of flame propagation in randomly arranged droplet arrays was derived [56]. Those investigations provide valuable insight on the principles controlling flame propagation when little fuel exists in the interdroplet spacing. Results for such configurations will be given in Chapter 5.

Regarding the flame propagation rate, Ballal and Lefebvre [47] showed that as the initial droplet size became relatively large, the flame speed decreased. In addition, very small droplets evaporated before the flame front and resulted in a flame propagation speed slightly lower than the purely gaseous flame due to the evaporation heat loss [43]. An important observation was the existence of an optimum droplet size, in the range 10-30μm (as found by the following references), for a given fuel and overall

equivalence ratio ϕ_0 that resulted in enhanced laminar flame propagation compared to the purely gaseous fuel flame. This enhancement has been observed for the entire range of overall equivalence ratio by Hayashi et al. [57] in a closed volume with laminar flames of ethanol. For overall lean mixtures, a flame speed enhancement was shown experimentally for tetralin [44, 58], n-decane [51], kerosene [59, 60], and ethanol [61]. The phenomenon was attributed to the wrinkling of the flame by the droplets which increased the flame surface area and promoted propagation [57, 62] and to local inhomogeneities of the mixture between droplets leading to optimal equivalence ratio (e.g. diffusion flames around droplets) [46, 51, 54, 63, 64]. With an overall rich flame, the existence of an optimum droplet size was related to the incomplete evaporation of large droplets, which produced a gaseous mixture close to stoichiometry that led to high flame propagation speed. The gaseous stoichiometry at the flame front was denoted "effective equivalence ratio" ϕ_{eff} by Hayashi et al. [57]. It was suggested by theoretical [49], experimental [57, 61] and numerical one-dimensional studies [63, 65] that the optimum conditions were a combination of droplet size and overall equivalence ratio that resulted in ϕ_{eff} near 1. In addition, the fact that regions with stoichiometric mixture fraction exist in an overall too lean or too rich spray also implies a widening of the flammability limits of flames in sprays [3].

Furthermore, investigations of the effect of fuel volatility on flame propagation indicate that less volatile fuel leads to a lower flame speed [63]. This is generally explained by the low evaporation rate of less volatile fuels resulting in low fuel concentration in the gas and thus too low ϕ_{eff}. Studies on the effect of low pressure on spray flames are rare. Still, Ballal and Lefebvre [47] provided valuable results for stoichiometric mixtures of diesel oil and air with a Sauter mean drop diameter (SMD) of 60μm. They showed that the pressure dependence of the flame speed varies from $P^{-0.3}$ with pure gas to $P^{-0.5}$ with sprays.

To conclude, flame propagation in a uniform spray is a complicated problem with many physical aspects. Many studies have shown the enhancement of the flame

speed by droplets of finite size [44, 46, 51, 51, 54, 57, 57–64]. Although a single explanation has not been universally accepted, some guidelines have been suggested: (a) the wrinkling of the flame by droplets widens the flame burning surface; (b) under overall lean conditions, local inhomogeneities of the mixture fraction due to evaporation, possibly leading to flames surrounding droplets, can substantially accelerate the reactions; (c) under overall rich conditions, the amount of fuel evaporated at the flame front by large droplets may be optimum and increase the reaction rates compared to the equivalent rich gaseous mixture. Some more data, and additional explanations, are given in Chapter 3. Measurements of the MIE in premixed sprays are reported next.

2.2.3 MIE measurements in premixed sprays

Spray ignition has been reviewed by Aggarwal [3]. Factors such as initial droplet diameter, fuel volatility, diameter distribution, overall equivalence ratio ϕ_0 and vapour fraction play an important role in the MIE. Moreover, even in sprays without turbulence, where the spray distribution seems uniform at the large scale, ignition is probabilistic. This is because at the spark scale, the distribution of droplets in the flame kernel is random [4]. As with homogeneous mixtures, the MIE was generally defined at 50% ignition probability [3].

It is generally expected that the presence of droplets is detrimental to ignition as they act as additional heat sink for the kernel and because incomplete evaporation reduces the amount of fuel vapour available for flame propagation [3]. For $\phi_0 \leq 1$ and relatively large droplets (typically $\geq 30\mu$m), an important result shown for various fuels is the strong negative dependence of the MIE on the Sauter Mean Diameter (SMD) [3, 41, 66–72]. Rao and Lefebvre [66] observed a spectacular increase of the MIE with mildly increasing SMD in a turbulent flow with kerosene spray. This was attributed to a decrease of the rate at which the fuel evaporated and in turn the amount of fuel burnt in the spark gap. Ballal and Lefebvre also showed that

for $\phi_0 \leq 1$, all parameters which promoted evaporation, such as high volatility and small SMD, reduced the MIE [67, 68, 73]. Another conclusion for $\phi_0 \leq 1$ was that an increase in ϕ_0 induced a decrease in MIE [66, 67, 69–71, 73]. In addition, Ballal and Lefebvre showed that replacing a certain amount of liquid fuel by gaseous fuel resulted in a reduction of the MIE [69]. Note that the experiments reported focused on monodispersed spray (all droplets have the same initial diameter) in order to isolate the effect of the droplet diameter. Spark ignition in polydisperse sprays have also been studied [3] and it was shown that the SMD represents the best the spray behaviour in the ignition of a bidisperse spray [72].

Ballal and Lefebvre [67, 68, 73] carefully studied different fuels and the influence of various droplets and flow parameters on the MIE of overall lean monodisperse sprays. The authors found that the variation of MIE with electrode spacing, spark duration, ϕ_0, turbulence intensity, temperature and pressure followed the same trends as that described for premixed gas spark ignition. The relation $MIE \sim P^{-n}$ was still valid with spray and n varied from 0.5 when evaporation rates were controlling ignition process (i.e. large droplets) to 2 when chemical kinetics were controlling (i.e. small droplets) [69]. Based on their experimental results, Ballal and Lefebvre [69] developed a model to calculate the MIE which assumed that the time required for droplets to evaporate and burn was equal to the time of heat diffusion from the kernel once the critical size was reached. The premise of the model was that the factors which favoured evaporation reduced the MIE. Another model based on time scales has been developed by Peters and Mellor [74].

All the findings reported in this section involved sprays with $\phi_0 \leq 1$. However, if the spark is located in a region where $\phi_0 > 1$, complete evaporation is not preferable since a stoichiometric gas is more favourable to ignition than a rich gas. Under those conditions, a relatively large SMD may be preferred if the amount of fuel evaporated is close to the stoichiometric value [3].

In fact, an important feature is the existence, for all ϕ_0, of an optimum SMD ranging between 10 and 30μm for different fuels [3] which yields MIE smaller than

the gaseous MIE. For $\phi_0 \leq 1$, this was shown experimentally by Danis et al. [70] with n-heptane. For $\phi_0 > 1$, the advantage of relatively large droplets was suggested experimentally by Danis et al. [70], Singh and Polymeropoulos with tetralin [71] and numerically using single-step chemistry for decane in closed volume by Aggarwal and Sirignano [75]. The existence of an optimum diameter is related to the optimum diameter for the flame speed in a uniform spray [3], reviewed in Section 2.2.2.

2.3 Forced ignition in non-premixed gases

Realistic configurations often involve turbulent non-premixed flows. In a turbulent non-premixed flow, the kernel is generated in a spatially and temporally non-uniform mixture and the flame propagates in a stratified mixture. In addition, forced ignition in turbulent non-premixed flows is highly probabilistic and the probability of ignition is used instead of the MIE [4]. First, we present the implications of generating a spark in a laminar non-premixed gas and in a turbulent non-premixed gas. Then, we summarise some findings on the flame propagation in highly stratified mixtures.

2.3.1 Kernel generation in a gaseous mixing layer

Ignition in a non-premixed gas involves spatially varying mixture fraction. The canonical problem is the spark ignition in a fuel-air mixing layer. We might expect that the location of the spark relative to the position of the flammability limits ξ_L and ξ_R, and to the position of the stoichiometric mixture fraction ξ_{st}, will have a large influence on the ignition success. In addition, the width of the spark will have a role because a wide spark may overlap with flammable region even if it is not centred at a flammable mixture fraction. Furthermore, the energy dissipation of the kernel will increase with the mixing layer strain rate. Therefore, the spark location, its width and the local mixing layer strain rate are factors peculiar to non-premixed forced ignition that will impact on the kernel growth. Numerical investigations in

laminar counterflow methane air mixing layer [76, 77] and hydrogen mixing layer [78] showed that ignition was prohibited if the kernel was far away from the stoichiometric contour and if the bulk strain rate was excessive. The effect of the strain rate was attributed to high heat and radical diffusion [77]. Moreover, Ref. [77] showed that the critical strain rate that prevented ignition could be well below the extinction strain rate. In addition, the critical strain rate was reduced if the spark was in a region of the counterflow where the local scalar dissipation rate was high [77]. Furthermore, ignition could occur even if the spark was not within the nominal flammability limits [77]. This was attributed to the finite width of the spark and the heat diffusion from the spark that could ignite flammable mixtures. In case of successful ignition, two reaction zones propagated away from the spark to consume the premixed reactants in the lean and rich parts of the mixing layer denoting a tribrachial structure [77]. Forced ignition experiments of laminar non-premixed mixtures are rare and focused on the successful stabilisation of a flame following laser ignition in jets, e.g. Ref. [79]. Forced ignition in turbulent non-premixed flows has been more widely studied and is presented next.

Previously, we saw that in premixed flows turbulence introduced a stochasticity in the ignition process due to the randomness of the strain rate at the moment and the location of the spark. In a non-premixed gas, the fluctuations of the mixture fraction make ignition even more probabilistic. For this reason, the concept of ignition probability is preferred to the MIE [4, 80]. In early experiments on ignition probability, Smith et al. [80, 81] studied turbulent jets of natural gas or propane. They used a fixed electrode gap, spark duration and a spark energy well above the MIE of the homogeneous mixtures at stoichiometry. The spark duration was taken as small as possible, relatively to the eddy integral timescale, in order to "freeze" the value of the mixture fraction at the spark. In the experiment, the probabilistic nature of the ignition was observed and the probability P_{ker} of initiating a kernel that fully developed was distinguished from the probability P_{ign} that the flame successfully propagated upstream and ignited the whole jet [81]. The spatial contour of the

probability P_{ker} was compared to the measurement of a flammability factor F [80]. The flammability factor was defined as the local probability of finding a flammable mixture

$$F = \int_{\xi_L}^{\xi_R} P(\xi) d\xi \tag{2.3}$$

where $P(\xi)$ was the mixture fraction PDF measured at every point. It was shown that on the axis, P_{ker} was similar to F and that P_{ker} could be positive outside the mean flammability limit. It was concluded that the mean mixture fraction contours are not meaningful to define the boundary of ignition and that fluctuations and intermittency of the mixture fraction have an influence on the ignition success and thus on P_{ker} [80]. It was thought that the instantaneous mixture fraction at the spark would determine if the kernel would grow or not. Furthermore, it was found that P_{ign} became very different from P_{ker} if the spark was deposited further than a certain downstream position [81]. This was also observed in other studies of turbulent methane jets [82, 83]. These references suggested that if the kernel was created downstream of a certain distance, the mean flow would convect it downstream beyond the mean lean contour. By the time it becomes a self sustained flame, the local mixture fraction would be too lean to help the flame propagating against the flow velocity and the flame would be blown out. Note also that Ahmed et al. [82] showed that P_{ign} could be increased with a longer spark duration, attributed to the higher probability of sampling flammable mixture at the spark location.

The ignition probability has also been examined in other configurations. Ahmed et al. [84] studied a turbulent non-premixed methane air counterflow configuration to examine the effect of the global strain rate on F and the ignition probability along the centreline. An increase of the bulk velocity resulted in a decrease of P_{ign} due to the detrimental effect of the higher bulk strain rate on the kernel growth. The maximum strain rate that could allow ignition was not higher than 90% of the extinction strain rate. Ahmed et al. also compared the contours of F and P_{ign} and found that ignition could be achieved even if the spark was created in a region

where there was virtually zero probability of finding flammable mixture [84]. The suggested explanation was that the finite size of the kernel, the heat diffusion from it and the kernel convection toward the stagnation plane could ignite flammable mixture. This was in agreement with the beneficial effects of transport mentioned for laminar mixing layers [77]. The findings are also supported by DNS work of kernel generation in a turbulent methane-air mixing layer [85], where the long range effect of the spark was demonstrated. In addition, it was shown that kernel development was favoured in regions of low turbulent scalar dissipation while misfire occurred for sufficiently high turbulence intensities [85].

The author is not aware of previous work related to spark ignition in a simplified non-premixed configuration with spray. Chapter 4 focuses on this problem. Most of investigations that involved non-premixed spray were done in realistic configurations and are presented in Section 2.4.

2.3.2 Flame propagation in a gaseous mixing layer

The propagation of a flame in a mixing layer, subsequent to the kernel growth, takes place along the stoichiometric contour. If the fluctuating mixture fraction remains on the lean side only or the rich side only, the flame is called stratified-charge premixed flame and its propagation is understood through the concept of premixed flame [86]. If the mixture fraction fluctuates around stoichiometry and takes both lean and rich values, the flame front will propagate with a lean branch, a rich branch and a trailing diffusion flame. This configuration is called triple flame or tribrachial flame and becomes an edge flame when the strain rate is high so that the lean and rich branches merge [87]. The point where the flame lean, rich and stoichiometric fronts merge into one is called triple point. In this section, we focus on the triple flame structure.

The triple flame and edge flame structures and their speed have been studied in their laminar form [78, 79, 87–91]. Phillips [88] early observed the triple flame and

noticed that the flow was disturbed as it approached the triple flame front. The heat release expansion caused the streamlines to diverge away immediately ahead of the triple flame thereby causing a decrease of the flow velocity. Two flame propagation velocities can be defined: the velocity relative to the disturbed flow at the triple point, lower but close to $S_{L,0}$, and the velocity relative to the upstream undisturbed flow which can exceed $S_{L,0}$. The velocity relative to the disturbed flow at the triple point decreases with increased strain rate and it is bounded by the stoichiometric laminar flame speed $S_{L,0}$ [89, 91]. This is because a higher strain rate increases the heat lost by the edge flame on its side and ahead of it. Nevertheless, due to the diverging effect of heat release, the propagation velocity relative to the upstream undisturbed flow can be greater than the planar flame speed. Reutsch et al. [91] estimated the far field velocity for an infinitely long freely propagating laminar edge flame, in the limit of sufficiently low scalar dissipation, through the expression $S_{L,0}(\rho_u/\rho_b)^{1/2}$ with ρ_u and ρ_b the unburnt and burnt density of the gas respectively. The acceleration of laminar triple flames by the flow divergence effect has been observed experimentally [79, 92, 93] and numerically [94] and the importance of flame curvature was recognised. Interestingly, an increase in mixing layer strain rate reduces both flame propagation velocities and can even result in retreating fronts [87] as observed experimentally by Cha and Ronney [92]. Furthermore, a too large strain rate can lead to extinction and the associated critical strain rate is lower than the extinction strain rate of an established diffusion flame [87]. Cha and Ronney [92] also observed that the laminar edge flame speed increased with fuels associated with low Lewis number.

The propagation of turbulent edge flames has been little investigated so far. Interesting results from the stabilisation of lifted flames in turbulent non-premixed jet has been reviewed by Lyons [95]. The stabilisation of the flame base by a propagating edge flame has been evidenced and it was found that in turbulent flows, the edge flame also disturbs and slows down the flow ahead of it by diverging streamlines due to heat release [96]. Heeger et al. [97] measured the edge velocity relative to the

disturbed flow in a turbulent counterflow and found an average value of $0.75S_{L,0}$ consistent with laminar predictions [89]. Two-dimensional DNS with detailed chemistry were performed by Ray el al. [98] with a methane jet, who found that after igniting on the rich side, a kernel propagated towards the stoichiometric region and then left two turbulent edge-flames propagating in each direction of the stoichiometric line. Chakraborty et al. carried out three-dimensional DNS study of ignition in stagnant turbulent methane-air mixing layer and the subsequent propagation of the flame [14, 85, 99]. The spark was simulated by using a source term in the energy equation and the turbulence Reynolds number remained low. They showed that as the flame expanded, it first took the form of a triple flame and became an edge flame at later stages as the lean and rich fronts merged [14]. Measurements showed that the velocity relative to the disturbed flow depended on the scalar dissipation rate, the local flame curvature and the fuel mass fraction gradient [99]. The most probable value of the edge flame speed relative to the undisturbed flow was found to be close to $S_{L,0}(\rho_u/\rho_b)^{1/2}$ at low turbulent levels and decreased as the turbulence intensity increased [14]. This showed that the turbulent edge flame behaved as a strained laminar edge flame. As the turbulence intensity increased, the heat loss ahead of it and on its sides increased, and the flame speed decreased from the laminar edge flame speed [14]. We can conclude that relatively low turbulence levels not only have a detrimental effect on the kernel growth due to increased strain rate [85] but also on the subsequent edge flame propagation [14]. This is contrary to premixed ignition where the propagation phase is promoted by low turbulence levels due to the increase in flame burning area. Consequently, in non-premixed ignition, adverse conditions to the propagation of an edge flame will intensify the difference between P_{ker} and P_{ign}.

The flame propagation in a simplified non-premixed configuration with spray has received little attention. Reveillon and Vervisch [100] have recently described the propagation of a flame along a jet of dilute fine spray and classified different regimes in a group combustion diagram. Under conditions where the core of the spray was

rich, a tribrachial structure was observed. It has also been observed experimentally [101] and with DNS [102] that the stabilisation zone of a lifted spray flame had a tribrachial structure. More work is required to understand the flame structure in a non-premixed spray. Such work is presented in Chapter 4 and 5.

2.4 Forced ignition of realistic flows

Studies presented so far have been carried out on simplified academic configurations although many results are relevant for industrial applications. However, realistic configurations involve high flow velocities, strong turbulence, recirculation zones and swirl. This can lead to a different flame development from that observed in simplified flows. Hence, it is important to understand the relative importance of these fluid mechanics effect. In this section, we summarise findings regarding the ignition and the flame development in realistic configurations. These investigations are few, but they offer interesting discussion on the ignition behaviour. First, we present work performed with realistic academic burners. Then we present studies with practical combustors.

2.4.1 Academic burners

In Section 2.3.1, we reported investigations of the ignition probability in turbulent non-premixed jet and counterflows. Measurements of the ignition probability have also been performed in turbulent bluff-body flows with methane [103] and hydrogen-air burner [104] with recirculation zones. As with previous studies, ignition was favoured by flammable mixtures and low turbulence levels. Zimmer et al. [104] measured the instantaneous local mixture fraction at the moment of the spark but found no clear correlation with P_{ign}. Ahmed et al. [103] showed that P_{ker} was below F. They attributed this discrepancy to the bulk and turbulent strain rate at the spark location which could hinder the early development of the kernel. For example,

they showed that sparking inside the recirculation zone, despite it having $F \simeq 1$, led to low P_{ker}. This was attributed to the rich mixture and the high turbulence there. Near the rich limit, the turbulence easily quenched the kernel. Ahmed et al. [103] discussed the flame propagation and ignition process and showed the influence of the flow convection. It was observed that downstream of the recirculation zone the mixture was flammable and that a kernel could be generated there. However, the flame had to propagate against the flow which was difficult due to the high convection [103]. This resulted in a large difference between P_{ker} and P_{ign}, the latter being almost zero. It was also suggested that successful ignition was favoured on the side of the recirculation zone because the flow convected the kernel along the stoichiometry contour. The large amount of gas ignited increased the likelihood that burned material diffused into the recirculation zone and eventually ignited the burner [103]. In this case, successful propagation was aided by the flow convection. LES simulations of this configuration also showed that the establishment of a flame following ignition was faster when sparking in optimum regions of stoichiometry and that convection of the kernel was a driving factor for the flame propagation [105, 106] .

A similar investigation was carried out by Marchione et al. [107] with an academic configuration of a swirling burner using n-heptane. The mean local SMD and ϕ_0 were measured in the turbulent flow field but the relative amount of fuel vapour was not determined. Results were presented with a single spark and with a multiple spark. With the single spark, it was found that P_{ign} was high if the spark was located in regions of relatively small SMD and with a mean ϕ_0 within the flammability limits. Moreover, ignition was facilitated in regions of negative velocity which convected the kernel inside the recirculation zone and resulted in easier flame establishment. Successful overall ignition was associated with kernels that moved without getting extinguished towards the bluff body [107]. The multiple spark was placed on the wall in a region very lean on the average where a single spark could not ignite. The ignitor produced spark sequences lasting 1 to 5s, each spark lasting 8ms, and

its position could be varied axially. It was shown that the spark was stretched away from the electrodes by turbulence and that a long spark sequence increased ignition efficiency. It was suggested that the energy deposited by multiple sparks and the spark stretching in a turbulent flow can have spatially far reaching effect to initiate combustion [107]. This shows the importance of transport effects mentioned in Section 2.3.1 for mixing layer configurations. In addition, the ignition probability reached a maximum of 100% where the recirculation zone had maximum width [107]. At this location the kernel was more easily bodily convected towards the recirculation zone.

2.4.2 Practical combustors

The importance of spark ignition for aviation gas turbine has encouraged the investigation of relight at altitude conditions in aviation gas turbines [1, 108–112], although they remain limited. However, in such configurations, parametric investigations as thorough as the one presented for academic burners are harder to perform. The conclusions of those studies are reported herein.

Foster and Straight studied the MIE in a turbojet combustor at ground and altitude conditions [108]. They concluded that well atomised and high volatile fuel were easier to ignite. Furthermore, Read et al. [111] have carried out the imaging of the flame motion following spark ignition in a low pressure, low temperature combustor. They have shown that in realistic configuration with strong convection of the flow, successful ignition was promoted by a flowfield which convected the spark kernel from the electrodes towards the fuel injector. Since the kernel remained small during this process and since its motion was dominated by the gas-phase velocity rather than flame propagation, the success of ignition was deemed to be characterised by the ability of the kernel to survive long enough to reach the main recirculation zone [111]. Mosbach et al. [112] studied an industrial combustion chamber at low pressure and low temperature and also found that successful ignition was associated

with a kernel that moved upstream towards the injector. Hence, in contrast to the jet or counterflow configurations, high flame speeds do not directly imply an expansion towards the rim of the burner but instead decrease the odds that the kernel will shrink before being brought to the injector by the flowfield. This agrees with the results in recirculating academic burners discussed earlier [107] and is substantiated by a recent LES calculation of the ignition in a full helicopter gas turbine combustion chamber [110]. There, two key phenomena were suggested to explain the propagation of an initial hot volume of gas from one burner to the other: First, the hot gas volume was captured by the recirculation zone of a neighbouring burner and reached the flammable mixture near the injector. Once the burner was ignited, the expansion of burning gas enabled to thrust the flame front rapidly towards the next burner. It was proposed that the propagation speed was then largely enhanced.

These studies have shown that the understanding of simple configurations help the interpretation of the ignition behaviour of complex geometries. In addition, they showed that the flow convection has a dominant effect over the flame propagation.

2.5 Area of future research

In this review, we summarised research material on ignition of premixed gas, premixed spray, non-premixed gases and realistic burners. We saw that substantial knowledge has been collected for premixed gas forced ignition and that a large amount of MIE data is available for the forced ignition of premixed sprays.

However, the physics associated with a spark kernel in a spray is little understood. The interpretation of the kernel development can be done by referring to the canonical problem of a one-dimensional flame freely propagating in a uniform spray. Nevertheless, progress in this area is still required. A parametric study of the structure and the speed of such a flame is performed in Chapter 3. Moreover, the kernel growth in a premixed spray is studied with complex chemistry 3D DNS in Chapter 5. Furthermore, we saw that the simplified problem of ignition and flame

propagation in a spray mixing layer has received very little attention. It is expected that findings with this configuration helps to understand forced ignition in real flows. Spark ignition and flame propagation in a spray mixing layer is studied in Chapter 4. Finally, we saw that in realistic configurations, fundamental findings offer insight for the success of the spark and that the flow convection drives the flame propagation process. A model for the computation of ignition probabilities that attempts to incorporate the physics that dominate in realistic flows is presented in Chapter 6.

Chapter 3

One dimensional simulation of laminar spray flames

3.1 Introduction

In Section 2.2.2 of Chapter 2, we have summarised findings on the flame propagation in a uniform spray. It is important to understand this problem for the propagation phase of forced ignition. It also has the potential of offering insight in the spark kernel structure. The typical flame structure presented Fig. 2.1 has not been explored in detail with complex chemistry simulations so far. Moreover, we mentioned in Section 2.2.2 that the concept of effective equivalence ratio offered an interesting approach for the interpretation of the flame propagation speed. In this chapter, we attempt to elucidate the effects of droplet size, overall equivalence ratio and the residence time of droplets before the flame (which affects the degree of pre-evaporation) and we examine the importance of complex chemistry. Finally, we look at the effect of high altitude (relight) conditions, i.e. low pressure and low temperature, on the flame speed since few investigations have focused on this regime. In order to examine the effects of fuel volatility, n-heptane and n-decane are used as typical fuels with high and low volatility respectively. n-Heptane is employed in academic

configurations [107] while n-decane is used as a surrogate for kerosene [113].

The numerical model implemented is presented in the next section, followed by the results and their discussion. The particular features revealed by the use of complex chemistry are emphasized, and summarised in the conclusion.

3.2 Numerical formulation

The code Run1DL [65, 114, 115] is used here. The spray is assumed to be monodisperse. The coupling between the gas and the liquid phase implemented in the code is essentially the same as the one presented by Abramzon and Sirignano [116]. The code solves a one-dimensional form of the governing equations with a distance coordinate x. A steady solution with constant pressure is presented. This one-dimensional formulation corresponds to an integrated form of the problem over a plane orthogonal to the flow. The governing equations are repeated below for completeness.

3.2.1 Gas Phase

The Eulerian gas phase equations include a source term from the liquid phase. Assuming a dilute spray allows the treatment of the spray in a simple statistical manner: the source term for a particular scalar is equal to the scalar production from one droplet multiplied by the number of droplets per unit volume n. The conservation of mass, species, momentum and absolute enthalpy and the ideal equation

of state in the gas-phase are given by

$$\frac{\partial(\epsilon\rho)}{\partial t} + \frac{\partial(\epsilon\rho U_x)}{\partial x} = \Gamma_m \tag{3.1}$$

$$\frac{\partial(\epsilon\rho Y_i)}{\partial t} + \frac{\partial(\epsilon\rho Y_i U_x)}{\partial x} = -\frac{\partial(\epsilon\rho Y_i V_i)}{\partial x} + \epsilon\omega_i + \Gamma_{m,i} \tag{3.2}$$

$$\frac{\partial(\epsilon\rho U_x)}{\partial t} + \frac{\partial(\epsilon\rho U_x U_x)}{\partial x} = -\frac{\partial P}{\partial x} + \frac{\partial}{\partial x}(\epsilon\mu\frac{\partial U_x}{\partial x}) + \Gamma_{U_x} \tag{3.3}$$

$$\frac{\partial(\epsilon\rho h)}{\partial t} + \frac{\partial(\epsilon\rho h U_x)}{\partial x} = \frac{\partial}{\partial x}(\epsilon\lambda\frac{\partial T}{\partial x}) - \frac{\partial}{\partial x}(\epsilon\sum_i \rho Y_i V_i h_i) + \Gamma_h \tag{3.4}$$

$$P = \rho RT(\sum_i \frac{Y_i}{W_i}) \tag{3.5}$$

The gaseous properties used in those equations are the density of the gas, ρ, the one-dimensional velocity U_x, the pressure P, the mass fraction of species i, Y_i, the chemical production of species i, ω_i, the viscosity μ, the temperature T, the conductivity λ, the mixture enthalpy $h = \sum_i Y_i h_i$, the absolute enthalpy of species i, h_i, the ideal gas constant R and the molecular mass of species i, W_i. The diffusion velocities V_i are calculated by $V_i = -\frac{D_i}{X_i}\nabla X_i + V_c$ where D_i is the mixture averaged diffusion coefficient of species i and V_c is a correction velocity used to enforce the constraint $\sum_i \rho Y_i V_i = 0$. Moreover, $\epsilon = 1 - n\frac{\pi}{6}a_d^3$ is the void volume fraction defined as the volume occupied by the gas only divided by the total volume. For our simulations $0 \leq 1 - \epsilon \leq 10^{-4}$ which supports the assumption of dilute spray. The liquid source terms are given by

$$\Gamma_m = n\dot{m} \tag{3.6}$$

$$\Gamma_{U_x} = -n[\frac{d(m_d v_{d,x})}{dt}] \tag{3.7}$$

$$\Gamma_h = -n[\dot{m}\frac{C_{P_f}}{B_{T,d}}(T(\mathbf{x}_d, t) - T_d^s) - \dot{m}h_F(T_d^s) + \frac{1}{2}\frac{dm_d \mathrm{v}_{d,x}^2}{dt}] \tag{3.8}$$

where $\dot{m}$ is the mass evaporation rate of the droplet, m_d is the instantaneous mass of the droplet, x_d is the coordinate of the droplet, $v_{d,x}$ is the velocity of the droplet, T_d^s is the surface temperature of the droplet, C_{P_f} and C_{P_F} are respectively the

film heat capacity and the heat capacity of the fuel vapour calculated at the thin film temperature. The liquid source term for species i, $\Gamma_{m,i}$, is zero except when we consider the fuel and then $\Gamma_{m,F} = \Gamma_m$. In Eq. 3.8, the first term represents the convective heat transfer. The second term represents the enthalpy of the evaporated fuel at the droplet surface temperature T_d^s. The third term corresponds to the variation of the kinetic energy of the droplets.

3.2.2 Liquid Phase

The liquid phase is computed in a Lagragian manner by tracking one individual droplet and solving the associated equations for its mass, momentum and energy. A thin film assumption is used to calculate the droplet evaporation and heat exchange with the surroundings [116]. The parameters inside the thin film, denoted f, are taken as average between the droplet surface and the gas properties. The interpolation of gas phase properties at the droplet location is explained later. The variation of the mass of a droplet is given by

$$\frac{dm_d}{dt} = -\dot{m} \tag{3.9}$$

$$m_d = \rho_L \frac{1}{6}\pi a_d^3 \tag{3.10}$$

where a_d is the instantaneous diameter of the droplet and ρ_L is the density of the liquid fuel. The rate of evaporation $\dot{m}$ is calculated using a corrected Sherwood number $\mathrm{Sh_c}$ and the thin film properties. The Sherwood number and the Nusselt number are corrected through a function $F(B) = \frac{\ln(1+B)}{B}(1+B)^{0.7}$ so as to take into

account the change in film thickness due to the Stefan flow [116]. Hence,

$$\dot{m} = \pi a_d \rho_f D_f \mathrm{Sh_c} \ln(1 + B_{M,d}) \tag{3.11}$$

$$\mathrm{Sh_c} = 2 + \frac{1}{F(B_{M,d})}[(1 + \mathrm{Re_d Sc})^{1/3} \max(1, \mathrm{Re_d})^{0.077} - 1] \tag{3.12}$$

$$\mathrm{Re_d} = \frac{\rho_f a_d |U_x(\mathbf{x}_d, t) - v_{d,x}|}{\mu_f} \tag{3.13}$$

$$B_{M,d} = \frac{Y^s_{F,d} - Y_F(\mathbf{x}_d, t)}{1 - Y^s_{F,d}} \tag{3.14}$$

where ρ_f is the thin film density and D_f is the binary diffusion coefficient of fuel vapour inside the thin film. $\mathrm{Re_d}$ is the droplet Reynolds number, always below 100 in our problem, and μ_f is the film viscosity. The mass fraction of fuel at the droplet surface $Y^s_{F,d}$ is found through the Clausius-Clapeyron equation by assuming phase equilibrium at the droplet surface

$$Y^s_{F,d} = \frac{W_F X^s_{F,d}}{W_F X^s_{F,d} + (1 - X^s_{F,d})\overline{W}} \tag{3.15}$$

$$X^s_{F,d} = \frac{P_{ref}}{P} \exp[\frac{L_v}{R}(\frac{1}{T_{ref}} - \frac{1}{T^s_d})] \tag{3.16}$$

where P_{ref} and T_{ref} are state reference pressure and temperature, W_F is the molecular mass of the fuel and $\overline{W}$ is the molecular mass of the mixture excluding the fuel. L_v is the latent heat of evaporation at the boiling point. For n-heptane, $P_{ref} = 1$bar, $T_{ref} = 371.58$ K and $L_v = 31.80$ kJ/mol. For n-decane, $P_{ref} = 1$ bar, $T_{ref} = 447.30$ K and $L_v = 39.70$ kJ/mol.

Inter-droplet interactions and gravity being neglected, the drag force only affects the droplet movement and the momentum equation reduces to

$$\frac{d^2 x_d}{dt^2} = \frac{18\mu_f}{\rho_L a_d^2}[1 + \frac{\mathrm{Re_d}^{2/3}}{6}](U_x(\mathbf{x}_d, t) - v_{d,x}) \tag{3.17}$$

In one-dimension, the conservation equation for the flux of droplets becomes

$$n v_{d,x} = n_0 v_{d,x0} \tag{3.18}$$

where 0 denotes the conditions at the cold boundary.

The internal droplet temperature is calculated by a finite-conductivity model [117]. The temperature within the droplet, assumed to be a sphere, is given by

$$\frac{\partial T_d}{\partial t} = D_{th}^L \frac{1}{r^2}\frac{\partial}{\partial r}(r^2\frac{T_d}{r}) \tag{3.19}$$

with D_{th}^L the thermal diffusivity of the liquid and r the radial coordinate in the droplet framework. The droplet is subject to the initial condition

$$T_d(r,0) = T_{d0} \tag{3.20}$$

and the boundary conditions

$$\frac{\partial T_d}{\partial r}(r=0) = 0 \tag{3.21}$$

$$\frac{\partial T_d}{\partial r}(r=\frac{a_d}{2}) = \frac{\dot{q}}{\pi a_d^2 D_{th}^L \rho_L C_P^L} \tag{3.22}$$

where C_P^L is the heat capacity of the liquid fuel. The surface temperature, T_d^s, is found by solving Eq. (3.22) in which $\dot{q}$ is found through [116]

$$\dot{q} = \dot{m}[\frac{C_{P_f}(T(\mathbf{x}_d,t)-T_d^s)}{B_{T,d}} - \frac{L_v}{W_F}(\frac{T_{crit}-T_d^s}{T_{crit}-T_{ref}})^{0.38}] \tag{3.23}$$

$$B_{T,d} = (1+B_{M,d})^{\zeta}-1 \tag{3.24}$$

$$\zeta = \frac{C_{P_F}\mathrm{Sh_c}}{C_{P_f}\mathrm{Nu_c Le_F}} \tag{3.25}$$

$$\mathrm{Nu_c} = 2+\frac{1}{F(B_{T,d})}[(1+\mathrm{Re_d Pr})^{1/3}\max(1,\mathrm{Re_d})^{0.077}-1] \tag{3.26}$$

where Le_F is the Lewis number of the fuel vapour in the thin film. $\mathrm{Nu_c}$ is the corrected Nusselt number. The critical temperature T_{crit} is 540.15 K for n-heptane and 619.0 K for n-decane. In Eq. 3.23, the first term is the convective heat transfer at the droplet surface while the second term is the heat lost due to evaporation. Note that the second term is temperature dependent.

On the left boundary, droplets have a uniform temperature which is the cold gas temperature and their velocity is the cold gas velocity. The flame speed is given as the speed of the fluid at the cold boundary. An initial flame speed is provided and iterations are performed until a steady state is established. The procedure for the

coupling of the two phases is as follows. First, the liquid phase equations are solved using the initial field of the gas phase and liquid source terms are calculated. This is done with a high-order accurate ODE solver whose maximum time-step size is selected sufficiently small for at least two liquid-phase solution points to lie in each gasphase control volume. This ensures that in each gasphase control volume linear interpolation of the liquid-phase source terms on the Eulerian nodes is meaningful and sufficiently accurate. A local source term is attributed to each Eulerian node, without smoothing being added, and the gas-phase equations are solved. The liquid phase is then solved anew based on the new gas field. The iterations are repeated until convergence is achieved. As indicated in Section 3.3.2, convergence was not always achieved (e.g. with large equivalence ratio and small droplets).

It is important to mention that the evaporated fuel mixes instantaneously with the gas and that the source term exists everywhere in space where $a_d > 0$. As said before, this one-dimensional formulation could be viewed as an integrated form of the problem over a plane orthogonal to the flow. This precludes inhomogeneities in the mixture fraction due to evaporation and flames surrounding individual droplets. Hence, we cannot expect the flame speed enhancement due to local inhomogeneities discussed earlier in Section 2.2.2.

The overall equivalence ratio ϕ_0 was determined by the incoming mass fluxes of gaseous air, gaseous fuel and liquid fuel. At the cold boundary, the mass flux of gaseous fuel was set to zero so that the liquid fuel flux only determined the overall equivalence ratio.

Adaptive gridding based on all variables was used and grid independence was ensured with about 160 points for all solutions. The gaseous flame speeds were validated at atmospheric conditions against experimental and other numerical data and yielded good agreement but are not presented here for the sake of brevity.

In this study, we examine the effect of the overall equivalence ratio ϕ_0, the initial droplet diameter a_d, the length of the primary evaporation zone l, the fuel and the ambient conditions (T_0,P_0) on the flame propagation. Table 3.1 summarises the

conditions investigated.

Table 3.1: Range of conditions studied. Case C is referred to as "relight".

	T_0(K)	P_0(bar)	ϕ_0	a_d(µm)	l(mm)	fuel
case A	298	1	0.6-6	5-140	2-25	n-heptane
case B	298	1	0.6-6	5-140	2-25	n-decane
case C	265	0.4137	0.6-6	5-140	2-25	n-decane

3.2.3 Chemical Mechanisms

For n-heptane, we used a skeletal mechanism [118] developed to describe high-temperature oxidation and pyrolysis (107 species and 723 reactions). The mechanism has been validated at atmospheric conditions against extensive experimental data including premixed laminar flame speed, variable pressure flow reactor, shock tube ignition delay and jet-stirred reactor species profiles with remarkably good agreement [118]. Low-temperature oxidation chemistry, however, is not included.

For n-decane, the skeletal mechanism of Ref. [119] which predicts high-temperature oxidation and pyrolysis was used. This mechanism comprised 86 species and 641 reactions and was validated at atmospheric pressure for laminar flame speed, oxidation in flow reactor [119] and strain rate extinction limit [120]. It was also validated for ignition delay at high and low pressure (down to 0.3 bar) [119]. To our knowledge, no validation was done for reactant temperatures lower than 300 K. We use this mechanism for high altitude relight conditions anyway (i.e. 230-260 K), in anticipation of the fact that the chemical reactions responsible for flame propagation occur at high temperatures and that these do not change much with the lower initial reactant temperature. Polynomials whose range of validity was above 300 K were used to compute thermodynamic properties although it is recognised that extrapolation to lower temperature is not a good option.

The gaseous flame speeds were validated with the code at atmospheric conditions

against experimental and other numerical data, see Ref. [118] for n-heptane and Ref. [119] for n-decane.

3.3 Results

In this Section, we present the dependence of the flame speed on various factors for the case denoted A in Table 3.1. The other cases are qualitatively similar and are mentioned only when significant differences exist. Results specific to cases B and C, concerning the influence of the fuel and the ambient conditions, are presented in Sections 3.3.3 and 3.3.4.

3.3.1 Typical spray flame structure

Before we introduce results regarding the flame speed, we compare, at an overall equivalence ratio ϕ_0=1, the structure of a gaseous n-heptane flame with two types of n-heptane spray flames: one, with an initial diameter a_d=10 µm, is similar to a gaseous flame while the other, with a_d=50 µm, is more characteristic of spray combustion. In Figs. 3.1-3.4 we present the variations of the temperature, the heat release and mass fractions of the main species through the simulated flame. The heat release has been normalised by the maximum value of the heat release of the stoichiometric gaseous flame. We can see in Fig. 3.1 that the temperature profile is very close to the gaseous case with a_d=10 µm while it differs substantially with big droplets. Moreover, we can observe in Fig. 3.2 that the heat release with small droplets is very similar to that of the gaseous case, that is with a pronounced thin peak. This is due to the large extent of fuel evaporated before reaching the flame. The plots of the mass fractions (Fig. 3.3) show that the biggest droplets provide little fuel vapour before the flame front. The resulting lean mixture reacts less intensively and this explains why the peak of heat release is lower in the case of the big droplets (Fig. 3.2). Nevertheless, the large droplets keep evaporating

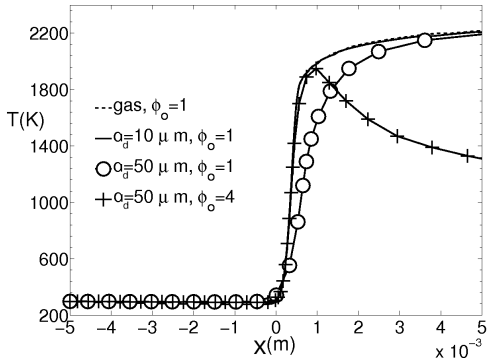

Figure 3.1: Temperature variation through n-heptane flames with l=5 mm and the indicated equivalence ratio and droplet size.

after the "homogeneous" reaction zone. The fuel is then consumed as soon as it is generated in a droplet burning zone. This can be deduced from Figs. 3.3 and 3.4, where Y_{O_2} and Y_{CO_2} respectively decreases and increases slowly over a relatively long length behind the flame front. Here, the oxidation continues until droplets finish evaporating and finally disappear. The reactions are complete with big initial droplets although the rate at which they occur is slower. The description presented here agrees well with the structure of a spray flame presented in Section 2.2.2.

3.3.2 n-Heptane flame

Figure 3.5 presents the variation of the flame speed with the initial droplet diameter for three different ϕ_0 and for different lengths l of the primary evaporation zone.

For $\phi_0 = 1$, the general trend is that the flame speed is reduced as the droplet diameter increases. As the droplet size falls below 30 μm, the flame speed comes close to the gaseous flame speed at the same overall equivalence ratio. This agrees well with previous findings [44, 57, 63]. It is also evident that the flame speed is not a monotonic function of the droplet size and that a maximum exists at a finite droplet diameter. The corresponding optimum diameter increases from 14 μm to 25

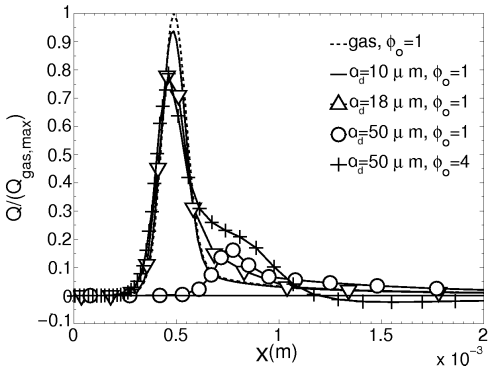

Figure 3.2: Heat release through n-heptane flames with l=5 mm and the indicated equivalence ratio and droplet size.

μm when the residence length l varies from 2 to 25 mm. This range of diameters has been interpreted as a transition range below which the flame behaves like a gaseous flame [58]. Figure 3.5 also compares our data with a theoretical formula based on considerations of evaporation rates and chemical reaction rates in the framework of steady flames and $\phi_0 \leq 1$. The expression given by [47] is:

$$S_{L,0} = D_{th}[\frac{C_3^3(1-\Omega)\rho_L D_{32}^2}{8C_1\rho \ln(1+\mathrm{B_{M,d}})} + \frac{D_{th}^2}{S_{L,0}^2}]^{-0.5} \quad (3.27)$$

D_{32} is the Sauter Mean Diameter at the start of the preheat zone and $B_{M,d}$ the transfer number. D_{th} and ρ are respectively the thermal diffusivity and the density of the gas at 1200 K. $S_{L,0}$ is the gaseous flame speed at the same overall stoichiometry. For a monodisperse spray containing no fuel vapour, the vapour fraction Ω is equal to 0 and $C_3 = C_1 = 1$ [69]. An effective evaporation constant was employed $\lambda_{eff} = \frac{8D_{th}\rho}{\rho_L}\ln(1+B_{M,d})$. λ_{eff} was plotted for various conditions and was evaluated at 1200 K [48]. For n-heptane, λ_{eff}=4.7 mm^2/s while for n-decane, λ_{eff}=3.8 mm^2/s. The good agreement for a_d ≥30 μm implies that the basic premise of the theory is substantiated from the complex chemistry and complex transport simulations presented here.

At an overall lean equivalence ratio ϕ_0=0.6, we observe the same trend. There is

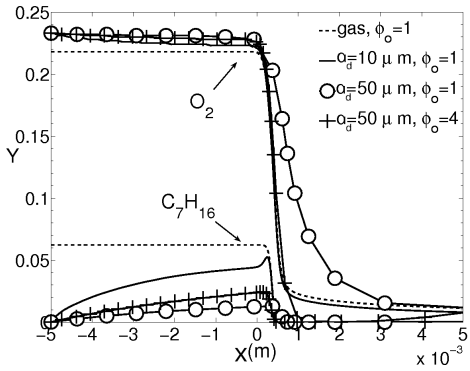

Figure 3.3: Reactants mass fractions through n-heptane flames with l=5 mm and the indicated equivalence ratio and droplet size.

an optimum droplet that increases from a_d =26 µm to a_d =34 µm as l is made longer, see Fig. 3.5a. As mentioned in the Introduction, enhanced flame speed for finite size was observed in past studies. However, the phenomenon was often attributed to diffusion flames surrounding droplets and burning at optimum stoichiometry. The model we use precludes the occurrence of such diffusion flame, see Section 3.2.2.

Finally, Fig. 3.5c also depicts the flame speed against the initial droplet diameter for $\phi_0 = 4$. A gaseous flame cannot propagate at $\phi_0 = 4$, whereas the droplet flame can. Let $S_{L,0}$ be the gaseous flame speed at an overall equivalence ratio $\phi_0 = 1$. We can infer from the graph that as the droplet diameter decreases from a_d =140 µm, the flame speed increases. It also reaches a value *higher* than $S_{L,0}$ for a droplet diameter between 50 and 90 µm, depending on the degree of pre-evaporation. Although this is not supported clearly by the curves in the graph, because convergence of the code was not achieved with very small droplets, we can expect very small droplets to behave like a gaseous flame and thus to result in very low flame speeds. Following this reasoning, there should be an optimum droplet size for which the flame velocity is maximum. As we will explain later, this optimum droplet size should depend on the length l which affects the degree of evaporation. In Section 3.4.1 we will relate the flame speed to an effective equivalence ratio ϕ_{eff} calculated inside the flame,

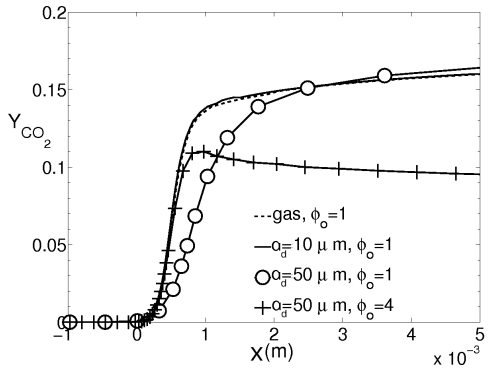

Figure 3.4: CO_2 mass fraction through n-heptane flames with l=5 mm and the indicated equivalence ratio and droplet size.

while in Section 3.4.2 we will discuss an explanation for the flame acceleration above $S_{L,0}$.

Figure 3.6 shows the variation of the flame speed with ϕ_0 for different droplet diameters at a fixed length l=5 mm. For a fixed initial droplet diameter, the laminar flame speed follows the same trend as the gaseous flame speed. It first increases with the equivalence ratio, reaches a maximum and finally decreases with higher fuel-air ratio. Although the last branch is not present on the graph, we can expect that if the equivalence ratio ϕ_0 becomes extremely high, the amount of fuel evaporated before the flame will be so large that it will preclude the propagation of the flame. This statement is supported by an analogous result [57] for ethanol with smaller droplets and a narrower range of stoichiometry. An important feature to notice is that for a given droplet diameter, the equivalence ratio giving rise to the highest flame speed may be higher than 1 and that the maximum flame speed may be higher than the maximum gaseous flame speed. This supports other results reviewed earlier [57, 61]. Furthermore, it is interesting to note that this plot is related to the one given in Ref. [70] regarding minimum ignition energy against overall equivalence ratio for different SMD: the conditions resulting in minimum ignition energy correspond to the conditions giving highest flame speeds in the present calculations.

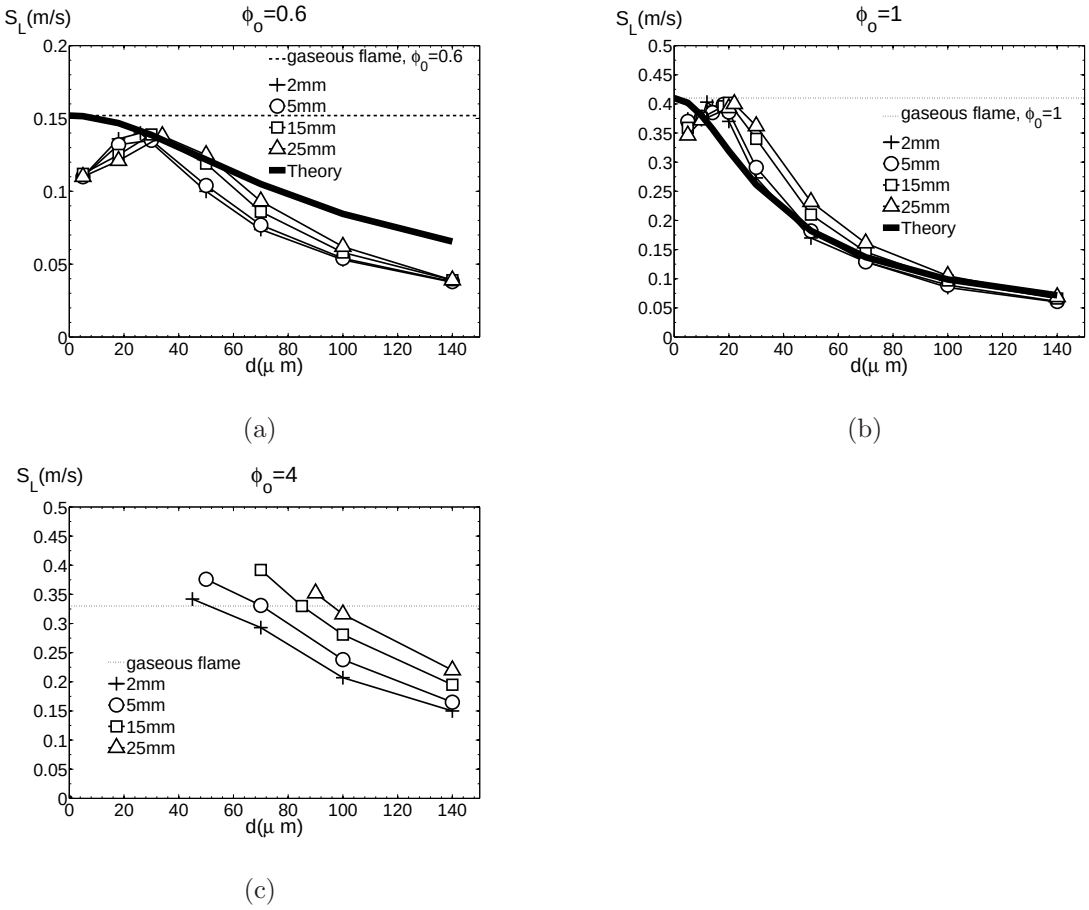

Figure 3.5: n-Heptane flame speed as a function of the initial droplet diameter for different lengths l. For $\phi_0 \leq 1$, the data are compared with the theoretical curve prescribed by Ballal and Lefebvre [47]. (a) $\phi_0 = 0.6$, (b) $\phi_0 = 1$, (c) $\phi_0 = 4$.

The control parameter used to assess the influence of the residence time of the droplets in the primary evaporation zone was the length l of the zone (i.e. the distance between the left boundary of the calculation domain and the preheat zone). Figure 3.5 shows that as the length l is increased the flame speed is enhanced, especially when the droplet diameter is small. We also observe that when an optimum diameter exists, its value is markedly affected by l. The trend of flame speed with l is consistent with experimental data (see, for example, Refs. [47, 48]) that show an increase in flame speed with increasing degree of pre-evaporation Ω at the preheat

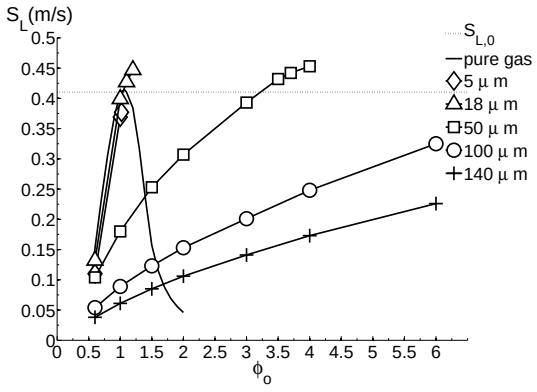

Figure 3.6: n-Heptane flame speed as a function of the overall equivalence ratio for different initial droplet diameters and l=5 mm.

zone. The amount of vapour created in the length l depends on the residence time l/S_L, where S_L is the flame speed of the particular flame we are studying. For each droplet size and fuel studied, a reference evaporation timescale, τ_{evap}, can be estimated from the single-droplet evaporation theory in stagnant surroundings (e.g. [121]). The ratio $(l/S_L)/\tau_{evap}$ is related to the amount of fuel evaporated before the preheat zone and can act qualitatively as a substitute for the vapour fraction Ω. For the n-heptane flames with ϕ_0=1, this timescale ratio is shown in Fig. 3.7 for different values of the diameter and compared with the theoretical curve from Eq. 3.27. With our results the diameter indicated is that at the beginning of the primary evaporation zone while in Eq. 3.27, D_{32} refers to the diameter at the beginning of the preheat zone. In spite of that, the theoretical curve yields a good agreement with our results. Our solution is consistent with the finding that the presence of fuel vapour in a mist is highly conducive to flame propagation [47].

3.3.3 n-Decane flame: atmospheric conditions

Flame speeds calculated with n-decane at atmospheric conditions (Flames B) generally show the same trends as presented above. However, some differences, which may be attributed to the lower volatility of n-decane, are worth pointing out. In

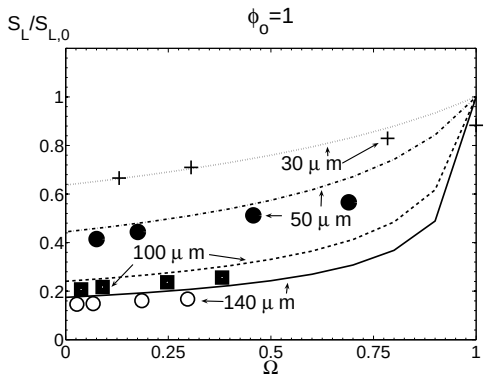

Figure 3.7: Influence of Ω and a_d on n-heptane flame speed based on the theoretical curve prescribed by Ballal and Lefebvre [47]. Data from the present simulations are included where the ratio $(l/S_L)/\tau_{evap}$ replaces Ω; see Section 3.3.2.

Fig. 3.8a we remark again the inverse dependence of the flame speed on the initial diameter. However, the diameter below which the flame speed is very close to the gaseous flame speed is around 15 µm, which is much smaller than for n-heptane. In fact, the reduction of the flame speed with larger diameters is stronger in the case of n-decane. This agrees with results reviewed previously. Furthermore, the value of the laminar flame speed is virtually independent of the length l of the primary evaporation zone. This suggests that no control of the flame speed can be done by extending the primary evaporation zone consistent with the little evaporation achieved with n-decane due to its low saturated vapour pressure.

Figure 3.9a shows the variation of the n-decane flame speed with the equivalence ratio for different droplet diameters at a fixed length l=5 mm. The same trends seen with n-heptane are followed, but with the heavy fuel the flame does not exceed $S_{L,0}$. Figure 3.10 compares our results with the theoretical curve presented in Section 3.3.2 and experimental results collected by [47] for heavy fuel oil. Our results are realistic and show that pure n-decane represents well, at least qualitatively, the influence of droplet size on flame propagation in commercial fuel.

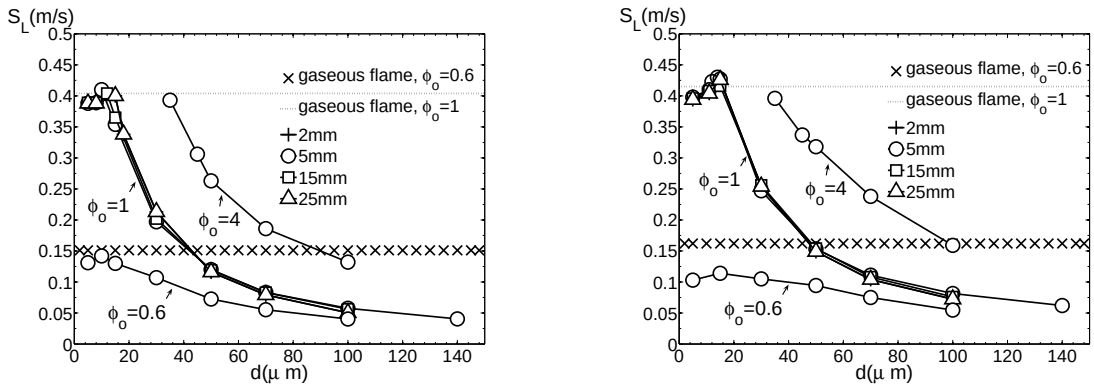

(a) (b)

Figure 3.8: n-Decane flame speed at various ϕ_0 as a function of the initial droplet diameter for different lengths l. The gaseous flame does not exist at $\phi_0 = 4$. (a) Atmospheric conditions, (b) relight conditions.

3.3.4 n-Decane flame: relight conditions

Figure 3.11 shows the gaseous flame speed versus ϕ_0 at atmospheric condition and two relight conditions, (1) P_0=41.37 kPa, T_0=265 K and (2) P_0=30 kPa, T_0=230 K. The former corresponds to the typical inlet stagnation conditions of a combustor at an altitude around 9,000 m, while the latter corresponds to the values of the standard atmosphere at the same altitude. Both are sometimes used by gas turbine engineers to denote the conditions inside the combustor if the flame has extinguished and must be relighted. It is readily seen that although relight conditions impose low temperatures detrimental to the reaction rates, the reduction of the flame speed is not large (less than 20%). This suggests that the negative effect of the low temperature is overcome by the benefits of the reduction in pressure, with the typical dependence $P^{-0.5}$ in pure gas [36]. Calculations performed at 298 K showed a pressure dependence $P^{-0.22}$ in fair agreement with the exponent -0.3 found by [47] for Diesel oil.

Now, we consider spray flames with P_0=41.37 kPa, T_0=265 K (Flames C). Figure 3.8b shows that the trends described for atmospheric conditions remain unchanged.

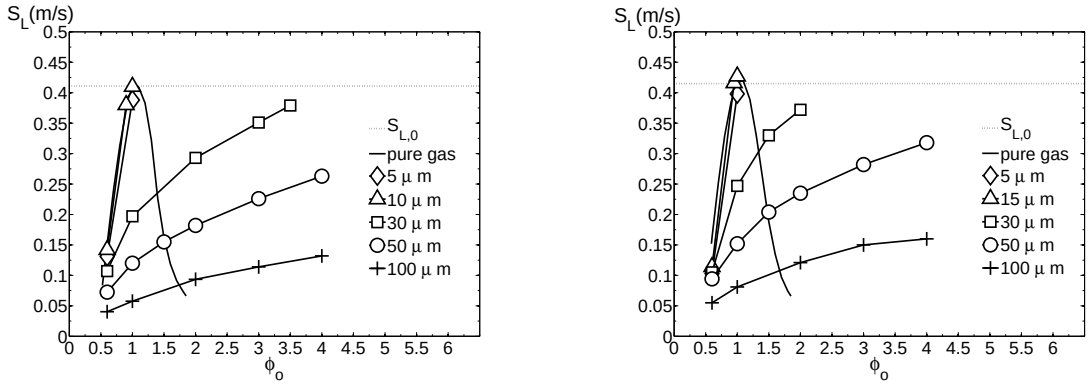

(a) (b)

Figure 3.9: n-Decane flame speed as a function of the overall equivalence ratio for different initial droplet diameters and l=5 mm. (a) Atmospheric conditions, (b) relight conditions.

The effect of the residence length l on the flame speed is also presented in Fig. 3.8b, which indicates that l has very little effect, consistent with the very small influence of l in the case of n-decane at atmospheric conditions. Finally, it is noteworthy that the flame speed variation with overall equivalence ratio ϕ_0 at relight conditions is quantitatively comparable to the one at atmospheric conditions, Fig. 3.9b. As with normal conditions, we notice that the flame speed at rich ϕ_0 can exceed the corresponding gaseous flame speed. However, the spray flame speed for n-decane does not exceed $S_{L,0}$; that phenomenon seems to be specific to n-heptane, which is more volatile.

3.4 Discussion

In this Section, we give some additional interpretations for the trends introduced previously. First, we discuss the effective equivalence ratio ϕ_{eff}, and then we examine in detail the flame structure. An explanation for the increase of the flame speed above $S_{L,0}$ for rich sprays is discussed, as well as the optimum diameter that maximises S_L.

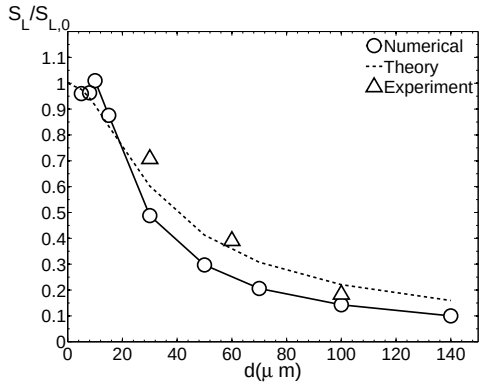

Figure 3.10: Comparison between the theoretical curve, experiments with heavy fuel oil ($S_{L,0}$=0.41 m/s) [47] and our results with n-decane at an $\phi_0 = 1$ and l=2 mm.

3.4.1 Effective equivalence ratio

As suggested by previous studies [49, 57, 61], the equivalence ratio in the gas at the front of the reaction zone should explain, at least partly, the different flame speeds observed under various conditions. The idea is that the closer the effective equivalence ratio ϕ_{eff} is to unity, the faster the reaction rates and the higher the flame speed. We can expect ϕ_{eff} to be influenced, on the one hand by the preheat zone where the evaporation rate is accelerated, and on the other hand by the length l of the primary evaporation zone where droplets evaporate in the cold gas.

The effective equivalence ratio ϕ_{eff} is here defined as the equivalence ratio in the gas in the inner layer of the reaction zone. The inner layer can be interpreted as the location where chemical reactions become very intense [122]. We chose to calculate the effective equivalence ratio by computing the total mass fraction of carbon elements at the location of maximum heat release. We then related that number to the corresponding mass fraction of fuel. Note that the carbon-to-oxygen ratio in the gas varies very sharply with space due to the evaporation and differential diffusion and hence ϕ_{eff} should be treated as an approximate concept, see Fig. 3.12.

Figure 3.13 shows ϕ_{eff} for the n-heptane flames as a function of the initial droplet

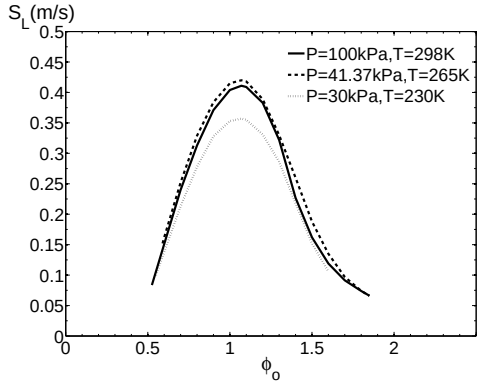

Figure 3.11: Flame speed of gaseous n-decane at three different conditions of pressure and initial temperature.

diameter for the lean, stoichiometric and rich cases and for different lengths l. We observe that as the initial SMD is reduced, the effective equivalence ratio increases towards the overall equivalence ratio ϕ_0 due to the higher evaporation rate. In fact, ϕ_{eff} is brought to a value very close to ϕ_0 when $a_d \leq$30 µm, which is in the transition range. Furthermore, we can notice that as the length l is increased, ϕ_{eff} increases as well. Under atmospheric conditions, n-heptane droplets have a high evaporation rate and produce substantially more fuel over a longer primary evaporation zone. Those trends are clearly correlated with the previous results on the flame speed, Fig. 3.5. By noticing that when ϕ_{eff} is closer to unity, the flame speed tends to be larger, we can infer that ϕ_{eff} influences to some extent the propagation rate. For example, under lean or stoichiometric conditions, as the droplet diameter goes below 10 µm, almost all the liquid fuel has evaporated before reaching the flame and thus ϕ_{eff} is equal to ϕ_0. This results in a flame speed close to, but slightly lower than, the gaseous laminar speed, probably because some of the combustion energy has been spent into evaporating all the liquid.

Furthermore, we saw in Section 3.3.2 that, for $\phi_0 = 4$, the flame speed can be high in a spray with large droplets although the overall equivalence ratio is well above the rich flammability limit. We observe in Fig. 3.13 that the conditions

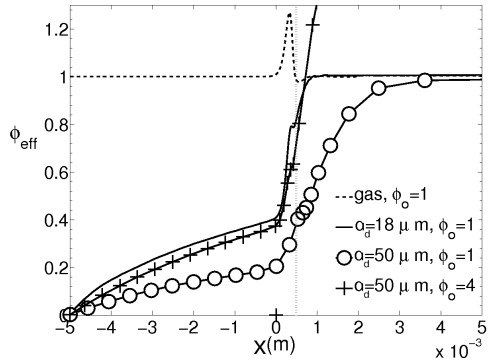

Figure 3.12: Effective equivalence ratio through n-heptane flames with l=5 mm and the indicated equivalence ratio and droplet size. The vertical line locates the peak of heat release rate in the gaseous case.

which involve high flame speeds correspond to the ones resulting in ϕ_{eff} close to 1. This occurs for a_d higher than 30 µm. Although this is not clearly evident in the graphs, very small droplets should result in very large ϕ_{eff}, which is not conducive to flame propagation. Therefore, at rich equivalence ratio, moderately large droplets are beneficial to flame speed. Still, too large diameters result in too lean effective equivalence ratio and thus slower flames. By comparing Fig. 3.13 and Fig. 3.5, we observe that the highest flame speed in the rich case corresponds to $0.7 \leq \phi_{eff} \leq 0.9$. We can expect that the optimum conditions are a combination of diameter, length l and ϕ_0 such that ϕ_{eff} is close to unity, consistent with analytical [49, 123] and experimental [57] conclusions. Since the extent of evaporation is affected by l, the optimum diameter varies with l.

Figure 3.14 presents ϕ_{eff} versus SMD for n-decane flames at relight and atmospheric conditions. Since n-decane is a heavy fuel with a low saturated vapour pressure, its evaporation rate under atmospheric conditions is very weak and this explains the small influence of l on ϕ_{eff} and in turn of l on the flame speed. This also explains why, under lean and stoichiometric condition, the flame speed is more easily reduced by an increase in diameter with n-decane than with n-heptane. The

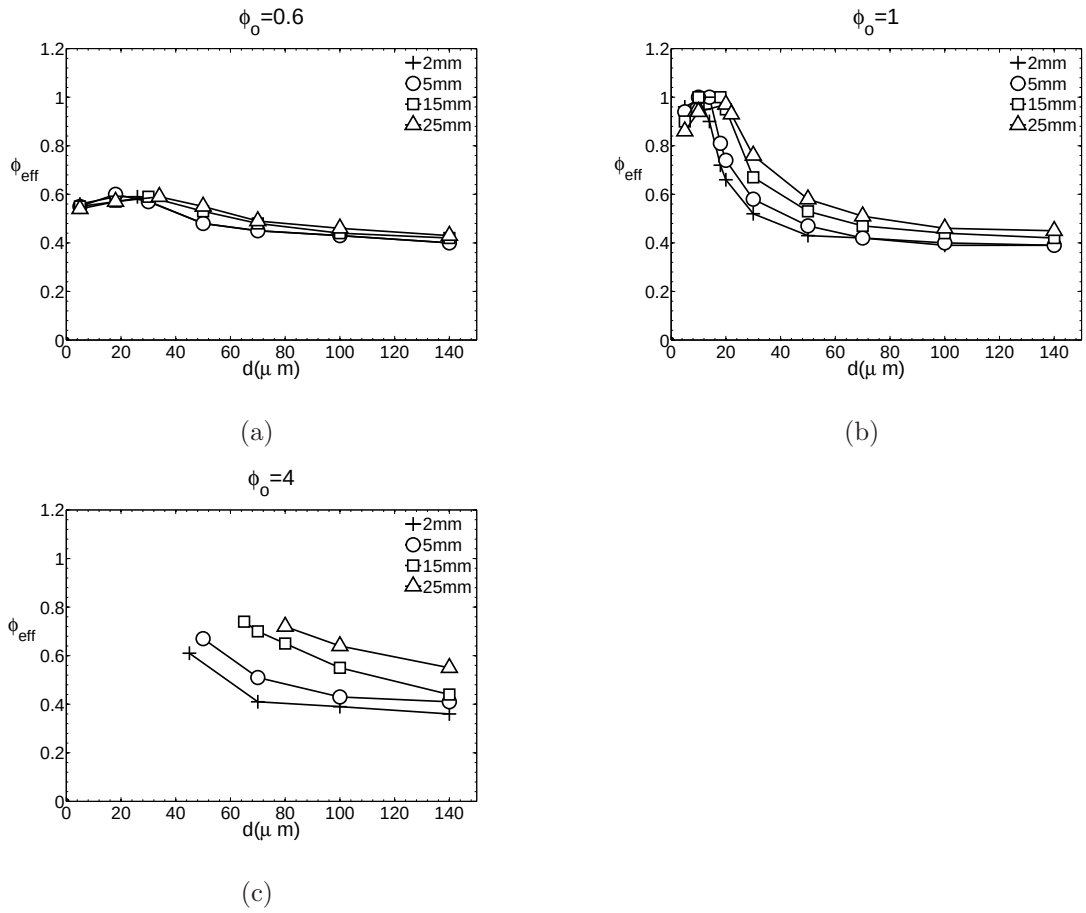

Figure 3.13: Effective equivalence ratio for n-heptane as a function of the initial droplet diameter for different lengths l. (a) $\phi_0 = 0.6$, (b) $\phi_0 = 1$, (c) $\phi_0 = 4$.

evaporation rate is so slow that much smaller droplets are needed to reach the same ϕ_{eff}. Finally, it accounts for the fact that the laminar flame has a high value for diameters down to 35 µm in the rich case ϕ_0=4. Even if the spray is rich, the low evaporation rates help keeping ϕ_{eff} below unity.

The effect of the residence length l on ϕ_{eff} for the n-decane flame at relight conditions is shown in Fig. 3.14b. It is apparent that all the curves merge into a single one implying that l has very little effect. We have already noted the negligible influence of l in the case of n-decane at atmospheric conditions. Our results show that this is even more pronounced at relight conditions, and imply that the vapour

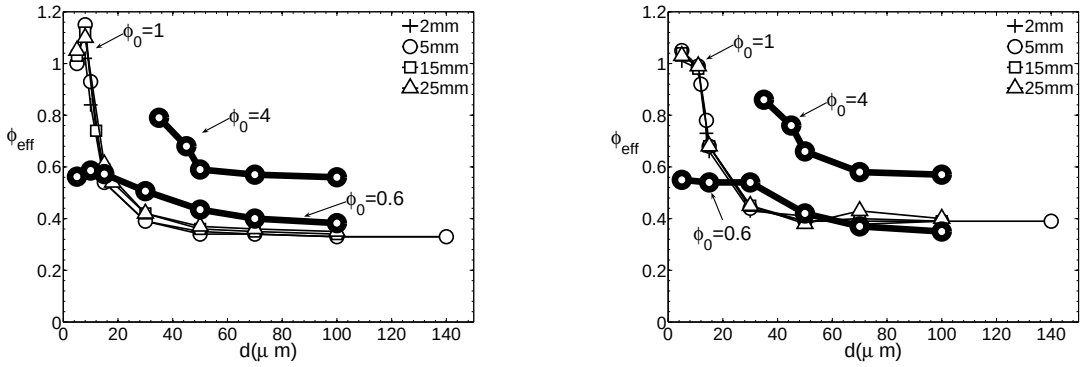

(a) (b)

Figure 3.14: Effective equivalence ratio for n-decane as a function of the initial droplet diameters for different lengths l. (a) Atmospheric conditions, (b) relight conditions.

generated by the heavy fuel in the low temperature primary evaporation zone is negligible. Hence, most of the fuel that burns in the "homogeneous" reaction zone evaporates in the preheat zone. We could expect ϕ_{eff} to be much lower at relight conditions than at atmospheric conditions, but interestingly, this is not the case as shown in Fig. 3.14. In the preheat zone, where the droplet temperature approaches the boiling temperature, the low pressure has a very positive effect on the evaporation rate since it increases the transfer number B_M through the Clausius-Clapeyron equation. Due to this phenomenon, the low pressure also has a positive effect on the flame speed, as long as $\phi_{eff} \leq 1$, since it increases ϕ_{eff}. As an overall result, the temperature and the pressure have two competitive effects. On one hand, the low temperature decreases the flame speed and reduces the amount of fuel evaporated, ϕ_{eff}. On the other hand, the low pressure increases the flame speed and enhances the evaporation rate and thus ϕ_{eff}. This twofold effect of the pressure agrees with the finding of Ballal and Lefebvre [47], who observed that for lean mixtures the flame speed has a stronger pressure dependence in a spray compared to a pure gas.

In Fig. 3.15 we plotted the flame speed normalised by $S_{L,0}$ against ϕ_{eff} for all the data collected. Although the parameter ϕ_{eff} is useful in explaining different

phenomena observed, there is no complete correlation between the flame speed and ϕ_{eff}. The large scatter observed implies that other phenomena affect the flame speed. For instance, for the same ϕ_{eff} and a_d, if ϕ_0 is different, the flame speeds are different. It is also evident that for a given ϕ_{eff}, the flame speed is practically always larger than the gaseous flame speed at the same value of equivalence ratio. Another interesting observation is that the flame speed is finite at very low ϕ_{eff}, even beyond the lean flammability limit. Although the governing equations used here do not fully account for flammability limits as there is no heat loss mechanism, the code converges for gaseous flames only in a range of equivalence ratios and gives very low speeds ($S_L/S_{L,0} < 0.2$) at $\phi_0 \approx 0.5$ and $\phi_0 \approx 2$. The spray flames, in contrast, show high flame speeds for ϕ_{eff} as low as 0.4. This widening of the flammability limits in sprays has been attributed to inter-droplet inhomogeneities, where locally the mixture may reach flammable values [44, 51, 64] and hence sustain flame droplet-to-droplet propagation. In the next section, we provide an alternative explanation for this phenomenon, that also accounts for the enhanced flame speed in sprays above the maximum gaseous flame speed (i.e. the fact that $S_L/S_{L,0}$ can be above unity in Fig. 3.15).

3.4.2 Structure of the flame and influence of chemistry

In this Section, we present some details on the chemical aspects of the spray flames, as revealed from the present complex chemistry calculations. All the examples are presented for n-heptane and l=5 mm, but the conclusions are valid for other fuels and lengths.

Three main structures of spray have been observed which are variants of Fig. 2.1. In the first one, almost all the droplets evaporate before reaching the flame front and ϕ_{eff} is close to ϕ_0. The flame is very similar to a gaseous flame and we observe a thin reaction zone, as depicted in Figs. 3.1-3.4 and 3.16-3.17 for a diameter a_d=10 µm and ϕ_0=1.

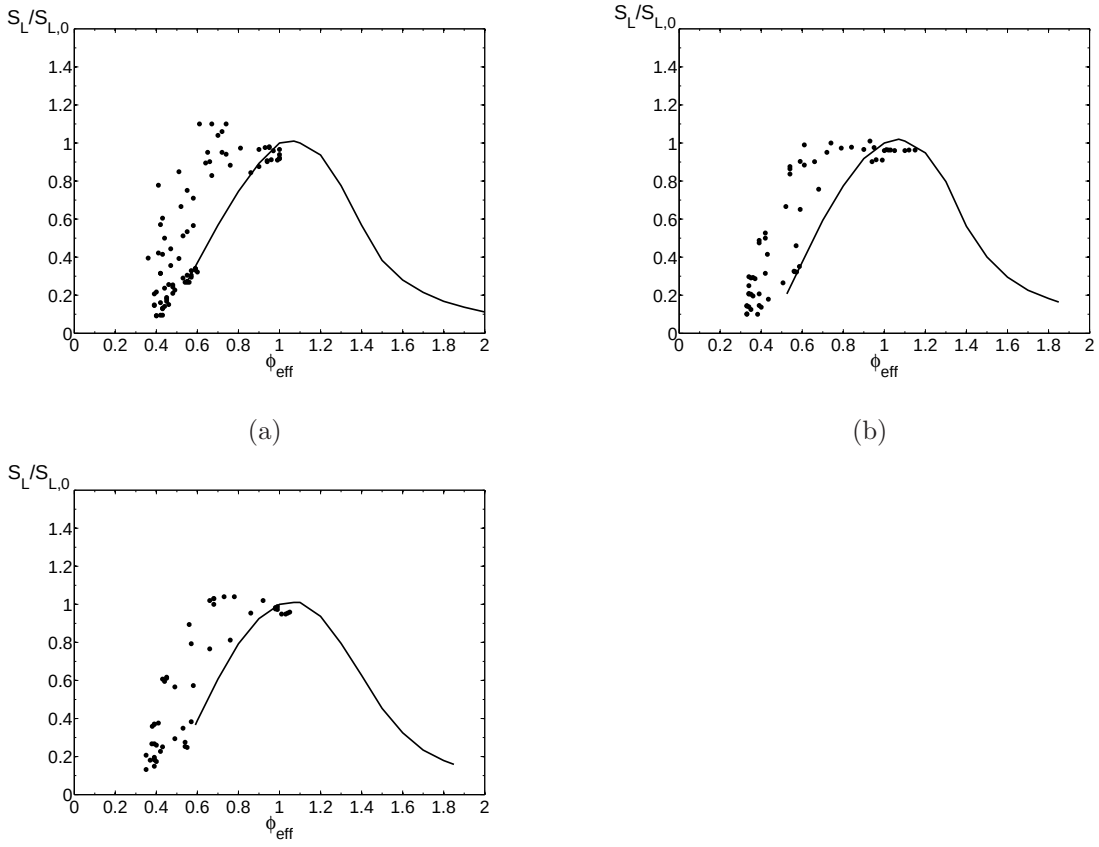

Figure 3.15: Normalised flame speeds as a function of ϕ_{eff}. (a) n-Heptane, (b) n-decane atmospheric, (c) n-decane, relight. Line: gas. Symbols: spray.

On the same graphs, we can notice a second structure in the case a_d=50 µm and ϕ_0=1 where the effective equivalence ratio is very low. We have already commented this structure in Section 3.3.1: little oxidiser is consumed in the first reaction zone and the rest is consumed in a droplet burning zone over a length of a few millimetres. This is illustrated by Fig. 3.16, which shows that Y_{OH} keeps increasing over a long length, denoting a long oxidation zone. Hence, although ϕ_{eff} is low, the droplet burning zone is wide and provides heat release. This explains why the flame speed may be relatively high even with ϕ_{eff} as low as 0.4.

Finally, a third structure has been observed for rich spray flames where $0.6 \leq$

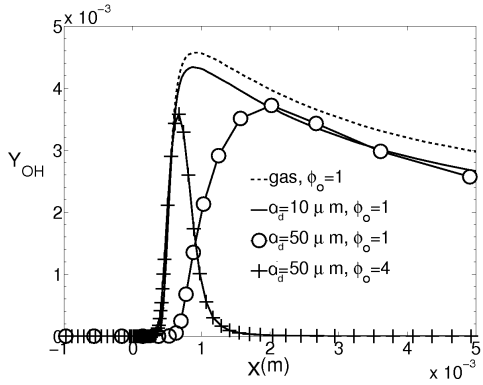

Figure 3.16: OH mass fraction through n-heptane flames with l=5 mm and the indicated equivalence ratio and droplet size.

$\phi_{eff} \leq 1$ and where the droplets still have a significant size at the inner layer of the reaction zone. As a result, the oxidiser is entirely consumed at the reaction zone and in a short droplet burning zone while droplets still exist behind it. There, instead of being oxidised, the fuel evaporated is pyrolysed. To illustrate this, we compare the three main structures: the gaseous case at stoichiometry, the flame with a long droplet burning zone (a_d=50 µm and ϕ_0=1), and the third structure represented by a_d=50 µm, ϕ_0=4. In Fig. 3.17, mass fractions of hydrogen, acetylene, ethylene and higher hydrocarbons show that in the third structure products of pyrolysis and subsequent reactions keep being formed after the main heat release zone.

The above arguments are substantiated by examination of the rates of direct oxidation and of pyrolysis for the fuel. Figure 3.18 shows the rates of the elementary reactions $C_7H_{16} + O \Leftrightarrow C_7H_{15} + OH$ and $C_7H_{16} + OH \Leftrightarrow C_7H_{15} + H_2O$ which have the highest rate of all n-heptane H abstraction reactions by OH and O. In the same graph, the rates of oxidation of smaller hydrocarbons ($CH_2O + OH \Leftrightarrow HCO + H_2O$ and $HCO + O_2 \Leftrightarrow CO + HO_2$) are presented. The first reaction is sometimes considered responsible for a significant part of the heat release in hydrocarbon combustion [124]. Finally, the rates of the pyrolysis reactions with the highest values, $C_7H_{16} \Leftrightarrow C_5H_{11} + C_2H_5$ and $C_7H_{16} \Leftrightarrow pC_4H_9 + nC_3H_7$, are

depicted in Fig. 3.19.

From Fig. 3.18 and 3.19, we notice that: in the gaseous case, all reactions are concentrated in a small region and they become negligible after 0.7 mm; in the case a_d=50 µm and ϕ_0=1, reactions involving oxygen atoms extend beyond 1 mm. In this structure, the reaction $CH_2O + OH \Leftrightarrow HCO + H_2O$ indicates that combustion occurs over a long length in a droplet burning zone; for the case a_d=50 µm, ϕ_0=4, reactions involving oxidant are insignificant after 1 mm implying that very little oxidiser remains and the droplet burning zone is short. This is consistent with the sudden decrease of OH seen in Fig. 3.16. After 1 mm, all reactions seem to be negligible except pyrolysis reactions. These reactions keep occurring over a long length because the droplets are large and survive far beyond the flame. The temperature and heat release profiles presented in Figs. 3.1 and 3.2 are consistent with the endothermic nature of pyrolysis: the temperature profile presents a negative slope behind the flame front, coincident with the change of the heat release sign. Note that the evaporation heat sink in the hot gas also contributes to the decrease in temperature.

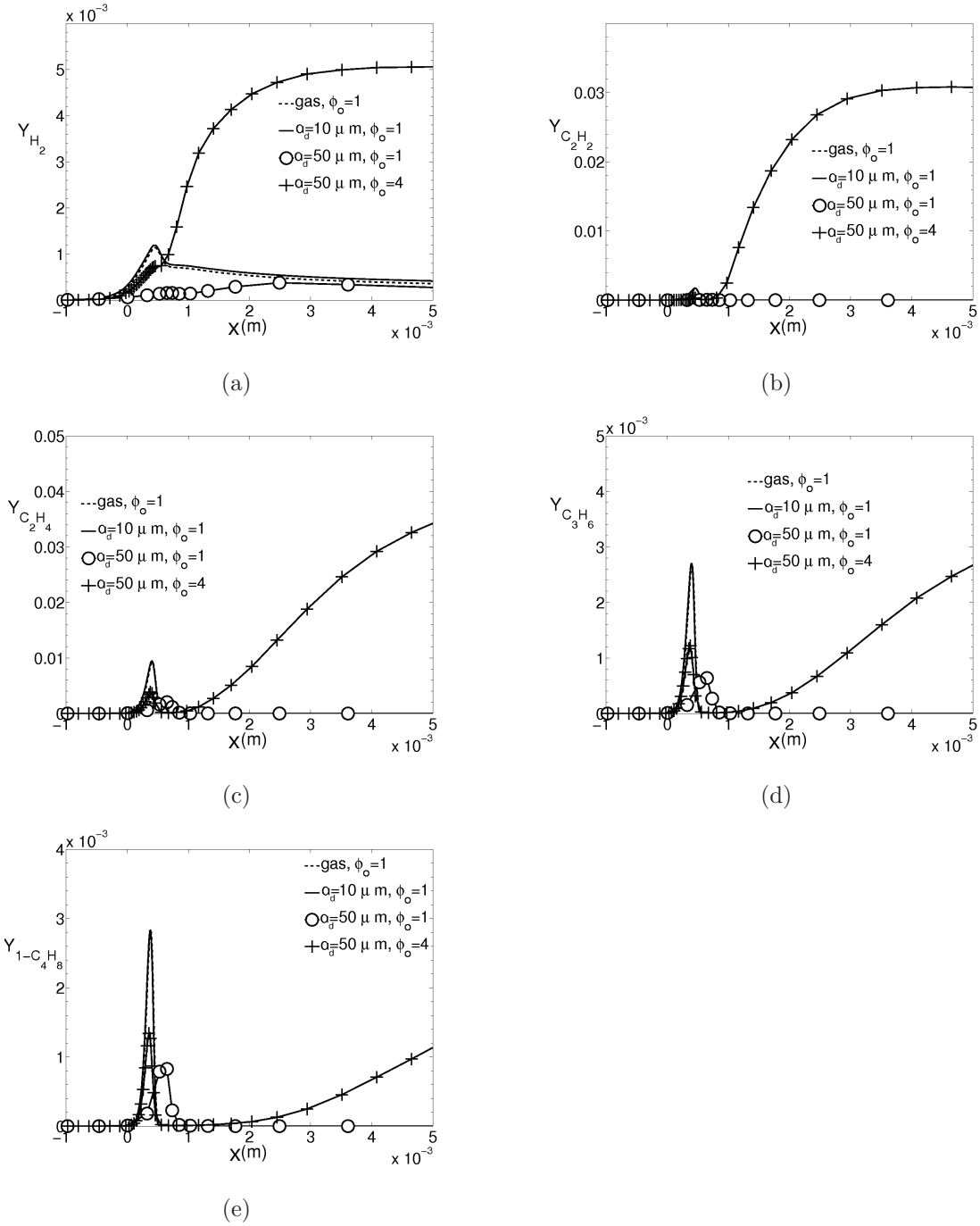

Figure 3.17: Mass fraction of intermediate species through n-heptane flames with l=5 mm and the indicated equivalence ratio and droplet size. (a) H_2, (b) C_2H_2, (c) C_2H_4, (d) C_3H_6, (e) $1-C_4H_8$.

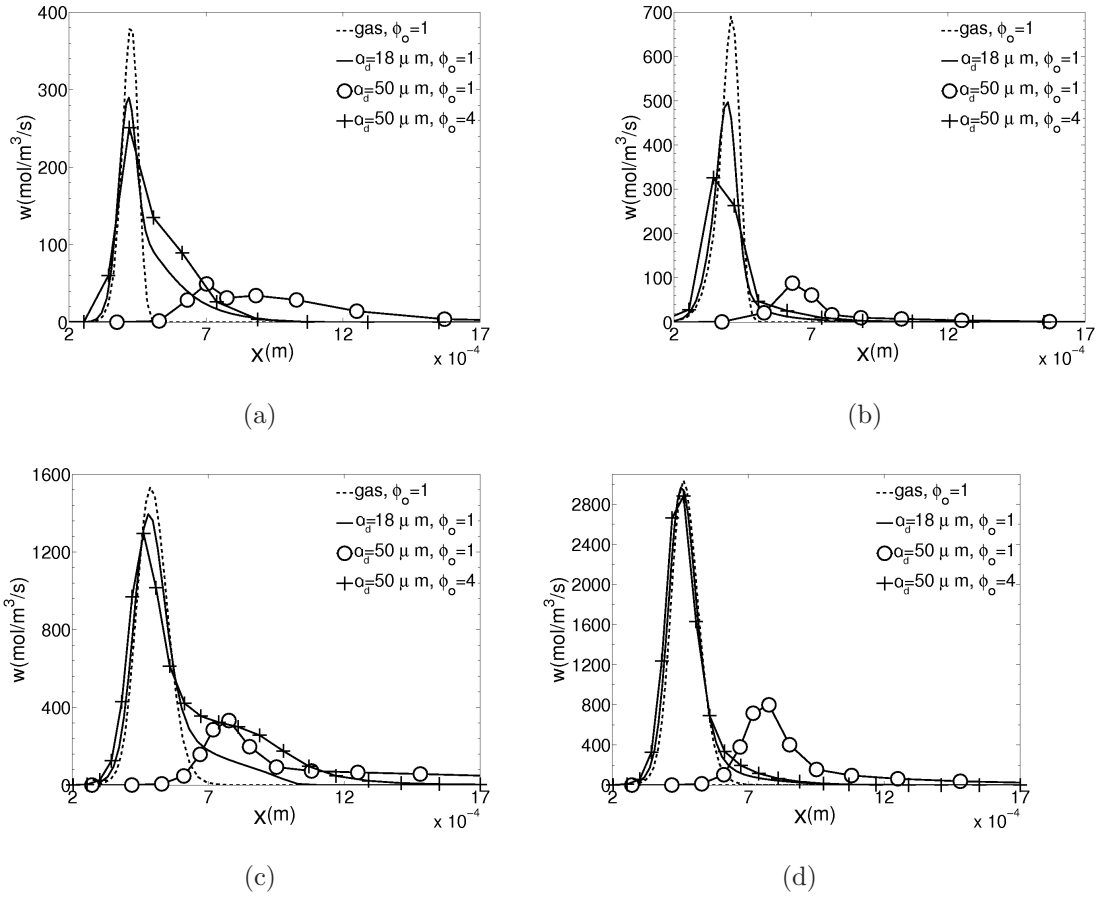

Figure 3.18: Rates of elementary reactions through n-heptane flames with l=5 mm and the indicated equivalence ratio and droplet size. (a) $C_7H_{16}+O \Leftrightarrow C_7H_{15}+OH$, (b) $C_7H_{16}+OH \Leftrightarrow C_7H_{15}+H_2O$, (c) $CH_2O+OH \Leftrightarrow HCO+H_2O$, (d) $HCO+O_2 \Leftrightarrow CO+HO_2$.

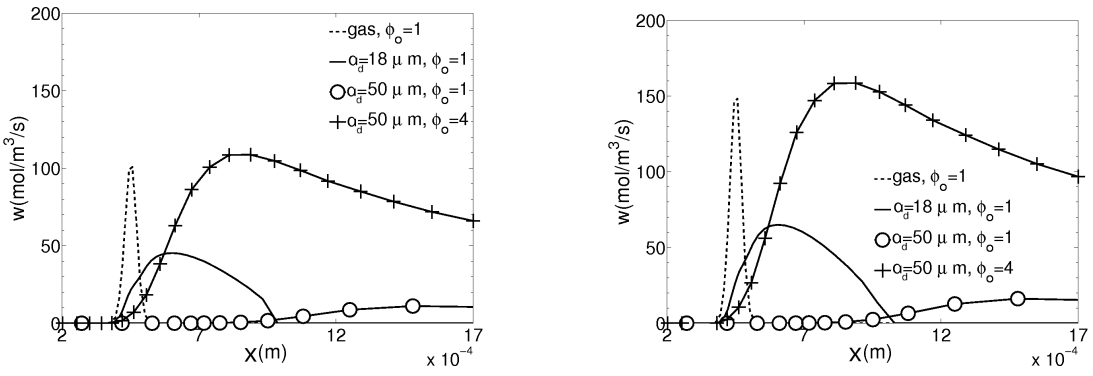

(a) (b)

Figure 3.19: Pyrolysis reaction rate through n-heptane flames with l=5 mm and the indicated equivalence ratio and droplet size. (a) $C_7H_{16} \Leftrightarrow C_5H_{11} + C_2H_5$, (b) $C_7H_{16} \Leftrightarrow pC_4H_9 + nC_3H_7$.

In Fig. 3.20 we present the net formation rate of some products of the decomposition of fuel: H_2 and C_2H_2, both of which are highly reactive. In the case a_d=50 µm, ϕ_0=4, the production rates of these species are very high in the pyrolysis zone because large amounts of fuel are being evaporated and subsequently pyrolysed. The rates are virtually zero in the other cases after 1 mm. It can be inferred that the existence of a pyrolysis zone leads to a build up of very reactive intermediate species, see Fig. 3.17. The fact that the flame speed of these species (H_2, C_2H_2 and C_2H_4) is high, if they are considered as separate fuels, implies the possibility of acceleration of the n-heptane flame because we may expect that the high positive gradient of the mass fractions of these species induces a back diffusion towards the oxidation zone where the reaction rates are enhanced. Hence, we can roughly consider that very rich spray flames are qualitatively equivalent to hydrogen- and acetylene- and ethylene-enriched lean or stoichiometric higher hydrocarbon flames.

In order to finally relate explicitly the formation of these species to the high flame speed observed in this case, we carried out a sensitivity analysis of flame speed for the cases presented in Fig. 3.21. It was found that, for the gaseous flame, the most sensitive reactions were the following: $H + O_2 \Leftrightarrow O + OH$; $OH + CO \Leftrightarrow H + CO_2$;

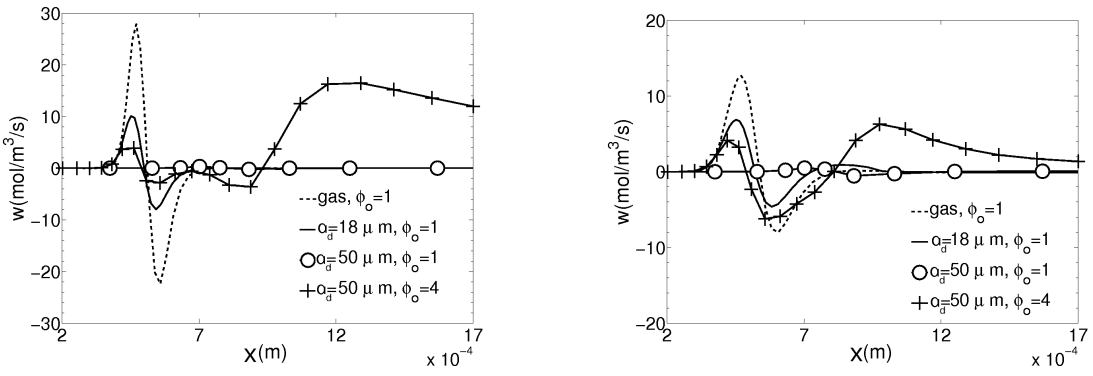

(a) (b)

Figure 3.20: Formation rate of some products of fuel decomposition through n-heptane flames with l=5 mm and the indicated equivalence ratio and droplet size. (a) C_2H_2, (b) H_2.

$H+OH+M \Leftrightarrow H_2O+M$; $HCO+M \Leftrightarrow H+CO+M$ and $OH+CH_3 \Leftrightarrow CH_2^*+H_2O$. It was also found that the same elementary reactions are the most sensitive in the spray flames, but also that as the droplet size increases, the normalized sensitivity goes down. In the graph, we also included the elementary reactions $H_2 + OH \Leftrightarrow H_2O + H$; $C_3H_6 + OH \Leftrightarrow aC_3H_5 + H_2O$; $C_2H_5 + O_2 \Leftrightarrow HO_2 + C_2H_4$, which are very sensitive in the stoichiometric gaseous case and for a_d=50 µm, ϕ_0=4. Many of these important elementary reactions involve species generated from pyrolysis.

Figure 3.22 shows that the reaction rates of some of these key reactions are intensified in the rich spray flames. Therefore, the presence of a pyrolysis zone improves the flame propagation rate. This would explain the very high flame speed observed in the case a_d=50 µm, ϕ_0=4. This flame structure is achieved in rich sprays where all the oxidiser is consumed in a relatively short reaction zone, and with surviving droplets in the post flame region.

Finally, we discuss here the existence of an optimum diameter for $\phi_0 = 1$ and $\phi_0 = 0.6$. As observed in Fig. 3.5a and 3.5b, S_L increases with a_d until about 30 µm and then decreases as a_d increases further. The decrease from the optimum as a_d increases can be understood due to the decreasing ϕ_{eff}, see Fig. 3.13a and 3.13b.

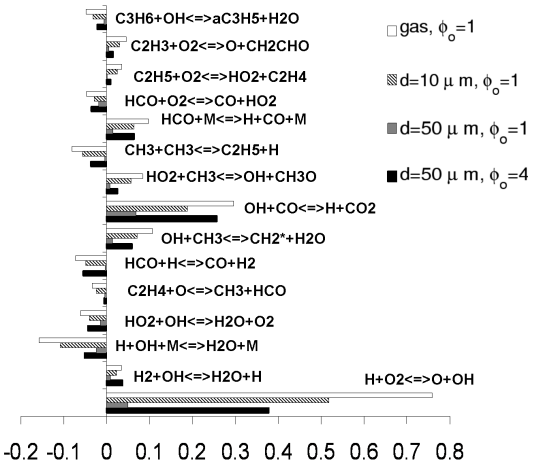

Figure 3.21: Normalised sensitivity coefficient of the velocity on reaction rates. The particular reactions selected have the highest degree of sensitivity.

The initial increase from very small a_d cannot be explained simply through ϕ_{eff}, because ϕ_{eff} is relatively independent of a_d, but can be understood by the following argument. For a gaseous premixed flame, simplified theory predicts the relation $S_L \sim \sqrt{\alpha \int Q dy}$, which states that the flame speed is increased by a higher thermal diffusivity and a higher integrated heat release Q [36]. Although not explicitly presented for the sake of brevity, the transport properties evaluated by the code show that in the preheat zone, the thermal diffusivity of the gas is higher with the optimum diameter than with a smaller diameter. This is a first factor contributing to the existence of an optimum diameter. In Fig. 3.13, we notice that the value of ϕ_{eff} associated with the optimum diameter is very close to or equal to ϕ_0. In the case a_d=18 µm, $\phi_0 = 1$, this implies that a large part of oxidiser is consumed in the homogeneous reaction zone while droplets still exist behind it. Furthermore, Fig. 3.19 shows that behind the homogeneous reaction zone, the fuel evaporated by droplets is intensively pyrolysed eventually resulting in non-negligible generation of H_2, see Fig. 3.20. Although this is not a proper pyrolysis zone because combustion reactions still occur, see Fig. 3.18, we can infer that a pool of intermediates such

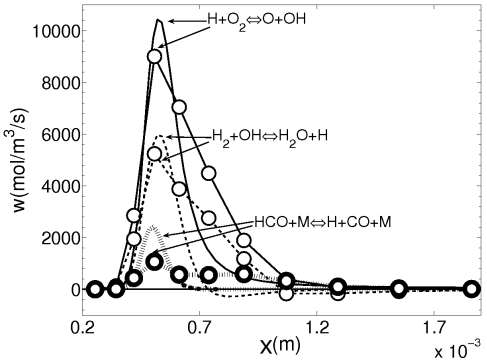

Figure 3.22: Rates of the indicated elementary reaction, selected as reactions with high degree of sensitivity through n-heptane flames with l=5 mm and the indicated equivalence ratio and droplet size. Lines: gas, $\phi_0 = 1$. Circles: a_d=50 µm, ϕ_0=4.

as H_2 is created. Those reactive species can then diffuse back and enhance the reaction rates, as in the a_d=50 µm, $\phi_0 = 4$ flame. To corroborate this statement, we calculated the integrated heat release for the case a_d=18 µm, $\phi_0 = 1$ and found a value of 5.32×10^7 W/m^3 which was higher than both the a_d=10 µm, $\phi_0 = 1$ and the gaseous stoichiometric cases. The overall result was that the ratio between $\sqrt{\alpha \int Q dy}$ for a_d=18 µm, $\phi_0 = 1$ and $\sqrt{\alpha \int Q dy}$ for a_d=10 µm, $\phi_0 = 1$ was 1.07, while the ratio of the flame speeds was 1.06. This close agreement supports the fact that incomplete evaporation at the reaction zone may be beneficial to the flame propagation.

3.4.3 Summary of main findings

Calculations of one-dimensional laminar flames in sprays of n-heptane and n-decane under atmospheric and high altitude ("relight") conditions have been presented. The effects of droplet diameter, overall equivalence ratio and residence time before the flame zone were examined. The trends were only marginally correlated with the effective equivalence ratio ϕ_{eff}, based on the total gaseous carbon mass fraction at

the location of maximum heat release rate. ϕ_{eff} was close to the total equivalence ratio ϕ_0 for small droplets and long residence times. High flame speeds were more likely to occur when ϕ_{eff} was close to unity. This implies that the maximum flame speed is achieved with small diameters and long residence time under lean conditions. Under rich conditions, the flame speed was greater for relatively large droplet sizes that caused ϕ_{eff} to be near unity. This was in agreement with previous studies.

Three different structures of a spray flame were observed. In the first one, droplets evaporated completely before the flame front and the structure was identical to a gaseous flame. In the second, droplets evaporated very little so that ϕ_{eff} was low. Little oxidiser reacted in the homogeneous reaction zone and the rest was consumed in a long droplet burning zone providing heat release. The third flame structure occurred for rich sprays where ϕ_{eff} was close to unity and the droplets large enough. In this case, the oxidiser was consumed in a relatively short reaction zone. The fuel evaporated behind it by the surviving droplets was pyrolysed and the reactive species generated (mainly H_2, C_2H_2, C_2H_4) diffused back towards the oxidation zone and enhanced the reaction rates. This could result in enhanced flame speed, above the maximum gaseous flame speed even for $\phi_0 = 4$.

The same trends were followed with the less volatile fuel, n-decane. However, the low evaporation rate generally induced a lower ϕ_{eff} than with n-heptane at atmospheric conditions. At high altitude relight conditions, the residence time had no effect on ϕ_{eff} and the flame speed. Despite the low temperature, the value of ϕ_{eff} was not markedly affected by the relight conditions thanks to the low pressure that enhanced the evaporation rate in the preheat zone. The flame speed was comparable to that at atmospheric conditions because the low pressure compensated for the detrimental effect of low temperature.

The present data show that the impact of complex chemistry on the laminar propagation speed of spray flames is important and provides an additional explanation for the high flame propagation speeds observed in sprays under some conditions. In Chapter 5, the development of a three-dimensional turbulent flame kernel in a spray

is investigated and reveals common features with those presented in this chapter.

Chapter 4

DNS of spark ignition in a droplet laden mixing layer with 1-step chemistry

4.1 Introduction

In Section 2.3.1, we summarised findings on spark ignition in gaseous mixing layers. The kernel development was shown to depend on the spark position and the local strain rate. Furthermore, the long range effect due to the spark size, the diffusion of heat and the flow convection was evident for laminar and turbulent gaseous mixing layers. In Section 2.4.1, it was reported that this effect has also been observed in realistic burners with sprays. Moreover, in Section 2.3.2, it was pointed out that the flame propagating in a gaseous mixing layer has a triple flame structure. It was also mentioned that triple flames were observed with non-premixed sprays but no flame speed measurements were performed. In this chapter, we perform a parametric study of the structure of a spark kernel in a turbulent non-premixed spray with fine droplets, we discuss long range effects and we provide measurements of the propagating flame speed. To this end, DNS simulations with single step chemistry

are performed.

The DNS code used has already produced simulations of kernel expansion in turbulent gaseous mixing layers [14, 85, 99]. The velocity of edge flames relative to the flow (edge flame displacement speed), was measured and negatively correlated with the flame curvature [99]. This DNS code (SENGA1) was also used to compute forced ignition in premixed sprays [42]. The study showed that ignition was favoured if fuel vapour was rapidly available, i.e. droplets of small size and large number density. In addition, flame propagation occurred over a large range of equivalence ratio due to the non-uniform droplet evaporation. This was caused by the local turbulent fluctuations and the fuel vapour inhomogeneities at the droplet scale [42].

A turbulent mixing layer between a stream of air and a stream of air carrying dispersed fuel droplets may be thought of as a canonical problem containing some of the physics of liquid-fuelled burner ignition. This problem is studied in the present chapter (Fig. 4.1) with DNS. The purpose of this work is to follow [85] on spark ignition in air-gaseous fuel mixing layers and to extend it towards fine sprays, and to follow the uniformly-dispersed spray ignition DNS study of Ref. [42] and extend it towards inhomogeneous distributions. We first examine the effect of the spark location, the droplet size and volatility, the spray distribution and the turbulence intensity on the structure and the development of the kernel. Then, we examine the response of the displacement speed to the different parameters investigated. The chapter closes with a summary of the most important conclusions.

4.2 Numerical formulation

4.2.1 Gas phase

In SENGA1, the conservation of mass, momentum, energy and mass fractions of fuel and oxidiser are solved in dimensionless form. The variables ρ, $\mathbf{U}$, T, E, P are non-dimensionalised by using the laminar flame speed at stoichiometry $S_{L,0}$, the

length of the domain L, the density of fresh air ρ_0, the initial temperature T_0, the dynamic viscosity μ_0, the heat conductivity λ_0, the mass diffusivity D_0 and the heat capacity at constant volume C_{v_0}:

$$\hat{\rho} = \rho/\rho_0, \hat{\mathbf{U}} = \mathbf{U}/S_{L,0}, \hat{T} = \frac{T - T_0}{T_{ad} - T_0}, \hat{E} = E/(C_{P_0}T_0), \hat{P} = P/(\rho_0 S_{L,0}^2) \tag{4.1}$$

T_{ad} is the adiabatic flame temperature of a stoichiometric mixture. C_{P_0} is the heat capacity at constant pressure, $C_{P_0} = \gamma C_{v_0}$ with $\gamma = 1.4$. The non-dimensional coefficients $\hat{\mu}$, $\hat{\lambda}$ and $\hat{\rho}\hat{D}$ are taken constant, equal to 1. The non-dimensional governing equations in Cartesian tensor notation are [85, 125]:

$$\frac{\partial \hat{\rho}}{\partial \hat{t}} + \frac{\partial \hat{\rho}\hat{U}_k}{\partial \hat{x}_k} = \hat{\Gamma}_m \tag{4.2}$$

$$\frac{\partial \hat{\rho}\hat{U}_i}{\partial \hat{t}} + \frac{\partial \hat{\rho}\hat{U}_k\hat{U}_i}{\partial \hat{x}_k} = -\frac{\partial \hat{P}}{\partial \hat{x}_i} + \frac{1}{\mathrm{Re}}\frac{\partial \hat{\tau}_{ik}}{\partial \hat{x}_k} + \hat{\Gamma}_{U_i} \tag{4.3}$$

$$\begin{aligned}\frac{\partial \hat{\rho}\hat{E}}{\partial \hat{t}} + \frac{\partial \hat{\rho}\hat{U}_k\hat{E}}{\partial \hat{x}_k} &= -(\gamma-1)\mathrm{Ma}^2\frac{\partial(\hat{P}\hat{U}_k)}{\partial \hat{x}_k} + \frac{1}{\mathrm{Re}}(\gamma-1)\mathrm{Ma}^2\frac{\partial \hat{\tau}_{ik}\hat{U}_i}{\partial \hat{x}_k} \\ &\quad + \frac{\partial}{\partial \hat{x}_k}\left[\frac{\hat{\mu}\tau}{\mathrm{RePr}}\frac{\partial \hat{T}}{\partial \hat{x}_k}\right] - \frac{\tau}{Y_{F_{st}}}\hat{\omega}_F + \hat{q}_{sp} + \hat{\Gamma}_E\end{aligned} \tag{4.4}$$

$$\frac{\partial \hat{\rho}Y_F}{\partial \hat{t}} + \frac{\partial \hat{\rho}\hat{U}_k Y_F}{\partial \hat{x}_k} = \frac{\partial}{\partial \hat{x}_k}\left[\frac{\hat{\mu}}{\mathrm{ReSc}}\frac{\partial Y_F}{\partial \hat{x}_k}\right] + \hat{\omega}_F + \hat{\Gamma}_m \tag{4.5}$$

$$\frac{\partial \hat{\rho}Y_{O_2}}{\partial \hat{t}} + \frac{\partial \hat{\rho}\hat{U}_k Y_{O_2}}{\partial \hat{x}_k} = \frac{\partial}{\partial \hat{x}_k}\left[\frac{\hat{\mu}}{\mathrm{ReSc}}\frac{\partial Y_{O_2}}{\partial \hat{x}_k}\right] + \mathrm{s}\hat{\omega}_F \tag{4.6}$$

with the following state relations

$$\hat{P} = \frac{1}{\gamma \mathrm{Ma}^2}\rho(1 + \tau\hat{T}) \tag{4.7}$$

$$\hat{E} = \frac{1}{\gamma}(1 + \tau\hat{T}) + \frac{1}{2}(\gamma - 1)\mathrm{Ma}^2\hat{U}_k\hat{U}_k \tag{4.8}$$

The non-dimensional viscous stress tensor is

$$\hat{\tau}_{ij} = \hat{\mu}\left(\left[\frac{\partial \hat{U}_i}{\partial \hat{x}_j} + \frac{\partial \hat{U}_j}{\partial \hat{x}_i}\right] - \frac{2}{3}\delta_{ij}\left[\frac{\partial \hat{U}_k}{\partial \hat{x}_k}\right]\right) \tag{4.9}$$

The non-dimensional parameters used in the equations are

$$\begin{aligned}\mathrm{Re} = \frac{\rho_0 S_{L,0} L}{\mu_0} \quad &, \quad \mathrm{Pr} = \frac{\mu_0 C_{P_0}}{\lambda_0}, \\ \mathrm{Sc} = \frac{\mu_0}{\rho_0 D_0} \quad &, \quad \mathrm{Ma} = \frac{S_{L,0}}{\sqrt{\gamma(R/W_{air})T_0}}\end{aligned} \tag{4.10}$$

where R is the universal gas constant. We assume unity Lewis number and Pr = Sc = 0.7. In the equations, Re = 30 and Ma = 0.014159 (equivalent to T_0 = 298K, L = 0.09mm and $S_{L,0}$ = 4.9m/s).

A single-step irreversible chemical reaction following an Arrhenius law was assumed

$$\text{Fuel} + \text{sOxygen} \quad \rightarrow \quad (1+\text{s})\text{Products} \tag{4.11}$$

where s is the mass of oxygen consumed per unit mass of fuel with the stoichiometric fuel mass fraction being $Y_{F_{st}}$=0.062. The fuel reaction rate takes the form

$$\hat{\omega_F} \quad = \quad -B^* \hat{\rho} Y_F Y_{O_2} \exp\left[-\frac{\beta(1-\hat{T})}{1-\alpha(1-\hat{T})}\right] \tag{4.12}$$

where the chemical parameters used are

$$\beta = \frac{E_a(T_{ad}-T_0)}{RT_{ad}^2}, \alpha = \frac{T_{ad}-T_0}{T_{ad}} = \frac{\tau}{1+\tau}, B^* = B\exp\left[-\frac{\beta}{\alpha}\right] \tag{4.13}$$

where E_a is the activation energy, R is the universal gas constant, B is the pre-exponential factor and $\beta = 6$. The heat release parameter $\tau = (T_{ad} - T_0)/T_0$ was set here to 6.68. This chemistry has been used in the past for premixed [125, 126] and non-premixed [14, 42, 85, 99, 127] combustion in 3D DNS, motivated by the need to place computational resources on the proper description of the turbulence. It over-predicts the flame speed for rich mixtures, as discussed at length in Ref. [85] and in Appendix A, but this deficiency is not expected to affect the trends revealed in the present study that focuses on the effects of the evaporation, turbulence, and spark location on the flame. In addition, it has been shown that the use of this single-step chemistry produces statistics of edge flame speed that are consistent with complex chemistry and experiment. In particular, this 1-step chemistry has been used in turbulent edge flame DNS, which produced probability density functions (PDF) of the edge displacement speed measured at stoichiometry virtually identical to similar PDFs produced experimentally [97, 127], hence ensuring the relevance of a 1-step

scheme for triple point displacement speed statistics. Therefore the use of single-step chemistry for our aims is not a prohibitive limitation. Results are presented extensively with classical 1-step chemistry in Section 4.3. Moreover, the present set of simulations was also computed with a modified 1-step chemistry (Appendix A), that reproduces the flame speed profile of heptane and is reported in Section 4.4. However, we must warn that there are chemical aspects of droplet combustion that go beyond the usual requirement to capture the flame speed at all equivalence ratios: the one-dimensional laminar flame simulations of Chapter 3 have shown that due to evaporation in the post-flame region, pyrolysis may occur which supplies hydrogen and other hydrocarbons to the reaction zone by diffusion and this results in increased flame speeds. Chemical mechanisms of this level of complexity are used in Chapter 5, in 3D DNS of spark ignited turbulent sprays.

The source term $\hat{q}_{sp}$ in the energy equation accounts for the energy deposition by the spherical spark and follows a Gaussian distribution in the radial direction [85]:

$$\hat{q}_{sp} = a\left[\frac{\sqrt{2}}{3\sqrt{\pi}}\tau\exp\left(-\frac{\hat{r}^2}{2\hat{R}_{ign}^2}\right)\right]\frac{H(\hat{t})-H(\hat{t}-\hat{t}_{sp})}{\hat{t}_{sp}} \tag{4.14}$$

where a is the parameter determining the total energy input, taken as 1.6 in our study. This value, found by trial and error, resulted in a spark sufficiently large to lead to a propagating flame and sufficiently small to leave the non-periodic boundaries of the domain free of temperature gradients. R_{ign} is the characteristic radius of the spark, H is a Heaviside function and t_{sp} is the duration of the spark. Therefore, the effect of the spark is purely thermal.

The terms $\hat{\Gamma}_m$, $\hat{\Gamma}_{U_i}$ and $\hat{\Gamma}_E$ represent, respectively, non-dimensional sources of mass, momentum and energy from the liquid phase. These are detailed in the next section.

4.2.2 Liquid phase

Fuel droplets are treated as point sources of mass, momentum and energy and are tracked in a Lagrangian manner. Non-uniformity of temperature inside the droplets and droplet interactions are neglected. The non-dimensional governing equations for position $\hat{\mathbf{x}}_d$, velocity $\hat{\mathbf{v}}_d$, diameter $\hat{a}_d$ and temperature $\hat{T}_d$ for droplet d are [100]:

$$\frac{d\hat{\mathbf{x}}_d}{d\hat{t}} = \hat{\mathbf{v}}_d \tag{4.15}$$

$$\frac{d\hat{\mathbf{v}}_d}{dt} = \frac{\hat{\mathbf{U}}(\hat{\mathbf{x}}_d,\hat{t}) - \hat{\mathbf{v}}_d}{\hat{\tau}_d^v} \tag{4.16}$$

$$\frac{d\hat{a}_d^2}{d\hat{t}} = -\frac{\hat{a}_d^2}{\hat{\tau}_d^p} \tag{4.17}$$

$$\frac{d\hat{T}_d}{d\hat{t}} = \frac{\hat{T}(\hat{\mathbf{x}}_d,\hat{t}) - \hat{T}_d - B_{M,d}L_v/(\tau W_F T_0 C_{P_0})}{\hat{\tau}_d^T} \tag{4.18}$$

$\hat{\mathbf{U}}$ is the local gas velocity, L_v is the molar latent heat of evaporation and W_F is the molecular weight of fuel taken as 0.1 kg/mol. The velocity relaxation time is

$$\hat{\tau}_d^v = \mathrm{Re}\frac{(\rho_L/\rho_0)\hat{a}_d^2}{18C_D\hat{\mu}} \tag{4.19}$$

with ρ_L the liquid droplet density (equal for all droplets) and

$$C_D = 1 + \frac{1}{6}\mathrm{Re_d}^{2/3} \tag{4.20}$$

where the droplet Reynolds number is defined as

$$\mathrm{Re_d} = \mathrm{Re}\frac{\hat{\rho} \mid \hat{\mathbf{U}}(\hat{\mathbf{x}}_d,t) - \hat{\mathbf{v}}_d \mid \hat{a}_d}{\hat{\mu}} \tag{4.21}$$

The particle and the temperature relaxation times are respectively:

$$\hat{\tau}_d^p = \mathrm{Re}\frac{(\rho_L/\rho_0)\hat{a}_d^2}{4\hat{\mu}}\frac{\mathrm{Sc}}{\mathrm{Sh_c}}\frac{1}{\ln(1+B_{M,d})} \tag{4.22}$$

$$\hat{\tau}_d^T = \mathrm{Re}\frac{(\rho_L/\rho_0)\hat{a}_d^2}{6\hat{\mu}}\frac{\mathrm{Pr}}{\mathrm{Nu_c}}\frac{B_{M,d}}{\ln(1+B_{M,d})}\frac{C_P^L}{C_{P_0}} \tag{4.23}$$

where C_P^L is the heat capacity of the liquid. Under the assumption of unity Lewis number, the corrected Sherwood and corrected Nusselt numbers are equal:

$$\mathrm{Sh_c} = \mathrm{Nu_c} = 2 + \frac{0.55\mathrm{Re_d}\mathrm{Sc}}{(1.232 + \mathrm{Re_d}\mathrm{Sc}^{4/3})^{1/2}} \tag{4.24}$$

The Spalding number $B_{M,d}$ is related to the mass fraction of fuel $Y_F(\mathbf{x}_d, t)$ in the surrounding gas and to the saturated mass fraction of fuel at the droplet surface $Y^s_{F,d}$ by

$$B_{M,d} = \frac{Y^s_{F,d} - Y_F(\mathbf{x}_d, t)}{1 - Y^s_{F,d}} \tag{4.25}$$

Phase equilibrium is assumed at the droplet surface and the Clausius-Clapeyron equation is used to calculate $Y^s_{F,d}$ for each droplet:

$$\hat{P}^s_{F,d} = \frac{P_{ref}}{\rho_0 S^2_{L,0}} \exp\left(\frac{L_v}{R}\left[\frac{1}{T^s_{ref}} - \frac{1}{\left(\hat{T}^s_d \tau + 1\right) T_0}\right]\right) \tag{4.26}$$

$$Y^s_{F,d} = \left(1 + \frac{W_{air}}{W_F}\left[\frac{\hat{P}(\mathbf{x}_d, t)}{\hat{P}^s_{F,d}} - 1\right]\right)^{-1} \tag{4.27}$$

where T_{ref} is the boiling temperature at the reference pressure P_{ref} and $\hat{T}^s_d$ is the non-dimensional surface temperature assumed equal to $\hat{T}_d$.

Two-way coupling holds between gas and liquid phases. The liquid source terms appearing in Eq. 4.2 to 4.6 are computed as

$$\hat{\Gamma}_m = -\frac{1}{\hat{V}} \sum_d \alpha_d \frac{d\hat{m}_d}{d\hat{t}} \tag{4.28}$$

$$\hat{\Gamma}_{U_i} = -\frac{1}{\hat{V}} \sum_d \alpha_d \frac{d\hat{m}_d \hat{\mathrm{v}}_{d,i}}{d\hat{t}} \tag{4.29}$$

$$\hat{\Gamma}_E = -\frac{1}{\hat{V}} \sum_d \alpha_d \left(\frac{d\hat{m}_d (C^L_P / C_{P_0})(1 + \tau \hat{T}_d)}{d\hat{t}} + \frac{1}{2}(\gamma - 1)\mathrm{Ma}^2 \frac{d\hat{m}_d \hat{\mathrm{v}}^2_{d,i}}{d\hat{t}}\right) \tag{4.30}$$

where a summation is done over all the droplets with mass $\hat{m}_d = (\rho_L/\rho_0)(\pi \hat{a}^3_d)/6$ present in the vicinity of the node. $\hat{V}$ is the non-dimensional volume of a cell. A weighted summation is done over all the droplets. The weighting factor α_d is the portion of the volume centred on the gas node that intersects a similar volume $\hat{V}$ centred on the droplet with subscript d. Gaseous properties are similarly interpolated at a droplet location by doing a weighted summation over all cells having non-zero α_d.

Equations 4.28 and 4.29 are similar to the source terms presented in Eq. 3.6 and 3.7. Equation 4.30 is a non-dimensional formulation of Eq. 33 of Ref. [128]. The first term in this expression accounts for the convective heat transfer and the evaporated vapor enthalpy at the droplet surface while the second term represents the change in droplet kinetic energy. Hence, the first term of Eq. 4.30 represents the two first terms of Eq. 3.8. However, the expression given in Eq. 4.30 assumes that in the gas, the heat capacities of species are independent of temperature [128]. In Eq. 3.8 the heat capacities of species were temperature dependent. Note that in Chapter 5, DNS with temperature dependent thermal properties was performed.

4.2.3 Solver

Solution of the gas equations was done by the three-dimensional compressible DNS code SENGA [42, 125, 126, 129]. The boundaries in the direction of inhomogeneity (x-direction) are partially non-reflecting and are treated with the Navier Stokes Characteristic Boundary Conditions (NSCBC). The transverse directions are periodic. The first and the second derivatives of the gas phase are evaluated with a 10th-order central difference scheme. The order of differentiation gradually decreases to second order one-sided finite difference near the non-periodic boundaries. Time advancement is done with a third-order, low storage, Runge-Kutta scheme. Equations 4.15 to 4.18 for the droplets are advanced with the same third-order, low storage, Runge-Kutta scheme.

4.2.4 Initial Conditions

The fuel was initially contained in a homogeneous dispersion of monodisperse droplets (same initial diameter) in a region of air surrounded from both sides by air without any droplets, see Fig. 4.1. The droplets were randomly distributed in space so that their average (over $y-z$ planes) number per unit volume resulted in an equivalence

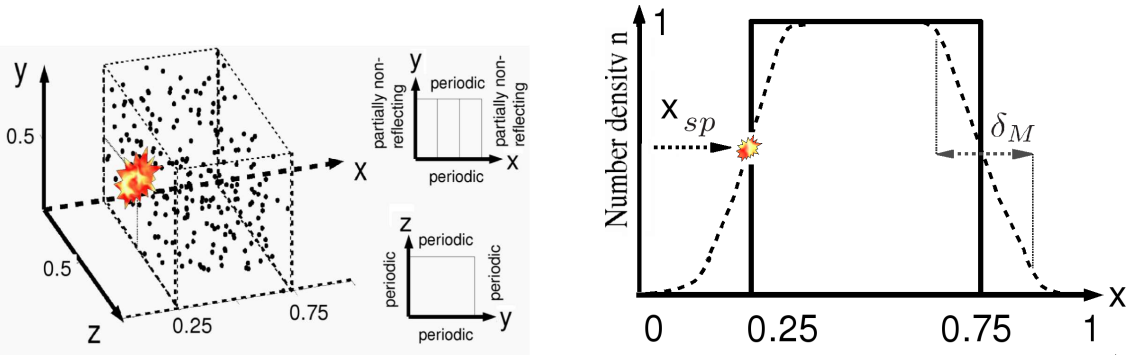

(a) (b)

Figure 4.1: (a) DNS Domain with non-dimensional coordinates. (b) Variation of the normalised number density in x-direction (direction of inhomogeneity). The location of the spark and the width of the droplet-air mixing layer are shown.

ratio given by

$$\Phi = \frac{\phi_0}{2}[1+\text{erf}(\frac{\hat{x}-0.25}{\hat{\delta_M}})(1-H(\hat{x}-0.5))- \text{erf}(\frac{\hat{x}-0.75}{\hat{\delta_M}})H(\hat{x}-0.5)] \quad (4.31)$$

with H the Heaviside function and $\hat{x}$ the non-dimensional coordinate. $\phi_0 = 2$ was the global equivalence ratio inside the droplet-laden fluid. This remains inside the flammability limit for the chemistry employed. $\hat{\delta}_M$ characterizes the initial thickness of the mixing layers between the droplet-laden region and the air and was zero for a top-hat function profile (base case), as shown in Fig. 4.1. Simulations were carried out in a 128^3 grid with periodic boundaries in the y- and z-directions, and non-reflecting conditions in the x-direction. The domain length was $L = 21\delta_r$ and approximately equal to 0.1 mm. $\delta_r = D_{th,0}/S_{L,0}$ is the laminar flame reaction zone thickness, while the non-dimensional flame thickness is $\hat{\delta}_r = 1/(\text{ReSc})$.

The initial turbulent velocity field was generated with a pseudo-spectral method based on the Batchelor-Townsend spectrum [129]. The initial integral length scale was $L_{11} = 4.5\delta_r$. For the base case, the initial turbulence intensity was $u' = 4.26S_{L,0}$, but a laminar case ($u' = 0$) and a higher turbulence case with $u' = 8S_{L,0}$ were also

computed. The Kolmogorov length scale η_K was about 1.4 grid spacings at the coarsest resolution and at least 10 grid points fitted in the thermal thickness of a stoichiometric laminar premixed flame $\delta_{th} = (T_{ad} - T_0)/(\max(\mid \nabla T \mid))$. The initial droplet diameter was always below $0.2\eta_K$ and the smallest initial average droplet spacing was about $1.5\eta_K$. In the base case, the initial diameter is $\hat{a}_d = 2 \times 10^{-3}$.

The spark source term of Eq. 4.14 had a characteristic width $R_{ign} = 1.1\delta_r$. It was centred at $(\hat{x}_{sp}, 0.5, 0.5)$ and was switched on at the start of the simulation for a time $t_{sp} = 0.2t_r$. $t_r = \delta_r/S_{L,0}$ is the dimensional characteristic flame time [14] and $\hat{t}_r = 1/(\mathrm{ReSc})$. Note that the simulations of Ref. [42] used sparks fully inside the droplet-laden fluid (i.e. at $\hat{x}_{sp} = 0.5$) and hence the ensuing flames did not clearly propagate along the interface between the air and the spray and therefore did not have any characteristics of edge flames. It was shown in that study that the fuel evaporated in the spark at the end of the energy deposition period was a controlling factor for the kernel development. In the present work, we examine droplets of different sizes and having various evaporation properties. A volatile fuel, L_v=25 kJ/mol and T_{ref}=371.60 K (0.03 in non-dimensional units), and a non-volatile fuel, L_v= 39.70 kJ/mol and T_{ref}=447.30 K (0.08 in non dimensional units), were studied. They correspond approximately to n-heptane and n-decane respectively. Note that for the volatile fuel, the rate of evaporation is significant even in the absence of flame, while for the non-volatile fuel, little vapour is produced at the cold (initial) temperature.

Eight cases were considered and case A is taken to be the base case, see Table 4.1. The parametric studies involved the initial diameter of the droplets a_d, the volatility parameters L_v and T_{ref}, the spark location x_{sp}, the intensity of turbulence u' and the droplet mixing layer thickness δ_M. For each case, one parameter at a time was modified so as to examine its effect solely. One exception is case E in which the volatility and the position of the spark are both modified. A simulation in every respect similar to case A except that the droplets are initially fully evaporated, was used for purpose of comparison. Simulations were run until $t = 4t_{sp}$ to preclude the

flame and droplets reaching the boundaries. In case H, the intense turbulence quickly transported the kernel to the non-reflecting boundary and data are not presented for $t > 3t_{sp}$.

The ratio τ_{evap}/t_{sp} is also given in Table 4.1. The evaporation times were estimated by observing the evolution of the square of the average droplet diameter $\langle a_d \rangle^2$ (the symbol $\langle\ \rangle$ denotes averaging over the entire DNS domain): after a rapid transient caused by the initial absence of fuel vapour in air, $\langle a_d \rangle^2$ became a quasi-linear function of time. Comparison of the base case with a cold evaporation case has shown that the rate of decay of the volume averaged droplet diameter was not significantly affected by the flame during the first half of the simulation and that the best estimate of the rate of droplet decay is at $2t_{sp}$ when the effect of the flame on the global evaporation is still weak. Extrapolation to zero diameter gave the average evaporation time. Note that this time is not necessarily equal to the evaporation time evaluated by the single-droplet evaporation theory into infinite, clean surroundings due to the accumulation of vapour in the domain. It offers, however, a more realistic estimate of the time droplets survive in our specific flow. It is clear from the values in Table 4.1 that cases with large droplets or non-volatile fuel have longer evaporation times. The Group number G of the slab of droplets was calculated through

$$G = 3(1 + 0.276\mathrm{Re_d}^{1/2}\mathrm{Sc}^{1/3})\mathrm{LeN}^{2/3}(\mathrm{a_d}/\mathrm{s_d}) \tag{4.32}$$

G is about 100 for case B and 200 for the other cases and correspond to the external combustion mode. G is based on the volume of the domain with size L and the droplet spacing s_d (found through the total number of droplets in the slab). The Lewis number is taken as 1 while the droplet Reynolds number is calculated using the turbulent intensity u' as velocity. According to the classification of Reveillon and Vervisch [100], we expect our flame to develop as a triple flame.

A gaseous mixture fraction ξ and an overall mixture fraction ξ_0, which takes into

Table 4.1: Parameters for the investigated cases. For all, $t_{sp} = 0.2t_r$, $t_r = \delta_r/S_{L,0}$, $L_{11} = 4.5\delta_r$, $t_{turb} = L_{11}/u'$, $R_{ign} = 1.1\delta_r$ ($R_{ign} = 1.4\delta_r$ with modified 1-step chemistry).

Case	$\frac{u'}{S_{L,0}}$	$\left(\frac{a_d}{a_{d,base}}\right)^2$	L_v & T^s_{ref}	$\hat{x}_{sp}$	$\frac{\delta_M}{\delta_r}$	τ_{evap}/t_{sp}	t_{sp}/t_{turb}
A	4.26	1	Volatile	0.25	0	11.0	0.19
B	4.26	2	Volatile	0.25	0	18.0	0.19
C	4.26	1	Non-volatile	0.25	0	90	0.19
D	4.26	1	Volatile	$0.25 - 1.1\hat{\delta}_r$	0	10.8	0.19
E	4.26	1	Non-volatile	$0.25 - 1.1\hat{\delta}_r$	0	100	0.19
F	4.26	1	Volatile	0.25	2.5	10.15	0.19
G	0	1	Volatile	0.25	0	12.3	-
H	8	1	Volatile	0.25	0	10.3	0.36
Gaseous	4	-	-	0.25	0	-	0.19

account both gaseous fuel and droplets in a cell of volume $\Delta\hat{x}^3$, are defined by

$$\xi = \frac{Y_F - sY_{O_2} + s0.233}{1 + s0.233} \tag{4.33}$$

$$\xi_0 = \frac{\sum_d \hat{m}_d + \xi\hat{\rho}\Delta\hat{x}^3}{\sum_d \hat{m}_d + \hat{\rho}\Delta\hat{x}^3} \tag{4.34}$$

Therefore, ξ_0 is related to the overall equivalence ratio ϕ_0 by

$$\phi_0 = \frac{\xi_0}{1 - \xi_0}\frac{1 - \xi_{st}}{\xi_{st}} \tag{4.35}$$

4.3 Results with classical 1-step chemistry

4.3.1 Distribution of fuel

Since the amount of fuel available for the kernel is expected to be a major parameter, it is instructive to comment on the time evolution of the droplet distribution and the gaseous mixture fraction ξ. The initial droplet distribution is given by Eq. 4.31. We

consider averages over the homogeneous directions (i.e. over $y-z$ planes). Figure 4.2 shows the number density of droplets as a function of $\hat{x}$ normalised by the initial value in the core of the spray ($\hat{x}=0.5$) so that its maximum value is 1. Only cases A, F, G and H are compared as all other cases are similar to the base case A. We observe that due to the wider initial distribution, droplets are more widely spread in case F than in the other cases. For cases A and H, with medium and high turbulence levels respectively, the profiles relax from a top-hat to a smooth profile with time due to the transport of droplets by turbulence. At $t=3t_{sp}$, the difference between cases A and F has considerably decreased. Moreover, the profiles relax faster with a high turbulence intensity, case H, than with a low one, case A, due to the intensified transport of droplets. In the laminar case, the profile does not relax in this manner. The only phenomenon which affects the droplets distribution is the gas expansion due to the temperature increase. This causes the droplets to drift away from the kernel creating some asymmetry in the profile. This effect was pointed out in an experiment carried out by Singh and Polymeropoulos [71]. In the turbulent case, the asymmetry is not significant due to the dispersion by turbulence.

In Fig. 4.3, we show profiles of the mean gaseous mixture fraction ξ (i.e. averaged over the $y-z$ plane). Cases D and E are not presented because they are similar to cases A and C respectively. At the end of the spark ($t=t_{sp}$), we observe a peak of mixture fraction in the kernel region because droplets have released most of their fuel there. Moreover, due to the finite evaporation rate even at the unreacted (cold) temperature, the mixture fraction has finite values even far from the spark. Far from the flame, cases B and C have the same distribution of droplets as case A but much lower values of gaseous mixture fraction due to the slower evaporation. In fact, the heavy fuel (case C) evaporates very little in the cold region. This results in thicker unreacted mixing layers for cases B and C. The mixture fraction increases with time for all cases and the levels reached at $3t_{sp}$ are consistent with our expectations concerning the initial droplet size and volatility (slow evaporation, therefore low ξ). Furthermore, it is evident that the differences between cases A, F,

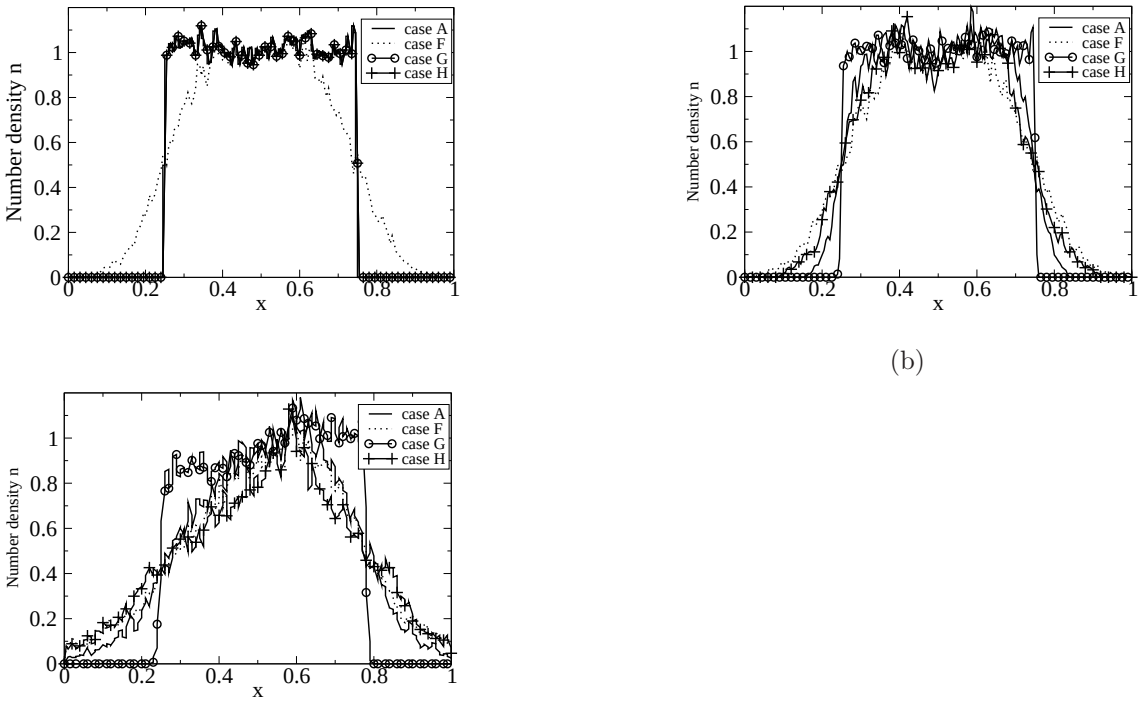

Figure 4.2: Distribution of the normalised mean droplet number density (i.e. $y-z$ plane averaged) along $\hat{x}$ at (a) $t=0$, (b) $t=t_{sp}$, (c) $t=3t_{sp}$.

G and H follow that depicted for the droplet distributions in Fig. 4.2. This shows that globally, the width of the gaseous mixing layer is directly linked to that of the droplet number density distribution. At the end of the simulation, the laminar case G has the highest value of ξ inside the droplet slab. The absence of turbulence reduces the dispersion of droplets and the diffusion of gaseous fuel which results in a thinner mixing layer.

4.3.2 General behaviour

In Fig. 4.4, we present the non-dimensional temperature in the $x-y$ plane at $\hat{z}=0.5$ (i.e. a plane passing through the spark) and $t=t_{sp}$ for cases A, D and E. The state of the flow at that time gives insight in the future development of the flame. The figure includes the contour of stoichiometric mixture fraction (ξ_{st}) and the sparked

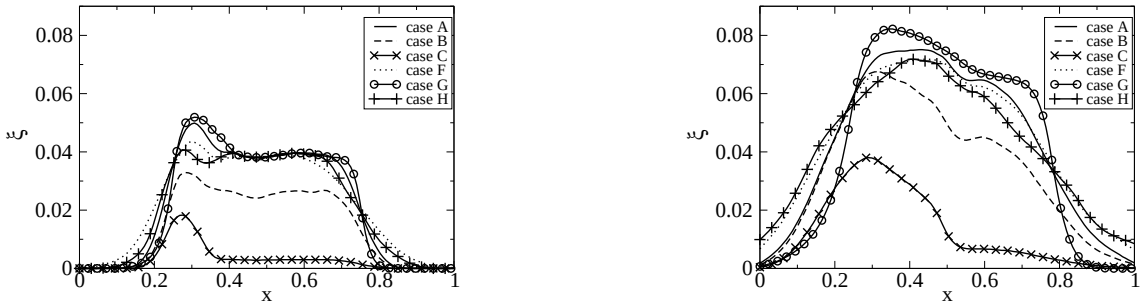

(a) (b)

Figure 4.3: Distribution of the mean gaseous mixture fraction ξ (i.e. $y-z$ plane averaged) along $\hat{x}$ at (a) $t = t_{sp}$, (b) $t = 3t_{sp}$.

region (circle of radius $\hat{R}_{ign}$). A large region of high temperature $\hat{T} > 1$ exists in all cases (similar to case A), except for case D and case E where the spark is located on the air side. There, the fuel-rich region is offset from the high temperature zone and the hot region is much smaller. In those two cases, no droplets are initially enclosed by the spark. The heat diffusing from the spark evaporates the droplets at the droplet-laden region while at the same time, the mixing layer width is increased by turbulence and results in some overlap with the spark. Once enough evaporated fuel meets high temperature, combustion eventually occurs. It is clear that in case E, much less fuel is generated than in case D due to the lower volatility. This results in much less heat release and hence a smaller kernel.

There is a greater overlap between the spark and stoichiometry in case D than in the base case. Indeed, in case A the maximum temperature is centred in a rich region. The location of the high temperature region relative to the stoichiometric mixture fraction is discussed more in detail later. The results show that the placement of the spark has an impact on the kernel development.

Figure 4.5 shows some additional details of the development of the flame kernel and the mixture fraction for different levels of turbulence and volatility of the droplets. Let us first consider the base case (row (a) in Fig. 4.5). At $t = t_{sp}$, the core of the spray is lean. The core of the spray eventually becomes richer as droplets

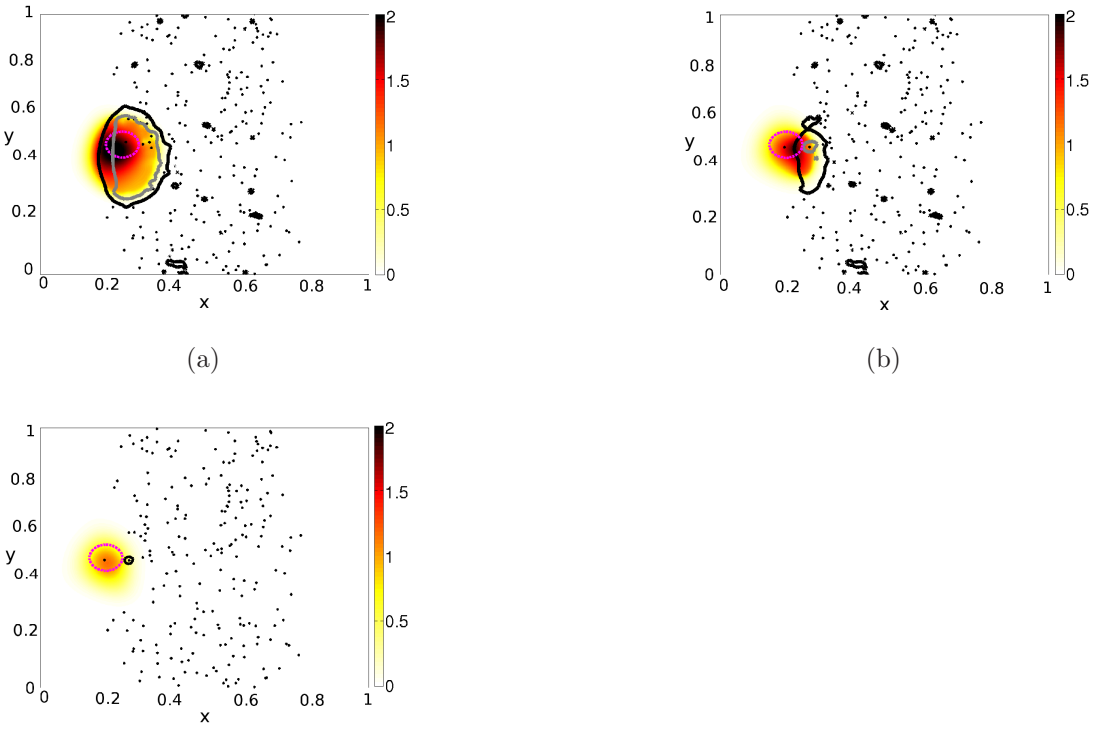

(a) (b)

(c)

Figure 4.4: $\hat{T}$ field in the plane $\hat{z}$=0.5. Magenta broken circle represents initial spark and black dots show the droplet locations. Contours of mixture fraction: $\xi = \xi_{st}$ black lines; $\xi = 0.155$ grey lines. (a) Case A, (b) Case D, (c) Case E, all at $t = t_{sp}$.

evaporate and the ξ_{st} iso-surface is eventually located at the interface between the droplet-carrying region and the surrounding air. The ξ_{st} iso-surface is wrinkled, at the droplet scale due to the localised nature of mixture fraction generation by evaporation, and at larger scales due to molecular mixing and the turbulent velocity fluctuations. The droplet-scale mechanism is present also for the laminar case (see $t = t_{sp}$, row (d) in Fig. 4.5), which explains why there are small-scale mixture fraction inhomogeneities even in the absence of turbulence in sprays. The flame is visualised in Fig. 4.5 by the red surface, which shows the iso-surface of $\hat{T} = 0.5$, i.e. half-way between the initial (cold) temperature and the adiabatic flame temperature. The presence of the flame on the lean and rich sides of the ξ_{st} iso-surface

is evident for all cases, more clearly so for the laminar flame (row (d)), where the deeper penetration of the flame into the rich spray core compared to the air side is also evident. The flame distortion by the turbulence is also evident (compare rows (d) (laminar) with (a) and (e)). In case E (row (c); less volatile fuel, spark away from the interface), the small size of the kernel at the end of the spark duration leads to failed ignition. The $\hat{T} = 0.5$ iso-surface shrinks and eventually disappears at $t_{sp} < t < 2t_{sp}$. Finally, an interesting detail is the visualisation of the generation of mixture fraction at the flame front due to the localised increased evaporation by the high flame temperature. Because of the lower saturation pressure associated with the less volatile fuel (row (b)), the core of the spray contains little fuel and the ξ_{st} iso-surface is found around the flame front during all the simulation.

In Fig. 4.6, we present the fuel reaction rate $\hat{w}_F$ distribution on a $x - y$ plane through the spark at $t = 4t_{sp}$, i.e. after the spark influence has largely diminished. The flame has a tribrachial structure, consistent with the mixing layer character of the problem. A small lean branch and a large rich branch are evident, especially in case F which has a thicker mixing layer. A trailing diffusion flame has been established on the stoichiometric iso-surface. The three branches meet at the triple point. The flame looks qualitatively similar to flames from simulations of ignition in gaseous mixing layers [14] and from experiments in lifted spray flames [101]. It is interesting to note that the lean and the diffusion branches in case G have almost merged due to the thinner mixing layer. The flame propagating in a mixing layer of fine spray has a tribrachial structure similar to that of a gas, and the propagation of the triple point will be analysed in greater detail in Section 4.3.4.

As pointed out in Ref. [42], the time evolution of the maximum temperature in the domain, $\hat{T}_{max}$, can be used to detect whether a flame establishes successfully. Figure 4.7 presents the evolution of this quantity for all simulations. In most successful cases, the temperature first increases linearly due to the source of energy from the ignitor. Thermal runaway follows and the temperature rapidly increases. For most cases, the highest $\hat{T}$ reached is about 2.2, being the highest (2.4) for the laminar flame

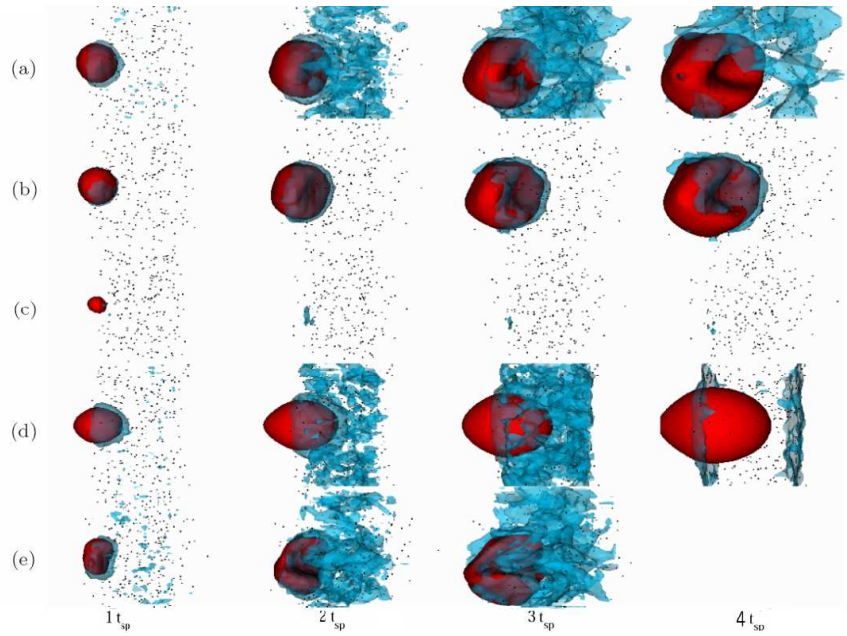

Figure 4.5: Evolution of the flame kernel in the spray with time for (a) Case A (base), (b) Case C (non-volatile), (c) Case E (non-volatile, air side), (d) Case G (laminar), and (e) Case H (higher turbulence). The temperature iso-surface $\hat{T} = 0.5$ is shown in red while the stoichiometric mixture fraction iso-surface $\xi = \xi_{st}$ is shown in blue. The dots represent droplet locations. Left column to right column: $t = t_{sp}$, $t = 2t_{sp}$, $t = 3t_{sp}$, and $t = 4t_{sp}$.

(case G) and the lowest (1.8) for the higher turbulence flame (case H) due to heat dissipation caused by turbulence. We note that the laminar flame (case G) ignites earlier than the base case, while an increase in u' (case H) further delays thermal runaway. Therefore, in the intense turbulence case, the ignitor must provide more energy for ignition to occur compared to the laminar and weak turbulence cases. It is evident that by the end of the simulation, all the flames have successfully developed and stabilise to the adiabatic flame temperature, with $\hat{T}_{max} \approx 1$, except for case E in which the spark kernel does not survive. It is also evident that the influence of the spark on $\hat{T}_{max}$ has been largely attenuated after about $3t_{sp}$.

In case D, $\hat{T}_{max}$ reaches unity in the long term, but the thermal runaway is

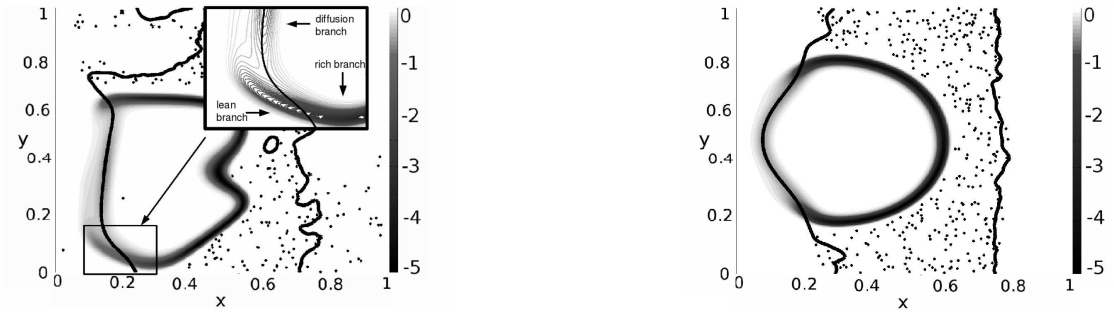

(a) (b)

Figure 4.6: Non-dimensional reaction rate distribution in the plane $\hat{z}$=0.5. Black dots show the droplet locations. Thick black lines show $\xi = \xi_{st}$. (a) Case F, (b) Case G, all at $t = 4t_{sp}$.

less steep. The highest temperature reached is only about 1.9. As we saw in Fig. 4.4, when the kernel is located on the air side it experiences much lower mixture fraction values. Consequently, the fuel mass fraction involved in the reaction is lower and results in limited heat release. Still, the success of ignition in case D implies that although the spark was initially in a location with few droplets, the flame eventually meets enough gaseous fuel to become self-sustaining. In the context of laminar non-premixed ignition, it was shown that the diffusion of heat could have a beneficial effect even if the spark was away from the flammability limits [77] while the same effect was observed experimentally in turbulent counterflows [84]. In case D, the heat diffusing from the spark first evaporates the droplets at the droplet-laden region before combustion is triggered. In case E, diffusion of heat from the kernel also occurs, but a large temperature rise associated with thermal runaway is not present. Hence, heat release is much lower at $t = t_{sp}$. At a later time, $\hat{T}_{max}$ has decayed to the cold value. The difference with case D lies with the volatility of the fuel and in turn with the amount of fuel evaporated. Therefore, the transport of heat to the spray core results in successful kernel growth only if fuel evaporation is substantial.

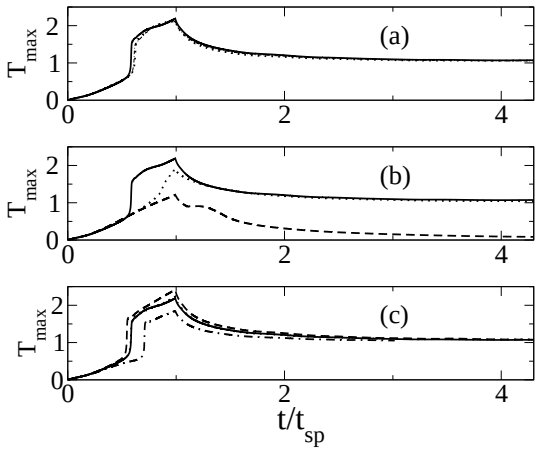

Figure 4.7: Maximum temperature in the domain. Case A: plain line; (a) Case B: dotted line ; Case C: dashed line; (b) Case D: dotted line; Case E: dashed line (c) Case F: dotted line; Case G: dashed line; Case H: dash-dotted line.

Figure 4.8 shows the time evolution of the heat release integrated over the domain and the volume of the flame (defined as fluid with $\hat{T} > 0.5$) normalised by δ_r^3 for all cases except for the failed case E. The plain line shows the evolution of those quantities for the pure gaseous case. It is evident that the cases assuming the highest heat release are those having the largest flame. It was observed that the size of the flame was mainly affected by that of the rich branch because most of the heat release occurs in this branch in the context of classical 1-step chemistry. It is interesting to note that the cases having the largest flame are those having fuel most readily available. Case D has a smaller flame because it contains initially no droplets. Cases B and C, with slow evaporation, produce less heat release because less fuel is available in the core of the spray for the propagation of the rich branch. In addition, the laminar case seems to produce less overall heat release while the turbulent case generates more heat. In our study, it was observed that a higher turbulence level led to a higher reaction rate. This tendency stems from the fact that the turbulent flames we study have a high Karlovitz number and low Damkohler numbers (less or equal to unity) and thus belong to the wrinkled thickened flame regime [6]. The

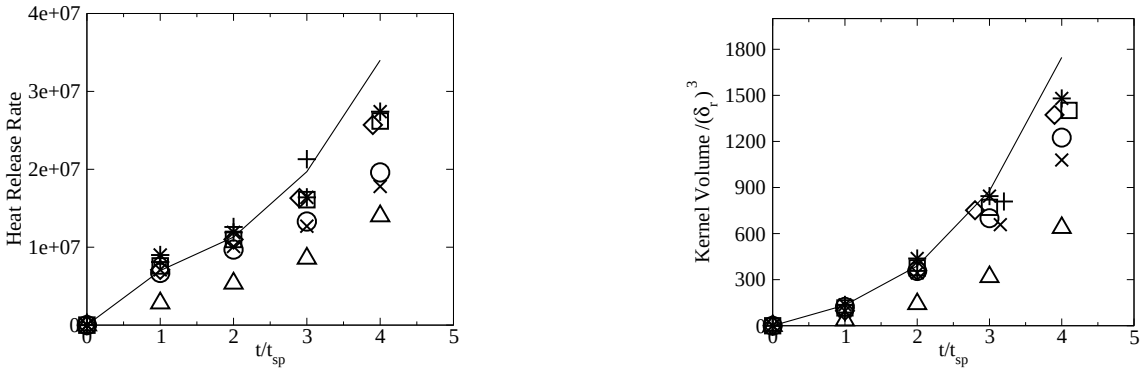

(a) (b)

Figure 4.8: Time evolution of (a) Non-dimensional heat release rate in the domain, (b) Kernel volume normalised by δ_r^3. Case A: $\square$; case B: $\diamondsuit$; case C: $\times$; case D: $\triangle$; case F: *; case G: $\bigcirc$; case H: +; Gaseous case: plain line.

purely gaseous case generates more heat and has a larger flame because the fuel is directly available for flame propagation in the rich core. Hence, the size of the flame is mainly determined by the total heat release generated and in turn the availability of fuel vapour.

The present simulations reproduce qualitatively our expectations from the experimental work of Ballal and Lefebvre [69], which showed the detrimental effect of slow evaporation on spark ignition. Our results also emphasize that in situations of inhomogeneous droplet number density, the spark location relative to the spray can introduce complicated behaviour. A combination of all these factors, including the polydispersity of realistic sprays, contributes to the probabilistic nature of recirculating spray ignition processes observed experimentally [107]. Note also the large effect of the droplet properties (size, volatility), the turbulence, and the flame itself on the location and wrinkling of the stoichiometric mixture fraction iso-surface, as visualised in Fig. 4.5. This implies that modelling of the statistics of the mixture fraction and its gradients in reacting sprays needs special attention that simple extrapolation from gaseous turbulent mixing knowledge may not cover. Work of this nature begins to appear [100, 130–135].

4.3.3 Flame kernel at the end of spark

In this section, we provide some additional details on the effect of spark location on the ignition kernel. It will be evident that the location of the maximum temperature inside the spark relative to the stoichiometric mixture fraction has an effect on the reaction rate and the subsequent edge flame propagation. In order to carry out statistics in the flame region, we define a progress variable c based on the oxygen mass fraction [42]

$$c = \frac{(1-\xi)Y_{O_2,i} - Y_{O_2}}{(1-\xi)Y_{O_2,i} - max(0, \frac{\xi_{st}-\xi}{\xi_{st}})Y_{O_2}} \tag{4.36}$$

There is a very strong correlation between c and the temperature, not shown here. Note that in a pure diffusion flame, $c = 1$ over the entire range of mixture fraction when Y_{O_2} follows the Burke-Schumann limit, while in a pure premixed flame, $c = 0$ in the unburnt gases and $c = 1$ in the burnt gases. In our study, the air side in the vicinity of the diffusion flame (i.e. very lean values) may have c close to 1. However, in the flammable region, a high c indicates a burning region. Figure 4.9 shows c against η, together with the conditional average $\langle c|\eta\rangle$ using data from all the DNS domain (η is the sample space variable for the mixture fraction). Only the base case A is shown because all the other simulations with successful ignition show similar trends. It is evident that a large scatter exists showing that the flame propagates in a wide range of mixture fractions. We can note that c is always smaller than unity in the vicinity of stoichiometric mixture fraction. In the context of tribrachial flame, this implies that the burnt region located in the trailing diffusion flame does not follow exactly the Burke-Schumann limit, which is expected in strained flames. The profile of $\langle c|\eta\rangle$ shows higher values in the rich region. This is because the rich mixture fractions are found mainly in the high temperature region where evaporation has been enhanced after combustion has occurred.

Figure 4.10 shows the temperature conditionally-averaged on the mixture fraction, $\langle \hat{T}|\eta\rangle$, for all cases at $t = t_{sp}$. Data are limited to the flame region ($c > 0.5$).

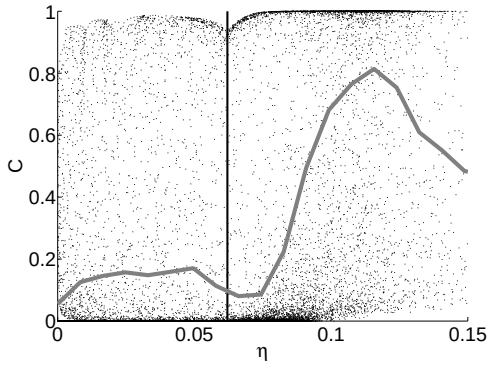

Figure 4.9: Scatter plot of c versus mixture fraction at $t = 3t_{sp}$ for case A. Data are from the entire domain, the vertical line denotes ξ_{st}. The grey line shows the conditional average of c on the mixture fraction.

With a spark at the mixing layer (case A, B, C, F, G and H), the maximum temperature occurs at rich mixture fractions. It is shown next that for those cases, the mean mixture fraction in the spark is rich. We now focus on the value of temperature near stoichiometry. The temperature peaks in richer region for cases B and C than in the base case. As a result, the temperature near stoichiometry is lower than in case A. The temperature at stoichiometry is higher for case D than the base case because the spark has a wider overlap with stoichiometry as described earlier. In case F with the wide mixing layer, it was observed that the spark is completely surrounded by rich mixtures and does not overlap with stoichiometry at $t = t_{sp}$. Hence the temperature peaks at very rich values and is only moderate near ξ_{st}. The highest value is obtained for the laminar case G because of the absence of turbulence while the temperature is much lower in case H, with higher turbulence intensity, because of the enhanced heat diffusion. It was observed that in the laminar case, the spark is surrounded by rich mixture. This can be attributed to the local gas expansion and to the large amount of fuel engulfed by the spark, as discussed next. The spark location, the properties of droplets and the turbulence have an effect on the value of temperature at stoichiometry at $t = t_{sp}$.

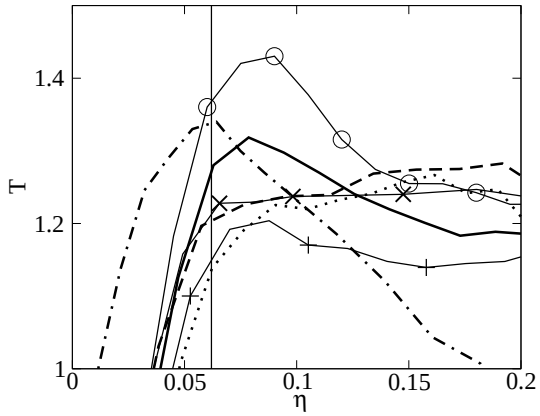

Figure 4.10: Variation of conditionally-averaged non-dimensional temperature vs. mixture fraction using data in the range $0.5 < c < 1$ at $t = t_{sp}$. The vertical line denotes ξ_{st}. Case A: plain line; Case B: dashed line; Case C: line with $\times$; Case D: dash-dotted line; Case F: dotted line; Case G: circled line; Case H: line with $+$.

In Fig. 4.11, we correlate the peak of temperature in mixture fraction space observed in Fig. 4.10 with the amount of fuel engulfed by the spark. In the plot, we show the mean overall (liquid+gas) mixture fraction ξ_0 and the mean gaseous mixture fraction ξ in the region $c > 0.5$ at $t = t_{sp}$. The mean ξ has a value close to the mean ξ_0 for all cases except B and C, which implies that almost all the fuel has evaporated in this region. In cases B and C, the slow evaporation leads to ξ equal to about 60% of ξ_0. In Fig. 4.11a, we notice that the values of ξ_0 for cases A, F, G and H are roughly the same and correspond to an equivalence ratio equal to 2.66. This is higher than the global equivalence ratio of the spray ($\phi_0 = 2$). This and Fig. 4.10 suggest that locally, very high values of mixture fraction are found. This can be attributed to the local inhomogeneities at the droplet scale. The ratio of the initial average droplet spacing to the spark diameter was measured for all cases and found to have a minimum value of 0.17 for the base case. At the spark scale, inhomogeneities tend to persist and influence the initial value of ξ_0. In cases B and C, a higher ξ_0 is present in the spark which can be explained with the

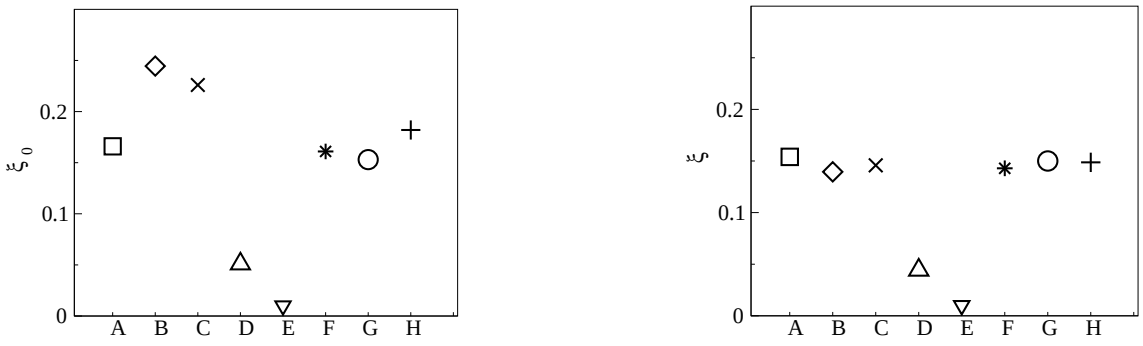

(a) (b)

Figure 4.11: Mixture fraction in burning region ($0.5 < c < 1$) at $t = t_{sp}$. (a) Gas+Liquid mixture fraction ξ_0. (b) Gaseous mixture fraction ξ. Case A: $\square$; case B: $\diamondsuit$; case C: $\times$; case D: $\triangle$; case E: $\triangledown$; case F: *; case G: $\bigcirc$; case H: +.

following argument. In those two cases, droplets evaporate much less at ambient temperature. Therefore, all the droplets that would disappear before reaching the high temperature region in case A can penetrate the spark in cases B and C. This results in more droplets engulfed by the spark. For case D, ξ_0 is very low after one spark duration because no droplets are initially contained inside the kernel. Consequently, the peak of temperature is at a lower mixture fraction and ignition is delayed. For case E, ξ_0 is zero because after one spark duration the kernel is very small with no droplets, which leads to extinction.

In Fig. 4.12, we observe that the peak of reaction rate occurs at $\xi \approx 0.15$, which is a characteristic of the simple 1-step chemistry used here. At $t = t_{sp}$, case D shows a higher $\langle|\omega_F||\eta\rangle$ at stoichiometry compared to case A, consistent with the higher $\langle\hat{T}|\eta\rangle$ at stoichiometry for this case (Fig. 4.10). However, at $t = 4t_{sp}$, $\langle|\omega_F||\eta\rangle$ has relaxed in both cases to fairly similar profiles. Hence, the effect of higher $\langle|\omega_F||\eta\rangle$ at stoichiometry is attenuated with time.

The above results suggest that the success of ignition depends on the integrated mixture fraction generated inside the spark region during the spark duration. The ensuing flame propagation phase will depend on the local turbulence, local fuel

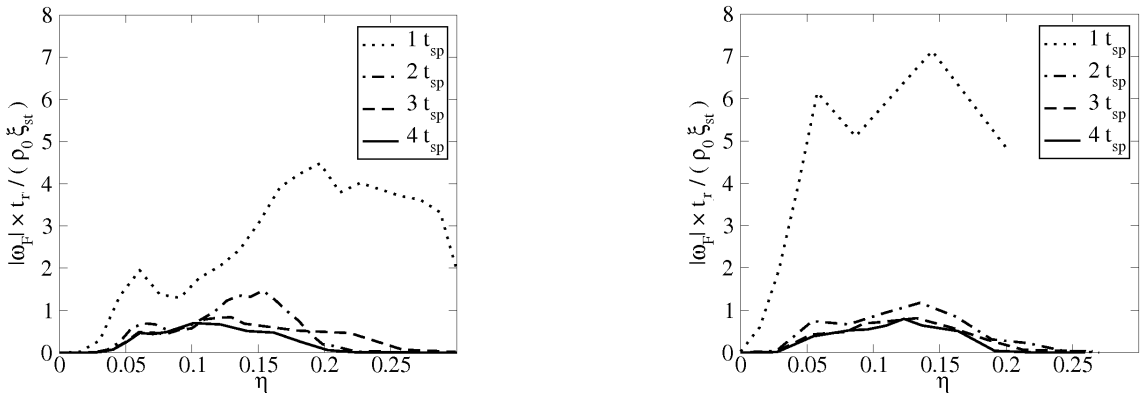

(a) (b)

Figure 4.12: Variation of conditionally-averaged normalised fuel reaction rate magnitude vs. mixture fraction using data in the range $0.5 < c < 1$; (a) Case A, (b) Case D.

vapour gradient and droplet properties, as discussed in the next section.

4.3.4 Flame displacement speed

Analysing the flame at $t = 3t_{sp}$, when the effect of the spark has faded away, provides information about the basic structure of an edge flame in sprays. From now on, we focus on the flame propagation and we do not consider the failed case E any longer. As mentioned in Section 2.3.2, such edge flames have been very little studied before and very sparse information is available about their propagation rate. We now determine the rate of spread along the stoichiometric surface of the different flames, which is quantified by the density-weighted displacement speed. This is the speed at which a mass fraction iso-surface moves normal to itself relative to the local gas [136]. This quantity is found at any point by recasting the dimensional mass fraction conservation equation in the form:

$$\frac{\partial Y_\alpha}{\partial t} + \mathbf{U} \cdot \nabla Y_\alpha \quad = \quad -S_d |\nabla Y_\alpha| \tag{4.37}$$

The displacement speed based on the fuel mass fraction has been used previously to study tribrachial laminar non-premixed flames [93, 136] and the spread of flames

following ignition in turbulent inhomogeneous flows [99, 127]. Here, we use a displacement speed based on Y_{O_2} because the gradients of fuel are strongly affected by evaporation and are therefore not as appropriate to describe the flame contour. The displacement speed is therefore calculated from

$$S_d = -\frac{\omega_{O_2} + \nabla(\rho D \nabla Y_{O_2}) - Y_{O_2}\Gamma_m}{\rho|\nabla Y_{O_2}|} \tag{4.38}$$

The density-weighted displacement speed is defined as

$$S_d^* = (\rho S_d)/\rho_0 \tag{4.39}$$

and minimises the effects of heat release. Note that the source term Γ_m originates from the continuity equation, but it does not affect the field of Y_{O_2} as strongly as that of Y_F. In addition, the definition of S_d^* is consistent with that of c (Eq. 4.36) since they are both based on Y_{O_2}. The data are presented for points with $0.1 < c < 0.85$ and with mixture fraction $\pm 10\%$ of ξ_{st} in order to measure the speed of the triple point of the edge flame. This restricted domain defines the propagating structure which includes the edge flame preheat zone and the propagating burning zone. The examination of the scatter of cross scalar dissipation $\chi_c = 2D\nabla Y_F \cdot \nabla Y_{O_2}$ against c (not shown here) has indicated predominant positive values for $c \leq 0.85$ and mainly negative values for $c > 0.85$. This revealed the presence of the trailing diffusion flame approximately beyond $c = 0.85$.

Figure 4.13 presents the probability density function of S_d^* for different cases (gaseous fuel, laminar spray and turbulent spray). In Fig. 4.13a, we first notice the finite width of the PDF in the base case, extending to positive and negative values, which indicates the presence of displacement speed fluctuations. The presence of negative values implies that the turbulence is responsible for creating locally retreating fronts. Second, the PDF extends to values much higher than $S_{L,0}$ at $t = t_{sp}$ due to the initial spark effect. As time passes, the peak moves to lower values and at the end of the simulation the peak of the PDF stabilises around 0.7 $S_{L,0}$ with little content at values beyond $2S_{L,0}$. This trend is in very good agreement with a previous

experimental study of turbulent non-premixed methane edge flames following spark ignition in the counterflow geometry (see Fig. 6 of Ref. [97]) and the PDF of the gaseous case shown in Fig. 4.13b. In Fig. 4.13c, the PDF of the laminar flame (case G) also peaks around 0.7 $S_{L,0}$ and does not extend to negative flame values at the end of the simulation. Note that even in the laminar case, the PDF shows a certain spread. This feature is due to the variation of the density weighted displacement speed with the progress variable and due to the variations of the flame curvature at the droplet scale because of the localised nature of evaporation. In the turbulent cases, the velocity fluctuations introduce additional S_d^* fluctuations. Finally, comparison of the different cases at $t = 3t_{sp}$ in Fig. 4.13d reveals that the PDFs are similar. Hence, the displacement speed S_d^* of an edge flame in a fine turbulent spray has similar characteristics to gaseous turbulent edge flames.

In Fig. 4.14, we present the variation of the volume average $\langle S_d^* \rangle$ with time for the different cases. The plain line shows the gaseous case. The initial value is quite high due to the initial effect of the spark. $\langle S_d^* \rangle$ then decreases to reach a nearly constant value. This trend is consistent with experimental results [97]. In the gaseous case, the final value is around $0.7S_{L,0}$, close to the value of $0.75S_{L,0}$ reported in the experiment [97]. In case A, the mean displacement speed stabilises around $0.65S_{L,0}$ which is slightly lower than in pure gas. All flames have $\langle S_d^* \rangle$ in the range $0.55 - 0.75S_{L,0}$, with a clearly slower flame for case D (ignition far from the interface) as also evident by the delayed ignition and the lower T_{max} achieved at the end of the spark (Fig. 4.7) and the slower kernel growth (Fig. 4.8).

The analysis of these results in the next section suggests that the major factor which controls the flame speed is the curvature of the flame at the triple point. In the context of premixed gas kernel, it was shown with DNS that the larger the kernel, the smaller the magnitude of the curvature component [126]. Furthermore, it has been shown theoretically that a laminar edge flame propagating in a gaseous mixing layer with a large thickness has a smaller curvature [137]. In Section 4.3.1, we saw that the effect of turbulence was to widen the mixing layer. However, a

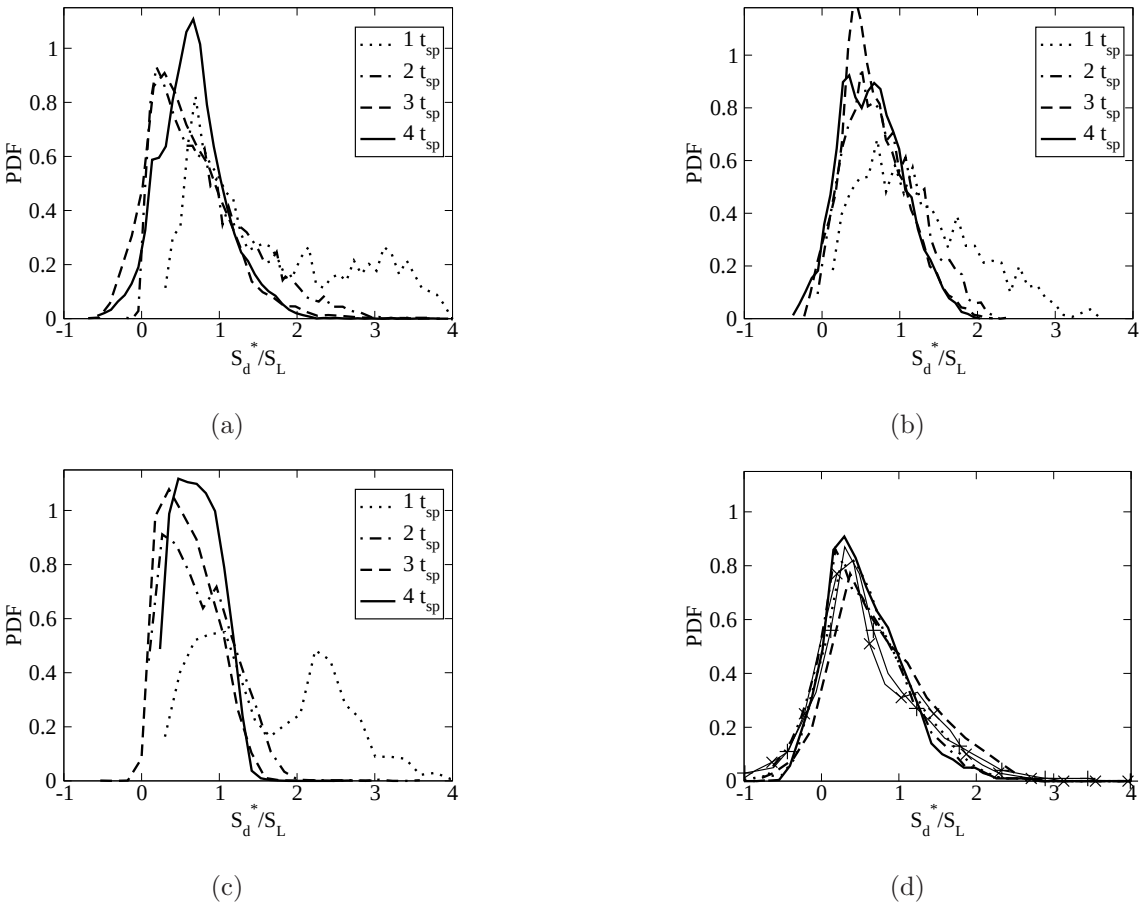

Figure 4.13: Probability density function (PDF) of the density weighted displacement speed at different times. (a) Case A, (b) Gaseous case, (c) Case G, (d) Cases at $3t_{sp}$, Case A: plain line; Case B: dashed line; Case C: line with $\times$; Case D: dash-dotted line; Case F: dotted line; Case H: line with $+$.

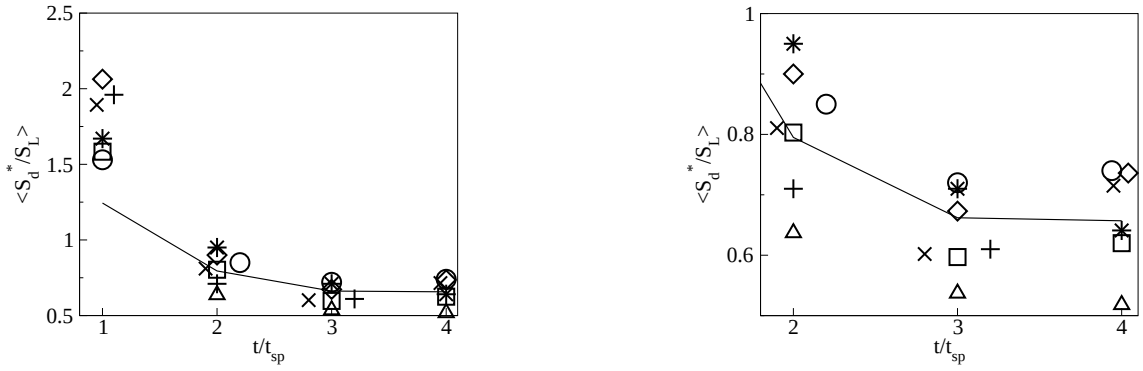

(a) (b)

Figure 4.14: Volume average of the density weighted displacement speed at the triple point normalised by the stoichiometric laminar flame speed. Details of the trends are shown with a smaller scale in (b). Case A: □; case B: ♢; case C: ×; case D: △; case F: *; case G: ◯; case H: +; Gaseous case: plain line.

higher turbulence intensity also has a detrimental effect on curvature through the deformation of the kernel. Figure 4.15 shows an iso-surface of oxygen ($Y_{O_2} = 0.12$) coloured according to curvature (defined later by Eq. 5.11). It can be seen that an increase of turbulence intensity distorts the flame and that this tends to increase the curvature magnitude which can be encountered along the triple point locus. In the next sections, we provide more details on the displacement speed components and the factors which influence their values.

4.3.5 Displacement speed components

In this section, we focus on the displacement speed of the triple point and its components. We present their statistical behavior in response to the flame curvature and we examine the relative influence of each component on the mean displacement

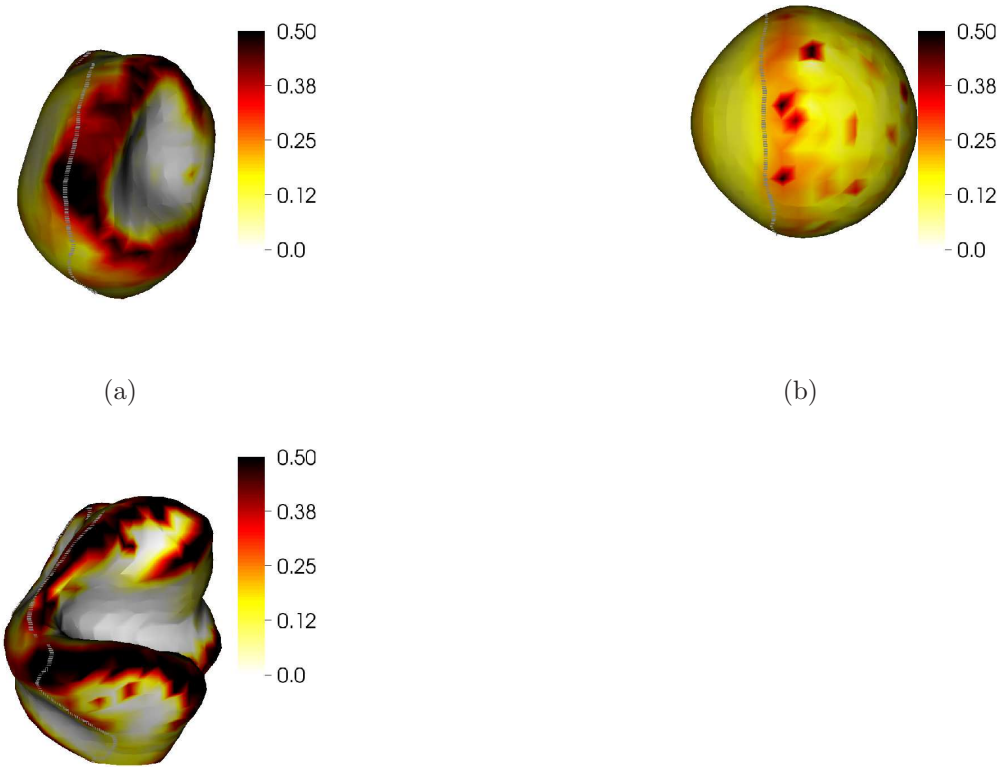

Figure 4.15: Iso-surface Y_{O_2}=0.12 coloured by normalised mean curvature ($k_m \times \delta_r$) at $t = 3t_{sp}$. The dotted line shows the ξ_{st} isoline. (a) Case A; (b) case G; (c) case H.

speed for the different cases. We decompose S_d^* into four components:

$$S_d^* = S_r^* + S_n^* + S_t^* + S_m^* \tag{4.40}$$

$$S_r^* = -\frac{\omega_{O_2}}{\rho_0 |\nabla Y_{O_2}|} \tag{4.41}$$

$$S_n^* = -\frac{\mathbf{N} \cdot \nabla(\rho D \mathbf{N} \cdot \nabla Y_{O_2})}{\rho_0 |\nabla Y_{O_2}|} \tag{4.42}$$

$$S_t^* = -2\rho D k_m / \rho_0 \tag{4.43}$$

$$S_m^* = \frac{Y_{O_2} \Gamma_m}{\rho_0 |\nabla Y_{O_2}|} \tag{4.44}$$

S_r^* is the reaction component, S_n^* is the normal diffusion component, S_t^* is the tangential diffusion component and S_m^* is the mass evaporation component. S_m^* is

an additional term compared to gaseous problems and relates to the change in local reactant mass fraction due to evaporation. We introduced the vector normal to Y_{O_2} isosurfaces, toward positive gradient, $\mathbf{N}$, and the local mean curvature k_m:

$$\mathbf{N} = \frac{\nabla Y_{O_2}}{|\nabla Y_{O_2}|} \tag{4.45}$$

$$k_m = \frac{1}{2}\nabla \cdot \mathbf{N} \tag{4.46}$$

Note that positively curved locations ($k_m > 0$) are convex towards the reactants. We now present statistics of the flame components for the base case at $t = 3t_{sp}$. The other cases follow the same qualitative description.

Figure 4.16 shows the variation of the different components of the displacement speed conditionally averaged on c on the stoichiometric isosurface. We can notice that S_m^* has negligible values beyond the preheat zone, due to the fact that fine droplets evaporate almost completely at the flame front. Furthermore, in our study where the average droplet spacing was at least twice the grid spacing, about 70% of the grid nodes do not have an evaporation source term due to the absence of neighbouring droplets, which results in small volume averages of S_m^*. The profiles of S_r^* and S_n^* follow those found for edge flames in gases [99, 127]. S_r^* has negligible values until $c = 0.5$ and peaks around $c = 0.8$, while S_n^* is positive towards the fresh gas and becomes negative in the burnt region.

The curvature component S_t^* constantly decreases with c. In our problem, k_m has predominantly positive values through the flame since the edge flame kernel is positively curved in nature. It is expected that the curvature is higher at higher values of c since the iso-surfaces of oxygen become more focused towards the burnt region and hence have a smaller radius of curvature. As in previous studies, the general effect of S_t^* is to reduce the flame speed because of the overall positive curvature. Finally, Fig. 4.16 shows that the density weighted displacement speed tends to decrease through the flame as already observed in DNS of premixed kernels [138].

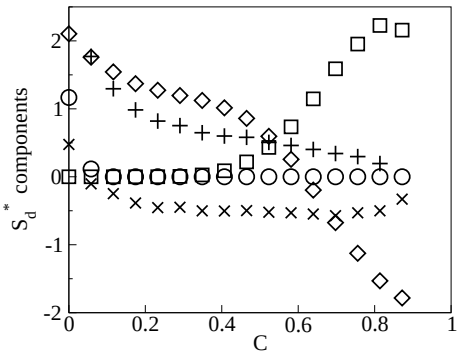

Figure 4.16: Components of the density-weighted displacement speed conditionally-averaged on the progress variable c, using data for $0.9 \leq \xi/\xi_{st} \leq 1.1$ for case A at $3t_{sp}$. $\langle S_d^* \rangle$: +; $\langle S_r^* \rangle$: □; $\langle S_n^* \rangle$: ◇; $\langle S_t^* \rangle$: ×; $\langle S_m^* \rangle$: ◯.

It is of interest to examine the curvature and ∇Y_{O_2} response of the different components of S_d^*. We proceed as in Section 4.3.4 and condition our statistics to $0.1 < c < 0.85$ and $\xi = \xi_{st} \pm 0.1\xi_{st}$. Figure 4.17a shows the scatter plot of ∇Y_{O_2} with the curvature k_m. It can be seen that for positive curvature, mainly present in the kernel, ∇Y_{O_2} is negatively correlated with k_m. In Fig. 4.17b and 4.17c, we present the scatter of S_r^* and S_n^* respectively with ∇Y_{O_2}. From the definition of S_r^*, it is not surprising to observe a negative correlation with ∇Y_{O_2}. The scatter of S_n^* with ∇Y_{O_2} shows both negative and positive correlating branches with a clearly dominant positive correlation. This behaviour is consistent with previous DNS studies of gaseous turbulent edge flame [99, 127]. Furthermore, Fig. 4.17d shows the scatter of the sum $(S_r^* + S_n^*)$ with ∇Y_{O_2} where a major negative branch appears. Since the gradient and the curvature of Y_{O2} are predominantly negatively correlated, it is not surprising to observe in Fig. 4.18, that $(S_r^* + S_n^*)$ is positively correlated with k_m. Finally, the curvature response of S_d^* is predominantly negative, see Fig. 4.18b, due to the strong negative contribution of the tangential diffusion component S_t^*. Once again, this conclusion follows the previous DNS study with gaseous flames [99, 127] and agrees with early theoretical work on laminar triple flames [89]. Therefore, the

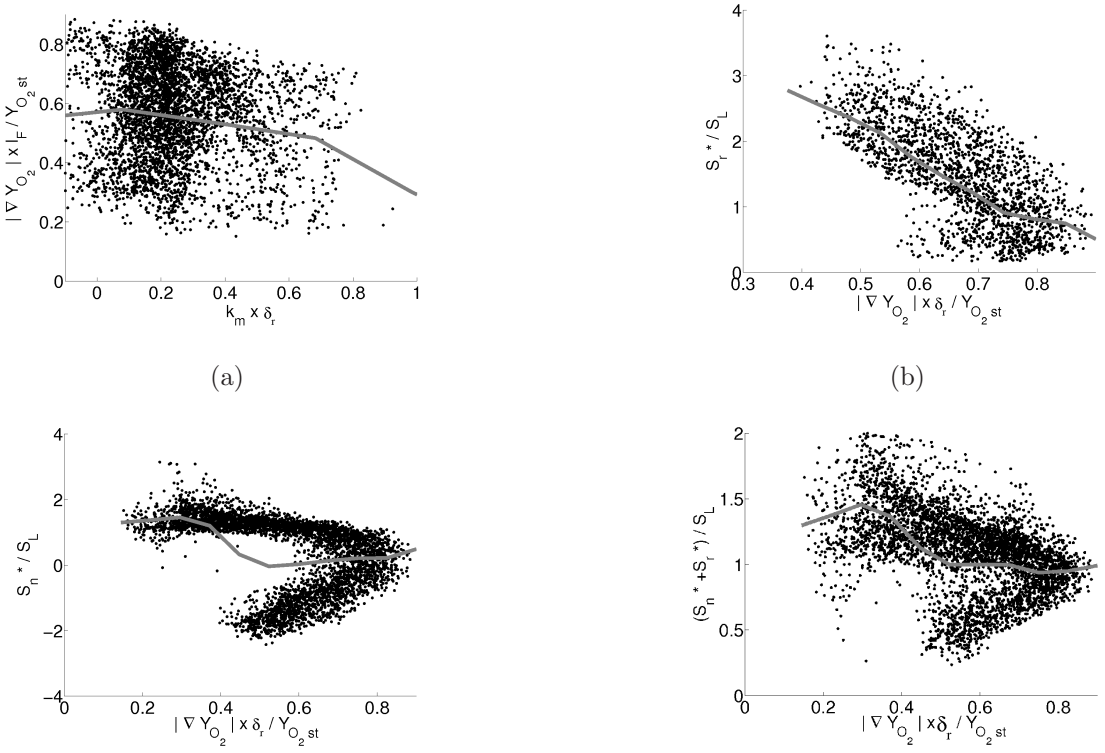

Figure 4.17: Scatter plot for case A in region $0.1 \leq c \leq 0.85$ at $t = 3t_{sp}$ of: (a) normalised ∇Y_{O_2} versus normalised mean curvature k_m. (b) Reaction component S_r^* versus normalised ∇Y_{O_2}. (c) Normal diffusion component S_n^* versus normalised ∇Y_{O_2}. (d) $(S_r^* + S_n^*)$ versus normalised ∇Y_{O_2}. The grey line shows the conditional averages.

tribrachial flame that propagates in a cloud of fine droplets has similar statistics and curvature response to that in pure gaseous fuel mixing layer. This is due to the fact that droplets rapidly disappear at the flame front.

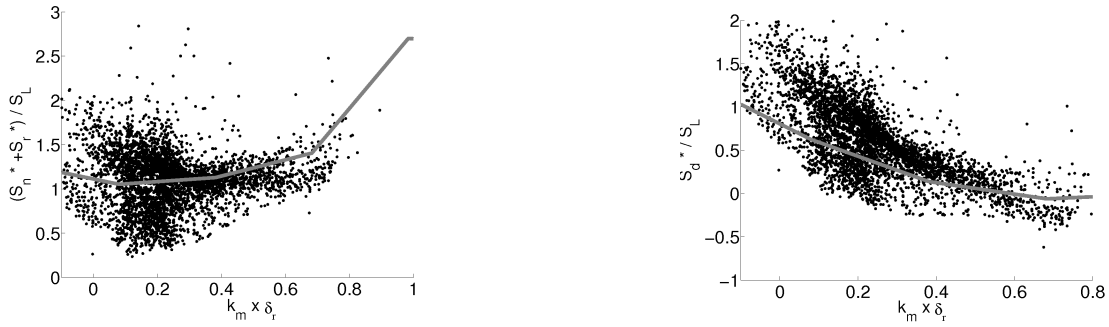

(a) (b)

Figure 4.18: Scatter plot for case A in region $0.1 \leq c \leq 0.85$ at $t = 3t_{sp}$ of: (a) $(S_r^* + S_n^*)$ versus normalised k_m. (b) S_d^* versus normalised k_m. The grey line shows the conditional average.

4.3.6 Influence of parameters on displacement speed components

In order to understand the influence of the different spray and flow parameters on the mean displacement speed, Fig. 4.19 presents the evolution of each component conditioned on c in the triple point region ($\xi = \xi_{st} \pm 0.1\xi_{st}$) at $t = 3t_{sp}$. Firstly, it can be seen that S_m^* is positive only for $c < 0.1$. Interestingly, the peak of S_m^* occurs at higher values of c in case C (non-volatile) because the evaporation of the non-volatile fuel is triggered only when a sufficiently high temperature is reached.

Secondly, all cases have approximately the same S_n^* over the range of progress variable.

Thirdly, in Fig. 4.19b, the reaction component S_r^* is clearly higher for case D than in case A. This is a direct consequence of the effect of the value of the temperature conditioned on stoichiometry at the end of the spark discussed in Section 4.3.3. Cases B and C are consistent with this argument since they have fairly lower reaction components than in case A. Hence, the reaction component at $3t_{sp}$ is sensitive to the temperature on the stoichiometric contour and thus to the location of the spark. However, cases F, G and H do not seem to be consistent with this argument. Case

F has a higher S_r^* despite a lower temperature at stoichiometry. It was observed that the reaction rate is indeed lower than in the base case but the flame in that case was thicker which implied a lower gradient of oxygen $|\nabla Y_{O_2}|$. As an overall effect S_r^* happened to be higher. Furthermore, the laminar case G and the higher turbulence case H had respectively higher and lower temperature at $t = t_{sp}$. This order is the same at $3t_{sp}$, but the reaction rates do not follow the same trend. As mentioned in Section 4.3.2, a higher turbulence intensity led to a higher reaction rate in our problem. This resulted in higher S_r^* for case G and lower S_r^* for case H. The analysis of the results revealed that the flame speed was higher in the pure gas case because the spark location is closer to the stoichiometric contour than in case A. However, this advantage disappears with time and by the end of the simulation the flame speed is only slightly higher than in case A. As mentioned in section 4.3.3, the effect of higher reaction rate due to spark location is attenuated with time and has a short term effect only.

Finally, we discuss the tangential component S_t^* from Fig. 4.19d. S_t^* is directly related to curvature by its definition in Eq. 4.43. A positive curvature k_m induces a negative S_t^* and reduces the flame speed. In Section 4.3.4, we have suggested that the kernel size, the mixing layer width and the turbulence intensity affect curvature. In case D, the kernel development was delayed and the kernel volume is substantially lower than in the other cases, as shown in Fig. 4.8. Therefore, it is expected to observe in Fig. 4.19d that S_t^* has a higher negative magnitude in case D. This component impacts strongly on the flame speed of case D and makes it lower than in the other cases. The difference in the magnitude of S_t^* for the other cases cannot be attributed to the kernel size only. In cases B and C, we showed that the mixing layer is thick due to the slow evaporation. Furthermore, the initial wide spread of droplets in case F induces a wider gaseous mixing layer than in case A. The consequence of the wide layers in cases B, C and F is that the magnitude of S_t^* is lower than that of case A. However, it must be pointed out that the initial distribution of droplets in case F has an impact on the flame speed through the curvature but without a

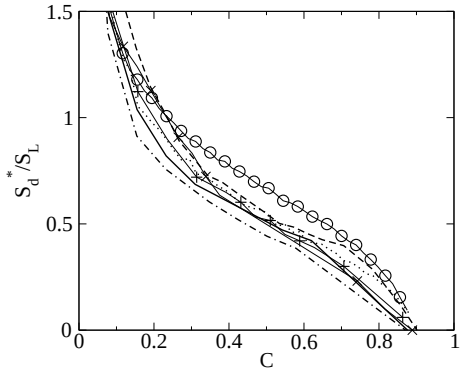

(a)

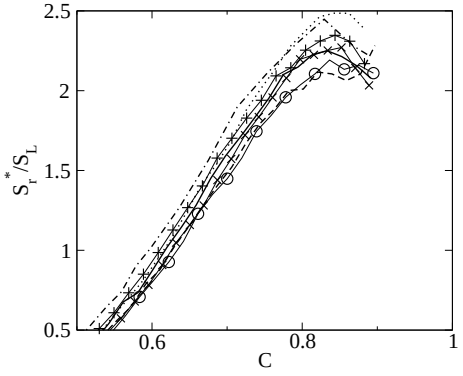

(b)

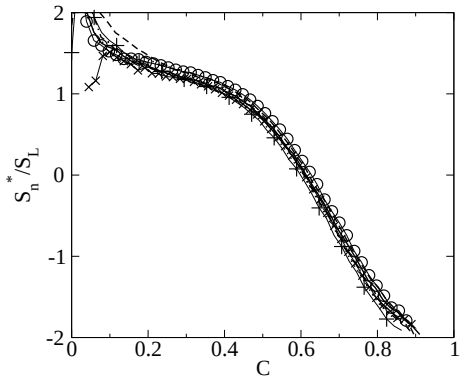

(c)

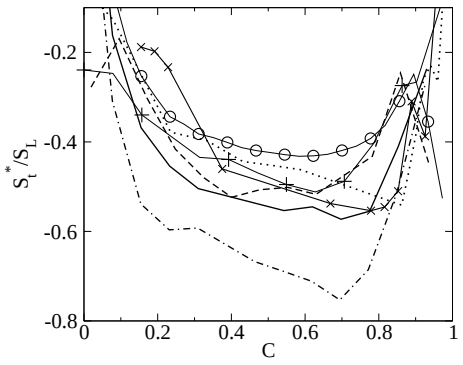

(d)

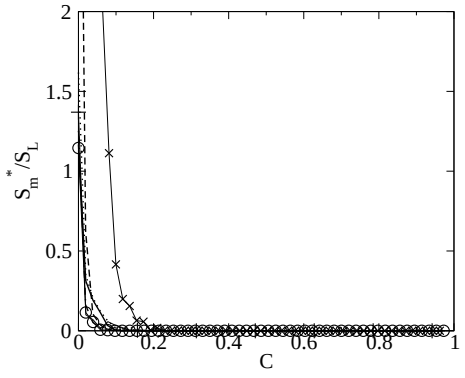

(e)

Figure 4.19: Data as in Fig. 4.16 but for all cases studied. (a) $\langle S_d^* \rangle$. (b) $\langle S_r^* \rangle$. (c) $\langle S_n^* \rangle$. (d) $\langle S_t^* \rangle$. (e) $\langle S_m^* \rangle$. Case A: plain line; Case B: dashed line; Case C: line with $\times$; Case D: dash-dotted line; Case F: dotted line; Case G: circled line; Case H: line with $+$.

long term effect because turbulence relaxes the mixing layers to the same shape. Finally, two competitive effects act on the triple flame curvature when increasing the turbulence intensity. On one hand, the flame is distorted which may locally lead to high values of curvature. On the other hand, the mixing layer widens and in turn the curvature decreases. The overall effect is that the laminar case G has a much lower magnitude of S_t^* than the base case and in case H, with higher turbulence, the magnitude of S_t^* is lower than in case A. Finally, it is interesting to observe that the component which is the most sensitive to droplet parameters is the curvature component. Curvature has a long term effect and a higher impact on S_d^* compared to the reaction component.

4.4 Results with modified 1-step chemistry

The results of Section 4.3 showed that the classical 1-step chemistry resulted in very good agreement between the computed and the experimental PDFs of the gaseous edge flame. However, since the classical 1-step chemistry does not account properly for the flame speed variation with mixture fraction, it is interesting to look at the results with a modified 1-step chemistry which has the correct variation, developed by Richardson [7] with the method of Fernandez-Tarrazo et al. [139], see Appendix A. In order to compare the results, the cases of Table 4.1 are computed again with the modified chemistry, except for the gaseous case. A drawback of this chemistry, is that a flame is harder to ignite with the present configuration. Indeed, the fact that a flame cannot propagate in the rich mixture results in a smaller flame volume and hence a higher curvature, detrimental for its growth. For this reason, no flame could be ignited by using the same spark radius ($R_{ign} = 1.1\delta_r$) as with the classical 1-step chemistry. We decided to use a larger spark radius, $R_{ign} = 1.4\delta_r$, in order to generate a kernel.

In this section, we do not present results as extensively as in Section 4.3. Instead, we try to cover the major common points and differences found using a classical and

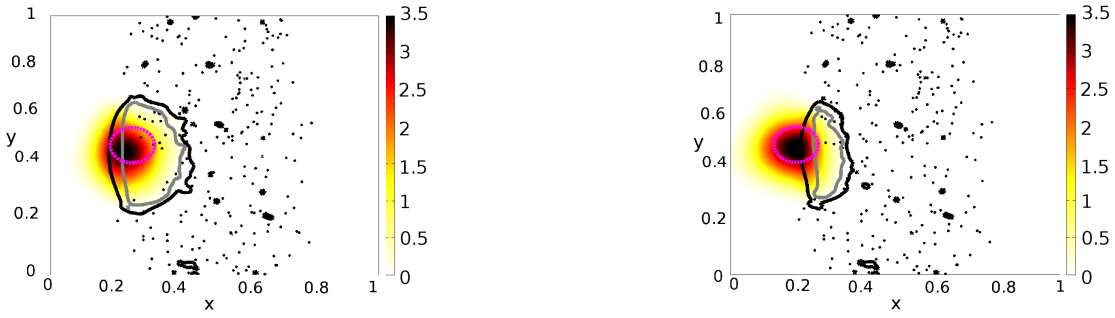

(a) (b)

Figure 4.20: $\hat{T}$ field in the plane $\hat{z}$=0.5. Magenta broken circle represents initial spark and black dots show the droplet locations. Contours of mixture fraction: $\xi = \xi_{st}$ thick black lines; $\xi = 0.12$ thick grey lines. (a) Case A, (b) Case D at $t = t_{sp}$.

a modified 1-step chemistry. Results are not presented for case E, because a failed ignition event was observed and no new features are added by the use of a different model of chemistry.

4.4.1 Distribution of fuel with modified chemistry

The evolution of the distribution of droplet number density and gaseous mixture fractions are not presented because the trends are the same as those described in Section 4.3.1.

4.4.2 General behaviour with modified chemistry

In Fig. 4.20, we present the non-dimensional temperature in the $x - y$ plane at $\hat{z} = 0.5$ (i.e. a plane passing through the spark) and $t = t_{sp}$ for cases A and D. Note the larger spark used in the present simulations. By comparing with Fig. 4.4, it is clear that essentially the same result is found with the modified chemistry. The heat diffusion from the spark in case D enables fuel evaporation in the mixing layer. In addition, we find again that case D has a greater overlap with stoichiometry than case A. The location of the high temperature region relative to the stoichiometric

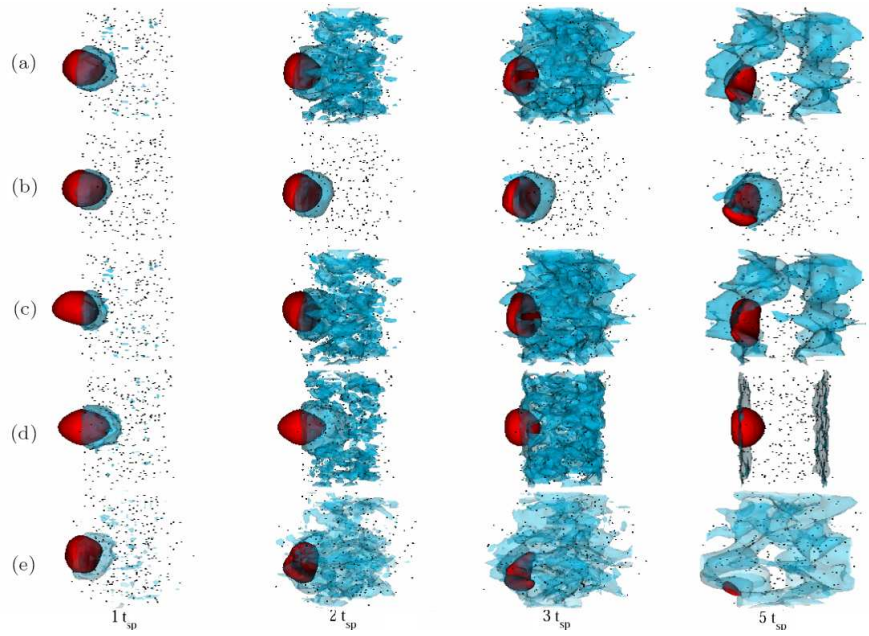

Figure 4.21: Evolution of the flame kernel in the spray with time for (a) Case A (base), (b) Case C (non-volatile), (c) Case D (air side), (d) Case G (laminar), and (e) Case H (higher turbulence). The temperature iso-surface $\hat{T} = 0.5$ is shown in red while the stoichiometric mixture fraction iso-surface $\xi = \xi_{st}$ is shown in blue. The dots represent droplet locations. Left column to right column: $t = t_{sp}$, $t = 2t_{sp}$, $t = 3t_{sp}$, and $t = 5t_{sp}$.

mixture fraction is discussed more in detail later. Note that this time, the kernel size in case D is not much smaller than in case A. This is due to the larger R_{ign} used which results in more overlap with the spray in case D.

Figure 4.21 shows some additional details of the development of the flame kernel and the mixture fraction for different levels of turbulence and volatility of the droplets. A clear difference with Fig. 4.5 is that the kernels hardly grow and are much smaller at the end of the simulation. This is attributed to the modified chemistry which prevents the rich branch from penetrating into the core of the spray. For the case where the spark is on the air side (row (c)), the $\hat{T} = 0.5$ is first offset and smaller but eventually develops similarly as in the base case. The flame distortion

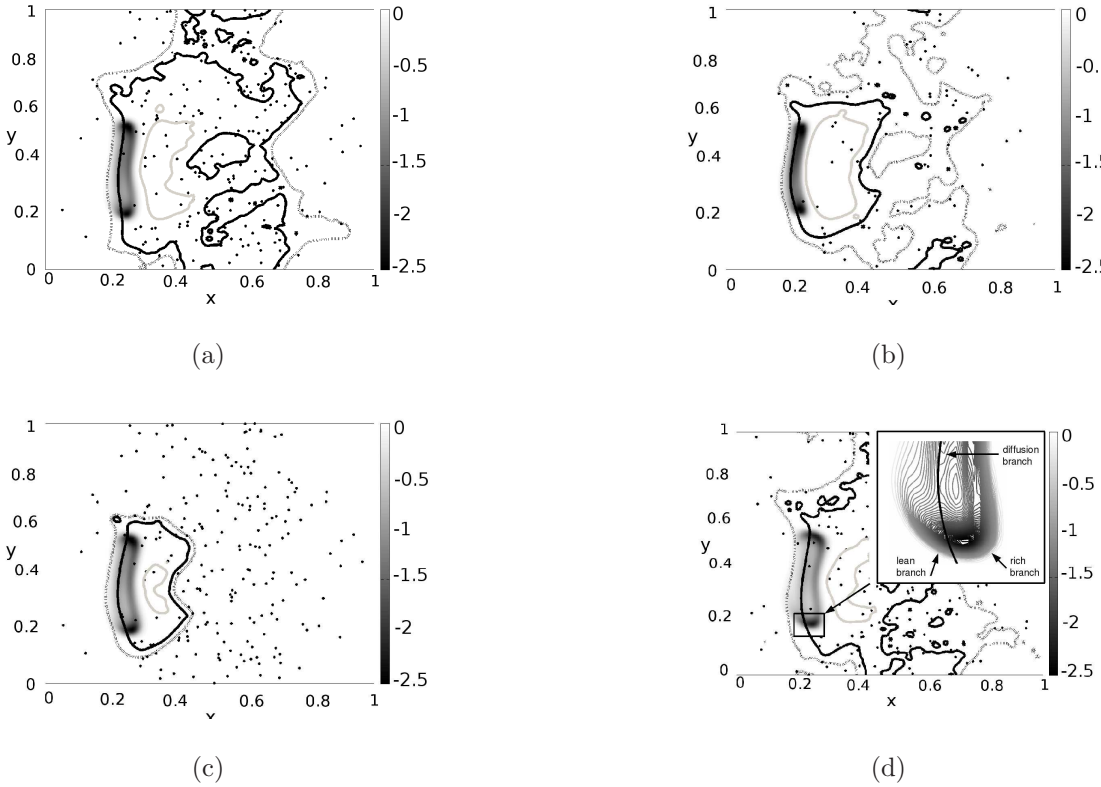

Figure 4.22: w_F field in the plane $\hat{z}$=0.5. Black dots show the droplet locations. Contours of mixture fraction: $\xi = \xi_{st}$ thick black lines; $\xi = 0.12$ thick grey lines; $\xi = 0.038$ dashed black lines. (a) Case A, (b) Case B, (c) Case C, (d) Case F, all at $t = 3t_{sp}$.

mentioned in Section 4.3.2 by the turbulence is evident (compare rows (d) (laminar) with (a) and (e)). However, with the modified 1-step chemistry, the kernel is very small at $t = 5t_{sp}$ in the turbulent case, suggesting failed ignition.

In Fig. 4.22, we present the fuel reaction rate $\hat{\omega}_F$ distribution on a $x - y$ plane through the spark at $t = 3t_{sp}$, i.e. after the spark influence has diminished. The flame has a tribrachial structure, but the rich branch is much smaller compared to what was observed in Fig. 4.6. The fact that the flame is localised on the ξ_{st} iso-surface is the main effect of the modified 1-step chemistry. It is interesting to note that the premixed branches in case A have almost merged into a very thin edge

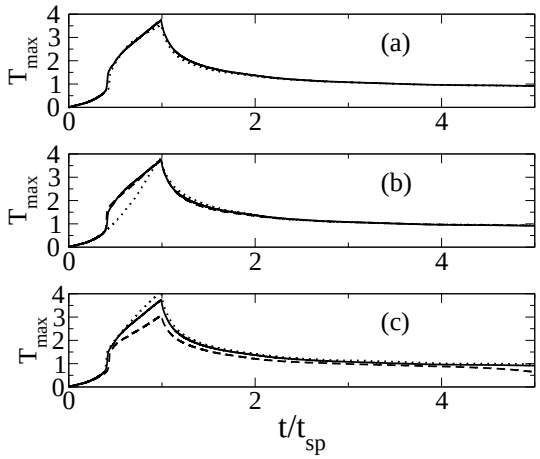

Figure 4.23: Maximum temperature in the domain against time. Case A: plain line; (a) Case B: dotted line ; Case C: dashed line; (b) Case D: dotted line; Case F: dashed line (c) Case G: dotted line; Case H: dashed line.

flame due to the thinner mixing layer. In case B, we can observe a large rich region on the right of the flame. Although the average mixing layer over the $y-z$ planes is thick, as shown in Fig. 4.3, locally, this rich region results in a thin mixing layer which prevents the edge flame to spread across the mixing layer. In case C, there is no such local rich region. The lower saturation vapour pressure in case C leads to a wider mixing layer, as shown in Fig. 4.3, that enables the flame front to expand across the mixing layer. As mentioned in Section 4.3.6, the thickness of the mixing layer has an effect on the flame curvature and the edge flame propagation.

Figure 4.23 presents the evolution of $\hat{T}_{max}$ for all simulations. The general behaviour is the same as in Fig. 4.7. Case D has a delayed ignition due to the offset of the spark but successful kernel generation still occurs. Hence, the beneficial effects of transport, mentioned in Section 4.3.2 are also observed with the modified chemistry. In addition, as with the classical chemistry, a higher temperature is obtained in the case G (laminar) and a lower one in case H (highly turbulent), attributed to turbulent dissipation. Moreover, in Fig. 4.23, the temperature in case H eventually decreases below T_{ad}, consistent with the shrinking of the kernel observed in Fig.

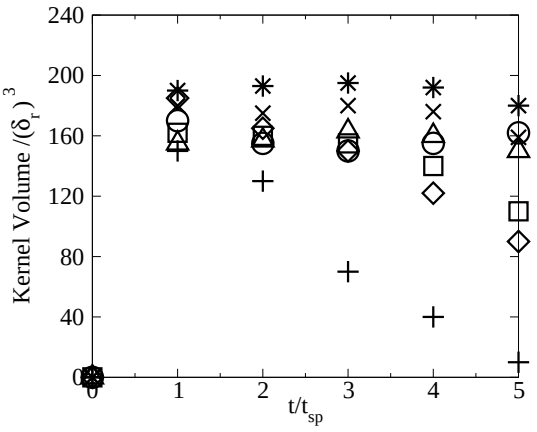

Figure 4.24: Volume of the kernel $\hat{T} \geq 0.5$ against time. Case A: $\square$; case B: $\diamondsuit$; case C: $\times$; case D: $\triangle$; case F: *; case G: $\bigcirc$; case H: +; Gaseous case: plain line.

4.21. Note that the maximum temperature $\hat{T}_{max}$ is higher, about 3.5, due to the higher spark energy used.

Figure 4.24 shows the time evolution of the volume of the flame (defined as fluid with $\hat{T} > 0.5$) normalised by δ_r^3 for all cases. It is evident that the kernel does not grow as in Fig. 4.8. Instead, the kernel volume stays of the order of the spark volume and tends to decrease at the end of the simulation, expect for case G (laminar) which increases slightly. In addition, the kernel volume in case H (highly turbulent) decreases to zero at the end of the simulation. This is a further evidence that the kernel shrinks in this case. This graph shows quantitatively the effect of using a modified 1-step chemistry. The rich premixed branch does not penetrate the spray core, resulting in a much smaller kernel. As pointed out in Section 4.3.6, the reduced size of a kernel implies a higher curvature, detrimental for the propagation. As will be seen in Section 4.4.4, curvature prevents flame propagation and leads to the shrinking of the kernel. Note that the kernel size is not smaller in case D than in case A, as was observed earlier in Fig. 4.20.

The present simulations with modified 1-step chemistry reproduce the physics found with the non-modified chemistry. The spark location has an effect on the

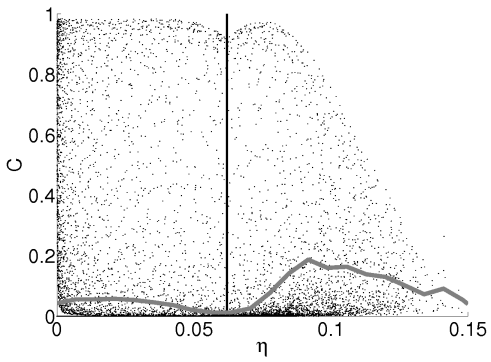

Figure 4.25: Scatter plot of c versus mixture fraction at $t = 3t_{sp}$ for case A. Data are from the entire domain, the vertical line denotes ξ_{st}. The grey line shows the conditional average of c on the mixture fraction.

kernel generation and the flame has a tribrachial structure. However, due to the small rich branch, the kernel sizes are smaller and eventually the flames shrink. A different range of u' and spark size may, however, have resulted in successful ignition with this chemical scheme.

4.4.3 Flame kernel at the end of spark with modified chemistry

Figure 4.25 shows the progress variable c against η, together with the conditional average $\langle c|\eta\rangle$ using data from all the DNS domain. The graph shows similar trends as in Fig. 4.9 on the lean side only. On the rich side, c is reduced with higher η, as a consequence of the modified chemistry.

Figure 4.26 shows the temperature conditionally-averaged on the mixture fraction, $\langle\hat{T}|\eta\rangle$, for all cases at $t = t_{sp}$. Data are limited to the flame region ($c > 0.5$). The comments given in Section 4.3.3 for Fig. 4.10 apply here. In particular, the temperature at stoichiometry is higher in case D than in case A due to the wider overlap of the kernel with the stoichiometry contour, shown earlier. Moreover, we

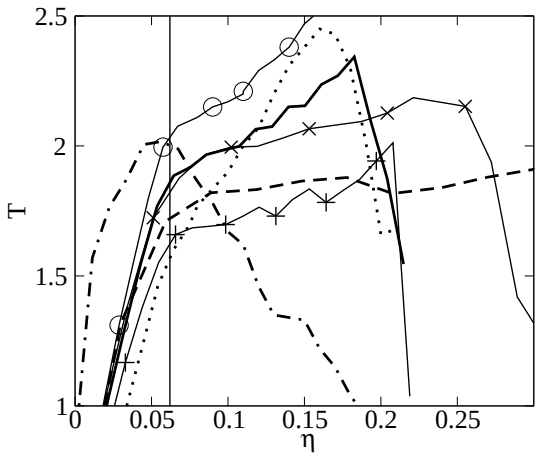

Figure 4.26: Variation of conditionally-averaged normalised temperature vs. mixture fraction using data in the range $0.5 < c < 1$ at $1t_{sp}$. The vertical line denotes ξ_{st}; Case A: plain line; Case B: dashed line; Case C: crosses; Case D: dash-dotted line; Case F: dotted line; Case G: circled line; Case H: line with +.

note again that the temperature peaks in richer region for cases B and C. We suggest the same explanation given in Section 4.3.3 based on Fig. 4.11. This figure is not presented with the modified chemistry because the results are alike. Hence, we suggest that locally, high values of mixture fraction are found due to the inhomogeneities at the droplet scale. This is consistent with the observation of a local rich zone in case B in Fig. 4.22. Finally, the comment made in Section 4.3.3 that $\langle|\omega_F||\eta\rangle$ is higher at stoichiometry in case D because of the higher $\langle T|\eta\rangle$ at stoichiometry, is still valid with the modified chemistry. The figures of reaction rates are not shown for the sake of brevity.

The edge flame propagation displacement speed is discussed in the next section.

4.4.4 Flame displacement speed with modified chemistry

In this section, we analyse the flame displacement speed of the triple point following the procedure described in Section 4.4.4. Figure 4.27 presents the probability density

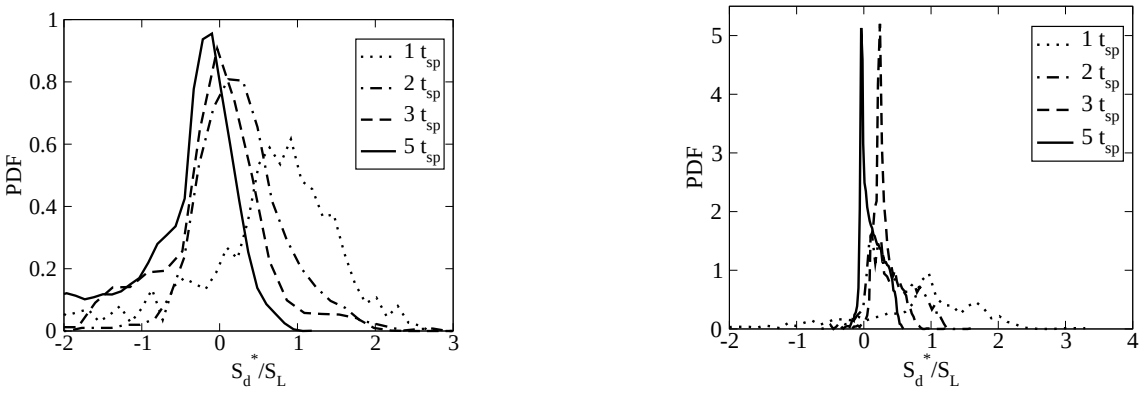

(a) (b)

Figure 4.27: Probability density function (PDF) of the density weighted displacement speed at different times. (a) Case A, (b) Case G.

function of S_d^* for different cases (laminar spray and turbulent spray). In Fig. 4.27a, the PDF evolves approximately the same way as in Fig. 4.13a. A clear difference is that the PDF does not stabilise to a shape with a peak at a positive value, but rather shifts to negative values of the displacement speed. At the end of the simulation, it peaks at about $-0.1S_{L,0}$, consistent with the reduction of the kernel volume observed in Section 4.4.2. In Fig. 4.13b, the PDF in the laminar case has a more narrow peak due to the absence of turbulence. Moreover, the PDF peaks at about 0 at the end of the simulation, with a certain spread towards positive values. As in Section 4.3.4, this is attributed to the variation of S_d^* with the progress variable and the variation of the flame curvature at the droplet scale.

In Fig. 4.28, we present the variation of the volume average $\langle S_d^* \rangle$ with time for the different cases. The values are much lower than in Fig. 4.14 and they decrease to negative values with time for all cases except the laminar case G. The highly turbulent case H has very low value of $\langle S_d^* \rangle$ due to the rapid shrinking of the kernel.

As with the classical chemistry, it will be shown in next section that the curvature is the major factor that controls the triple point flame speed. A negative correlation of the flame speed with curvature was shown in Section 4.3.5. Results

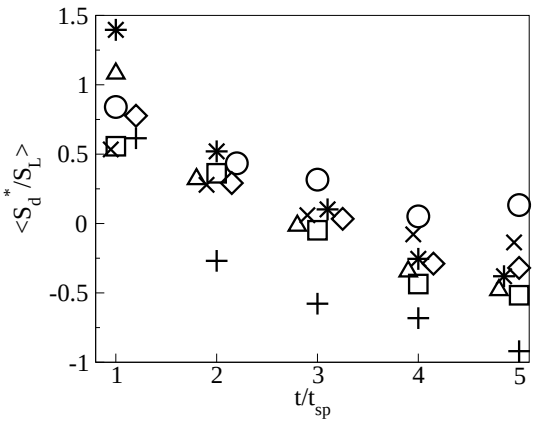

Figure 4.28: Volume average of the density weighted displacement speed at the triple point normalised by the stoichiometric laminar flame speed at 1, 2, 3, 4 and 5 t_{sp}. Symbols are not always centred on their time value to make the graph more clear. Case A: □; case B: ♢; case C: ×; case D: △; case F: *; case G: ◯; case H: +.

with the modified 1-step chemistry lead to the same conclusion and the analysis is not repeated. Figure 4.29 shows an iso-surface of oxygen ($Y_{O_2} = 0.12$) coloured according to curvature. The values of curvature are higher than in Fig. 4.15. As explained before, this is an effect of the modified 1-step chemistry. In addition, we can see the distortion of the flame with higher turbulence intensity which can result in very high values of curvature.

The use of a modified 1-step chemistry induces negative values of displacement speed. They indicate that the kernels are shrinking and do not provide any information on the displacement speed of a growing edge flame in a spray mixing layer. The absence of the rich branch is responsible for the low displacement speed because of the increased curvature. In the next section, we analyse the displacement speed components and the factors which impact on their values.

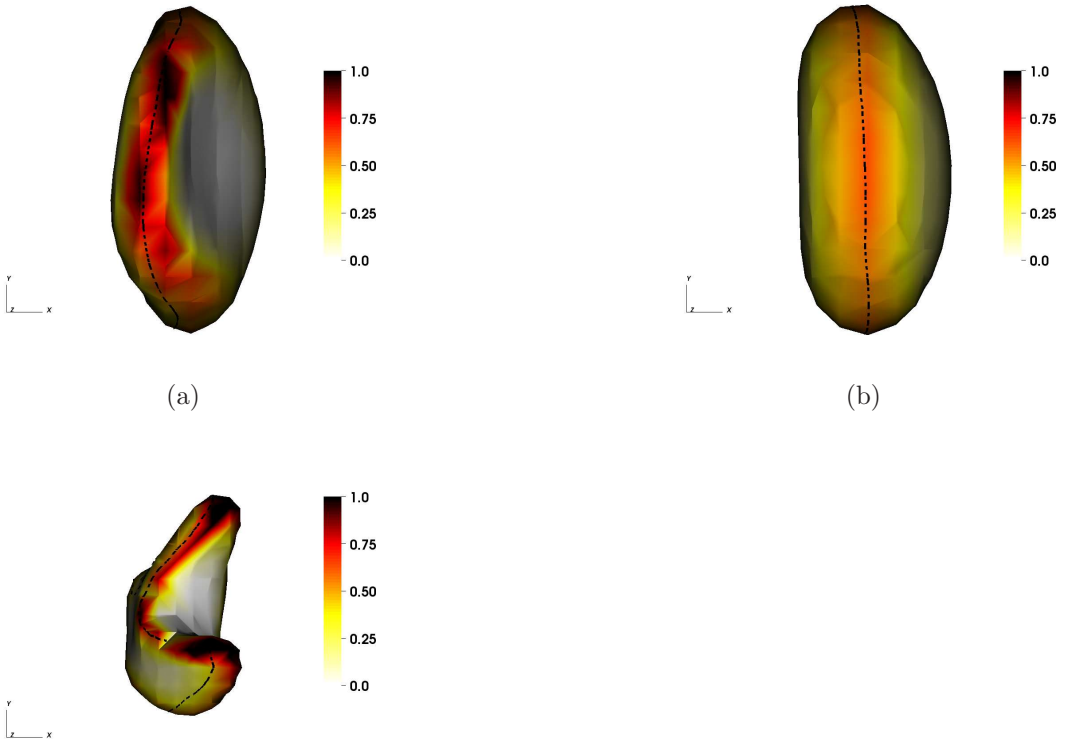

Figure 4.29: Iso-surface Y_{O_2}=0.12 coloured by curvature k_m at $t = 3t_{sp}$. The dotted line shows the ξ_{st} isoline. (a) Case A; (b) case G; (c) case H.

4.4.5 Influence of parameters on displacement speed components with modified chemistry

Figure 4.30 presents the evolution of each component conditioned on c in the triple point region ($\xi = \xi_{st} \pm 0.1\xi_{st}$) at $t = 3t_{sp}$. We demonstrate here that the major conclusions follow that of Section 4.3.6. Firstly, it can be seen that S_m^* is null for $c > 0.1$. Secondly, all cases have approximately the same S_n^* over the range of progress variable except case H, with high turbulence intensity. In fact, the case with higher turbulence intensity and the laminar case have respectively a lower and a higher normal diffusion component S_n^*. The reason is simply that turbulence tends to homogenise the scalars at the flame front. As a result the profile of Y_{O_2} has less

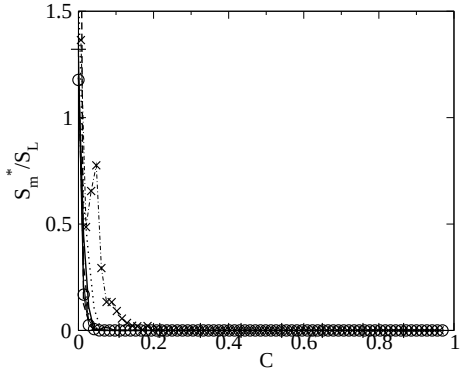

(a)

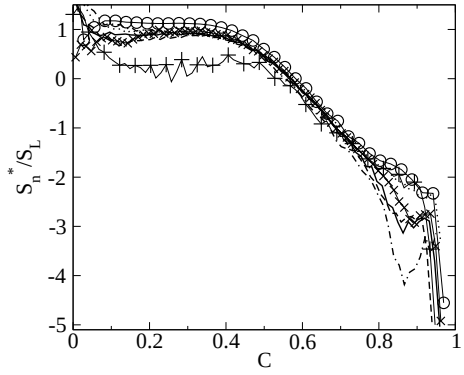

(b)

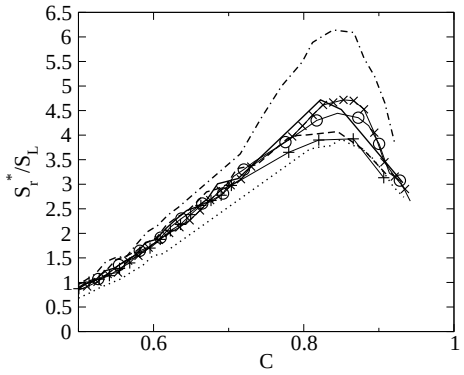

(c)

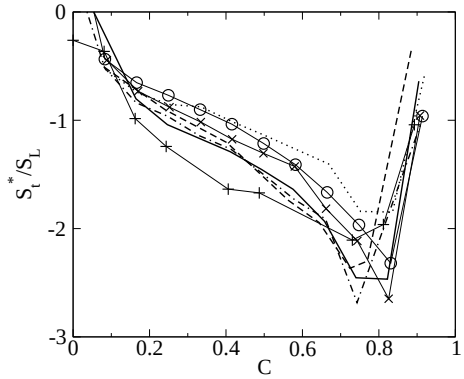

(d)

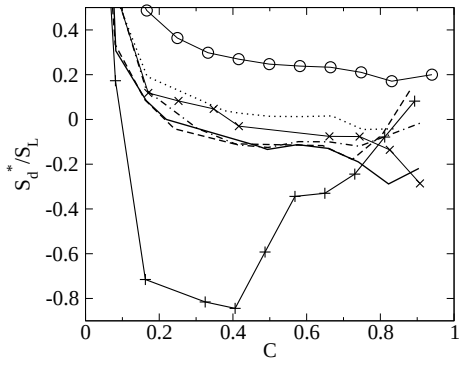

(e)

Figure 4.30: Data as in Fig. 4.16 but for all cases studied. (a) $\langle S_m^* \rangle$. (b) $\langle S_n^* \rangle$. (c) $\langle S_r^* \rangle$. (d) $\langle S_t^* \rangle$. (e) $\langle S_d^* \rangle$. Case A: plain line; Case B: dashed line; Case C: crosses; Case D: dash-dotted line; Case F: dotted line; Case G: circled line; Case H: line with +.

steep gradients along the flame with high turbulence and steeper gradient in the laminar case. This induces respectively lower and higher normal diffusion.

In Fig. 4.30c, the results follow the arguments put forward in Section 4.3.6. The location of the spark relative to the stoichiometric contour has an effect on the temperature there and in turn on S_r^*. However, this is a short term effect only since the temperature relaxes to the adiabatic flame temperature.

We now discuss the tangential component S_t^* from Fig. 4.30d. First, we can note the higher magnitude of S_t^* compared to cases computed with classical 1-step chemistry, see Fig. 4.19. This implies that the curvature is much higher when using modified chemistry. This is consistent with the observation made in Section 4.4.2 that the modified chemistry prevents the growth of the rich branch and results in a small kernel size. The component S_t^* has a higher magnitude in case A than in case C and F. As in Section 4.3.6, this is attributed to the initially wider mixing layer in case F and to the thicker mixing layer in case C. Note that the magnitude of S_t^* is not lower in case B, as in Section 4.3.6, because of the locally thin mixing layer near the edge flame, as mentioned in Section 4.4.2. Moreover, the curvature in case D is not higher to that of case A. This is contrary to the results presented in Section 4.3.6. This is because the size of the kernel in case D is not smaller than that of case A ,as mentioned in Section 4.4.2. Finally, case G (laminar) and case H (turbulent) have respectively a lower and a higher magnitude of S_t^*, in agreement with the results presented in Section 4.3.6. Hence, the same conclusions are suggested.

It can be concluded from this section that the trends followed by the displacement speed components are similar, whether a classical or a modified 1-step chemistry was used. Only results computed with the classical 1-step chemistry could provide quantitative values of the displacement speed of a growing edge flame kernel. As observed in Section 4.3.4, those results are valuable since they agree with experimental data.

It is also important not to overplay the accuracy of the modified 1-step for this problem, even if it reproduces the correct $S_L vs \phi$ curve. In particular, the modified scheme artificially enforces the reaction rate to be null if $\phi > 2.15$. However, in

the presence of diffusion from neighbouring fluid that is burning, or from the spark, chemical reactions can proceed even at rich mixture fractions where nominally a laminar premixed flame cannot propagate in a self-sustained way, which was the condition that motivated the construction of this scheme. In order to properly account for chemical reactions in all mixture fractions, in the presence of deposition of energy, we need skeletal chemical schemes and such simulations are shown in Chapter 5.

4.5 Summary of main findings

The growth of an edge flame following spark ignition in a turbulent droplet-laden mixing layer has been examined with DNS with classical and modified single-step chemistry. The modified scheme captured the correct $S_L vs \phi$ distribution by artificially quenching reactions at $\phi > 2.15$ and by adjusting the heat release as a function of the local ϕ. A parametric study was performed and involved the initial size of the droplets, their volatility, the location of the spark, the initial intensity of turbulence and the initial droplet-air mixing layer thickness. The use of classical chemistry resulted in growing kernels at the end of the simulation, while the use of modified chemistry resulted in extinguishing kernels. This was attributed to the reduced kernel size obtained with the latter model. However, the trends obtained with the modified chemistry were similar to that obtained with the classical chemistry, summarised below.

Successful and rapid development of the flame happened when gaseous fuel was readily available in the flame kernel. This was the case when the spark overlapped with the droplet-laden region of the layer. When the spark was far away, diffusion of heat from the kernel could still result in flame establishment provided that droplets evaporated fast enough. The flame had a tribrachial structure and propagated in a wide range of mixture fraction. The density-weighted displacement speed S_d^* at the triple point, defined relative to the O_2 mass fraction, had PDF shapes very close to

those from previous experimental and DNS results from gaseous-fuel spark ignition, and, for successful ignitions and at long times from the spark when its effects have been dissipated, the mean value was in the range $0.55-0.75S_{L,0}$, close to the gaseous value.

The components of S_d^* showed similar features as those observed in previous DNS studies of turbulent edge flames in gaseous fuel mixing layers. S_d^* exhibited a dominant negative correlation with the curvature. The reaction component S_r^* and the tangential diffusion component S_t^* of the displacement speed depended significantly on the parameters of the problem while the others did not. S_t^* was negative due to the mean positive curvature of the kernel. This negative effect was increased for kernels of small size because of the higher curvature. This kernel size was substantially reduced by sparking on the air side, due to the much slower development of the kernel. The tangential component magnitude was reduced with a larger mixing layer thickness. A wide initial distribution of droplets resulted in a thicker mixing layer than in the base case. This was beneficial on the short term only because turbulence increased the mixing layer width and wiped out the initial difference. Slower evaporation, due to larger diameter or non-volatile droplets, led to wider mixing layer which could reduce the curvature magnitude. The influence of turbulence on the curvature was twofold. Although a higher turbulence level widened the mixing layer, the curvature of the kernel could also reach higher values due to the distortion of the kernel.

Turbulent edge flames in sprays following ignition may occur in realistic configurations, e.g. gas turbine combustors. The present results suggest that, since the mean local edge flame displacement speed is a fraction of the laminar burning velocity, flame expansion in a combustor from the ignitor is mostly due to favourable convection and turbulent diffusion.

The data from these simulations can be used for validating theories of turbulent spray combustion, such as CMC (Conditional Moment Closure), PDF and flamelet methods.

Chapter 5

DNS of spark ignition in turbulent sprays with complex chemistry

5.1 Introduction

In Section 2.2.1, it was pointed out that little is known about the structure of a growing spark kernel in a spray. Physical aspects of the kernel can be examined by considering the Group Combustion Theory or the problem of a flame propagating in a uniform spray. However, only accurate experimental measurements or numerical simulations of the real problem can reveal its complete physics. In this chapter, we investigate the kernel growth in a turbulent premixed spray using three-dimensional DNS with complex chemistry. The results are compared with the concepts suggested by the Group Combustion Theory and the flame propagation in a uniform spray (results from Chapter 3).

Recent spark ignition DNS was limited to simple chemistry and fine droplets where strong inhomogeneities could not appear [42]. Furthermore, the role of complex chemistry in spray ignition and spray flame propagation has received little attention although its effect on laminar flame speed has been demonstrated in Chapter 3. Two-dimensional simulations with reduced chemical schemes have shown

the role of complex chemistry with low hydrocarbons on premixed [138, 140] and non-premixed gaseous spark ignition [78, 98]. Wang and Rutland [141] performed two-dimensional DNS of n-heptane spray autoignition and incorporated a skeletal chemical scheme. Nevertheless, 3D complex chemistry DNS of spark ignition in sprays have not been performed.

In this chapter, DNS of spark ignition in a turbulent, uniformly dispersed cloud of mono-sized droplets with high volatility and moderate size is performed with the DNS code SENGA2. The investigation involved the implementation of the liquid phase and complex chemistry, detailed in Appendix B and C respectively. The effects of the overall equivalence ratio, the droplet size and the spark size on the kernel are studied. In the next Section, the numerical methods are introduced. Then, the results and their discussion are presented. We close the chapter with a summary of the main conclusions.

5.2 Mathematical modelling

5.2.1 Liquid phase

A Lagrangian point-source formulation has been adopted for the liquid phase. Temperature is assumed uniform inside the droplets and droplet-droplet interactions are neglected. A thin film (subscript f) assumption is used to calculate the droplet evaporation and heat exchange with the surroundings [116]. For each droplet d, equations for its position $\mathbf{x}_d$, velocity $\mathbf{v}_d$, diameter a_d and temperature T_d are identical to those of Section 3.2.2. The formulation of the spray equations together with the implementation of the liquid phase in the code is detailed in Appendix B. The fuel considered is n-heptane ($P_{ref} = 1$bar, $T_{ref} = 371.58$ K and $L_v = 31.80$ kJ/mol).

5.2.2 Gas phase

For the gas phase, dimensional transport equations are solved for mass, momentum, total energy and $N-1$ species (N being the number of species appearing in the chemical mechanism used). Temperature-dependent transport coefficient are evaluated through 5-th order polynomials and the molecular viscosity through the expression $\mu = 2.58 \times 10^{-5}(T/298)^{0.7}\mathrm{Pr}$ kg m^{-1} s^{-1}, with Pr $= 0.7$. Diffusion coefficients, $D_\alpha = (\mu \mathrm{Pr})/(\rho \mathrm{Le}_\alpha)$, are found assuming constant Lewis number Le_α for each species α. The values of Le_α for the following species were taken from [142]: 1.11 (O_2), 0.18 (H), 0.73 (OH), 0.30 (H_2), 0.83 (H_2O), 1.10 (HO_2),1.12 (H_2O_2), 1.10 (CO), 1.39 (CO_2), 1.28 (CH_2O), 0.97 (CH_4), 1.00 (N_2). The diffusivity coefficients for the following species were calculated using the Fuller-Schettler and Giddings equation [143]: 2.89 (C_7H_{16}), 1.41 (C_2H_2), 1.00 (CH_3), 1.49 (C_2H_4), 1.80 (C_3H_4), 1.87 (C_3H_6), 2.19 (C_4H_8), 2.72 (C_6H_{12}), 3.09 ($OC_7H_{13}OOH$), 3.08 ($C_7H_{15}O2$). The liquid source terms are given by

$$\Gamma_m = -\frac{1}{V}\sum_d \alpha_d \frac{dm_d}{dt} \tag{5.1}$$

$$\Gamma_{U_i} = -\frac{1}{V}\sum_d \alpha_d \frac{dm_d \mathrm{v}_{d,i}}{dt} \tag{5.2}$$

$$\Gamma_E = -\frac{1}{V}\sum_d \alpha_d \left(C_P^L m_d \frac{T(\mathbf{x}_d,t) - T_d}{\tau_d^T} + \frac{dm_d}{dt} h_F(T_d) + \frac{1}{2}\frac{dm_d \mathrm{v}_{d,i}^2}{dt} \right) \tag{5.3}$$

where $m_d = \rho_L(\pi a_d^3)/6$ is the mass of droplet d, $h_F(T_d)$ is the fuel vapour enthalpy at the droplet surface and V is the volume of the Cartesian grid cell centred on the DNS node. A weighted summation is done over all the droplets. The weighting factor α_d is the portion of the volume centred on the gas node that intersects a similar volume V centred on the droplet with subscript d. Gaseous properties are similarly interpolated at a droplet location by doing a weighted summation over all cells having non-zero α_d (8 cells maximum). Note that the three terms of Eq. 5.3 are similar to those of Eq. 3.8. The expression for the timescale τ_d^T is given in Appendix B.

The spherical spark was modeled as a source term of duration t_{sp} in the transport energy equation, set to reach two adiabatic flame temperature T_{ad}, with a Gaussian radial profile centred in the domain as described in [85].

5.2.3 Numerical procedure and problem parameters

Table 5.1: Turbulence and spark characteristics for the investigated cases. Turbulent velocity rms u', initial integral length scale L_{11}, $t_{turb} = L_{11}/u'$, Kolmogorov length scale η_k, $Re_t = u'L_{11}/\nu$, mean droplet spacing $s_d = n^{-1/3}$, initial droplet diameter a_d, overall equivalence ratio ϕ_0, Group combustion number G [39], spark diameter d_{sp}, spark energy E_{sp}, and quenching diameter d_q and minimum ignition energy E_{min} of the equivalent laminar mixture [69]. For all, $t_{sp} = 0.6\delta_r/S_{L,0}$, $L_{11} = L/6$, $L = 3$ mm, $S_{L,0} = 0.7$ m/s, $\delta_r = 32$ μm.

Case	$\frac{u'}{S_{L,0}}$	Re_t	η_k (mm)	$\frac{\eta_k}{\Delta X}$	$\frac{t_{sp}}{t_{turb}}$	d_{sp} (mm)	d_q (mm)	$\frac{d_{sp}}{d_q}$	$\frac{d_{sp}}{L_{11}}$
A	4	85	0.023	1	0.15	0.736	0.470	1.57	1.5
B	4	85	0.023	1	0.15	0.448	0.470	0.95	0.9
C	4	85	0.023	1	0.15	0.736	0.343	2.15	1.5
D	4	85	0.023	1	0.15	0.736	0.405	1.82	1.5
Gas	4	85	0.023	1	0.15	0.490	0.312	1.57	1.0

Case	E_{sp} (mJ)	$\frac{E_{sp}}{E_{min}}$	s_d (mm)	$\frac{s_d}{\eta_k}$	$\frac{s_d}{d_{sp}}$	a_d (mm)	ϕ_0	G
A	0.926	7.7	0.332	14.0	0.45	0.02	1	0.85
B	0.209	1.7	0.332	14.0	0.74	0.02	1	0.31
C	0.926	19.9	0.167	1.8	0.06	0.02	8	6.60
D	0.926	12.1	0.332	14.0	0.45	0.04	8	1.91
Gas	0.289	7.7	-	-	-	-	1	-

The three-dimensional compressible DNS code SENGA2 [129, 138] including com-

plex chemistry has been used. The first and the second derivatives of the gas phase equations are evaluated with a 10th-order central difference scheme. The order of differentiation gradually decreases to fourth order one-sided finite difference near the non-periodic boundaries. The boundaries in the x-direction are partially non-reflecting and are treated with the Navier Stokes Characteristic Boundary Conditions (NSCBC). The transverse directions are periodic.

Operator splitting between transport (the advection and diffusion treated together) and chemistry is used. DNS with operator splitting was studied in detailed in Ref. [144, 145]. A fourth-order, low storage, explicit Runge-Kutta scheme [146], with a time-step of $\Delta t = 5 \times 10^{-9}$ s, was used to advance gaseous spatial transport equations (i.e. without chemical source term ω_i). The time step used was chosen to be ten times smaller than the smallest time scale, that is the acoustic timescale in a grid cell $\Delta x/\sqrt{\gamma(R/W_{air})T}$. In addition, a criterion for reaction-diffusion problems was suggested by [145] in order to keep the splitting error small. The ratio of $\sqrt{\Delta t}$ to the thermal thickness of a stoichiometric flame (given later) should be much smaller than 1. The value for the present simulation was 0.2. The implicit solver VODPK [147] was then used for gas phase chemical reactions for every grid node. The droplet equations were advanced at the beginning of each time step with the same explicit fourth-order Runge-Kutta scheme.

A skeletal mechanism for n-heptane with 22 non-steady species undergoing 112 reactions, validated mostly for auto-ignition problems in non-premixed strained flows, has been used [148]. One-dimensional unstrained laminar premixed flames were calculated at ambient pressure and temperature and the laminar stoichiometric flame speed of heptane with this mechanism was found to be $S_{L,0} = 0.7$ m/s and the reaction zone thickness $\delta_r = D_{th,0}/S_{L,0}$ was about 32 μm. In addition, the thermal thickness (temperature rise across the flame divided by peak temperature gradient in the flame [6]) of a stoichiometric one-dimensional flame was found to be 0.33 mm. This $S_{L,0}$ is higher than experiment, but this influences little the value of the present results that aim to explore the flame structure and its modification due

to the droplet phase and the turbulence. Profiles of flame speed normalised by $S_{L,0}$ *vs.* equivalence ratio (see Appendix C) were consistent with other numerical and experimental results [118], indicating that the mechanism performs well in all flammable mixture fractions. The flammability limits are found to be $\xi_L = 0.035$ and $\xi_R = 0.116$. More details on the validation of the chemistry implementation in the present code is given in Appendix C.

The cubic domain with length $L = 3$ mm was discretised by a 128^3 grid, resulting in a grid resolution $\Delta x = 23.6$ μm corresponding to 14 points in a 1D thermal flame thickness. The initial turbulent field was generated according to a Batchelor-Townsend energy spectrum [149]. The initial temperature and pressure are $T_0 = 300$ K and $P_0 = 1$ bar. The fuel was initially contained in a homogeneous slab of monodisperse droplets (same initial diameter) which spanned from $x = 0.2L$ to $x = 0.8L$ so as to leave the x boundaries free of inhomogeneities. The configuration resembled that shown in Fig. 4.1, but with a spark at the centre of the domain. Initial droplets velocity and temperature were set equal to that of the surrounding gas. The initial diameter was set to $a_{d,0} = 20$ μm ($0.6\delta_r$). Details of the various simulations (cases A-D and gaseous fuel only) are found in Table 5.1.

The spark size of case A is chosen greater than the quenching distance derived by Ballal and Lefebvre [69] in order to ensure successful ignition, while in case B it is smaller. Note that the spark diameter and energy are the same in cases A, C and D. In Table 5.1, a group combustion number G [39] is calculated through

$$G = 3(1 + 0.276\mathrm{Re_d}^{1/2}\mathrm{Sc}^{1/3})\mathrm{LeN}^{2/3}(\mathrm{a_d}/\mathrm{s_d}) \tag{5.4}$$

For G to be representative of the early kernel, we used the number of droplets in the spark volume with size d_{sp}. The Lewis number is taken as 1 while the droplet Reynolds number is calculated using the turbulent intensity u' as velocity.

In the data processing, a mixture fraction ξ based on elemental mass fractions

[150] has been used. For a fuel C_mH_n, the mixture fraction is given by

$$\xi = \frac{\beta - \beta_O}{\beta_F - \beta_O} \tag{5.5}$$

$$\beta = \sum_{i=1}^{N_S} (\gamma_C W_C \alpha_{C,i} + \gamma_H W_H \alpha_{H,i} + \gamma_O W_O \alpha_{O,i}) \frac{Y_i}{W_i} \tag{5.6}$$

$$\gamma_C = \frac{1}{mW_C} \tag{5.7}$$

$$\gamma_H = \frac{1}{nW_H} \tag{5.8}$$

$$\gamma_O = -\frac{1}{(m + n/4)W_O} \tag{5.9}$$

where N_S is the number of species, $\alpha_{l,i}$ is the number of elements l in species i and W_l is the molecular mass of element l. In strict absence of differential diffusion, β is a conserved scalar [150]. The values of the coefficient γ_C, γ_H and γ_O are chosen so that at stoichiometry, $\beta_{st} = 0$. β_O and β_F denote values in the oxidiser stream (pure air) and the fuel stream (pure fuel). With n-heptane, it results that $\xi_{st} = 0.062$.

5.3 Results

5.3.1 Visualisation of flame front

Figures 5.1 to 5.5 show various contours that demonstrate the evolution of the flame kernel. An iso-surface of an intermediate temperature (1400 K) is shown in grey. The small black surfaces denote the stoichiometric mixture fraction. As this is generated around the droplets, these regions also demonstrate approximately the location of the droplets. The coloured surfaces denote heat release rate.

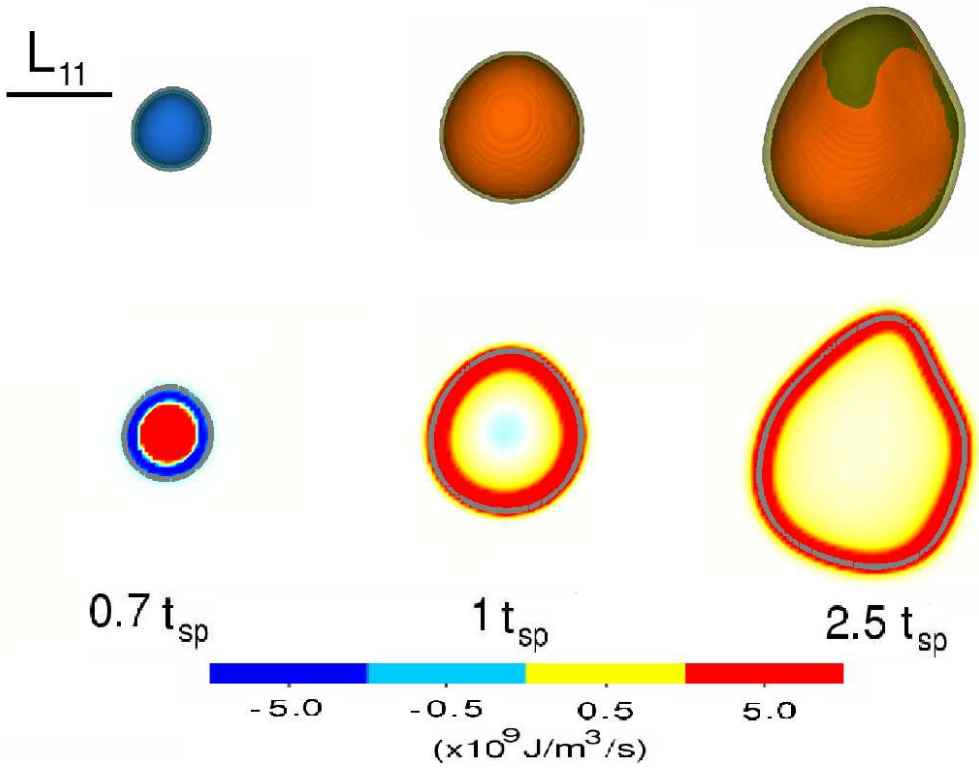

Figure 5.1: Coloured iso-surfaces of heat release rate in 3D (upper) and contours in a 2D slice passing through the spark centre (lower). The temperature iso-surface $T = 1400$K is in grey while the stoichiometric mixture fraction iso-surface $\xi = \xi_{st}$ is shown in black. The initial integral length scale L_{11} is shown for reference. Gas case.

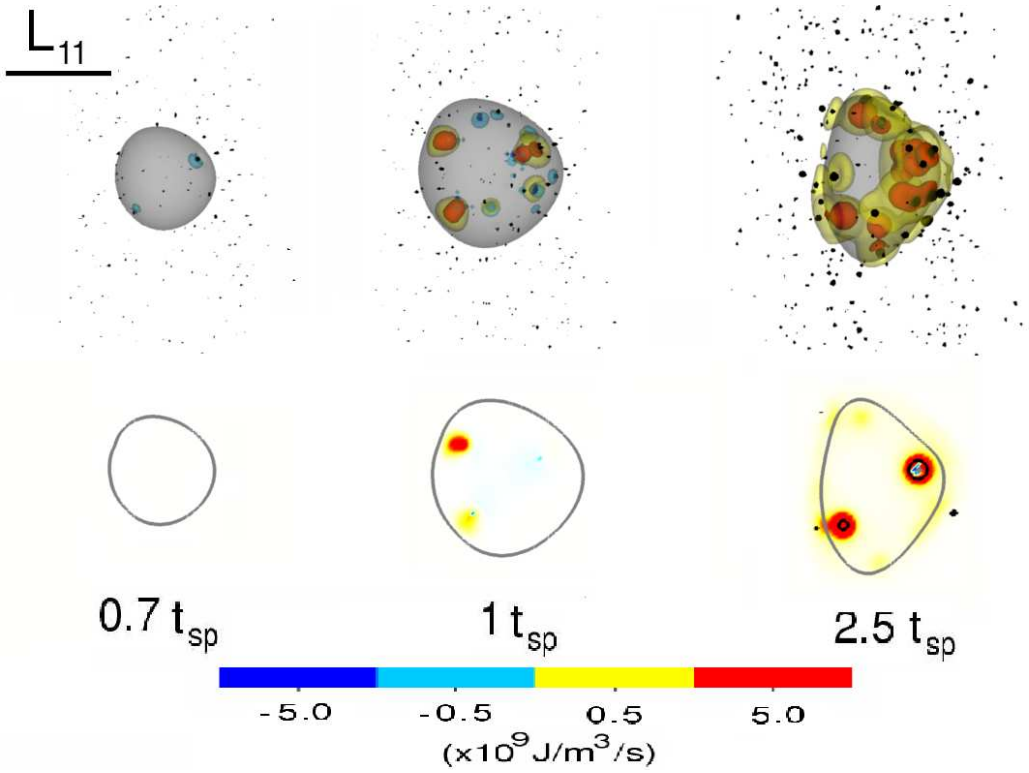

(a)

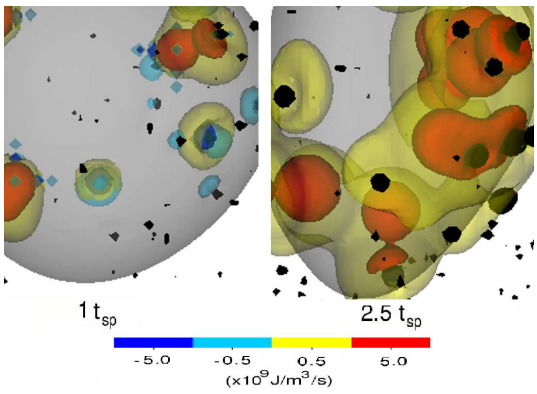

(b)

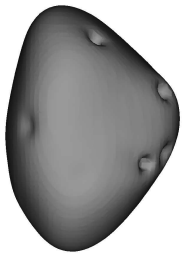

(c)

Figure 5.2: (a) Coloured iso-surfaces of heat release rate in 3D (upper) and contours in a 2D slice passing through the spark centre (lower). The temperature iso-surface $T = 1400$K is in grey while the stoichiometric mixture fraction iso-surface $\xi = \xi_{st}$ is shown in black. (b) Magnified view of iso-surfaces of heat release rate. (c) Temperature iso-surface $T = 1400$K at $t = 2.5t_{sp}$. The initial integral length scale L_{11} is shown for reference. Case A.

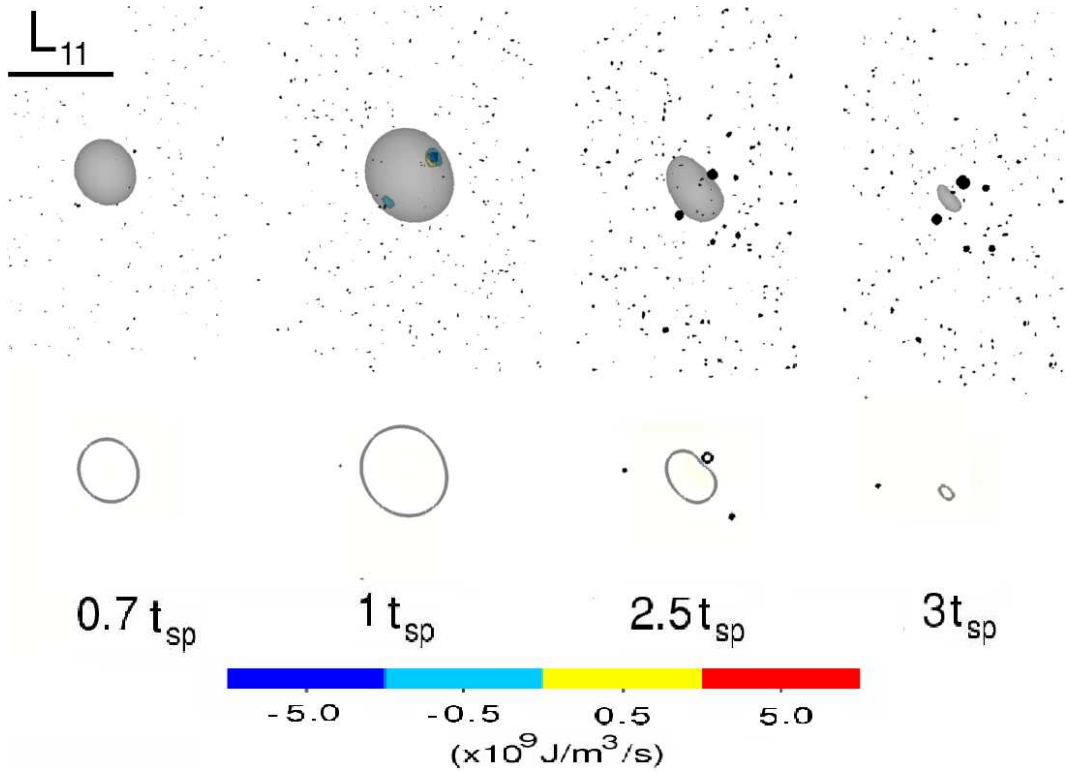

Figure 5.3: Coloured iso-surfaces of heat release rate in 3D (upper) and contours in a 2D slice passing through the spark centre (lower). The temperature iso-surface $T = 1400$K is in grey while the stoichiometric mixture fraction iso-surface $\xi = \xi_{st}$ is shown in black. The initial integral length scale L_{11} is shown for reference. Case B.

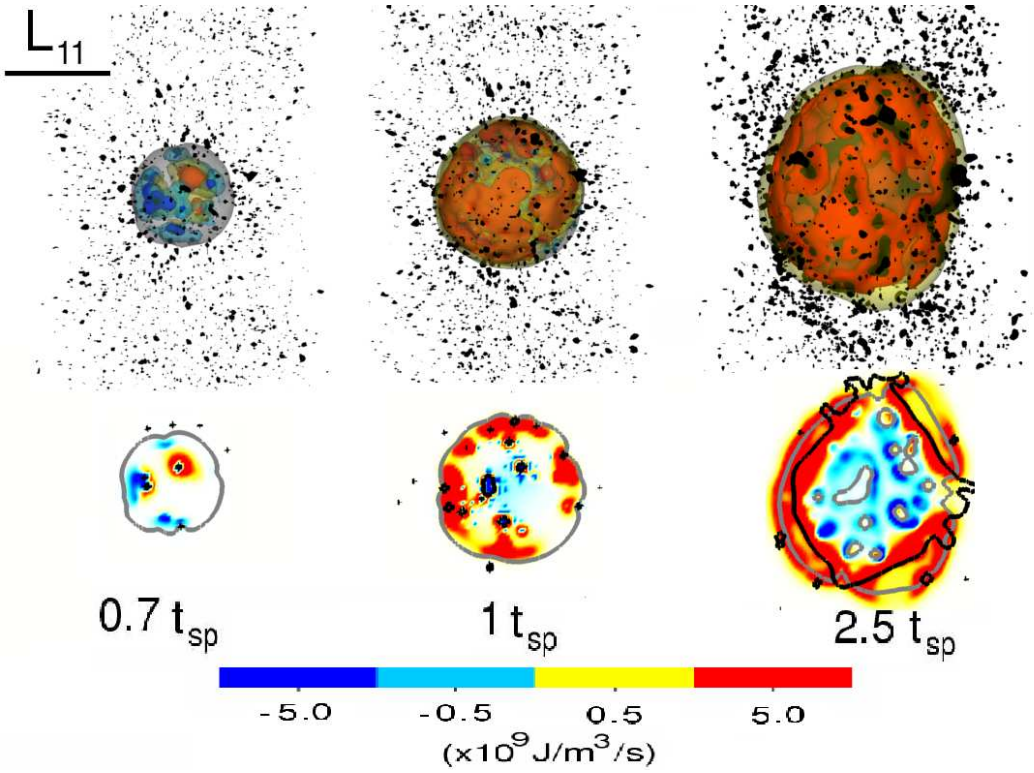

(a)

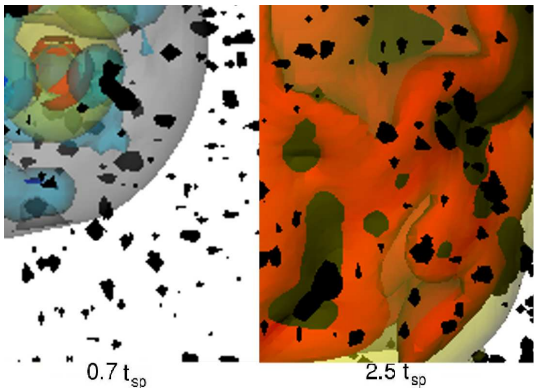

(b)

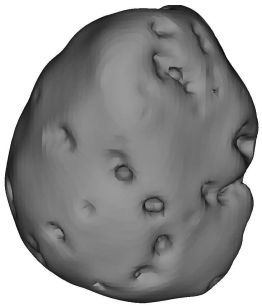

(c)

Figure 5.4: (a) Coloured iso-surfaces of heat release rate in 3D (upper) and contours in a 2D slice passing through the spark centre (lower). The temperature iso-surface $T = 1400$K is in grey while the stoichiometric mixture fraction iso-surface $\xi = \xi_{st}$ is shown in black. (b) Magnified view of iso-surfaces of heat release rate. (c) Temperature iso-surface $T = 1400$K at $t = 2.5t_{sp}$. The initial integral length scale L_{11} is shown for reference. Case C.

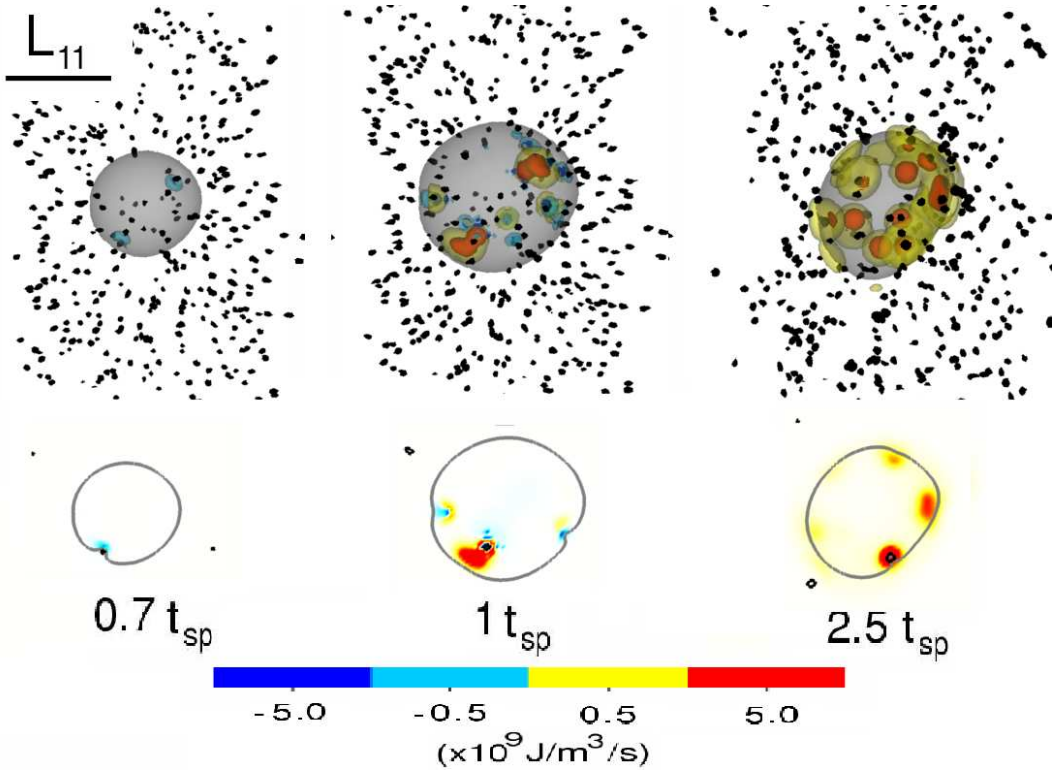

Figure 5.5: Coloured iso-surfaces of heat release rate in 3D (upper) and contours in a 2D slice passing through the spark centre (lower). The temperature iso-surface $T = 1400$K is in grey while the stoichiometric mixture fraction iso-surface $\xi = \xi_{st}$ is shown in black. The initial integral length scale L_{11} is shown for reference. Case D.

First, Fig. 5.1 shows the evolution of spark ignition with pure gas. At $t = 0.7t_{sp}$, a small volume with exothermic reactions is surrounded by endothermic reactions. It has been shown that, when igniting a premixed gas, heat release is first endothermic, then exothermic [151]. The centre of the kernel warms up faster and becomes exothermic earlier than the edge of the kernel, as observed at $t = 0.7t_{sp}$. Endothermic reactions are due to the initial break up of fuel in absence of radicals. Once enough radicals are produced, exothermic reactions become dominant [151]. At $t = t_{sp}$, heat release is predominantly exothermic. Note however, some weak endothermic reactions now occurring at the spark centre. We comment on this later. At $t = 2.5t_{sp}$, only exothermic reactions can be observed. The flame grows mildly disturbed by the turbulence. This is because the kernel size remains smaller or equal to the turbulence lengthscale throughout the simulation [17].

Figure 5.2a shows the flame evolution in case A. We first notice that heat release, whether positive or negative, is always located near droplets engulfed by the kernel. Ignition occurs at the droplet scale. During the early development of the kernel ($t = t_{sp}$), isolated flames around droplets are evident in the magnified view in Fig. 5.2b. At this time, it seems that not all droplets have ignited to the same degree. Droplets near the spark are surrounded by highly exothermic reactions. Away from the spark centre, there are still endothermic reactions around droplets. At $t = 2.5t_{sp}$, exothermic reactions dominate. Contours of high heat release rate ($5 \times 10^9 J/s/m^3$) are localised near individual or groups of droplets while those of low heat release rate ($5 \times 10^8 J/s/m^3$) are larger. They have merged to form a continuous, but very convoluted surface. In addition, we can note that the temperature iso-surface is much larger than the surface of low heat release rate. The temperature iso-surface (Fig. 5.2c) is not spherical, but distorted. This is attributed to different reasons. First, the turbulence tends to wrinkle the flame surface. However, this effect is limited given the small size of the kernel. Second, the heat release rate is non uniformly distributed. Third, in Fig. 5.2c, we observe local dents on the temperature iso-surface. They are caused by evaporative cooling at the droplet

scale and the suppression of combustion close to the droplets where the mixture is very rich, also observed in the 2D DNS of Ref. [152]. The suppression of combustion near droplets is shown in more detail in Section 5.3.7. This causes an extra wrinkling mechanism for the temperature, which results in additional spatial variations of the heat release rate. Therefore, in contrast to spark ignition of homogeneous gaseous mixtures, ignition of sprays in case A creates (at least in the beginning) a very fragmented flame surface.

Figure 5.3 shows that in case B (small spark), fewer droplets are ignited. The number of droplets in the high temperature region is small because of the smaller spark. At the end of the simulation, the kernel has shrunk and little heat release is produced. This implies a failed ignition event.

Figure 5.4 shows the time evolution of the flame in case C ($a_d = 20\mu m$, $\phi_0 = 8$). The heat release occurs earlier than in case A and at the end of the simulation, the flame is larger. At $t = 0.7t_{sp}$, exothermic reactions at the spark centre are surrounded by localised endothermic reactions. At $t = t_{sp}$, a large part of the kernel is reacting with predominant exothermic heat release. Note endothermic reactions now occurring at the centre. At $t = 2.5t_{sp}$, strong exothermic reactions occur near the iso-temperature of 1400K while endothermic reactions occur in the burned mixture, near the centre of the kernel. The contours of heat release rate are much more uniform than in case A. They resemble that of the Gas case but they are more wrinkled. In addition, the stoichiometric contour is large and forms a continuous surface inside the flame. Moreover, Fig. 5.2c shows clearly that the temperature iso-surface is distorted. As in case A, this is due to the non-uniform heat release rate, the local droplet cooling and to a lesser extent to the effect of turbulence.

Figure 5.5 shows that the kernel growth in case D ($a_d = 40\mu m$, $\phi_0 = 8$) is very similar to that of case A ($a_d = 20\mu m$, $\phi_0 = 1$). Ignition occurs at the droplet scale with local exothermic reactions surrounding droplets or group of droplets. It is interesting to note that cases D and C have the same mass of fuel. However, a doubling of the droplet diameter in case D compared to case C results in a very

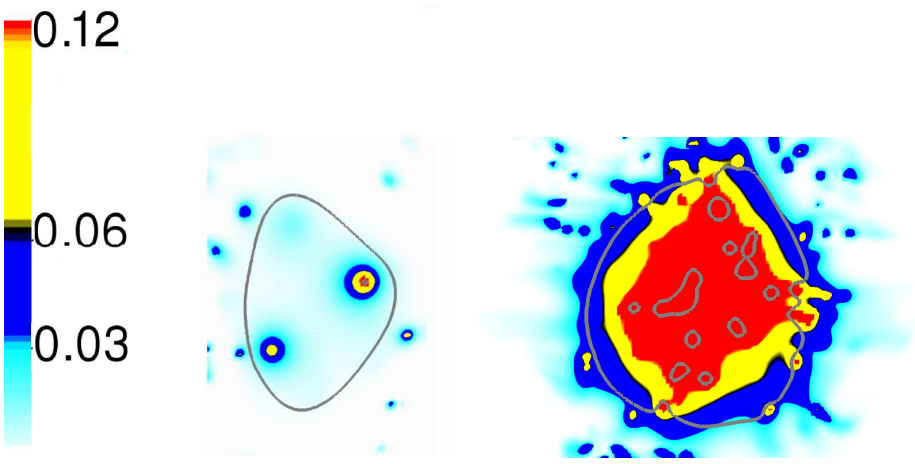

(a) (b)

Figure 5.6: Contours of mixture fraction in a 2D slice passing through the spark centre at $t = 2.5t_{sp}$. The grey line is the temperature iso-surface $T = 1400$K. (a) Case A. (b) Case C.

different ignition behaviour.

Figure 5.6 shows 2D contours of mixture fraction for cases A and C at $t = 2.5t_{sp}$. Cases B and D are qualitatively similar to case A. In the figures, we can identify droplets as spots of rich mixture fraction. We notice that outside the kernel, the mixture is richer in case C than in case A. In both cases, it remains lean overall. In the high temperature region, the difference is striking. In case A, stoichiometric mixtures exist only around the droplets and the interdroplet spacing has very lean value. In case C, the stoichiometric contour is wide. Near the $T = 1400K$ region, the mixture fraction in the interdroplet spacing is within the flammability limits. This is because the higher number of droplets than in case A, in the same spark volume, results in more evaporated fuel. This allows exothermic reactions to occur over a wider surface, as seen in Fig. 5.4a.

Based on the visualisation of the kernel evolution in different cases, we can categorise two modes of spray ignition. In the first one, cases A and D, flammable mixtures and high heat release rate are very localised. Intense reactions surround

single droplets and small groups of droplets. In the second one, case C, the mixture is relatively uniformly distributed throughout a large volume and the interdroplet spacing contains mixtures within the flammability limits. Consequently, the reaction zone is more continuous although wrinkled.

5.3.2 Volume averaged quantities

Figure 5.7 shows the evolution of the volume-integrated heat release rate, mass evaporation rate and evaporation sink in the region $T \geq 400K$ for the different simulations performed. In all cases, the integrated heat release rate first takes negative values, due to dominant endothermic reactions. At around $t = t_{sp}$, it becomes positive and then increases with time. Note that in the Gas case, exothermic reactions occur earlier because the fuel is readily available in vapour form for burning. At the end of the simulation, only case B has very low integrated heat release. This implies failed ignition. Moreover, the heat release is an order of magnitude larger in the Gas case and in case C than in cases A, B and D. This difference is consistent with the two different modes of spray ignition.

According to Ballal and Lefebvre [69], the burning rate of sprays is controlled by two time scales: the evaporation time and the chemical time. For relatively large droplets, they show that the evaporation rate is an impeding factor since it limits the amount of fuel that reacts in the gas phase. Our results agree with this statement. Figure 5.7b presents the integrated mass evaporation rate in the kernel for different cases. A higher evaporation rate is achieved with a larger number of droplets (case C compared to case A) or with a smaller initial droplet diameter (case C compared to case D). It is evident that cases having a larger rate of evaporation have a higher heat release rate.

In case B with failed ignition, the heat generated has much lower values than in case A and eventually decreases to zero. This behaviour is due to the limited number of droplets present inside, and therefore ignited by, the small kernel. This is

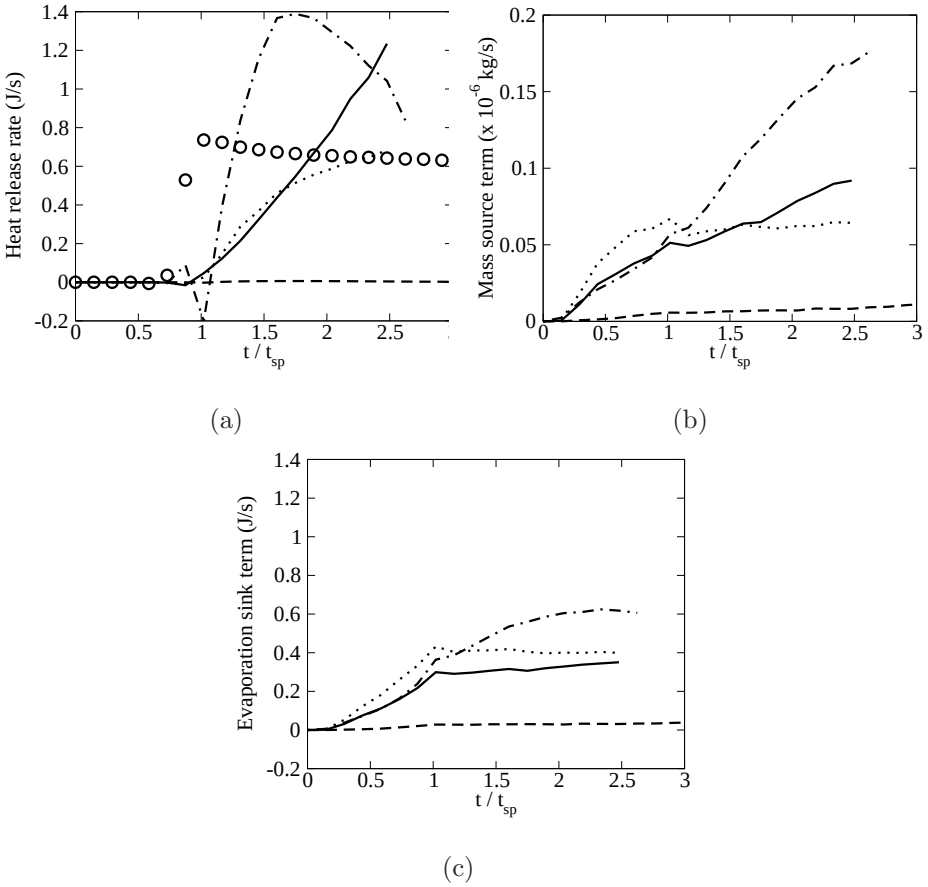

Figure 5.7: Volume integrated quantities in region $T > 400K$ *vs.* normalised time. (a) Heat release rate, (b) Mass source term magnitude. (c) Evaporation sink term magnitude. Case A: solid line; Case B: dashed line; Case C: dash-dotted line; Case D: dotted line; Gas case: circles. All values for case C and Gas case are divided by 10.

consistent with the recent observation that the likelihood of ignition depends on the number of droplets in the hot volume [41]. The hot kernel needs to reach a minimum size to overcome molecular and turbulent diffusion and to ignite enough droplets for heat production. This follows the criteria suggested by Ballal and Lefebvre [69] for successful kernel generation. Note that the stochasticity of the problem has to be considered: the distribution of droplets in the kernel is random and different ignition events could result from the same ignition energy. In that sense, the quenching distance d_q derived by Ballal and Lefebvre is more significant for an average set of realisations than for one particular event. Despite this consideration, our DNS simulations demonstrate the validity of this approach: the spark diameter of $1.57d_q$ in case A resulted in successful ignition, while the value of $0.95d_q$ in case B led to failed ignition.

In case D, the integrated heat release rate is of the same order as that of case A, as shown by Fig. 5.7a. Closer examination shows that it is actually larger than in case A immediately after ignition but it becomes lower at later times. Figure 5.7b shows that the mass evaporation rate in the kernel follows the same trend. It is initially larger in case D than in case A but lower at later times. Note that cases A and D have the same total number of droplets. The difference can be attributed to the following factors. First, the number of droplets ignited by the kernel is not the same because of the different distribution of droplets. Secondly, the droplets in case D have twice the diameter as droplets in case A. This has a twofold effect. In the cold mixtures, large and small droplets are at the same temperature and have the same mass Spalding number $B_{M,d}$. There, the mass evaporation rate will be twice larger for the larger droplets, see Eq. B.3. In the kernel, large and small droplets do not heat at the same rate. Figure 5.8 shows the evolution of the mean droplet temperature in the volume $T \geq 400K$. It is clear that in this region, small droplets warm up faster. Their mass Spalding number $B_{M,d}$ can become accordingly large. That is why, in the kernel, the evaporation rate in case A becomes larger than in case D. Interestingly, the mass evaporation rate in the whole domain (not shown

here) is found higher in case D for all times. This is because most of the droplets are not in the kernel. Hence, increasing the droplet diameter whilst keeping the same number of droplets has two main effects: a higher evaporation rate in the cold mixture but a lower evaporation rate in the hot kernel.

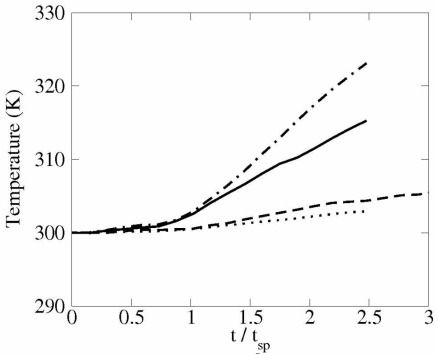

Figure 5.8: Mean droplet temperature in region $T > 400K$ *vs.* normalised time. Case A: solid line; Case B: dashed line; Case C: dash-dotted line; Case D: dotted line.

Furthermore, the evaporation sink term has a negative effect. Comparing Fig. 5.7a and 5.7c shows that in all spray cases, more energy is lost to evaporation in the kernel than generated by heat release for $t < t_{sp}$. In cases A, C and D, the overall power produced by combustion eventually overcomes that lost by evaporation. In case B (failed ignition), the heat generated remains low and is below the evaporation heat sink at the end of the simulation. Note also that the heat sink magnitude is higher in case D than in case A. In Eq. 5.3, the two last terms of the heat sink are higher in magnitude in case A than in case D, due to the higher mass evaporation rate. However, this is not the case for the first term, which increases with $\ln(1 + \mathrm{B_{M,d}})/\mathrm{B_{T,d}}$ (through the timescale τ_d^T). For large Spalding numbers, as in case A, the ratio is lower than 1 but for small Spalding numbers, as in case D, the ratio is near 1. For this reason, the first term in Eq. 5.3 is much higher in case D than in case A. As a result, the heat sink is higher in case D than in case A, despite a lower evaporation rate. Evaporation heat sink is an impeding factor for ignition and

should be taken into account in ignitability models. This is consistent with previous DNS investigations that demonstrated the detrimental impact of evaporation on n-heptane spray auto-ignition [141].

5.3.3 Radial distributions

In this section, we present radial averages of different scalars. Here, a radial average denotes the average of a scalar over a spherical shell at a given radius r around the spark centre. The thickness of the shell was about $18\mu m$, of the order of the cell size. We normalise this radius by the spark radius of case A, R_{ign}. The plot of the radial average against a radius originating at the spark centre can be useful to analyse the macroscopic flame structure in space. Figures 5.9 to 5.17 show the evolution of the radial averages of temperature, the mixture fraction, the heat release rate and the mass fraction of species O_2, CO_2, H_2, C_2H_4, H and OH for all cases.

In the Gas case, the figures show the rise of temperature due to the spark, the trigger of heat release at $t = 0.7t_{sp}$, the initial generation of species and eventually the relaxation of the profiles to that of a typical premixed flame. The comparison between the Gas case profiles and that of a 1D laminar premixed flame is done in Section 5.3.4. Note the slight change of mixture fraction over the flame caused by differential diffusion in Fig. 5.10e. Figure 5.9e also informs us on the contribution of heat release to the rise of temperature in the spark. At $t = t_{sp}$, the Gas case has a temperature about 700K higher than a non-reacting stoichiometric case, with the same spark characteristics. Interestingly, at this time, the heat release rate is positive except near the centre of the spark where it becomes negative. This was already observed in Fig. 5.1. A previous numerical study showed that after combustion has occurred in the spark centre, the additional spark energy causes endothermic dissociation of the product [151]. Hence, at $r = 0$, the very high temperature of about 3500K causes endothermic dissociation.

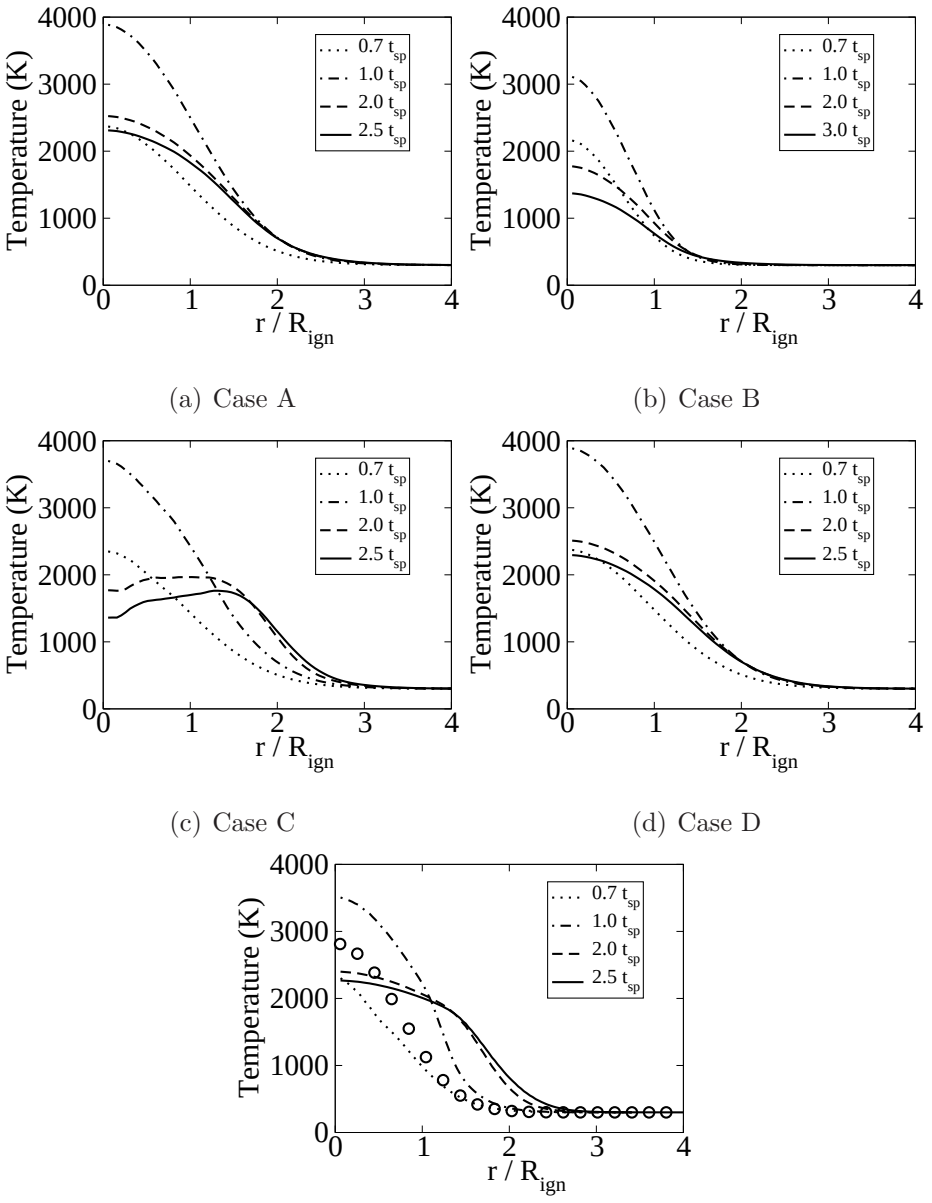

(a) Case A

(b) Case B

(c) Case C

(d) Case D

(e) Gas

Figure 5.9: Temperature averaged over a spherical shell of radius r as a function of normalised r for (a) Case A , (b) Case B, (c) Case C , (d) Case D and (e) Gas case. Circles denote a non-reacting Gas case at $t = t_{sp}$.

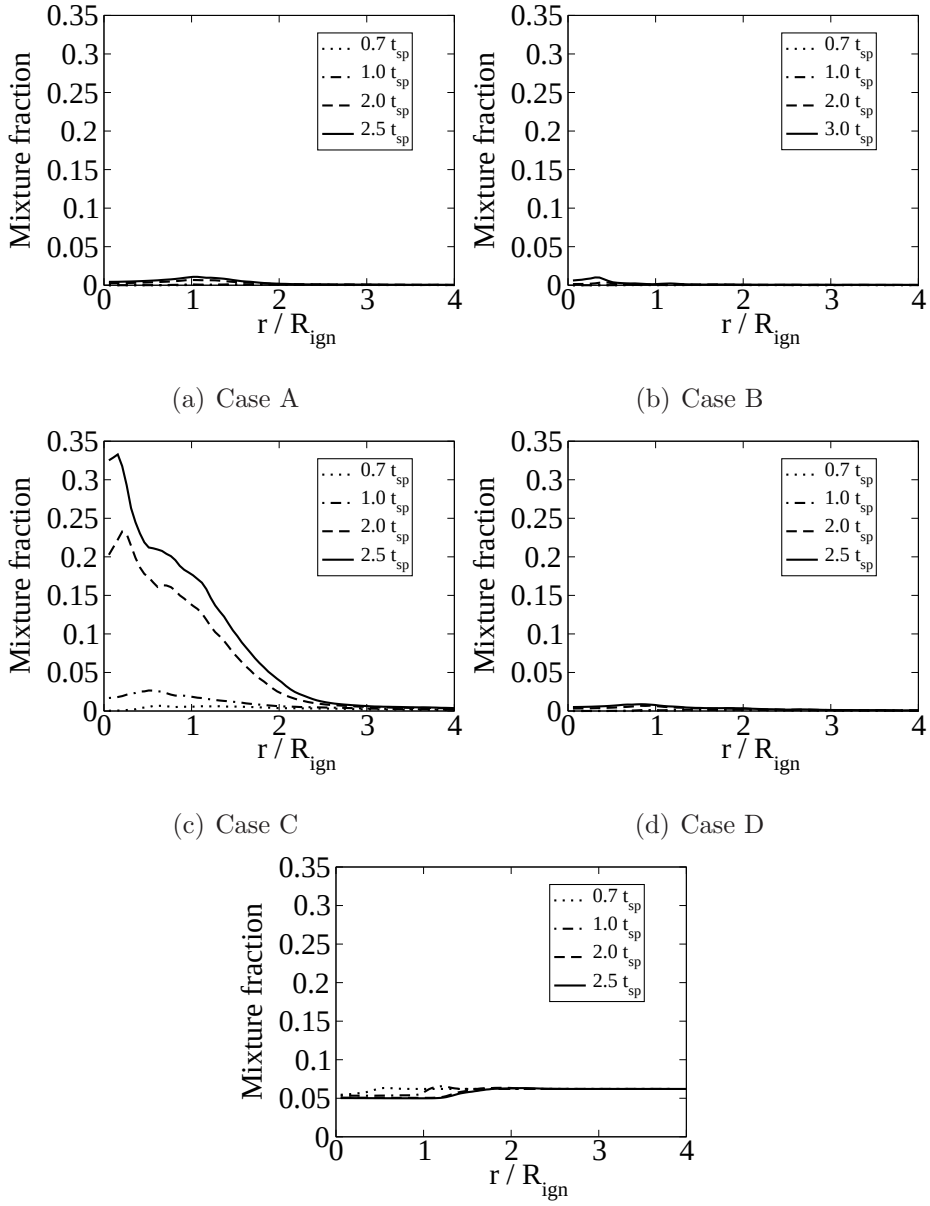

(a) Case A

(b) Case B

(c) Case C

(d) Case D

(e) Gas

Figure 5.10: Mixture fraction averaged over a spherical shell of radius r as a function of normalised r for (a) Case A , (b) Case B, (c) Case C , (d) Case D and (e) Gas case.

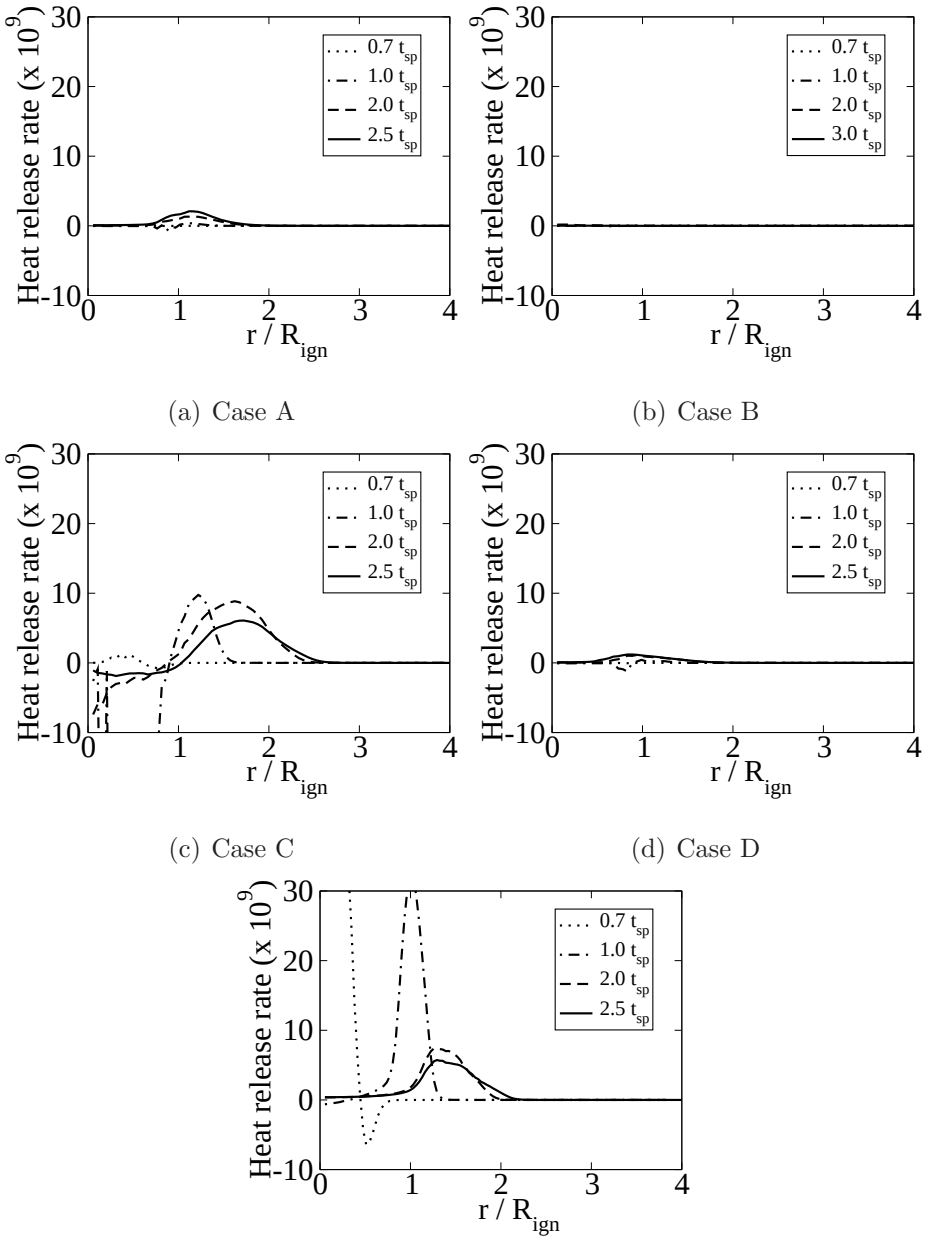

(a) Case A

(b) Case B

(c) Case C

(d) Case D

(e) Gas

Figure 5.11: Heat release rate averaged over a spherical shell of radius r as a function of normalised r for (a) Case A , (b) Case B, (c) Case C , (d) Case D and (e) Gas case.

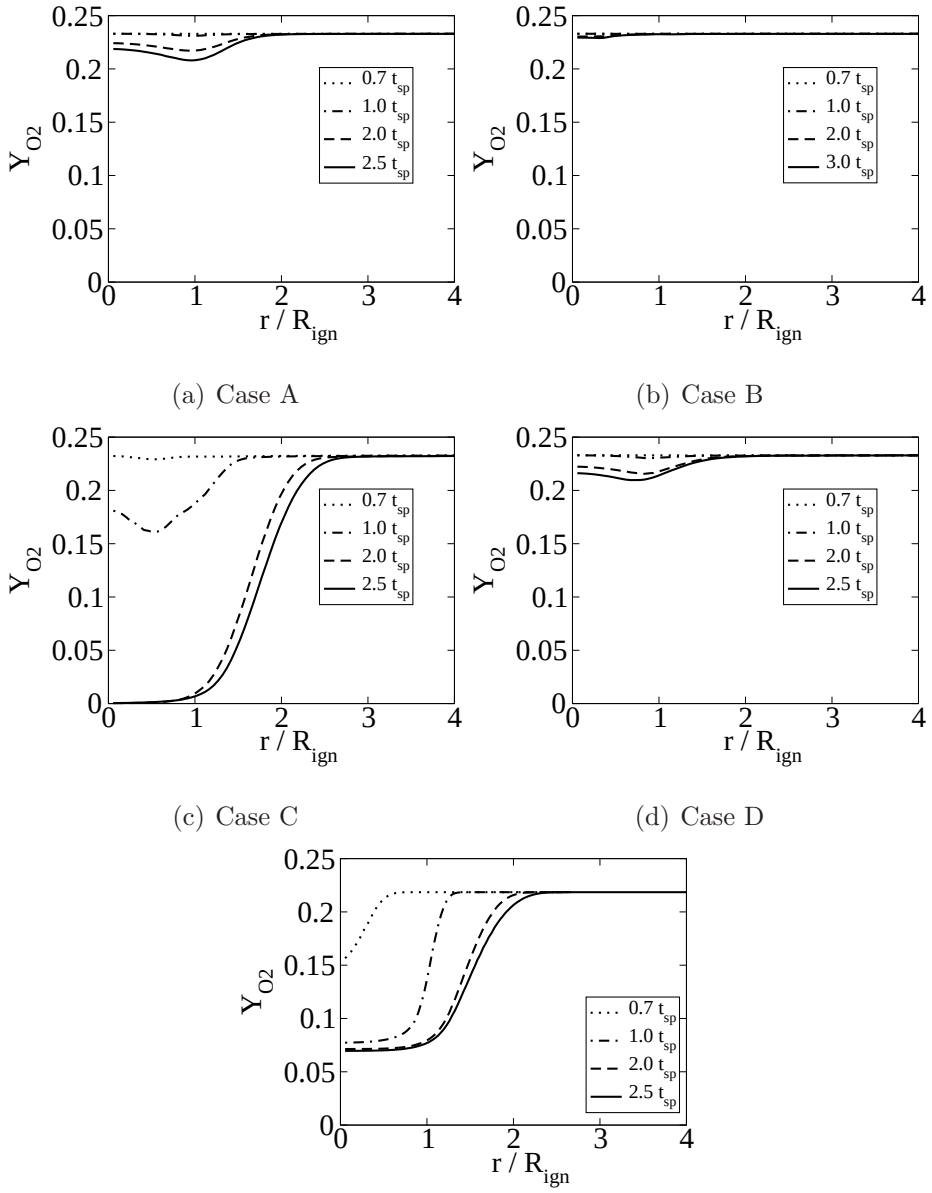

(a) Case A

(b) Case B

(c) Case C

(d) Case D

(e) Gas

Figure 5.12: Y_{O_2} averaged over a spherical shell of radius r as a function of normalised r for (a) Case A , (b) Case B, (c) Case C , (d) Case D and (e) Gas case.

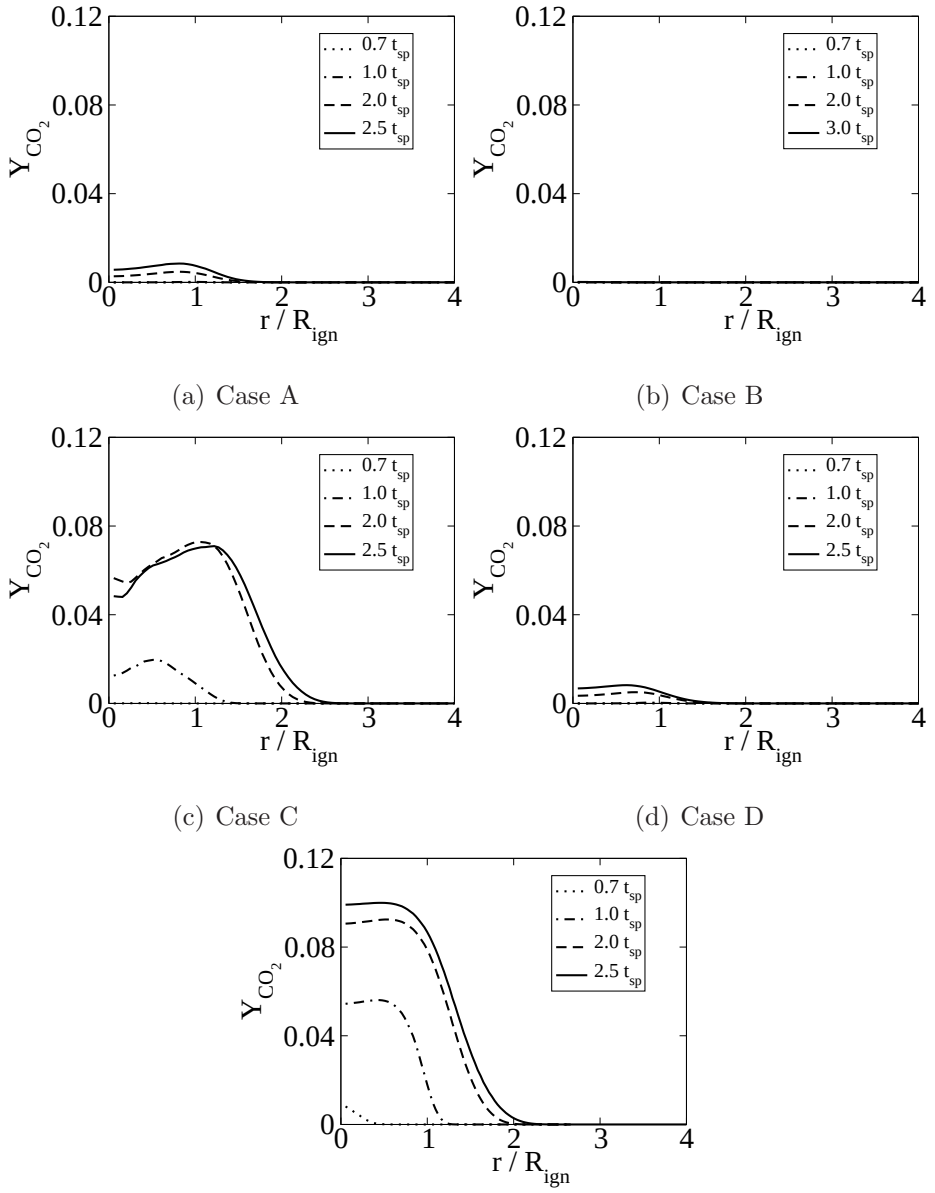

(a) Case A

(b) Case B

(c) Case C

(d) Case D

(e) Gas

Figure 5.13: Y_{CO_2} averaged over a spherical shell of radius r as a function of normalised r for (a) Case A , (b) Case B, (c) Case C , (d) Case D and (e) Gas case.

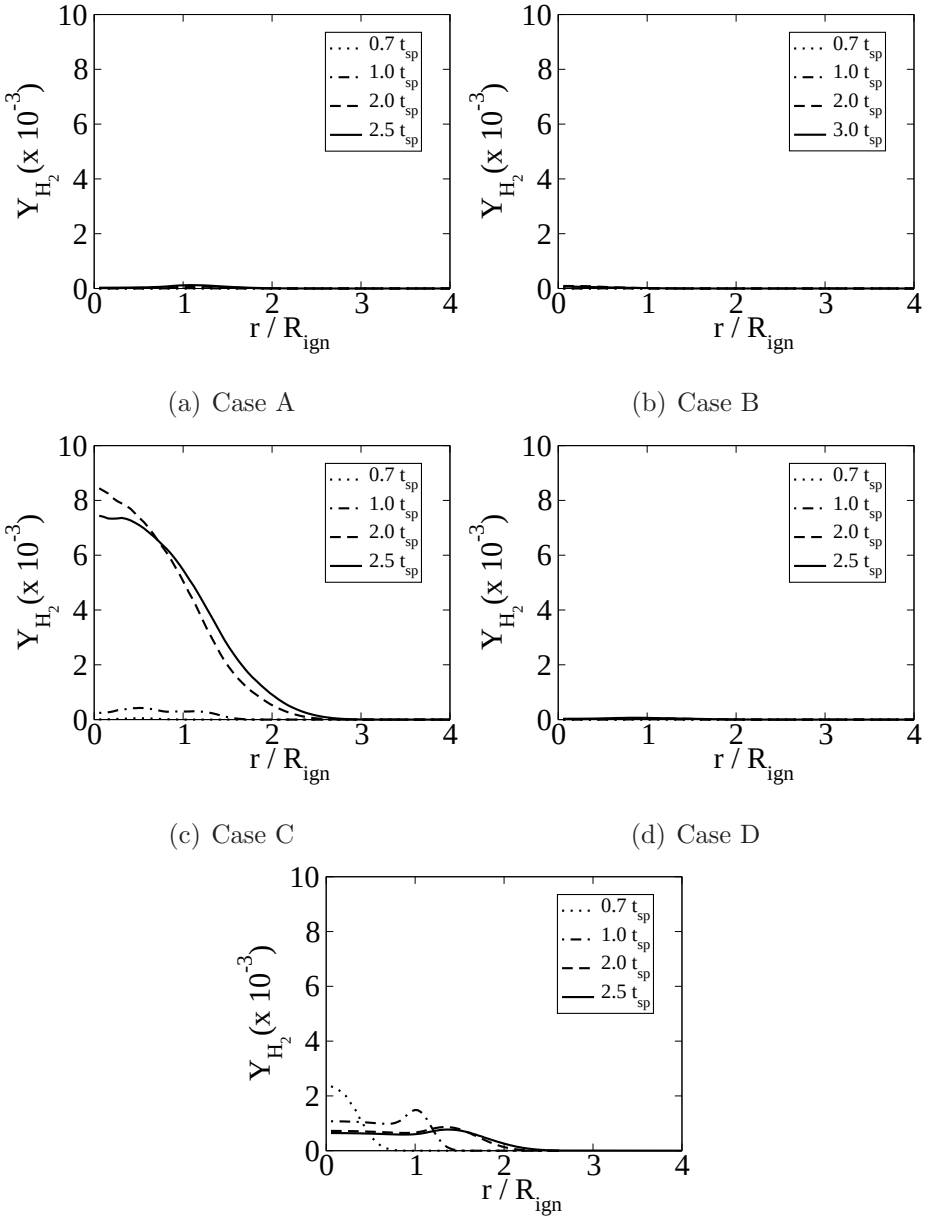

(a) Case A

(b) Case B

(c) Case C

(d) Case D

(e) Gas

Figure 5.14: Y_{H_2} averaged over a spherical shell of radius r as a function of normalised r for (a) Case A , (b) Case B, (c) Case C , (d) Case D and (e) Gas case.

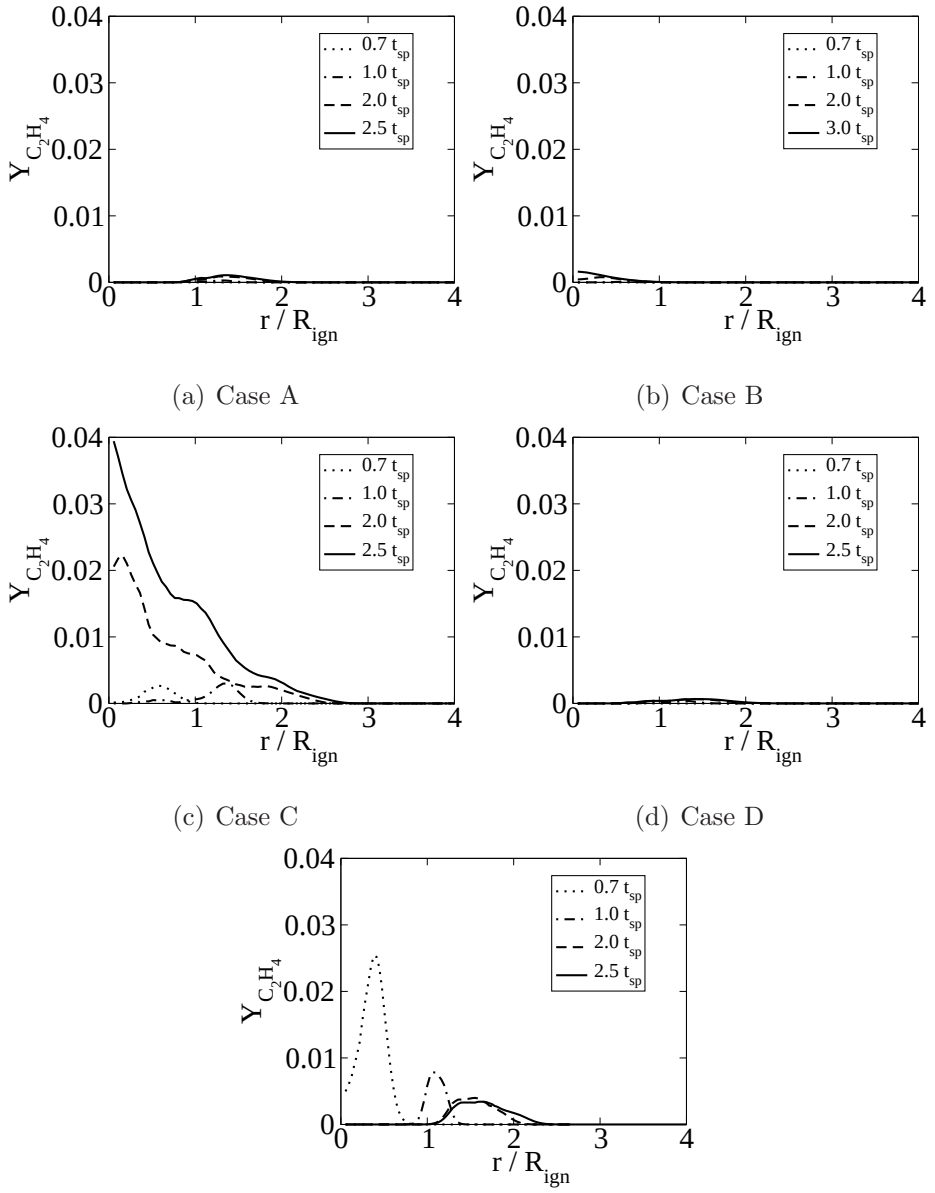

(a) Case A

(b) Case B

(c) Case C

(d) Case D

(e) Gas

Figure 5.15: $Y_{C_2H_4}$ averaged over a spherical shell of radius r as a function of normalised r for (a) Case A , (b) Case B, (c) Case C , (d) Case D and (e) Gas case.

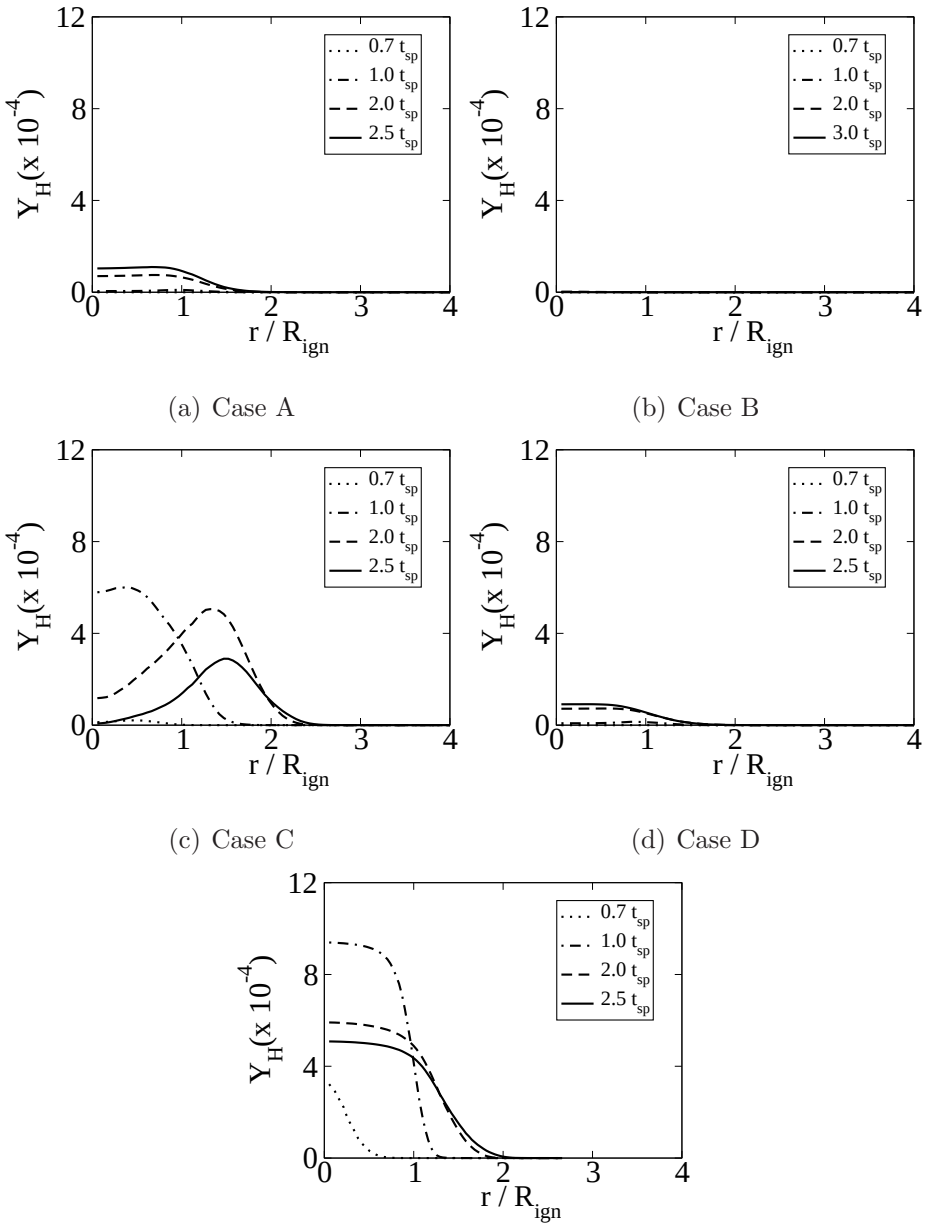

(a) Case A

(b) Case B

(c) Case C

(d) Case D

(e) Gas

Figure 5.16: Y_H averaged over a spherical shell of radius r as a function of normalised r for (a) Case A , (b) Case B, (c) Case C , (d) Case D and (e) Gas case.

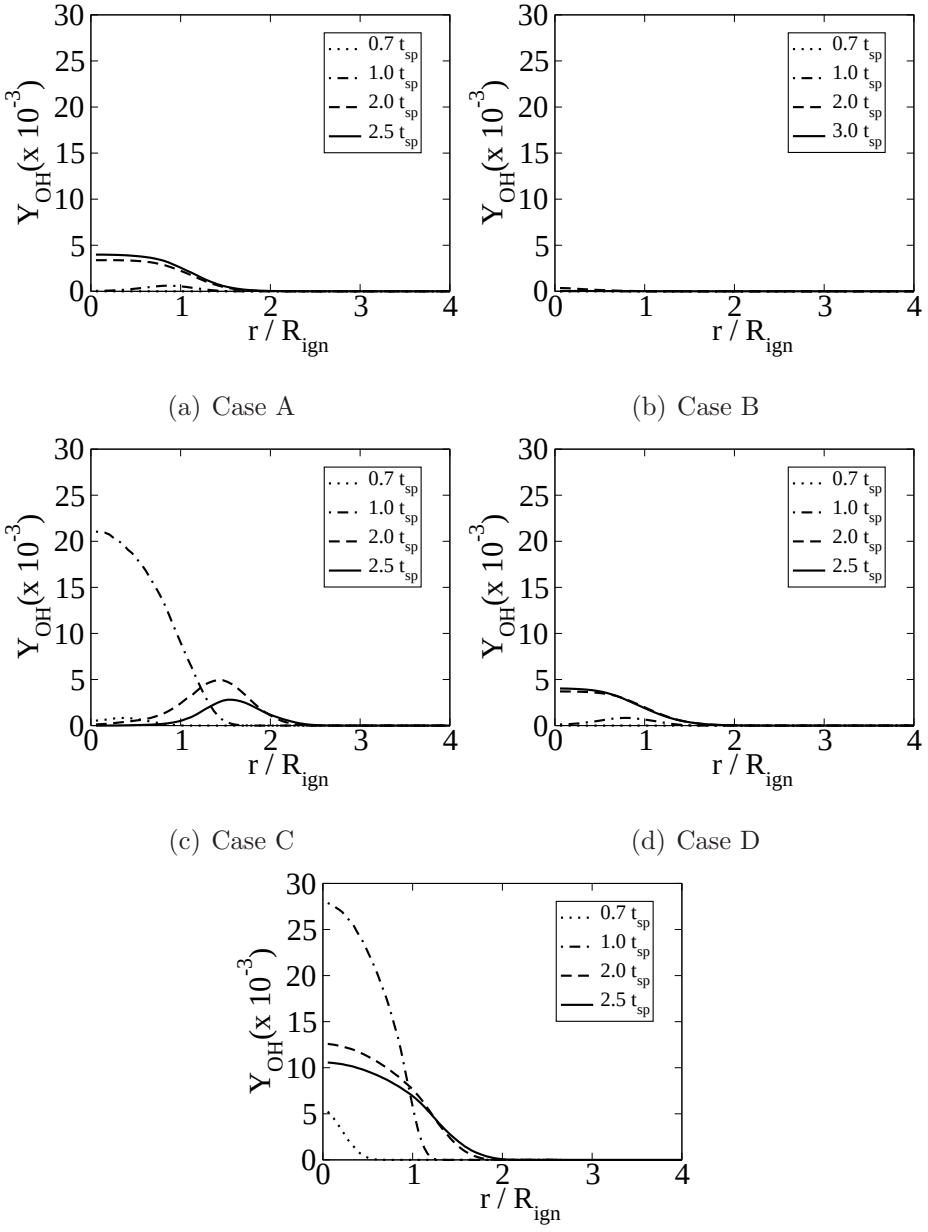

(a) Case A

(b) Case B

(c) Case C

(d) Case D

(e) Gas

Figure 5.17: Y_{OH} averaged over a spherical shell of radius r as a function of normalised r for (a) Case A , (b) Case B, (c) Case C , (d) Case D and (e) Gas case.

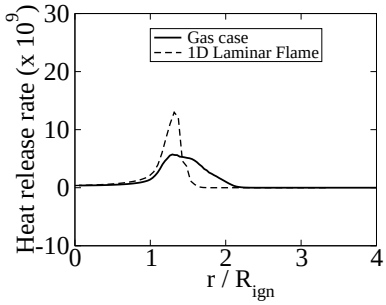

(a) Heat release rate

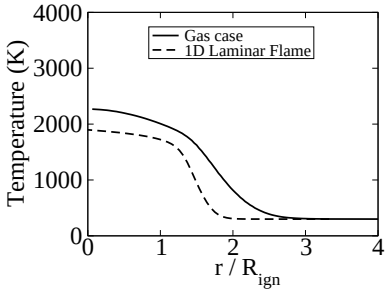

(b) Temperature

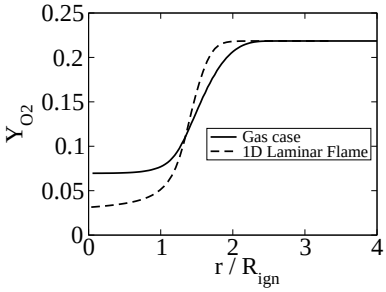

(c) Y_{O2}

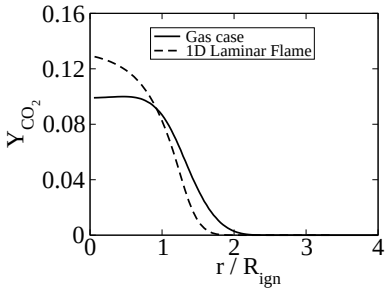

(d) Y_{CO2}

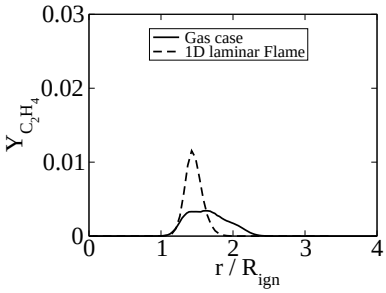

(e) Y_{C2H4}

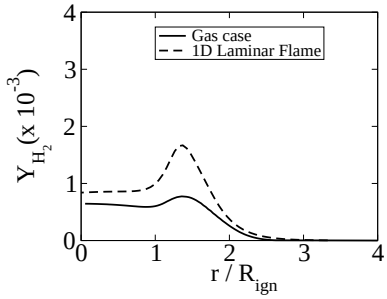

(f) Y_{H2}

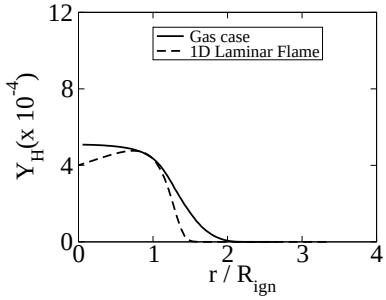

(g) Y_H

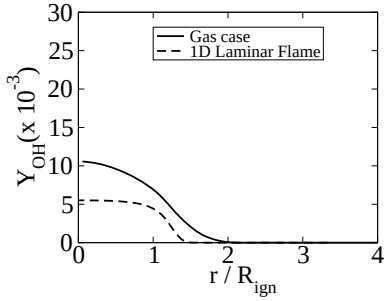

(h) Y_{OH}

Figure 5.18: Plain lines show averages over a spherical shell of radius r as a function of normalised r for Gas case at $t = 2.5t_{sp}$. Dotted lines show stoichiometric 1D laminar flame profiles.

In case A, the temperature peaks near 2200K at the end of the simulation as shown by Fig. 5.9a. The profiles of mixture fraction (Fig. 5.10a), heat release rate (Fig. 5.11a), Y_{C_2H4} (Fig. 5.15a) and Y_{H_2} (Fig. 5.14a) have very low values and have finite values only locally. However, profiles of Y_{CO_2} (Fig. 5.13a), Y_H (Fig. 5.16a) and Y_{OH} (Fig. 5.17a) have finite values from $r = 0$ to $r = 1.5R_{ign}$. In Fig. 5.6, we saw that in case A the mixture fraction was high only near the droplets. Similar graphs, not presented here, were examined for all other quantities. First, they showed that heat release rate, and most intermediate species mass fractions (e.g. C_2H_4, H_2) were finite only near droplets. The low values of the radial averages of those quantities is related to small number of droplets in a spherical shell, evident from Fig. 5.2a. Second, the graphs showed that the mass fraction of radicals OH and H and products CO_2 and H_2O remained finite away from the droplets. This explains the finite radial averages of those quantities. Case B, with misfire, has very low values of radical concentrations and heat release rate throughout the simulation while the maximum temperature falls below 1500K at $t = 3t_{sp}$. Case D has similar profiles to case A. We conclude that in cases A, B and D, all quantities that are finite only near droplets have low radial averages because of the low spray density. Furthermore, the radial averages show that in cases A and D, with successful ignition, the kernel contains non-negligible concentrations of products and radicals OH and H.

In case C, the values of the radially averaged mixture fraction and heat release rate are much higher than in case A because mixture fraction and heat release rate are high over a large volume around the spark centre (see Section 5.3.1). The large reaction zone also results in high values of radially averaged mass fractions of secondary species (for example C_2H_4 in Fig. 5.15c). In Fig. 5.11c, the profiles evolve according to the description done in Section 5.3.1. At $t = 0.7t_{sp}$, exothermic reactions occur near the centre while endothermic occur further away. At this time, Fig. 5.10c shows that the radially averaged mixture fraction is below the lean limit ($\xi_L = 0.035$). The low mixture fraction causes the low magnitude of heat release rate. At $t = t_{sp}$, the mixture fraction is above the lean limit until $r = R_{ign}$.

Figure 5.11c shows that exothermic reactions occur near $r = R_{ign}$ and endothermic reactions occur at $r = 0$. At this time, the spark centre reaches a temperature of about 3800K, see Fig. 5.9c. As in the Gas case, the negative heat release rate can be attributed to the dissociation of the products at high temperature. At $t = 2.5t_{sp}$, the profiles have stabilised to a structure that is described in next paragraph.

In Fig. 5.10c, the mixture fraction increases monotonically from large radii to low radii. The cold mixture is lean while the burned mixture is rich. This is due to the increased evaporation rate induced by the propagating high temperature surface. In addition, the location of the peak of heat release rate in Fig. 5.11c corresponds approximately to stoichiometric mixture fraction. Figure 5.11c shows that the heat release rate profile is similar to the Gas case for $r \geq R_{ign}$. However, for $r \leq R_{ign}$, in the burned gases, the heat release rate is negative. This was already observed in Fig. 5.4. In addition, the averaged temperature in Fig. 5.9c peaks near 1800K at $r = R_{ign}$ and decreases to about 1500K at $r = 0$. Hence, endothermic reaction at $r = 0$ cannot be attributed to dissociation at very high temperature. Furthermore, mass fractions of O_2 (Fig. 5.12c), and OH (Fig. 5.17c), become negligible in the burned gas, while the mass fractions of H_2 (Fig. 5.14c), C_2H_4 (Fig. 5.15c), and other intermediates (e.g. CH_3, CH_4, C_2H_2) not shown here, increase substantially.

In fact, this description is very similar to that observed in Chapter 3 with one-dimensional freely propagating spray flames under conditions of rich sprays and near stoichiometric value of gaseous mixture fraction at the peak of heat release. It can be explained as follows. The burned region corresponds to a very rich zone. In our configuration, droplets are large enough to survive past the flame and keep evaporating in the burned zone. Moreover, it was shown in Chapter 3 that the high value of the mixture fraction in the reaction zone results in complete consumption of oxygen and OH in the flame reaction zone. As a consequence, oxygen and OH do not penetrate the rich post-flame region. There, the fuel evaporated by the droplets is pyrolysed into smaller hydrocarbons. Those endothermic reactions and the evaporation heat sink cause a decrease in the burned gas temperature. In Chapter 3, it

was shown that the small hydrocarbons generated in the post flame region diffused towards the main reaction zone and enhanced the heat release rate. This positive effect on flame propagation must exist to a certain extent in case C.

To conclude, the radial averages enabled an insightful description of the flame in case C but less so for cases A, B and D due to the smaller number of droplets. In case C, the average mixture fraction is close to stoichiometry in the high heat release region, while in the burned gas the mixture fraction is rich with post-flame pyrolysis occurring. It is evident that sparking a globally very rich spray, beyond the rich flammability limit, can still result in a successful flame, with a pool of intermediates (e.g. H_2, C_2H_4) in the sparked region. This observation may explain, to an extent, the practical finding with gas turbine combustors that ignition can be successful even with large amounts of liquid fuel close to the ignitor [153].

5.3.4 Comparison with a laminar 1D premixed flame

In this section, key quantities are compared between the radially averaged Gas case and a 1D laminar stoichiometric premixed flame, computed with the same chemistry. In Fig. 5.18, the profiles for the Gas case and the 1D case are shown and are positioned such that the heat release rate peaks at the same location. The graphs show that the various quantities have a similar behaviour along the flame and the same order of magnitude, but the profiles do not match exactly. The discrepancies can be attributed to turbulence and to the curved shape of the kernel. Results not shown here demonstrate a clear negative correlation between heat release rate and curvature in the reaction zone region ($1200 \leq T \leq 1600$). Moreover, species mass fraction are also affected by differential diffusion in a curved kernel. In addition, it is possible that at $t = 2.5t_{sp}$, the initial effect of the spark has not completely dissipated. Since the focus of this study is not the detailed study of a gaseous premixed kernel, we do not quantify further the contribution of curvature, differential diffusion or the spark effect. Nonetheless, it can be concluded that the

kernel in the Gas case has a structure close to the equivalent 1D premixed flame.

5.3.5 Distribution in mixture fraction space and comparison with a 1D diffusion flame

Given the stratified nature of the problem, it is instructive to examine the flames in mixture fraction space. As a reference case, a 1D laminar diffusion flame with low scalar dissipation rate ($0.4s^{-1}$ at stoichiometry) was calculated with the same chemistry. The fuel side and the oxidiser side of this flame have respectively a mixture fraction of 1 and 0. First, we comment on the evolution of scatter plots of heat release rate. Then, we show different quantities in mixture fraction space for cases A and C.

Figure 5.19 shows the scatter plots of the heat release rate *vs.* ξ for case A. Note the progressively increasing population of samples at high mixtures fractions due to evaporation. Before ignition ($t = 0.7t_{sp}$) heat release is exclusively negative (Fig. 5.19a). The fuel evaporated chemically breaks up leading to endothermic heat release while exothermic reactions are negligible due to lack of radicals. Figure 5.19b shows that at the end of the spark ($t = t_{sp}$), heat release takes both positive and negative values. Examination of Fig. 5.19d shows that endothermic reactions are mainly located in the region of temperature $T \leq 1800$ K whilst exothermic reactions occur in the region $T \geq 1800$ K. In the region $T \geq 1800$ K, ignition has been triggered and locally, enough radicals have been produced to sustain exothermic reactions. Hence, droplets located near the spark centre tend to produce heat release faster than droplets further from the spark. In addition, negative heat release occurs, albeit more rarely, for $T \geq 2400$ K. This can be attributed to endothermic dissociation at high temperature. Figure 5.19c shows that at the end of the simulation, $t = 2.5t_{sp}$, heat release is mainly positive and peaks around the stoichiometric mixture fraction. Note that even at this time, some endothermic reactions exist. They occur at some droplet locations where the mixture is rich. Positive heat release spans ξ with lean to

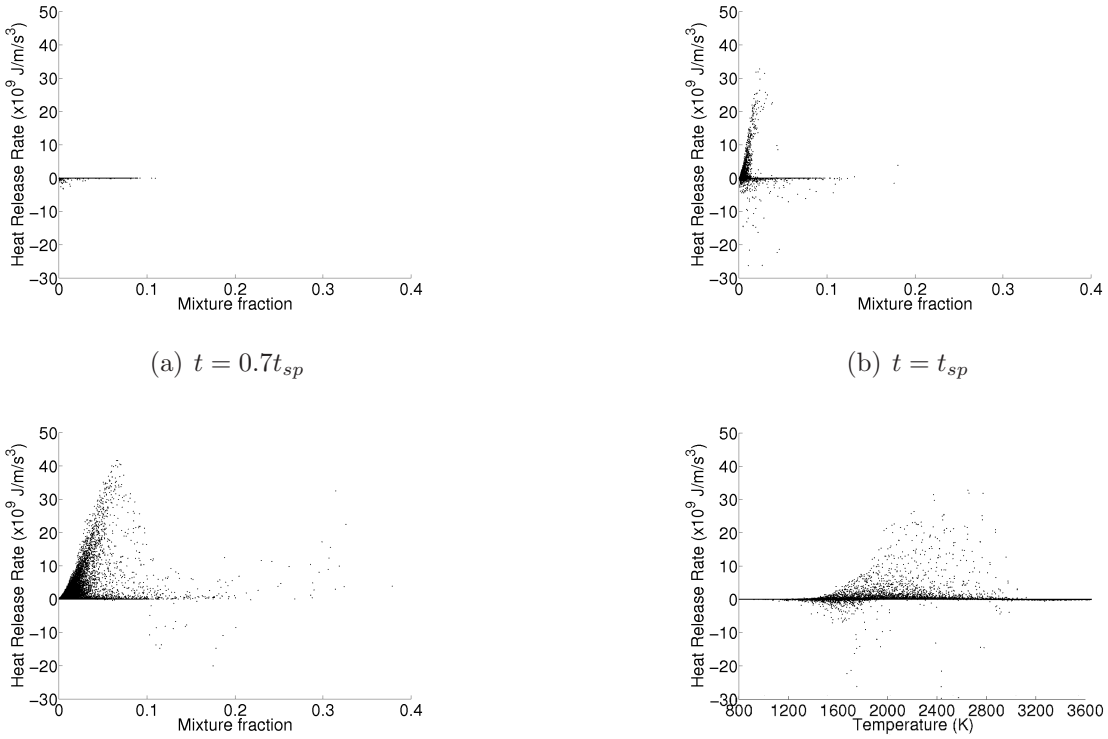

(a) $t = 0.7t_{sp}$

(b) $t = t_{sp}$

(c) $t = 2.5t_{sp}$

(d) HR *vs.* T, $t = t_{sp}$

Figure 5.19: Scatter plot for case A of heat release rate *vs.* mixture fraction at (a) $t = 0.7t_{sp}$, (b) $t = t_{sp}$, (c) $t = 2.5t_{sp}$ and (d) heat release rate *vs.* T at $t = t_{sp}$.

rich values. Furthermore, it is important to notice that there are numerous samples with finite positive heat release at $\xi < 0.035$, the nominal lean flammability limit.

Similar scatter plots for case C are shown in Fig. 5.20. Note the earlier occurrence of positive heat release rate and the faster generation of rich mixture due to the higher density of droplets. At $t = t_{sp}$, positive heat release rate dominates for $1400K \leq T \leq 2200K$. For larger temperatures, both positive and negative values occur. Negative values can be attributed to dissociation of products. Furthermore, the scatter plot at $t = 2.5t_{sp}$ shows a peak near stoichiometry and negative values towards the rich side. The negative values are related to the post-flame pyrolysis described in Section 5.3.3. Interestingly, the heat release rate is finite over a wide range of mixture fractions, even below the lean limit.

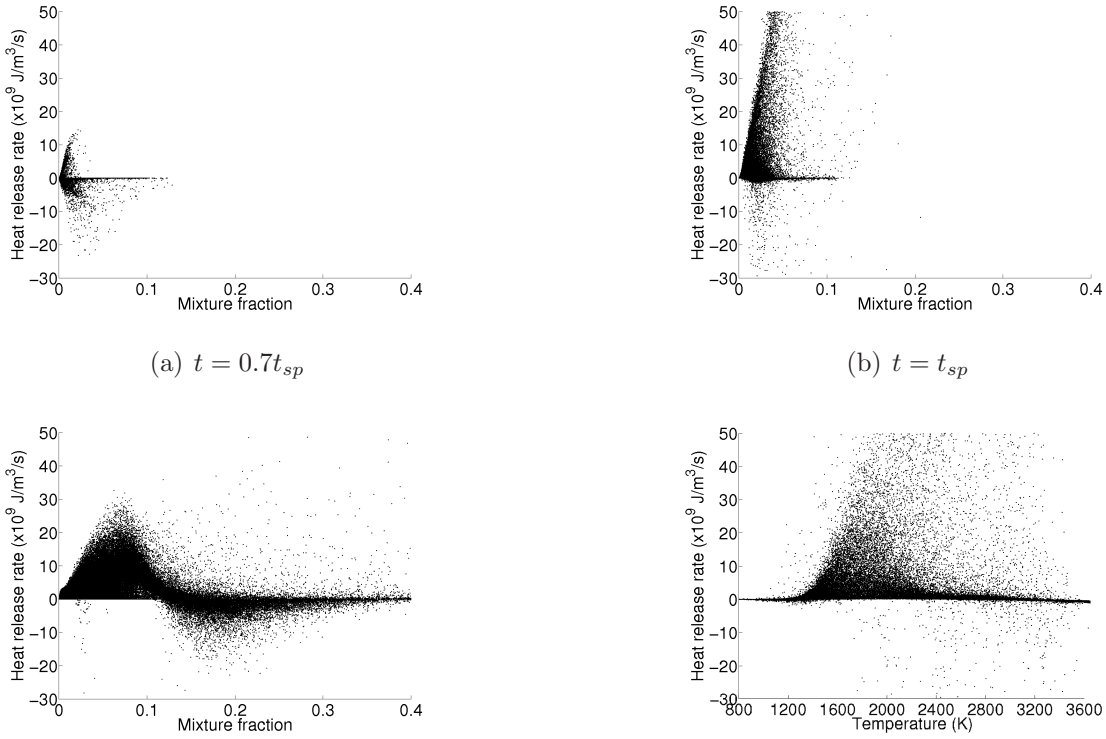

(a) $t = 0.7t_{sp}$

(b) $t = t_{sp}$

(c) $t = 2.5t_{sp}$

(d) HR *vs.* T, $t = t_{sp}$

Figure 5.20: Scatter plot for case C of heat release rate *vs.* mixture fraction at (a) $t = 0.7t_{sp}$, (b) $t = t_{sp}$, (c) $t = 2.5t_{sp}$ and (d) heat release rate *vs.* T at $t = t_{sp}$.

Figure 5.21 shows the same scatter plots for case B. The heat release rate is zero at $t = 0.7t_{sp}$, becomes finite but low at $t = 1t_{sp}$ and becomes zero again at $3t_{sp}$. Those scatters are consistent with the failed ignition event.

Figure 5.22 shows the scatter plots for case D. The striking similarity with case A supports the suggestion that cases A and D ignite in a similar way. Note that the heat release rate magnitude is lower in case D than in case A at $t = 2.5t_{sp}$. As mentioned in 5.3.2, the lower mass evaporation rate of droplets inside the kernel in case D, induces a lower heat release rate.

Figure 5.23 shows profiles of conditional heat release rate in mixture fraction space at $t = 2.5t_{sp}$. For cases A, C and D, with successful ignition, heat release rate is positive below the nominally lean limit. On the contrary, heat release in the

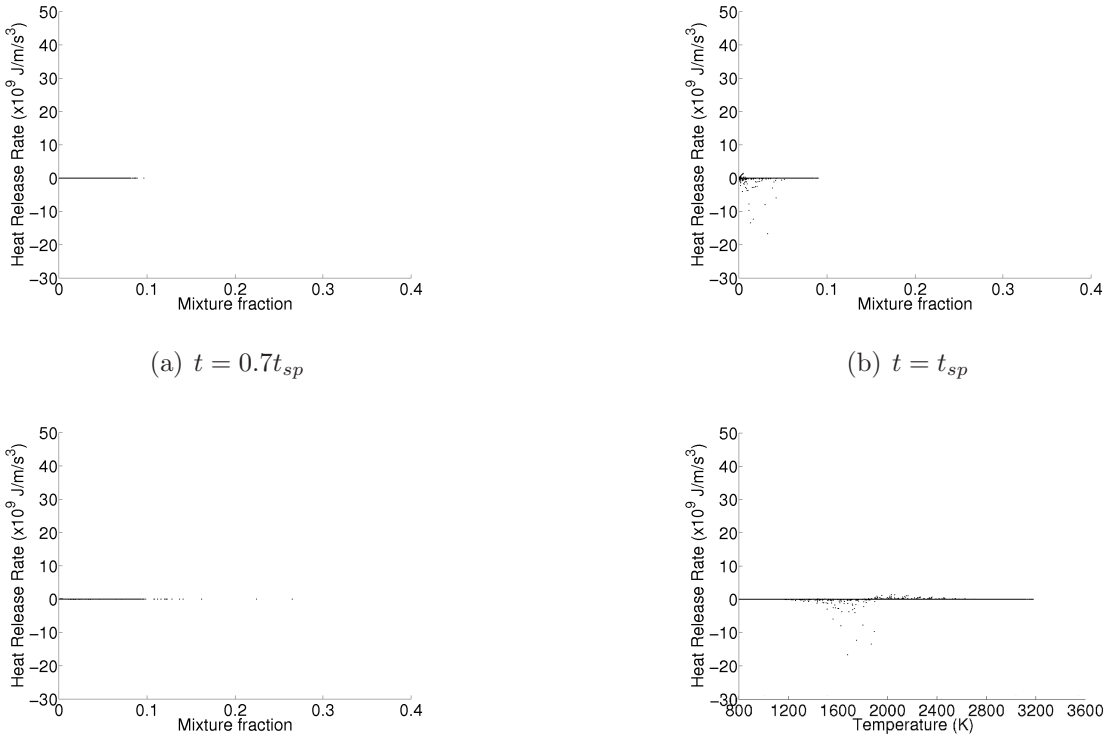

(a) $t = 0.7t_{sp}$

(b) $t = t_{sp}$

(c) $t = 3t_{sp}$

(d) HR *vs.* T, $t = t_{sp}$

Figure 5.21: Scatter plot for case B of heat release rate *vs.* mixture fraction at (a) $t = 0.7t_{sp}$, (b) $t = t_{sp}$, (c) $t = 3t_{sp}$ and (d) heat release rate *vs.* T at $t = t_{sp}$.

1D diffusion flame is negligible at those values. Hence, spark ignition in the present spray cases involve very lean combustion, not observed in a non-premixed laminar flame with low scalar dissipation rate.

Now, we present scatter plots of mass fractions and temperature in mixture fraction space at the end of the simulation for successful spark events. Cases A and C are discussed only. The successful case D has trends similar to that of case A.

Figure 5.24 shows that in case A the scatter plots and the conditional average do not follow the 1D non-premixed flame profiles. Figure 5.24b and 5.24c show an unburned and a burned branch with a large scatter between those two branches, especially for mixture below the nominal lean limit. Furthermore, there is a large number of points that have high mass fractions of intermediates H_2 (Fig. 5.24d),

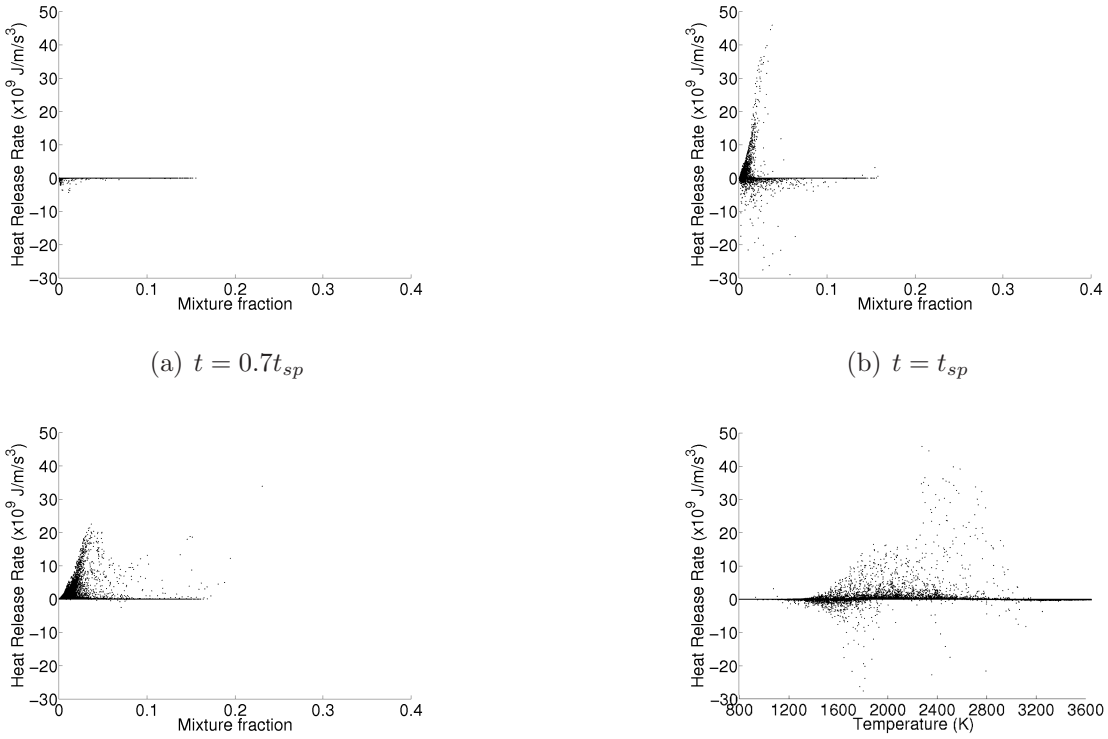

(a) $t = 0.7t_{sp}$

(b) $t = t_{sp}$

(c) $t = 2.5t_{sp}$

(d) HR *vs.* T, $t = t_{sp}$

Figure 5.22: Scatter plot for case D of heat release rate *vs.* mixture fraction at (a) $t = 0.7t_{sp}$, (b) $t = t_{sp}$, (c) $t = 2.5t_{sp}$ and (d) heat release rate *vs.* T at $t = t_{sp}$.

C_2H_4 (Fig. 5.24e) and CH_2O (Fig. 5.24f) and radicals H (Fig. 5.24g), OH (Fig. 5.24h) at those lean mixtures while they are zero for the 1D diffusion flame. This is consistent with the observation that positive heat release occurs at very lean mixture fractions. The "frozen" and the burned branches are expected since fuel evaporates outside the kernel as well as inside. The scatter between the branches is related to mixtures switching from a "frozen" state to a burned state. The process by which lean mixtures undergo combustion is discussed in Section 5.3.7.

In Fig. 5.25, it is evident that the conditional average of case C follows the 1D diffusion flame much closer than case A, see species C_7H_{16}, O_2, H_2, C_2H_4, H and OH. However, as in case A, an unburned branch and a burned branch are evident, see Fig. 5.25b and 5.25c, with a large scatter between them especially for mixture

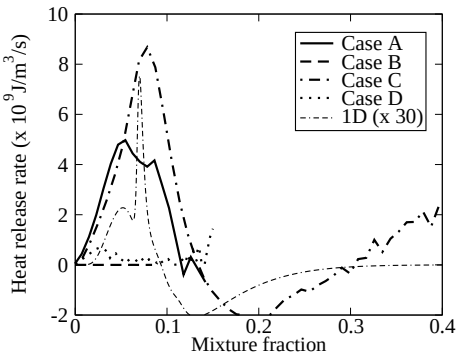

Figure 5.23: Conditional average of heat release rate on mixture fraction in region $T > 400K$ *vs.* mixture fraction at $t = 2.5t_{sp}$. Case A: solid line; Case B: dashed line; Case C: dash-dotted line; Case D: dotted line. The double dash-dotted line is the heat release rate profile in mixture fraction space for the 1D non-premixed flame, magnified 30 times.

fractions between 0 and 0.12. Figure 5.25d, e, f, g and h show that intermediates and radicals are also finite in this range. Hence, the averaged profiles in mixture fraction space of case C agree well with that of a 1D diffusion flame. However, a large population is in a transient state between the unburned and the burned state. This is true even for mixtures below the nominal flammability limit.

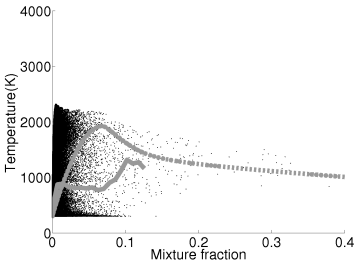

(a) Temperature

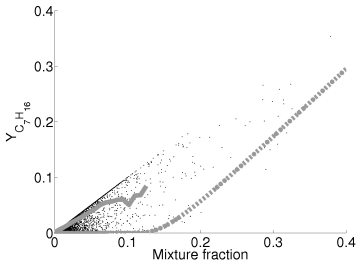

(b) Y_{C7H16}

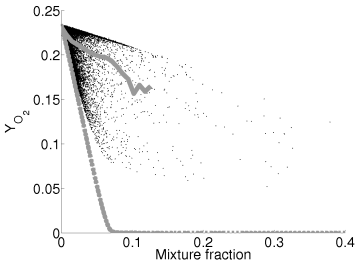

(c) Y_{O2}

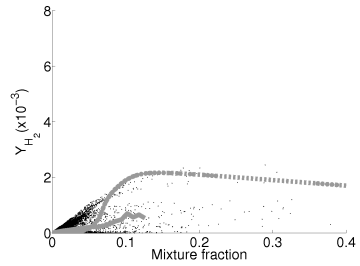

(d) Y_{H2}

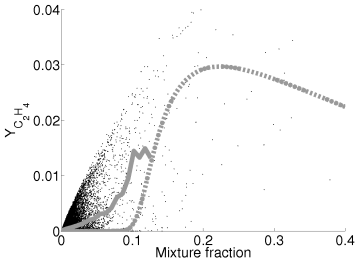

(e) Y_{C2H4}

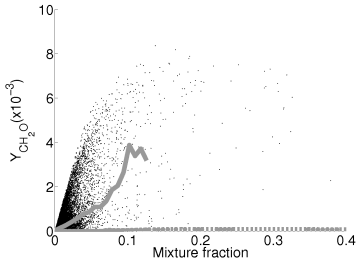

(f) Y_{CH2O}

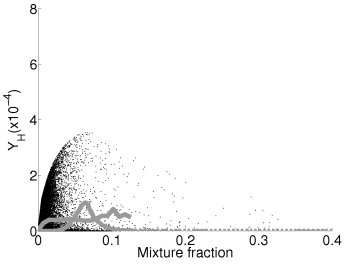

(g) Y_H

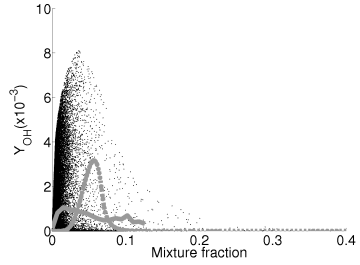

(h) Y_{OH}

Figure 5.24: Scatter plot *vs.* mixture fraction for case A at $t = 2.5t_{sp}$. The plain grey line shows conditional average, the dotted grey line shows the 1D diffusion flame profile. (a) Temperature, (b) $Y_{C_7H_{16}}$, (c) Y_{O2}, (d) Y_{H2}, (e) Y_{C2H4}, (f) Y_{CH_2O}, (g) Y_H, (h) Y_{OH}.

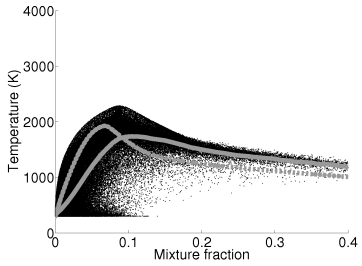

(a) Temperature

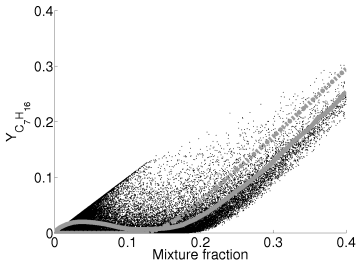

(b) Y_{C7H16}

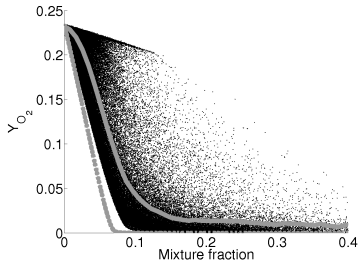

(c) Y_{O2}

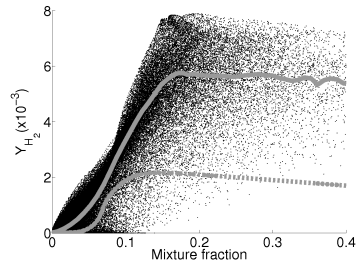

(d) Y_{H2}

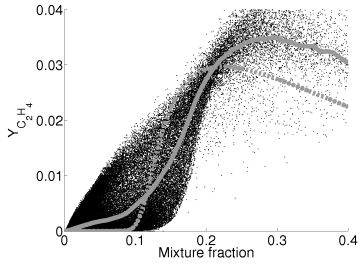

(e) Y_{C2H4}

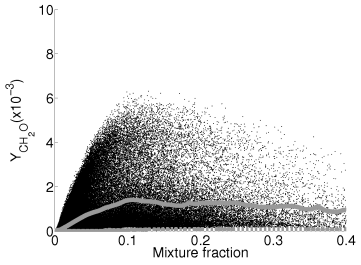

(f) Y_{CH2O}

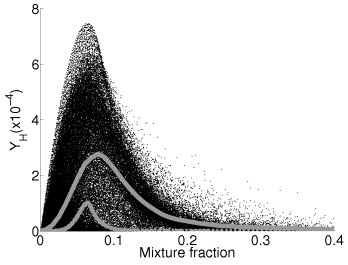

(g) Y_H

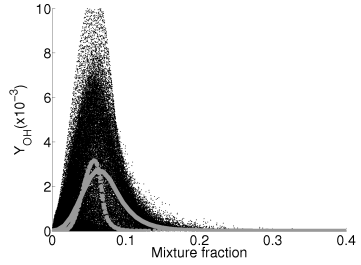

(h) Y_{OH}

Figure 5.25: Scatter plot *vs.* mixture fraction for case C at $t = 2.5t_{sp}$. The plain grey line shows conditional average, the dotted grey line shows the 1D diffusion flame profile. (a) Temperature, (b) $Y_{C_7H_{16}}$, (c) Y_{O2}, (d) Y_{H2}, (e) Y_{C2H4}, (f) Y_{CH_2O}, (g) Y_H, (h) Y_{OH}.

5.3.6 Scalar dissipation rate

A density weighted scalar dissipation rate is defined as

$$\chi = 2\frac{\rho}{\rho_0} D_{th} (\nabla \xi)^2 \tag{5.10}$$

with ρ_0 the initial density of the cold gas and D_{th} the thermal diffusivity. Figure 5.26 shows the scalar dissipation rate in mixture fraction space for cases A and C. Cases B and D are qualitatively similar to case A. The scalar dissipation rate spans a wide range of values. This is expected given the non-uniform mixture fraction field with peaks at droplet locations. In particular, scalar dissipation samples very large values at rich mixture fractions. Those high values are due to the very high gradients of mixture fractions created by the evaporating droplets. Fig. 5.27 shows the scatter of heat release rate against scalar dissipation rate, coloured by mixture fraction. In case A, heat release peaks at about 200s^{-1} and tends to become low at high scalar dissipation rates. However, there does not seem to be a clear correlation between heat release rate and scalar dissipation at a given mixture fraction. In case C, negative heat release rate related to pyrolysis occurs at rich values, concentrated in moderate values of the scalar dissipation, (below 3000s^{-1}).

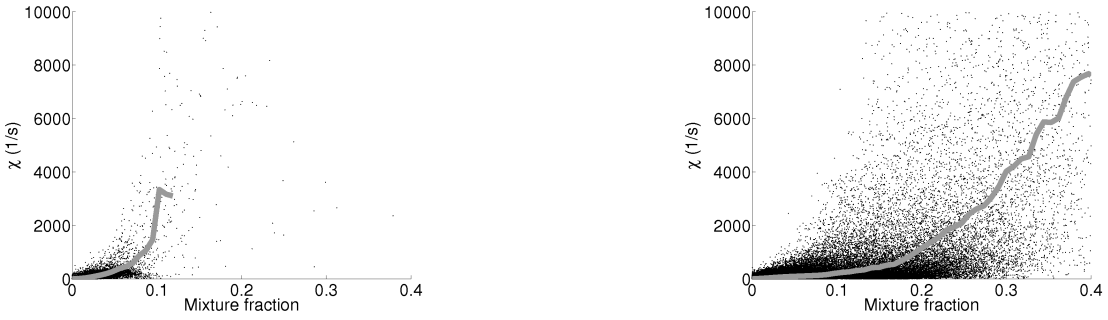

(a) (b)

Figure 5.26: Scatter plot of scalar dissipation rate *vs.* mixture fraction at $t = 2.5t_{sp}$ for (a) case A, (b) case C. The plain grey line shows conditional average.

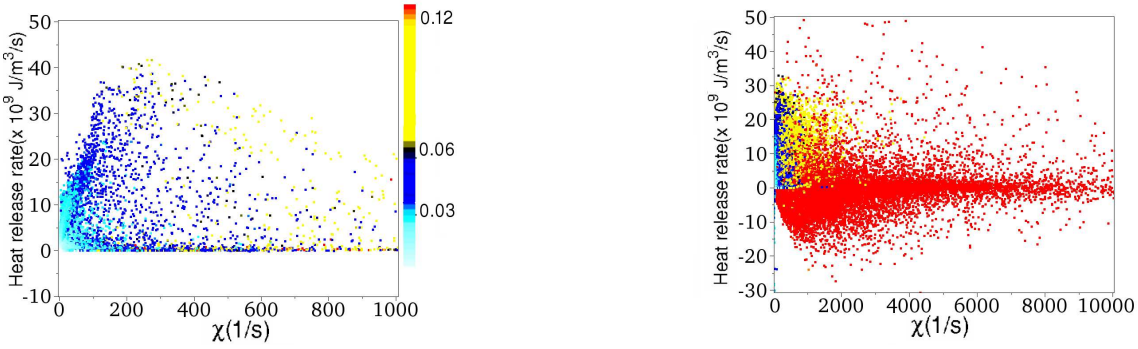

(a) (b)

Figure 5.27: Scatter plot of Heat release rate *vs.* scalar dissipation rate at $t = 2.5t_{sp}$ for (a) case A, (b) case C. Points are colored according to mixture fraction.

5.3.7 Flame propagation in cases A and D

The information collected suggests that cases A and D have the same behaviour, that is with lean interdroplet spacing and localised combustion, see Section 5.3.1. In addition, it was shown in Section 5.3.5 that heat release occurs also in mixtures that are below the lean flammability limit. In order to understand further this ignition process, quantities are examined at the droplet scale. Case A is considered.

Figure 5.28 shows the development of local droplet flames in a zone contained within 2 spark radii from the spark location. This region roughly corresponds to the zoomed view of Fig. 5.2b. The ignition of individual droplets and small clusters of droplets can be observed. The generation of a spherical contour of heat release around the droplet denoted D1 can be observed. D1 burns alone during most of the simulation. At the end of the simulation, the heat release contour around D1 starts spreading to a neighbouring droplet that has moved close to D1. The flame around the droplet denoted D2 rapidly expands to a neighbouring droplet D3 at $t = 2.04t_{sp}$. Finally, in the top right of the pictures, the heat release rate generated in the small group of droplets seems to propagate quickly. Interestingly, these findings can be associated with the experimental observation of Mikami et al. [54] who worked on flame spread in arrays of n-decane droplet. In Section 2.2.2, we described the three

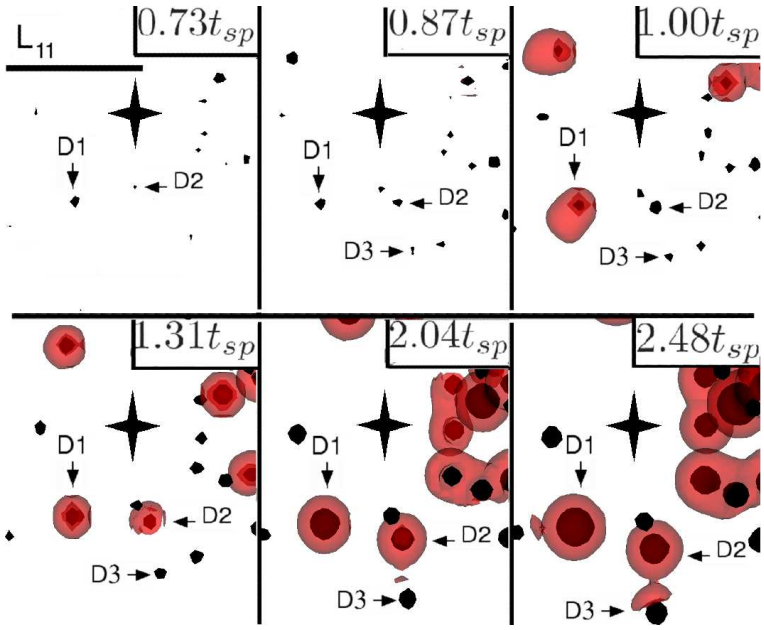

Figure 5.28: Ignition of droplets D1, D2 and D3 for case A. The heat release rate iso-surface $5 \times 10^9 J/s/m^3$ is shown in red while the stoichiometric mixture fraction iso-surface is shown in black. Small spheres show droplets locations while the central cross shows the centre of the spark. The initial integral length scale L_{11} is shown for reference.

modes of flame spread observed in that experiment. During most of the simulation, droplet D1 belongs to their mode 3 where the next droplet is relatively far. At the end of the simulation, a droplet comes close to the flame surrounding D1 which starts spreading. Droplet D2 belongs to their mode 2 where the diffusion flame reaches the fuel generated by the next droplet D3. Finally, the small group of droplets is characterised by their mode 2 and also by their mode 1, where the diffusion flame of one droplet surrounds the next one. The fact that the droplet distribution in our problem is random, and that the droplets move in space, results in the fact that all these different modes of flame spread are being observed simultaneously.

Figure 5.29 depicts contours of mixture fraction and heat release rate in a plane that passes through droplets D2 and D3. We can see that the contour of low heat re-

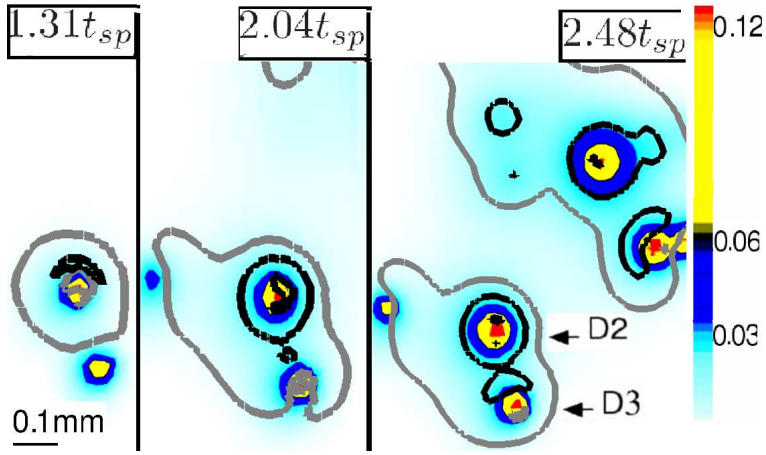

Figure 5.29: Focused view of contours of mixture fraction on a plane containing droplets D2 and D3 for case A. Black line and grey line are, respectively, heat release rate iso-surface $5 \times 10^9 J/s/m^3$ and $5 \times 10^8 J/s/m^3$.

lease rate (5×10^8J/m^3/s) is larger than that of high heat release rate (5×10^9J/m^3/s). The contour of low heat release samples very low mixture fractions. This illustrates the very lean combustion mentioned in Section 5.3.5. The figure additionally shows that lean burning occurs only in the neighbourhood of a contour of high heat release rate. It is possible that the combustion of nominally non-flammable mixtures is facilitated by the diffusion from mixtures burning intensively, a phenomenon also associated with stratified premixed flame propagation (e.g. see Section 3.4.1. of Ref. [4]). In addition, the diffusion of the spark heat may also help igniting such lean mixtures. The figure also shows how the contour of high heat release rate propagates from D2 to D3 in a narrow zone between the two droplets.

In order to demonstrate more details on the physics of droplet ignition and flame spread, attention is now focused on droplets D1, D2 and D3. Figure 5.30, 5.31 and 5.32 show the variation of temperature, heat release and different species near droplet D1, D2 and D3 respectively at different instants.

First, droplet D1 is considered. The data is plotted along a line originating at the droplet location and passing through the spark centre. Figure 5.30b shows how

the energy released by the spark increases the temperature near the droplet for $t \leq t_{sp}$. Consequently evaporation is enhanced and the mixture fraction at the droplet location builds up as shown by Fig. 5.30c. The generation of fuel at high temperature results in ignition. Figure 5.30a shows that at $t = 0.73t_{sp}$, heat release becomes finite and negative, although it is hard to see on the scale of the graph. The occurrence of negative heat release is related to fuel chemical break-up mentioned earlier and occurs only at the front of the droplet (i.e. towards the spark) where the temperature is highest. The next instant, $t = 0.87t_{sp}$, exothermic reactions are triggered in front of the droplet while endothermic reactions now occur behind it. At $t = t_{sp}$, exothermic reactions occur both in front and behind the droplet, while endothermic reactions occur at the droplet location where the mixture is slightly rich. At $t = 2.04t_{sp}$, exothermic reactions prevail with heat release peaking near the stoichiometric mixture fraction locations and being lower on the lean and the rich side. Note the dent of temperature at the droplet location caused by evaporation and the suppression of combustion at rich values in Fig. 5.30b. At the end of the simulation, a diffusion flame has established with very low positive heat release rate at the droplet location where the mixture fraction is very rich. Note the large mass fraction of radicals H and OH towards the spark centre in Fig. 5.30g and h. This is due to the concentration of those radicals being substantial in the kernel, as noted in Section 5.3.3. Therefore, the flame surrounding a droplet has the characteristics of a spherical diffusion flame with a heat sink on the rich side due to evaporation and substantial radicals concentration on the kernel side.

Figure 5.31 shows data plotted along a line originating at the D2 droplet location and passing through the spark centre. Droplet D2 has an initial ignition behaviour similar to that of D1, that is endothermic reactions followed by exothermic heat release rate and finally a diffusion flame surrounding the droplet. However, the initiation of chemical reactions in the vicinity of D2 is delayed compared to D1. Figure 5.30b shows that the temperature near droplet D1 rises faster and reaches higher value than that of D2 in Fig. 5.31b because D1 is closer to the spark location than

D2. Furthermore, the propagation of the flame from droplet D2 to the neighbouring droplet D3, mentioned above, can be observed at the end of the simulation as a third, smaller peak of heat release at the rear of D2, but also as secondary peaks of C_2H_4 and other intermediates mass fractions (e.g. CH_4, C_3H_4, CH_2O) not shown here. However, this flame spread cannot be properly described in Fig. 5.31 because the spark centre, D2 and D3 are not aligned.

In order to observe the ignition behaviour of droplet D3, Fig. 5.32 shows data along a line originating at droplet D3 and passing through D2. The locations of D3 and D2 are given in Fig. 5.32c by a peak of mixture fraction at the origin and a second peak at positive coordinates respectively. The second peak is not fixed in space due to the relative motion of the two droplets. Figure 5.32a shows that at $t = 1.31t_{sp}$, substantial heat release occurs near D2. However, no heat is produced near D3 despite nominally flammable values (i.e. $\xi_L \leq \xi \leq \xi_R$) at that location. This is not surprising since D3 is further from the spark and experiences a lower temperature. D3 has not ignited yet. In addition, it is interesting to note that at $t = 1.31t_{sp}$, heat release occurs in the interdroplet spacing, despite a very lean mixture ($\xi < \xi_L$) there. This cannot be only attributed to the high temperature caused by the spark. We already observed in Fig. 5.29 that heat release occurs in very lean zones, but only near regions with high heat release rate. Hence, we suggest that diffusion of heat and reactive species from the combustion of droplet D2, and from the spark's heat, helps combustion in the lean interdroplet spacing. Between $t = 1.31t_{sp}$ and $t = 2.48t_{sp}$, we observe the generation of heat (Fig. 5.32a), secondary hydrocarbons (Fig. 5.32e and f) and radicals (Fig. 5.32g and h) in the interdroplet spacing. Meanwhile, the mixture fraction (Fig. 5.32c) in the interdroplet spacing builds up due to evaporation. This allows larger heat release to take place (Fig. 5.32a). At the end of the simulation, a substantial amount of reactive species exists near D3 (Fig. 5.32e, f, g and h) and heat release begins to occur there (Fig. 5.32a). In Fig. 5.33, we show scatter plots of heat release rate in mixture fraction space in a sphere centred on D2 and containing D3 at $t = 2.5t_{sp}$. The graph clearly

shows a burned branch, a "frozen" branch and some intermediate points at lean mixtures. The rich branch corresponds to the burning droplet D2, the "frozen" branch corresponds to the unignited mixture near D3 and the intermediate states to the burning occurring in the interdroplet spacing.

The above analysis suggests that a mechanism for flame propagation in case A is the diffusion of heat and reactive species from a burning droplet to a cold evaporating droplet through an inter-droplet region of very lean mixtures. The visualization of the reaction zones in Fig. 5.28 and 5.29 shows flames around 0.1mm thick (approximate distance between iso-surface of heat release 5×10^8J/m^3/s and 5×10^9J/m^3/s), highly curved, with surfaces shifting due to sequential droplet ignitions, the turbulence, and the relative droplet motion.

The examination of the ignition and the propagation of local droplet flames in case A can be related the observations discussed above. The "frozen" branch of Fig. 5.24 corresponds to evaporating unignited droplets. The hot branch corresponds to diffusion flames established around droplets. The intermediate state between the "frozen" and the burned state correspond to the transient ignition of droplets and to the combustion of the lean interdroplet region assisted by the diffusion from burning droplets. This qualitative description is also valid for case D.

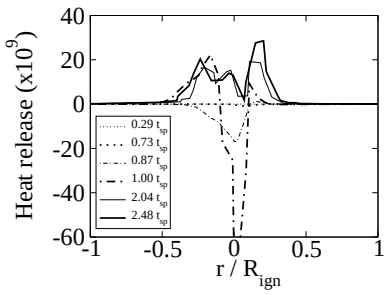

(a) Heat release rate

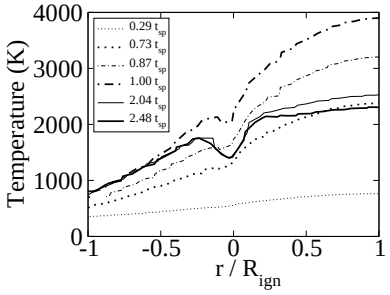

(b) Temperature

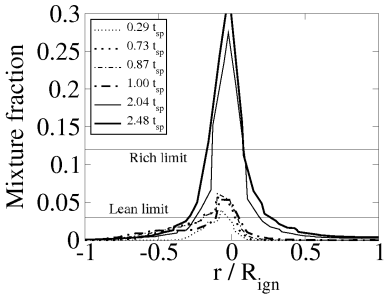

(c) Mixture fraction

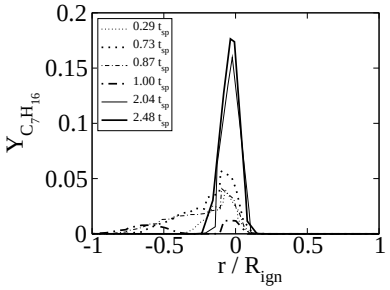

(d) $Y_{C_7H_{16}}$

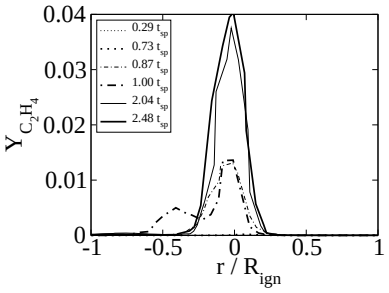

(e) $Y_{C_2H_4}$

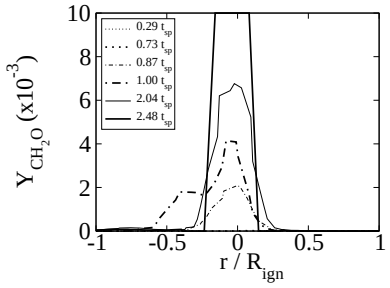

(f) Y_{CH_2O}

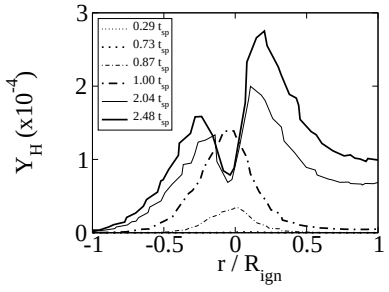

(g) Y_H

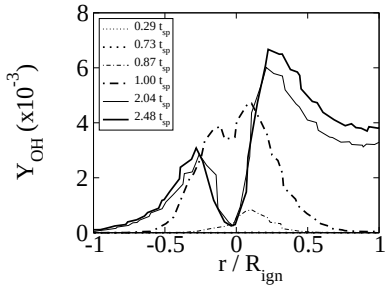

(h) Y_{OH}

Figure 5.30: Profiles along a line passing through droplet D1 ($r/R_{ign} = 0$) and the spark centre ($r/R_{ign} = 1$) of (a) Heat release rate, (b) Temperature, (c) Mixture fraction, (d) $Y_{C_7H_{16}}$, (e) $Y_{C_2H_4}$, (f) Y_{CH_2O}, (g) Y_H, (h) Y_{OH}.

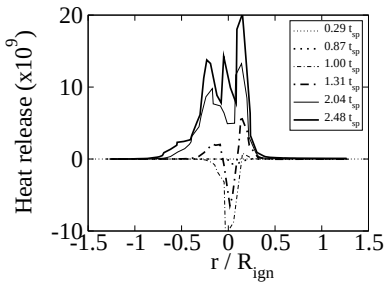

(a) Heat release rate

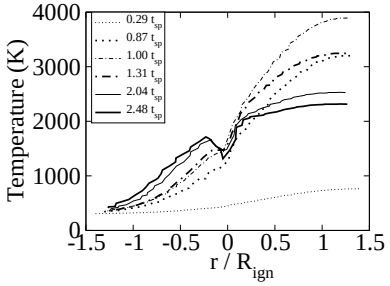

(b) Temperature

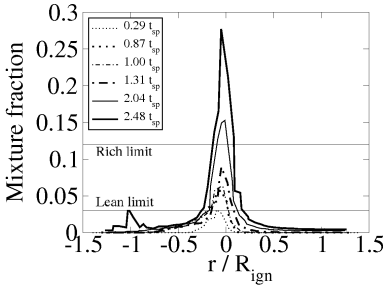

(c) Mixture fraction

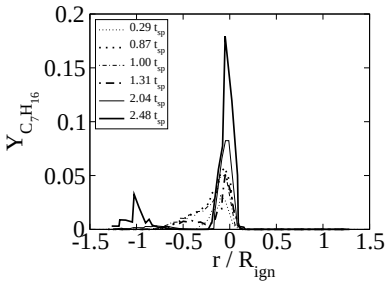

(d) $Y_{C_7H_{16}}$

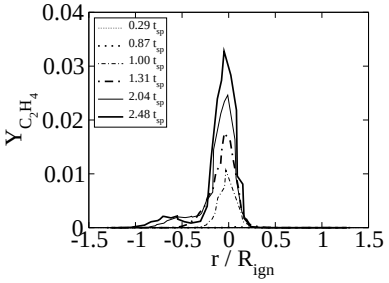

(e) $Y_{C_2H_4}$

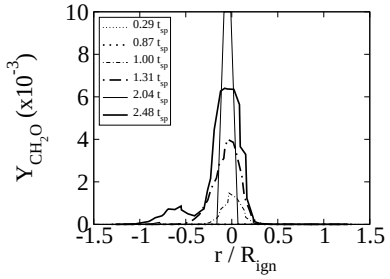

(f) Y_{CH_2O}

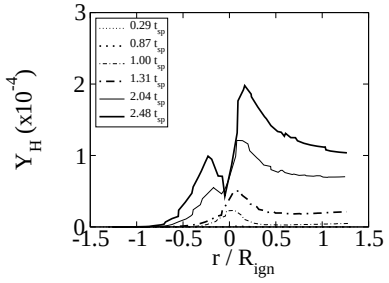

(g) Y_H

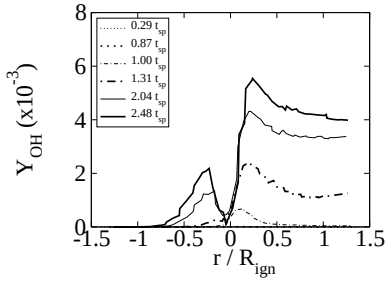

(h) Y_{OH}

Figure 5.31: Profiles along a line passing through droplet D2 ($r/R_{ign} = 0$) and the spark centre ($r/R_{ign} = 1.5$) of (a) Heat release rate, (b) Temperature, (c) Mixture fraction, (d) $Y_{C_7H_{16}}$, (e) $Y_{C_2H_4}$, (f) Y_{CH_2O}, (g) Y_H, (h) Y_{OH}.

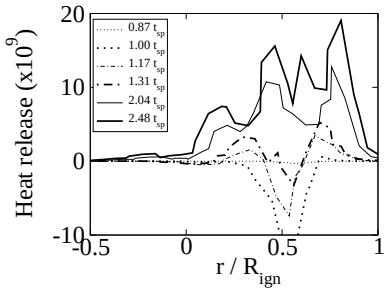

(a) Heat release rate

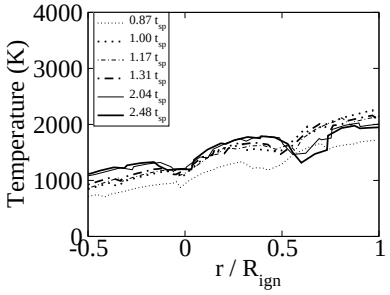

(b) Temperature

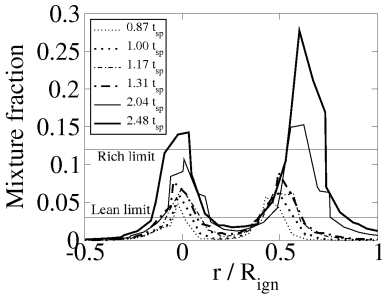

(c) Mixture fraction

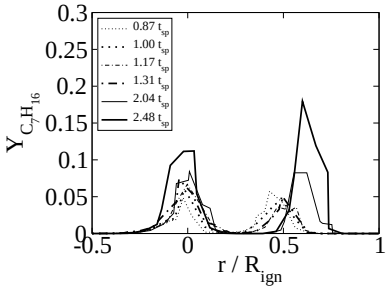

(d) $Y_{C_7H_{16}}$

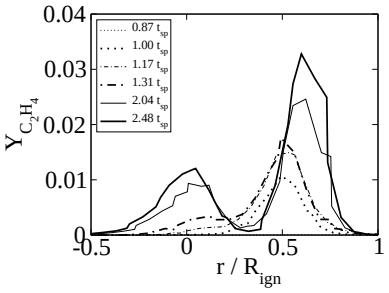

(e) $Y_{C_2H_4}$

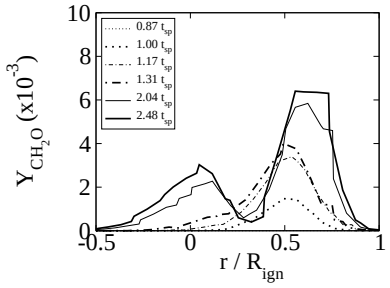

(f) Y_{CH_2O}

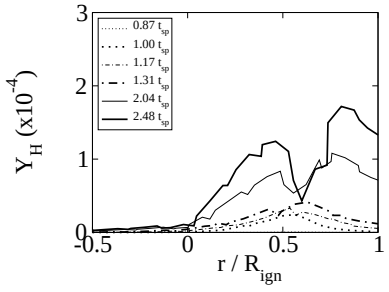

(g) Y_H

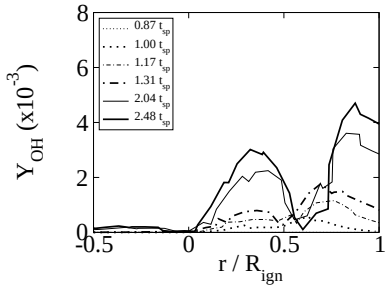

(h) Y_{OH}

Figure 5.32: Profiles along a line passing through droplet D3 ($r/R_{ign} = 0$) and droplet D2 of (a) Heat release rate, (b) Temperature, (c) Mixture fraction, (d) $Y_{C_7H_{16}}$, (e) $Y_{C_2H_4}$, (f) Y_{CH_2O}, (g) Y_H, (h) Y_{OH}.

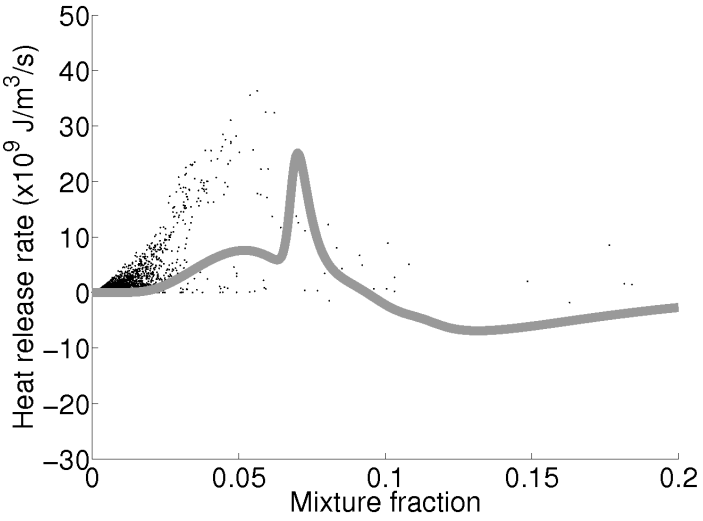

Figure 5.33: Scatter plot of heat release rate *vs.* mixture fraction in a sphere centred at droplet D3, with radius R_{ign} at $t = 2.5t_{sp}$. The grey line is the heat release rate profile in mixture fraction space for the 1D non-premixed flame, magnified 100 times.

5.3.8 Flame propagation in case C

Figure 5.34 shows contours of mixture fraction and heat release rate in a plane that passes through the spark centre for case C. It corresponds to a 2D cut of the magnified view in Fig. 5.4b. The propagation of the reaction zone through the stratified field, from the rich burned mixture to the lean cold mixture can be observed. As the flame approaches the cold gas, the mixture fraction increases beyond the nominal lean flammability limit. This enables high heat release and further propagation of the flame. The contours of high heat release rate are roughly in the region $0.03 \leq \xi \leq 0.12$. Note that the inhomogeneous mixture fraction causes wrinkling of the reaction zone surface. Moreover, we notice that the contours of low heat release rate are much wider than that of high heat release rate. They span a large range of mixture fractions and extend to very lean mixtures. As suggested by [4], in stratified propagating flames, the diffusion from highly flammable burning material can help the combustion in neighbouring fluid with mixture fractions below

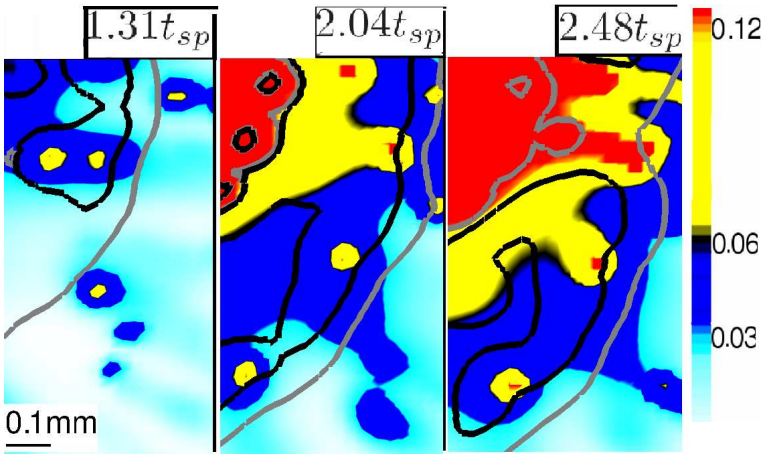

Figure 5.34: Contours for case C of mixture fraction on 2D Slice passing through the centre of the domain of the magnified view in Fig. 5.4(b). Black line and grey line are, respectively, heat release rate iso-surface $5 \times 10^9 J/s/m^3$ and $5 \times 10^8 J/s/m^3$.

the lean flammability limit. This phenomenon observed in case A is suggested in case C, but at a larger scale.

Based on Fig. 5.34, an interpretation of the scatter plots in Fig. 5.25 is suggested. The "frozen" branch corresponds to fuel evaporating in the cold gas. The burned branch corresponds to the non-premixed character that exists between the hot rich gas and the cold lean gas. This non-premixed character was also observed with 2D DNS and simple chemistry with rich sprays [152]. This non-premixed character is an important property of case C since the conditional averages follow closely the typical 1D non-premixed flame profiles, as mentioned in Section 5.3.5. The intermediate states between the two branches are related to the burning of the stratified mixture as the flame advances. Hence, the flame has features of a stratified structure propagating towards the cold gas and of a global diffusion flame between the burned and the cold gas.

5.3.9 Discussion on the two modes of ignition

In this section, we discuss cases A, C and D which had successful ignition. The results have shown common points between those cases. The flame ignites and propagates in a stratified mixture. Moreover, the heat release rate peaks in regions within the nominal flammability limits. In addition, the diffusion of heat and species from regions of high heat release and the diffusion of heat from the spark facilitates the burning of mixture fraction outside the nominal flammability limits. However, a clear difference was observed between the ignition process of cases A and D and that of case C.

In cases A and D, regions within the nominal flammability limits are confined near droplets while the interdroplet spacing is very lean. This results in local diffusion flames surrounding droplets or group of droplets. This mode is qualified as "droplet ignition mode". In case C, droplets evaporate substantially between the cold mixture and the hot kernel. As a result the interdroplet spacing contains mixture within the flammability limits in the high temperature region and high heat release occurs there. This mode is qualified as "interdroplet ignition mode".

Based on experimental observation of spray flames, Hayashi et al. [57] suggested that the flame propagated in the interdroplet spacing at a rate determined by the interdroplet equivalence ratio. This "effective equivalence ratio" depends on the fuel released by droplets between the cold mixture and the high temperature zone. In Chapter 3, the "effective equivalence ratio" of one-dimensional flames and their flame speed were correlated. The "effective equivalence ratio" was taken as the gaseous equivalence ratio at the peak of heat release rate. Following the same criterion and based on the radial averages in Fig. 5.10 and 5.11, the radial average "effective equivalence ratio" is very low ($\xi < \xi_L$) for cases A and D, in the droplet ignition mode, while it is near 1 for case C, in the interdroplet ignition mode. A measure of the flame speed is not obvious with the present results. However, it was shown in Section 5.3.2 that cases A and D have much lower volume integrated heat release

rate than case C, consistent with their lower "effective equivalence ratio".

It is interesting to analyse those two modes of ignition from the perspective of the group combustion number G. In the review of Ref. [3], it was suggested that one can expect spray autoignition to occur with individual droplet ignition for $G < 1$, but to occur around groups of droplets for $G \gg 1$. Although the Group combustion theory predicted the behaviour of a steady-state cloud of droplets [39], the transient behaviour of the flames studied here is consistent with their group number G (defined in Section 5.2.3). Cases A and D in the droplet ignition mode have a group combustion number less or equal to 1 while case C has a group combustion equal to 6.60, see Table 5.1. The group combustion theory predicts local diffusion flame around droplets or small clusters of droplets at low group numbers, below 1. At high group number, above 10, it predicts that a diffusion flame would surround the cloud of droplets [39]. Although the numerical values which distinguish the various regimes are not strictly respected, the different behaviour observed in our results are consistent with their group numbers.

5.3.10 Statistics of the flame curvature

The detrimental effect of curvature on a kernel growth in a premixed gas is known [2] and has been demonstrated in a recent DNS study of a premixed gaseous kernel [126], in Refs. [93, 99] for gaseous edge flames and in Chapter 4 for edge flames in fine sprays. The main argument is that high curvature results in high heat losses that must be balanced by the heat generated in the reaction zone. The curvature was measured using the mass fraction of Y_{O_2}, as we did in Chapter 4:

$$k_m = \frac{1}{2}\nabla \cdot (\nabla Y_{O_2}/|\nabla Y_{O_2}|) \tag{5.11}$$

The curvature is then normalised by the flame reaction zone thickness $\delta_r = D_{th}/S_{L,0}$. The curvature k_m is conditioned on the iso-surface $Y_{O_2} = 0.19$. It was observed (not shown) that the iso-surfaces of $Y_{O_2} = 0.19$ and the iso-surface of heat release rate $5 \times 10^9 J/m^3/s$, visualised in Fig. 5.1 to 5.5, coincide reasonably well. Hence, we

expect the present definition of the curvature to be representative of the curvature of the reaction zones. A curvature based on heat release rate was not chosen because it would not have a consistent sign. Indeed, heat release rate peaks in the flame and does not decrease monotonously from one side of a premixed or non-premixed flame to the other, as does Y_{O_2}.

Figure 5.35 shows the evolution of the PDF of the normalised curvature for all cases. In the Gas case, the PDF is narrow. As time evolves, the PDF peaks at lower values and becomes wider. At the end of the simulation, it also samples negative curvatures. The curvature decreases mainly because the kernel size increases. In addition, DNS of turbulent premixed kernel expansion have shown that turbulence wrinkles the flame and spreads the PDF of the curvature [13, 27, 154]. This accounts for low negative and high positive curvatures occurring in our simulation. Nonetheless, the effect of turbulence is limited because the duration of the simulation is less than the integral timescale and the kernel remains small compared to the initial integral lengthscale. In Fig. 5.35, the curvature given by the radius of the spark $2/d_{sp}$ is also shown. The radius of the spark is very close to the radius of the iso-surface of temperature $T = 1400K$ for the non-reacting Gas case at $t = t_{sp}$ (see Fig. 5.9e). Hence, this can be interpreted as the curvature of a non-reacting kernel at the end of the spark. However, the flame in the Gas case reacts and is larger at $t = t_{sp}$ than the spark size. As a result, the flame curvature is lower than the value found with the spark radius.

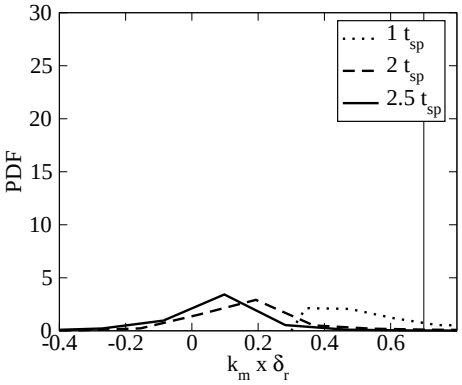

(a) Case A

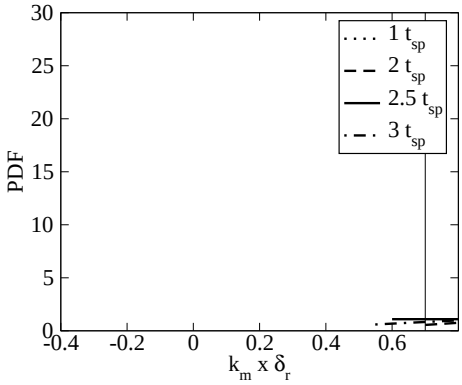

(b) Case B

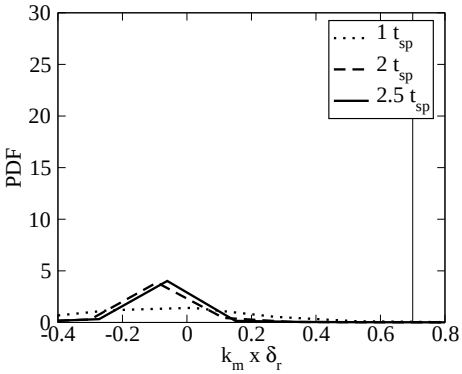

(c) Case C

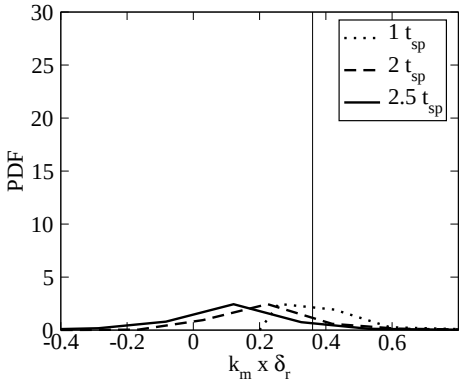

(d) Case D

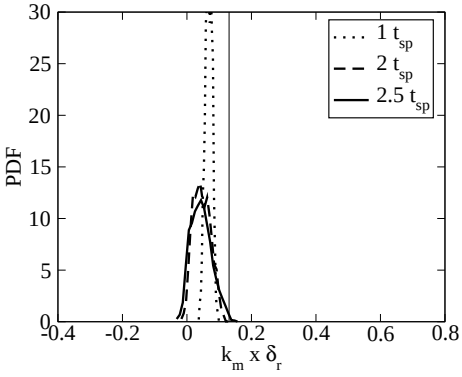

(e) Gas

Figure 5.35: Probability density function of normalised curvature for (a) Case A, (b) Case B, (c) Case C, (d) Case D, (e) Gas case. In (a), (b), (c), (d), the vertical line is $k_m = 2/(5a_d)$. In (e), the vertical line is $k_m = 2/d_{sp}$.

In case A, the curvature is much larger than in the Gas case and the PDF has a wider spread. In addition, the PDF reaches the highest curvatures at $t = t_{sp}$ and samples lower curvatures at $t = 2.5t_{sp}$. Moreover, the PDF becomes wider at $t = 2.5t_{sp}$. In Section 5.3.1 and 5.3.7, reaction zones surrounding droplets were observed. Those droplet flames have a very high curvature. Hence, a much higher curvature than in the gaseous flame, and a different curvature for each droplet flame, are expected. This explains the high curvature and the PDF's width at $t = t_{sp}$. Typically, the radius of a flame surrounding a droplet varies with time between 2 and 10 times the droplet radius [155]. In Fig. 5.35, the value of $2/(5a_d)$ is near the PDF peak at $t = t_{sp}$. Moreover it was noticed in Section 5.3.1 that reaction zones can merge and surround groups of droplets at the end of the simulation, thereby becoming larger. The curvature is expected to be lower there. This explains the reduced curvature at $t = 2.5t_{sp}$. The occurrence of more droplet flames and of group flames also causes the larger width of the PDF.

In case B, the curvature remains high throughout the simulation. This is attributed to the small size and the shrinking of the kernel due to failed ignition. In case D, the PDF follows trends similar to that of case A. Note that the curvature at which the PDF for case D peaks at $t = t_{sp}$ matches fairly well the value of $2/(5a_d)$.

Finally, the PDF of case C is wide and samples both positive and negative values. This cannot be explained by the effect of turbulence alone since the kernel is small. As mentioned in Section 5.3.1, the surface of high heat release resembles that of the Gas case but with much more wrinkling. In Section 5.3.8, this has been attributed to the distorted surfaces of mixture fraction. The wrinkling of the reaction zone induces a wide range of positive and negative curvatures. This accounts for the low mean curvature and the wide PDF.

Hayashi et al. [57] suggested the positive effect of the flame wrinkling by the droplets for the flame propagation rate. It is shown here that in the droplet ignition mode (cases A and D), curvature is high because of the droplet scale, localised reaction zones. In contrast, in the interdroplet ignition mode (case C), only the

stratification of the mixture wrinkles the reaction zone and results in relatively low curvature.

5.4 Summary of main findings

The use of 3D DNS with a skeletal chemical scheme to compute the spark ignition in uniformly-dispersed monosized droplets and homogeneous isotropic decaying turbulence revealed:

(a) That the structure of a spray kernel can be very different from that of a pure gas. Common features between all spray cases were that high heat release rate occurred for mixture fractions within the nominal flammability limits and that non-negligible heat release rate could occur in very lean regions, with $\xi < \xi_L$. This was attributed to the diffusion of heat and species from vigorously burning mixtures ($0.035 \leq \xi \leq 0.12$) and from the spark to very lean mixtures, therefore causing ignition there. Longer simulations are required in order to demonstrate whether this lean burning still occurs when the effect of the spark has fully dissipated.

(b) A relatively dispersed spray (Group Combustion number ≤ 1) resulted in a droplet ignition mode (typical view: Fig. 5.2a) while a denser spray (Group Combustion number equal to 6.60) resulted in an interdroplet ignition mode (typical view: Fig. 5.4a).

(c) With the droplet ignition mode, flammable mixtures were localised near droplets or groups of droplets. First, droplets close to the spark were ignited. If another droplet was close enough, the diffusion of heat and reactive species from the burning droplet through the lean interdroplet spacing could eventually ignite it. Successful flame ignition occurs when droplets are close enough to the source of energy and successful flame propagation occurs when droplets are close enough to each other. Hence, it is expected that a higher number of droplets will ease the flame propagation. At the end of the simulation ($t = 2.5t_{sp}$), the flame was in a transient state with some locally fully burning mixtures (local non-premixed flames

sitting around droplets or groups of droplets), some unburned mixtures (unignited droplets), some intermediate states with igniting droplets and some combustion in the very lean interdroplet spacing facilitated by diffusion and by the spark.

(d) With the interdroplet ignition mode, a substantial amount of fuel was evaporated between the cold and the hot gas. As a result, the interdroplet spacing was within the nominal flammability limits in the high temperature zone. The flame propagated in a stratified mixture towards the cold gas. The reaction zone occupied a large volume and resembled that of a pure gas with extra wrinkling due to the stratification. The mixture was lean in the cold gas and rich in the burned gas. This resulted in a global non-premixed character between burned and cold gas. In the burned gas, pyrolysis of evaporated fuel occurred. This led to substantial concentration of reactive species immediately behind the flame. Most of the features of this flame could be observed from one-dimensional (spherically-symmetric) averages.

(e) The curvature of the reaction zones is high with the droplet ignition mode because of the occurrence of small droplet flames. It is lower with the interdroplet ignition mode because only the mixture stratification wrinkles the large reaction zone.

The present data demonstrate the significant differences between conventional non-premixed and spray combustion and can provide a very challenging test case for turbulent spray flame models. Examination of spray combustion in mixture fraction space through experiment seems very worthwhile.

It can be concluded that realistic simulations can improve the current knowledge of forced ignition in sprays and that the Group Combustion Theory and the laminar flame propagation in a uniform spray are valuable backgrounds for the interpretation of the results.

Chapter 6

A numerical model for the computation of ignition probability

6.1 Introduction

In Section 2.3, it was reported that in turbulent non-premixed flows the calculation of the ignition probability P_{ign} was useful in understanding the behaviour of forced ignition. In Section 2.4, we reviewed evidence that in realistic configurations, the convection of the spark kernel by the turbulent flow had a strong impact on the success of ignition. The flame propagation was shown to be less important (e.g. the small displacement speed in Chapter 4). In this chapter, we propose a model that incorporates the main physical aspects of spark ignition in realistic flows. The model aims at tracking the growth of the flame from the spark to the entire burner and assessing the success of ignition. Results are presented and compared with experiments. This chapter extends and modifies a previous model [7] and incorporates the spray flame speed results of Chapter 3.

Complete CFD methods to compute the evolution of a spark in a non-premixed

environment, such as those based on LES [105, 106, 156], are very expensive if the ignition probability is to be calculated for every possible spark location. In contrast, simpler models [7, 157, 158] are based on the idea of using a cold CFD solution and exploring whether flames could possibly evolve from a particular spark location.

Apart from including sprays, the model in this chapter aims to compute in a very cheap way the ignition probability as a function of space and includes local extinction of the kernel, turbulent diffusion, mean convection, and flame propagation. Flame propagation here is modelled with concepts related to cellular automata.

The cellular automaton approach offers a simple way to compute the propagation of a flame and has been used before for the simulation of premixed turbulent flame [159]. It involves a regular grid of cells, each of which has a finite number of states. For example, each cell can have the state of cold or burned. By defining rules that change the state of the cell from cold to burned, the propagation of a flame can be reproduced. This approach offers cheap computation and a similar concept is adopted in the present work.

First, we introduce the mathematical model that was used. Then we present results computed with the model for three test cases: a methane bluff-body experiment [103], a turbulent counterflow experiment [84], and an industrial combustor geometry [160]. For each case, the computational time required by a desktop machine is given (2 CPU's, each is Xeon X5550 QuadCore @2.67Ghz, 6.4GT/s, 6 GB RAM. DDR2, 1333Mhz). The chapter concludes on the performance of the model and offers guidelines for future improvements.

6.2 Mathematical modelling

6.2.1 Model description: main idea

The model aims at representing a propagating turbulent flame front in flow configurations where the mean convection and the turbulence intensity are more important

than the flame propagation speed. This requirement is satisfied with flows having a recirculation zone (e.g. industrial combustion chambers) but not in jet flows for example. A time-averaged CFD solution of the cold flow is needed as an input for the model.

The present model is based on the following rules:

- The flow is filled with regular "grid cells" with an arbitrary size. These grid cells can have two states, cold or burned. Initially, all grid cells are in the cold state.

- The simulation is initialised by defining a spark volume in the domain. All grid cells that overlap with the spark volume are switched to the burned state and each of them releases a "flame particle".

- A flame particle is tracked with a Langevin model using the cold CFD field. A particle can extinguish according to a criterion based on a Karlovitz number, presented below. When a particle extinguishes, it is no longer computed.

- Every time a particle visits a grid cell in a cold state, the grid cell switches to the burned state and a new particle is emitted at its centre and follows its own random walk.

- Throughout the simulation, the number of cells in a burned state divided by the total number of cells is computed as a function of time. This ratio is named "ignition progress factor" and is given the symbol π_{ign}.

- At the end of the simulation, π_{ign} is compared to a threshold $\pi_{ign,crit}$. If $\pi_{ign} > \pi_{ign,crit}$, ignition of the entire flame is declared to be successful. If not, ignition fails. This step aims to mimic the experimental observation [103, 107] that a significant volume of the mixture in the combustor must ignite for the ignition event to be deemed successful.

- The computation is repeated many times with different realisations. The number of successful ignitions divided by the total number of events gives the ignition probability P_{ign} for this spark location.
- By repeating this calculation for different spark locations, a map of ignition probability is created.

6.2.2 Details of the model

The equations for the particle motion were described in Richardson's thesis [7] and are repeated here for completeness. Particles are tracked in the CFD solution of the cold flow containing averaged turbulent quantities. The CFD solution can be generated either with a RANS or by averaging a LES over time. The CFD field is then interpolated on a Cartesian grid, the resolution of which is that of the CFD solution. The choice of a Cartesian grid makes the particle tracking easier. The particle position in direction i evolves according to the stochastic differential equation:

$$dX_{p,i} = U_{p,i}dt \tag{6.1}$$

where $U_{p,i}$ is the particle velocity in direction i. $U_{p,i}$ follows the simplified Langevin model [161] and consists of a linear drift towards the local Favre averaged velocity of the flow and an added isotropic diffusion term:

$$dU_{p,i} = -(\frac{1}{2} + \frac{3}{4}C_0)\omega_p(U_{p,i} - \widetilde{U}_i)dt + (C_0\epsilon_p dt)^{1/2}N_{p,i} \tag{6.2}$$

where $\widetilde{U}_i$ is the local Favre averaged velocity in direction i, $N_{p,i}$ is a normally distributed variable (with mean zero and variance unity), C_0 is a constant assumed equal to 2.0 [161], ϵ_p is the turbulent dissipation at the particle location and ω_p is the inverse turbulent timescale at the particle location $\omega_p = u'_p/L_{turb,p}$, $u'_p = (2/3k_p)^{1/2}$ with k_p the local turbulent kinetic energy and $\epsilon_p = k_p\omega_p$. The random variable $N_{p,i}$ for one particle is independent from another (the velocity correlation between

particles is ignored). Hence, particles are simply convected by the turbulent flow and undergo random walk to model their dispersion.

Whether such a tracer particle can represent a flame element depends on the relative importance of flame propagation by molecular diffusion compared to turbulent dispersion. But neglecting propagation for the movement of the particle is not a bad assumption if the flame propagation speed is a fraction of the turbulence intensity. This assumption is supported by the results of Chapter 4 where it was shown that the propagation speed in non-premixed flows (gaseous or fine sprays) is low, of the order of the laminar flame speed.

At the end of each time step, a criterion based on a Karlovitz number is used to assess if the particle extinguishes. A Karlovitz number Ka_p is defined for each particle and is compared to a critical value Ka_{crit}. If $Ka_p > Ka_{crit}$, the particle extinguishes. Ka_p is defined as the ratio between the chemical time and the reciprocal eddy lifetime [162]:

$$Ka_p = 0.157 \left(\nu \frac{(u'_p)^3}{L_{turb,p}} \right)^{1/2} \frac{1}{S_{L,p}^2} \tag{6.3}$$

where ν is the mixture kinematic viscosity, taken as $1.57 \times 10^{-5} m^2/s$ and $S_{L,p}$ is the laminar flame speed, detailed below. The critical value Ka_{crit} was found by Abdel-Gayed and Bradley to be 1.5 for premixed flows [162]. It must be pointed out that the flows studied are not premixed. However, the physics incorporated in the Karlovitz number Ka, i.e. the comparison between chemical and turbulent timescale, is governing the growth of a kernel [1] while its simplicity makes it an easy quantity to use.

The laminar flame speed $S_{L,p}$ in a pure gas is a simple function of the gaseous mixture fraction ξ_p of the particle. The mixture fraction of a particle is governed by the equation:

$$\frac{D\xi}{Dt} = D\nabla^2\xi + (1-\xi)\frac{\Gamma_m}{\rho} \tag{6.4}$$

where D is the fuel mass diffusivity, ρ is the local flow density while Γ_m is the

mass source term due to evaporation. The corresponding stochastic differential equation assuming interaction by exchange with the mean [161], and applying the mean evaporation rate from the local CFD cell, is given by:

$$d\xi_p = -\frac{1}{2}C_\xi\omega(\xi_p - \widetilde{\xi})dt + (1-\xi_p)\frac{\bar{\Gamma}_m}{\bar{\rho}}dt \tag{6.5}$$

where ξ_p is the particle mixture fraction and $\widetilde{\xi}$ is the local Favre averaged mixture fraction of the flow. C_ξ is a constant taken equal to 2.0 [161]. The advancement of ξ_p enables the calculation of $S_{L,p}$ in a pure gas and in turn of Ka_p. The computation of $S_{L,p}$ in a spray is presented in Section 6.2.4.

The initial velocity of each particle is a random Gaussian variable with a rms equal to the local turbulent intensity. The initial mixture fraction of each particle follows a beta pdf with mean and rms coming from the local CFD solution. Different realisations are obtained by setting different random distributions. The beta pdf for the resolved gaseous mixture fraction is used even in presence of droplets, although this is not necessarily a good approximation [130].

6.2.3 Initialisation of the grid cells

In this approach, the maximum number of particles computed during a time step is given by the number of grid cells. In addition, grid cells in positions outside the flammability factor F (defined in Section 2.3.1) are not likely to be switched on, since particles entering such a region rapidly extinguish. It is therefore acceptable to consider only grid cells in the region where $F > 0.1$. This allows a reduction of the computational cost. Further reduction can be obtained by increasing the grid spacing, i.e. reducing the number of grid cells. A requirement on the cell size is derived next.

The fact that a particle is set into motion at the cell centre when it is switched to the burned state reproduces a mechanism of propagation. In order to resolve this mechanism of propagation, a minimum grid spacing is required. Consider a one

dimensional grid of cells all in the cold state. Let us assume uniform turbulence intensity, uniform mixture fraction and no mean flow. From Eq. 6.2, the motion of particles is controlled by the turbulence. Let us now consider that one cell switches to the burned state. The particle generated at its centre has a high probability of travelling a distance less than $(C_0\epsilon_p dt)^{1/2}dt$ during a time dt (see Eq. 6.2). Hence, in order to ensure the propagation of this one dimensional flame element, the next cell centre must be at a maximum distance of $2(C_0\epsilon_p dt)^{1/2}dt$. When meeting that requirement, the particle can enter the next cell volume and generate a new particle. Note that this propagation is controlled only by turbulence and does not include flame propagation by molecular diffusion. In addition, the effect of gas expansion which can accelerate the displacement of the flame front is neglected.

A drawback of this model is that once a grid cell has burned, it never returns to the cold state, since the CFD solution is frozen in time and reactants replenishment is not included. Thus, extinction of grid cells are not captured.

6.2.4 Flame speed calculation

The calculation of S_L, necessary to solve Eq. 6.3, requires special attention. For methane, a curve that fits experimental data, e.g. Ref. [163], is used within the flammability limits. The values for methane lean limit, rich limit and stoichiometric mixture fraction are respectively $\xi_L = 0.028$, $\xi_R = 0.089$ and $\xi_{st} = 0.055$ [121]. Outside the flammability limits, Ka_p is fixed to 10^6. However, in a spray, the flame speed is no longer a simple function of the gaseous mixture fraction ξ. In a uniform monodisperse spray, the flame speed depends on the local overall equivalence ratio ϕ_0, the droplet diameter a_d and the vapour fraction $\Omega = \xi/\xi_0$.

In Fig. 3.6 and 3.9 of Chapter 3, curves of flame speed against ϕ_0 were plotted for different droplet diameter a_d for n-heptane, n-decane at atmospheric conditions and n-decane at high altitude "relight" conditions. For those results, Ω was relatively small and is assumed to be 0. An expression for the flame speed S_L as a function

of ϕ_0, a_d and Ω has been fit to the data:

$$S_L = S_{L,max}\frac{2.5}{\sqrt{2\pi}}\exp\left(-\frac{(\phi_0-\mu)^2}{2\sigma^2}\right) \quad (6.6)$$

The flame speed is determined by the three parameters $S_{L,max}$, μ and σ. For pure gas, $S_{Lg,max} = 1.01S_{L,0}$ ($S_{L,0}$ is the gaseous laminar flame speed at stoichiometry), $\mu_g = 1.07$ and $\sigma_g = 0.33$. If $\phi_0 \leq 0.5$, the flame speed is set to zero. For $a_d \leq 5\mu m$, we assume that the spray flame speed is identical to the gaseous one, $S_{L,max} = S_{Lg,max}$, $\mu = \mu_g$ and $\sigma = \sigma_g$. For $a_d > 5\mu m$, we use the following expressions:
For n-heptane:

$$\begin{aligned} S_{L,max}(\Omega=0)/S_{L,0} &= -0.0417(\ln(a_d))^3 - 1.4337(\ln(a_d))^2 - & (6.7)\\ & \quad 16.2853(\ln(a_d)) - 60.0304 & (6.8)\\ \mu(\Omega=0) &= 0.2791(\ln(a_d))^3 + 10.3696(\ln(a_d))^2 + & (6.9)\\ & \quad 127.9209(\ln(a_d)) + 525.12998 & (6.10)\\ \sigma(\Omega=0) &= 0.2094(\ln(a_d))^3 + 7.6078(\ln(a_d))^2 + & (6.11)\\ & \quad 91.9853(\ln(a_d)) + 370.5209 & (6.12) \end{aligned}$$

For n-decane at atmospheric conditions:

$$\begin{aligned} S_{L,max}(\Omega=0)/S_{L,0} &= -0.008985(\ln(a_d))^3 - 0.430032(\ln(a_d))^2 - & (6.13)\\ & \quad 6.286641(\ln(a_d)) - 28.051339 & (6.14)\\ \mu(\Omega=0) &= -0.642446(\ln(a_d))^3 - 20.230655(\ln(a_d))^2 - & (6.15)\\ & \quad 208.8436(\ln(a_d)) - 702.2631 & (6.16)\\ \sigma(\Omega=0) &= -0.411650(\ln(a_d))^3 - 12.993910(\ln(a_d))^2 - & (6.17)\\ & \quad 134.428060(\ln(a_d)) - 453.188390 & (6.18) \end{aligned}$$

For n-decane at high altitude relight conditions (P_0=41.37 kPa, T_0=265 K):

$$\begin{aligned} S_{L,max}(\Omega=0)/S_{L,0} &= -0.0223743(\ln(a_d))^3 - 0.859171(\ln(a_d))^2 - && (6.19)\\ & \quad 10.839922(\ln(a_d)) - 44.034766 && (6.20)\\ \mu(\Omega=0) &= -0.973761(\ln(a_d))^3 - 30.892040(\ln(a_d))^2 - && (6.21)\\ & \quad 322.962590(\ln(a_d)) + 1109.328 && (6.22)\\ \sigma(\Omega=0) &= -0.565936(\ln(a_d))^3 - 17.764570(\ln(a_d))^2 - && (6.23)\\ & \quad 183.278705(\ln(a_d)) - 619.261998 && (6.24) \end{aligned}$$

The coefficients vary linearly between their value at $\Omega = 0$ to their value at $\Omega = 1$ (pure gas):

$$\begin{aligned} S_{L,max} &= (S_{Lg,max} - S_{L,max}(\Omega=0))\Omega + S_{L,max}(\Omega=0) && (6.25)\\ \mu &= (\mu_g - \mu(\Omega=0))\Omega + \mu(\Omega=0) && (6.26)\\ \sigma &= (\sigma_g - \sigma(\Omega=0))\Omega + \sigma(\Omega=0) && (6.27) \end{aligned}$$

Figure 6.1a, b and c shows that for $\Omega = 0$, there is a good agreement between the analytical expression of the flame speed and the numerical data of Chapter 3. The variation of the flame speed profile with Ω for n-heptane and a fixed diameter, $a_d = 100\mu m$ is shown in Fig. 6.1d. As Ω varies between 0 and 1, the flame speed profile relaxes to the gaseous curve.

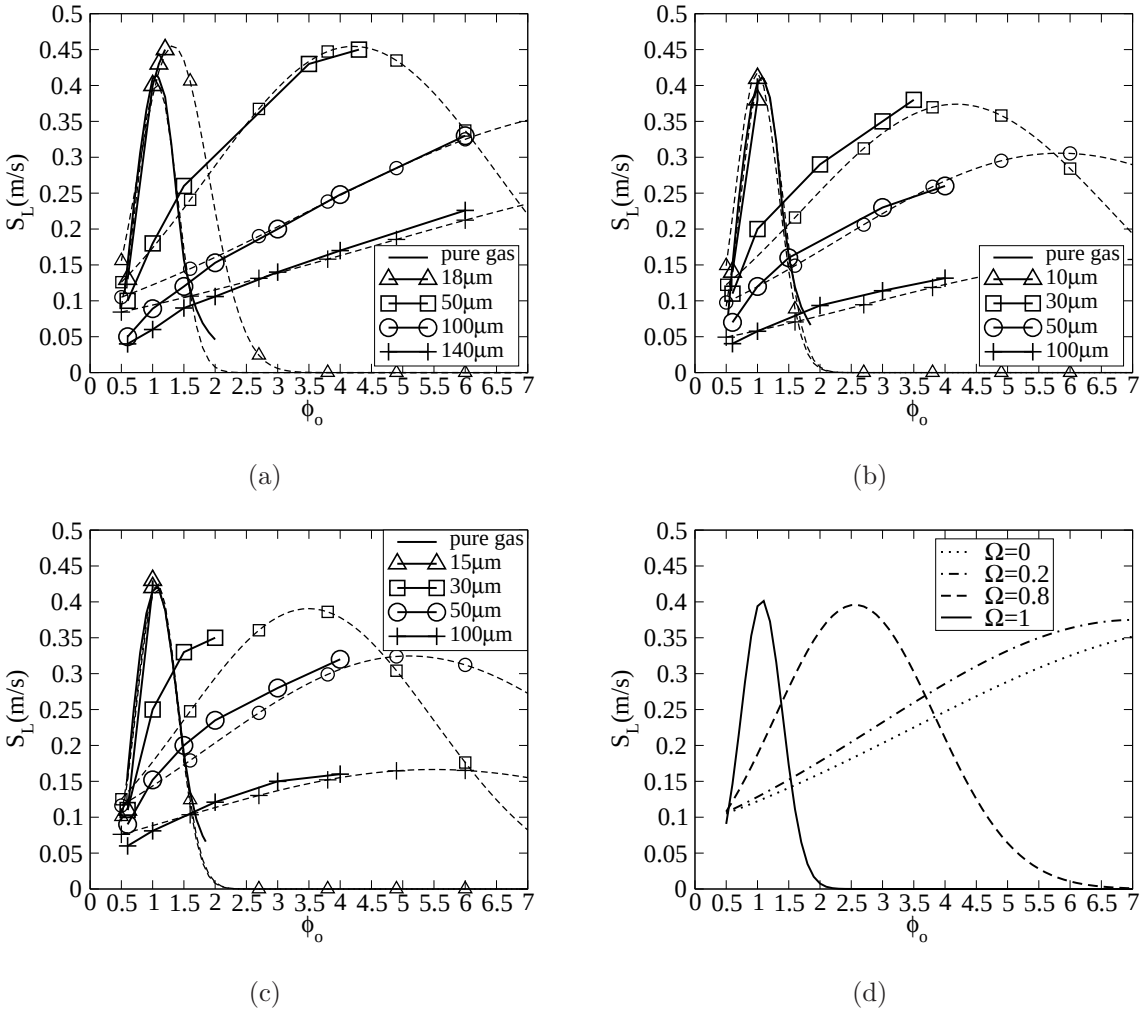

Figure 6.1: Flame speed against ϕ_0 for different initial droplet diameters for (a) n-heptane, (b) n-decane at atmospheric conditions and (c) n-decane at high altitude "relight" conditions (P_0=41.37 kPa, T_0=265 K). Plain lines are results shown in (a) Fig. 3.6, (b) Fig. 3.9a, (c) Fig. 3.9b. Dashed line is computed using Eq. 6.6 with $\Omega = 0$. (d) n-Heptane flame speed against ϕ_0 for different values of Ω with a fixed droplet diameter $a_d = 100\mu m$ using Eq. 6.6.

6.3 Methane Bluff-Body

6.3.1 Numerical setup

In this section, we consider case B of the methane bluff-body experiment of Ref. [103]. A cold LES simulation has been run over 100ms and results were provided by Dr A. Triantafyllidis [105]. The results have been time averaged, producing mean and rms of velocity, mixture fraction and scalar dissipation rate, and can be seen in Ref. [105]. This CFD solution is compared with experiments in Fig. 6.2. The stagnation point corresponds to the symbol I in Fig. 6.2a. Prior to the calculation, the region with $F > 0.1$ is computed and can be observed in Fig. 6.2b. In this zone, grid cells are initialised to the cold state.

The mean turbulence intensity in the region with $F > 0.1$ is about $u' = 2$ m/s. A constant turbulent length scale of $L_{turb} = 5$ mm is assumed [103]. The time step is taken as $dt = 0.5$ ms, lower than the mean turbulent timescale $L_{turb}/u' = 2.5$ ms. One event lasts 60 ms. The spark volume is a sphere of 2 mm diameter, in order to reproduce the experiment of Ref. [103]. Spark centres are located at each CFD cell of a 2D cut of the flow, assuming axi-symmetry. Table 6.1 shows the different configurations studied. Note that in all cases, the grid spacing is lower than the minimum spacing required to resolve the propagation $2(C_0\epsilon_p dt)^{1/2}dt$, based on mean quantities in the region with $F > 0.1$. Under those conditions, the CPU time to compute a map of ignition probability was about 60h.

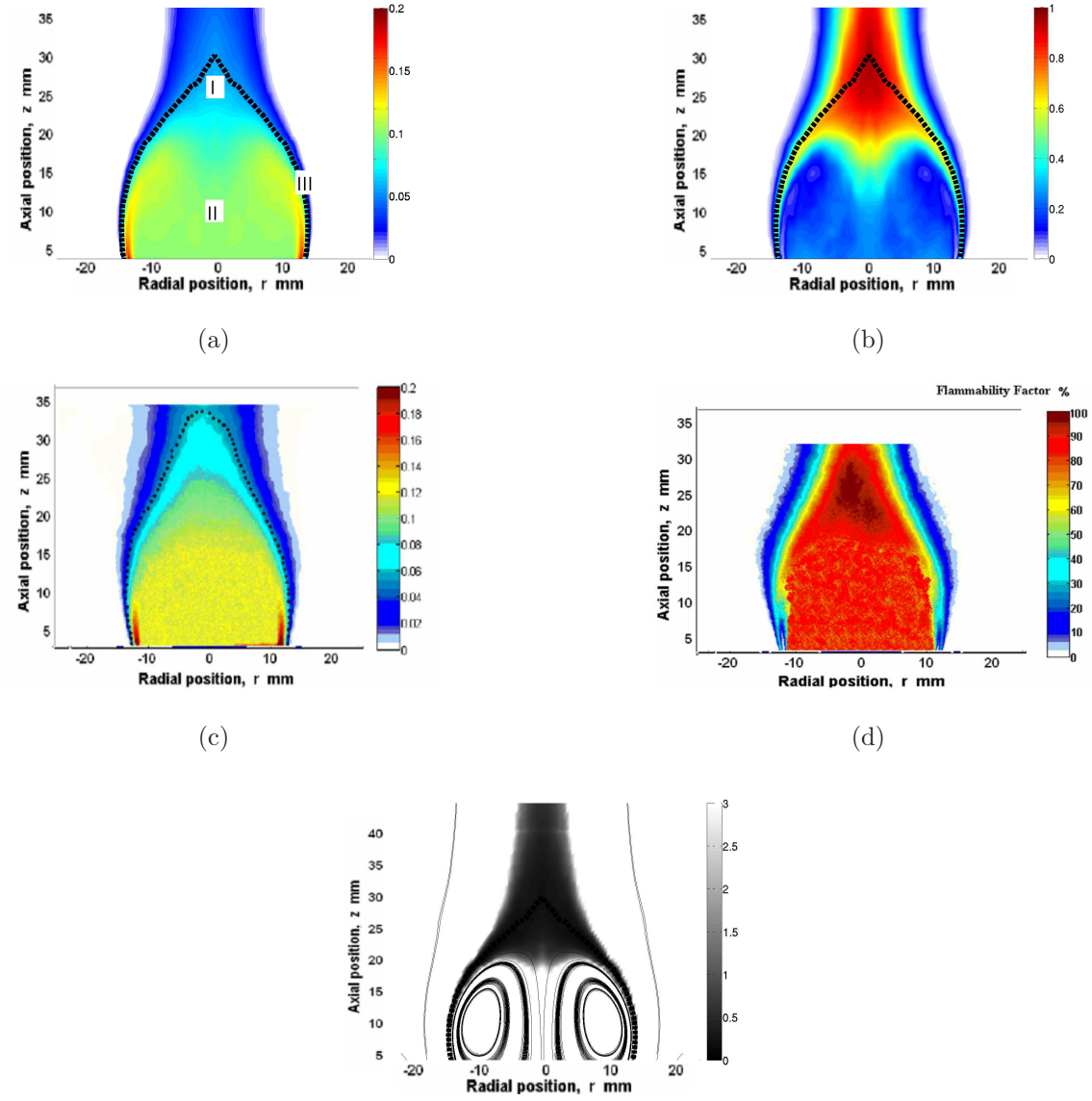

Figure 6.2: (a) LES mean mixture fraction with spark locations I, II and III, (b) LES Flammability factor [105], (c) Experimental mean mixture fraction for case B of Ref. [103], (d) Experimental flammability factor for case B of Ref. [103], (e) Karlovitz number based on averaged LES quantities. The dashed line shows the stoichiometric contour.

Table 6.1: Cases studied for the experiment of Ref. [103]. The value of $(C_0\epsilon_p dt)$ is estimated from the mean turbulence intensity $u' = 2$ m/s and the assumed turbulent length scale $L_{turb} = 5$ mm.

Case	Number of grid cells	Grid spacing
A	25,465	$0.6 \times 2(C_0\epsilon_p dt)^{1/2}dt$=0.9 mm
B	25,465	$0.6 \times 2(C_0\epsilon_p dt)^{1/2}dt$=0.9 mm
C	25,465	$0.6 \times 2(C_0\epsilon_p dt)^{1/2}dt$=0.9 mm

Case	$\pi_{ign,crit}$	Ka_{crit}	Number of events
A	0.05	1.5	50
B	0.07	1.5	50
C	0.05	0.5	50

In the next section, results are presented for π_{ign} and P_{ign}. The effect of the threshold $\pi_{ign,crit}$ and the effect of the critical Karlovitz number Ka_{crit} are investigated. In addition, the key physics that control successful ignition is reported and compared with the experiment [103]. The main experimental findings can be summarised as follows. First, when sparking inside the recirculation zone, the kernel experienced a mixture fraction near the rich flammability limit and a high turbulence intensity. This tended to immediately quench the kernel [103]. Moreover, a spark downstream of the recirculation zone experienced favourable mixture fraction and it was shown that the kernel did not extinguish immediately. However, it had to propagate against the mean flow that convected it downstream. Since the mean axial speed was high, this made ignition difficult [103]. Finally, the highest ignition probability was found on the side of the recirculation zone. The axial velocity moved the kernel along the stoichiometric contour which ignited a substantial length of stoichiometric isoline on its path. This increased the chance that the flame penetrated the recirculation zone and ignited the flow [103].

6.3.2 Results

In this section, data are presented based on the configuration of case A, except when mentioned otherwise. Figures 6.3a, b and c show the time evolution of π_{ign} for all events for spark locations I, II and III, respectively (see Fig. 6.2a). It is interesting to note that the process of ignition lasts between 10ms and 30ms, which is of the same order as in the experiments of Ref. [103]. The ignition probability is the number of curves above a given threshold $\pi_{ign,crit}$ at the end of the simulation divided by the total number of curves. From the graph, it is clear that, at location I, the number of ignited cells is highly variable between spark events. In some events, π_{ign} is low and stops increasing after 5 ms. In other events, π_{ign} increases over 30 ms and reaches much higher values. This results in a high rms of π_{ign} at the end of the simulation. For location II, π_{ign} almost never increases, which implies that a spark never leads to ignition. For location III, the evolution of π_{ign} over time is similar for all events. π_{ign} increases from 0 to a value between 0.07 and 0.09 over 20 ms. Hence, at the end of the simulation, the mean π_{ign} is high and its rms is low. In addition, the graphs indicate that if the threshold $\pi_{ign,crit}$ was moved from 0.05 to 0.07, this would result in a large change in P_{ign} for spark location I but a very small variation for spark location III. The evolution of π_{ign} provides interesting information on the success and the failure of some events, in addition to P_{ign} (to be discussed later).

By placing the spark at various locations and calculating π_{ign} for each of these events, the average of π_{ign} over all events and its rms at the end of the simulation can be calculated and are shown in Fig. 6.4. The average of π_{ign} in Fig. 6.4a is high near the mean stoichiometric contour and much lower inside the recirculation zone. Note that π_{ign} becomes very low above the stagnation point. It is also higher on the side of the stoichiometric contour than on the top. These observations show that on the average, more grid cells are ignited by a spark located near the stoichiometric contour, on the side of the recirculation zone. The rms of π_{ign} in Fig. 6.4b is high

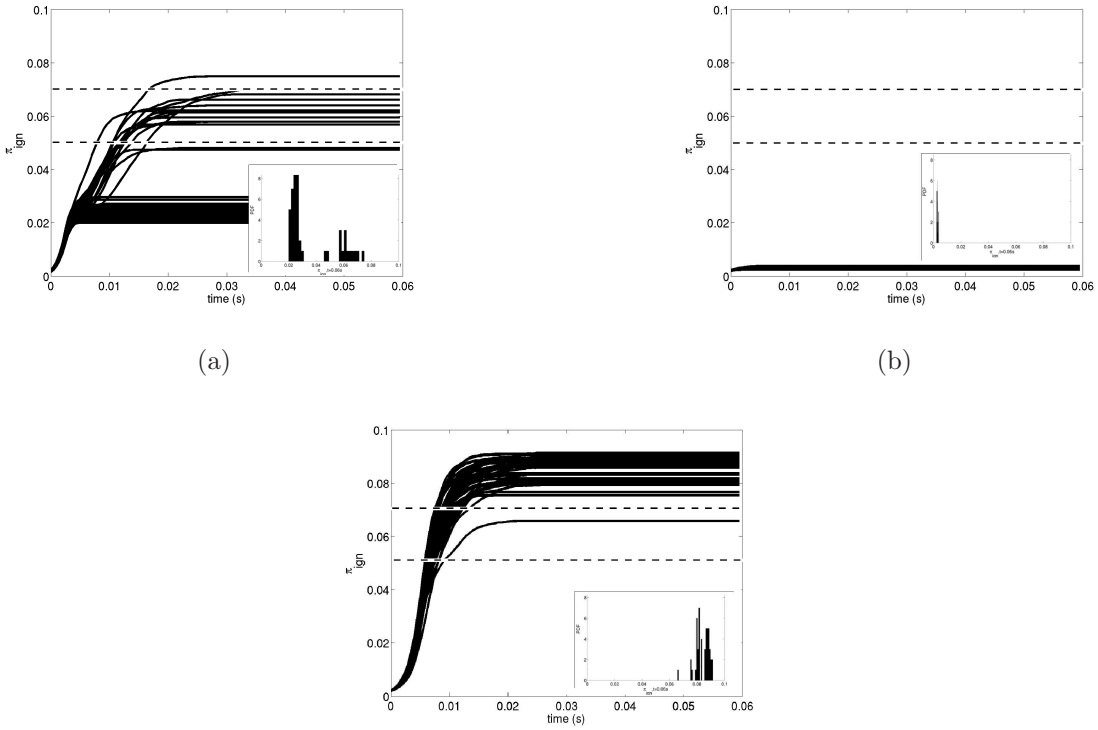

(a)

(b)

(c)

Figure 6.3: Time evolution of π_{ign} of each event for (a) spark I, (b) spark II, (c) spark III. From top to bottom, the dashed lines show $\pi_{ign,crit} = 0.07$ and $\pi_{ign,crit} = 0.05$. On the bottom right of the figure is the PDF of π_{ign} at the end of the simulation.

over two surfaces, near the stoichiometric surface towards the recirculation zone, and near the stoichiometric surface away from the recirculation zone. This corresponds to the shear layer where the mixture fraction has a high variation. The particles inside a spark located there experience very different mixture fractions for different events. If the mixture fraction results in high Karlovitz number, the particles can get easily extinguished. In addition, the rms of π_{ign} is high near the stagnation point. Particles at the stagnation point can be convected downstream in some events or inside the recirculation zone in others. This affects the success of ignition as discussed later. It is clear that by analysing the quantity π_{ign} and its statistics, very interesting insights on the ignition success and its variability can be inferred as

a function of the spark position.

(a) (b)

Figure 6.4: Statistics over 50 events at each spark location at $t = 60$ ms for case A (a) average of π_{ign} , (b) rms of π_{ign}. The dashed line shows the stoichiometric contour.

Figure 6.5 shows the field of ignition probability P_{ign} (defined as number of events giving $\pi_{ign} > \pi_{ign,crit}$) at 60 ms for cases A, B and C (Table 6.1). In all cases, P_{ign} is large near the stoichiometric contour only. Note the similarity between the region of large ignition probability and that of low averaged Ka in Fig. 6.2e. However, above the stagnation point of the recirculation zone, the ignition probability is small despite the low averaged Ka. This is because most particles are convected away and therefore do not ignite a substantial part of the combustor. In Fig. 6.5a, b and c, it is evident that the threshold $\pi_{ign,crit}$ has an effect on the ignition probability. For $\pi_{ign,crit} = 0.07$, the region of high ignition probability is restricted to the side of the recirculation zone. Furthermore, by comparing Fig. 6.5a and c, we observe the effect of changing Ka_{crit}. The configuration with $Ka_{crit} = 0.5$ has a much lower ignition probability than the configuration with $Ka_{crit} = 1.5$. This is expected since a lower Ka_{crit} implies that particles extinguish more easily. In case C, P_{ign} is finite only on the side of the recirculation zone. Hence, the region of favourable ignition is consistent for the different threshold Ka_{crit} and $\pi_{ign,crit}$, although the value of P_{ign} varies.

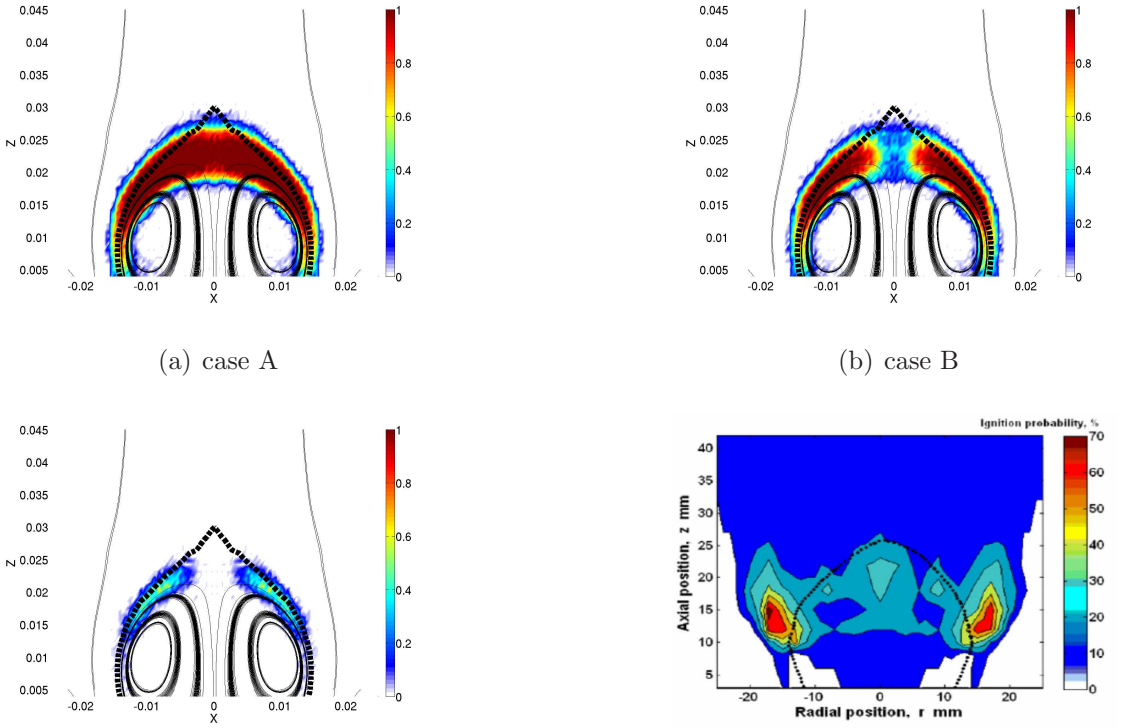

(a) case A

(b) case B

(c) case C

(d) Experiment

Figure 6.5: Ignition probability maps for (a) case A, (b) case B, (c) case C, (d) Experimental results for case B of Ref. [103]. The dashed line shows the stoichiometric contour. See Table 6.1 for details on cases A, B and C.

Comparison with experimental results, Fig. 6.5d, shows that the simulation captures reasonably the region with high ignition probability, on the side of the recirculation zone near the mean stoichiometric contour. In Ref. [103], it is suggested that ignition is likely to occur there because the flow convects the kernel along the stoichiometric isoline, igniting substantial material which helped flame propagation. The visualisation of individual events provides more evidence that experimental trends are reproduced and are presented next.

Figures 6.6, 6.7, 6.8 and 6.9 show the time evolution of the computed particles for different spark events at locations I, II and III. In the figures, the blue particles show the position of grid cells which are still in a cold state. The other colours

represent particles that have been released by a cell when it switched to the burned state. Green particles are those that are still being computed. Red particles are those that have extinguished. Since these pictures represent the propagation of the burned state of the grid cells, it can be compared to Fig. 14, 15, and 16 of Ref. [103] that give typical flame evolution images.

In Fig. 6.6, we can notice that immediately after ignition, a large portion of ignited particles are convected downstream while others penetrate the recirculation zone. If the spark is generated further downstream (not shown here), the particles are systematically convected downstream leading to failed ignition. This can be related to the fact that in Fig. 6.5 the ignition probability is very low downstream of the stagnation point. Figure 6.7 shows a different realisation for the spark location I. It is interesting to note that in this case, virtually all particles are convected downstream resulting in very little ignited material. Hence, some events bring particles in the recirculation zone while others convect them all downstream, consistent with the high rms of π_{ign} in Fig. 6.4a.

Spark location II results in very little flame propagation, see Fig. 6.8. This is because Ka is high where the kernel is generated. This follows the argument of Ref. [103] that in the rich recirculation zone, the kernel extinguishes easily due to the relatively high turbulent strain rate.

Finally, Figure 6.9 shows an ignition event for spark location III, on the side of the recirculation zone. In this event, the particles ignited by the spark are convected downstream along the mean stoichiometric contour. They ignite many grid cells located on their path. Many of the ignited particles enter the recirculation zone. This agrees with the argument given in Ref. [103] to explain the high ignition probability near the side of the recirculation zone.

It is worth concluding that this phenomenological model reproduces the underlying physics of ignition for the complicated flow field of Ref. [103].

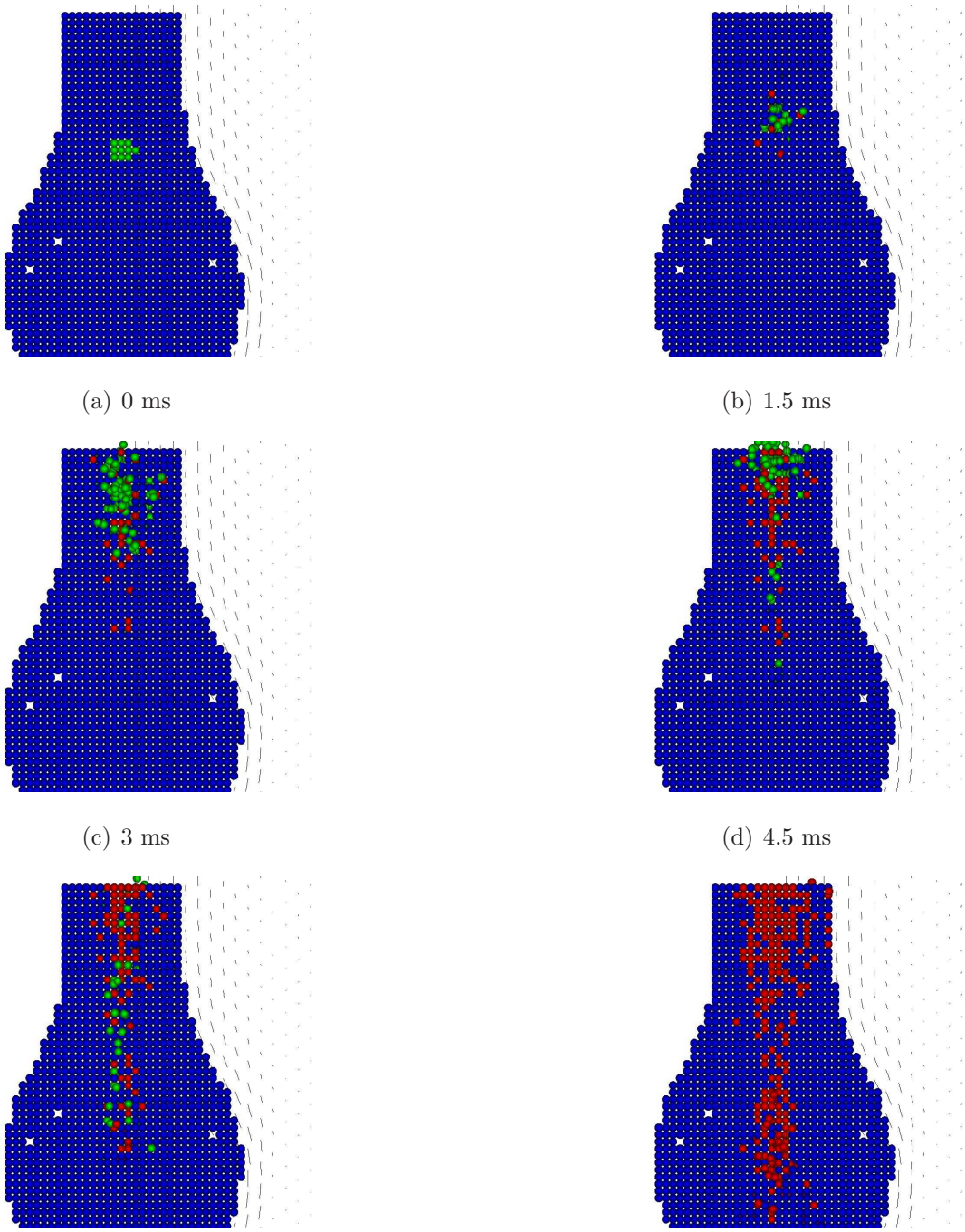

(a) 0 ms

(b) 1.5 ms

(c) 3 ms

(d) 4.5 ms

(e) 6 ms

(f) 60 ms

Figure 6.6: Evolution of particles for a successful event between t=0 ms and t=60 ms for spark location I. Blue particles represent grid cells that have not ignited. Green particles are those that are in motion. Red particles are those that have $Ka > Ka_{crit}$.

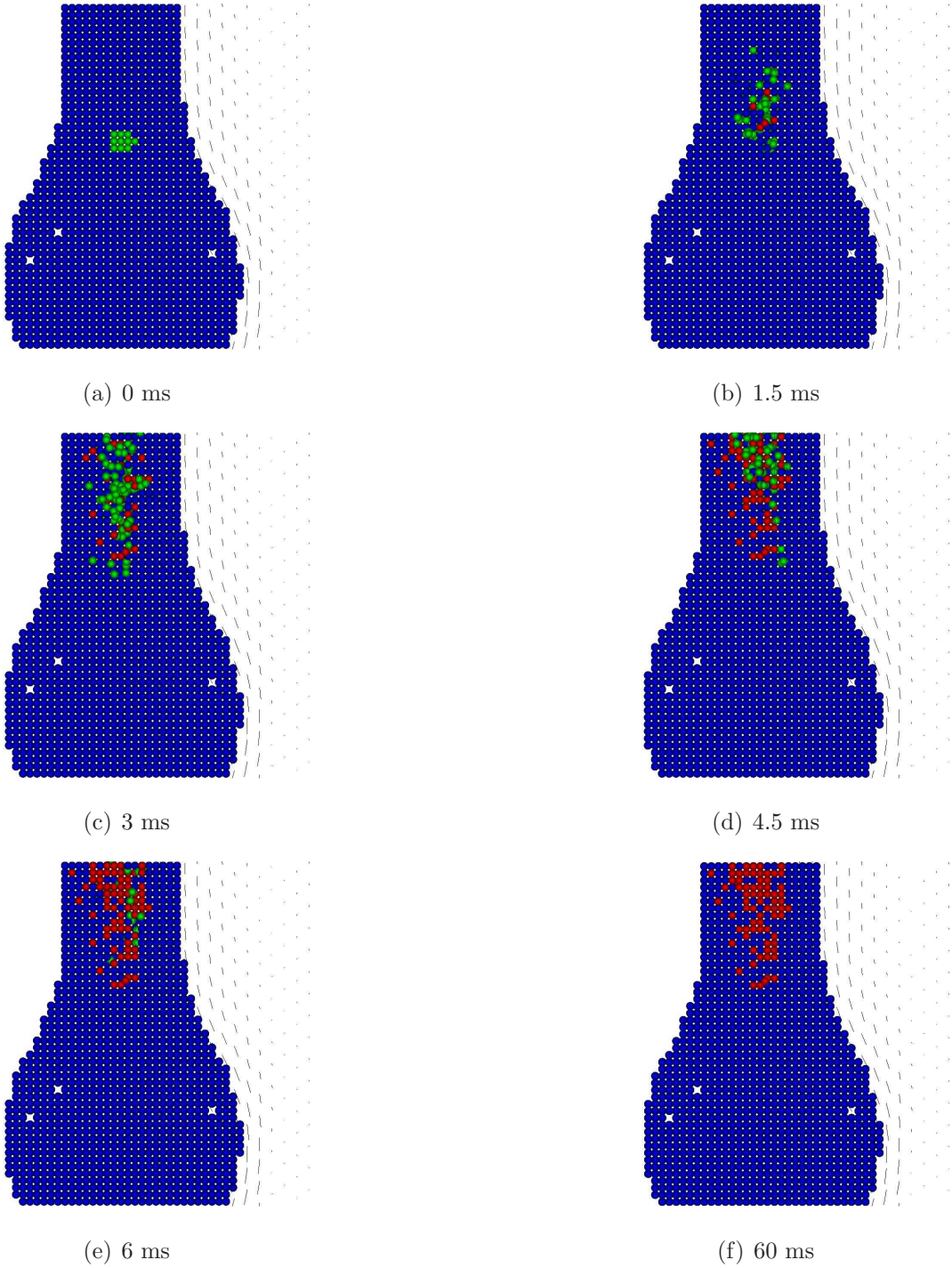

(a) 0 ms

(b) 1.5 ms

(c) 3 ms

(d) 4.5 ms

(e) 6 ms

(f) 60 ms

Figure 6.7: Evolution of particles for a failed event between t=0 ms and t=60 ms for spark location I. Blue particles represent grid cells that have not ignited. Green particles are those that are in motion. Red particles are those that have $Ka > Ka_{crit}$.

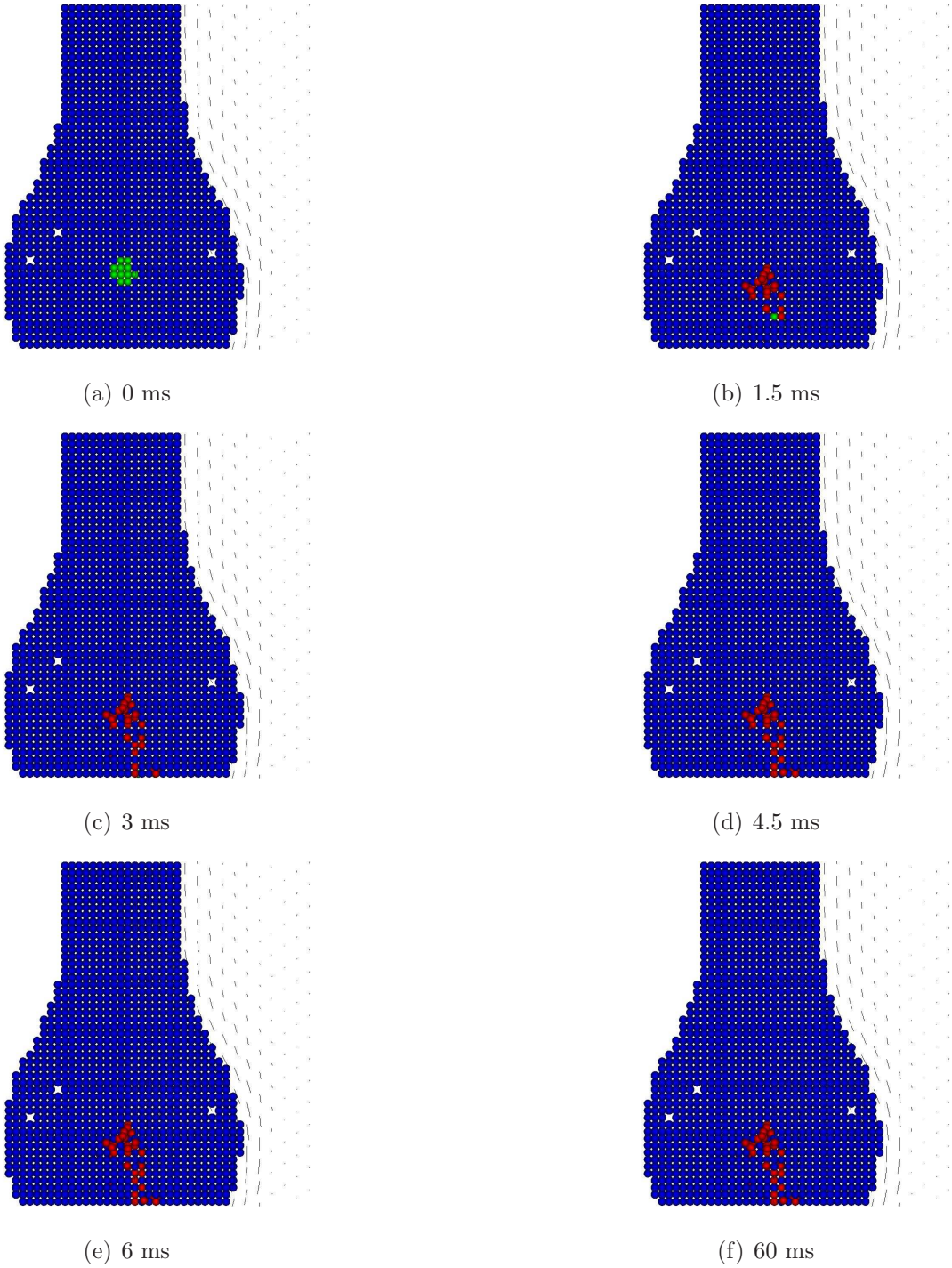

(a) 0 ms

(b) 1.5 ms

(c) 3 ms

(d) 4.5 ms

(e) 6 ms

(f) 60 ms

Figure 6.8: Evolution of particles for a failed event between t=0 ms and t=60 ms for spark location II. Blue particles represent grid cells that have not ignited. Green particles are those that are in motion. Red particles are those that have $Ka > Ka_{crit}$.

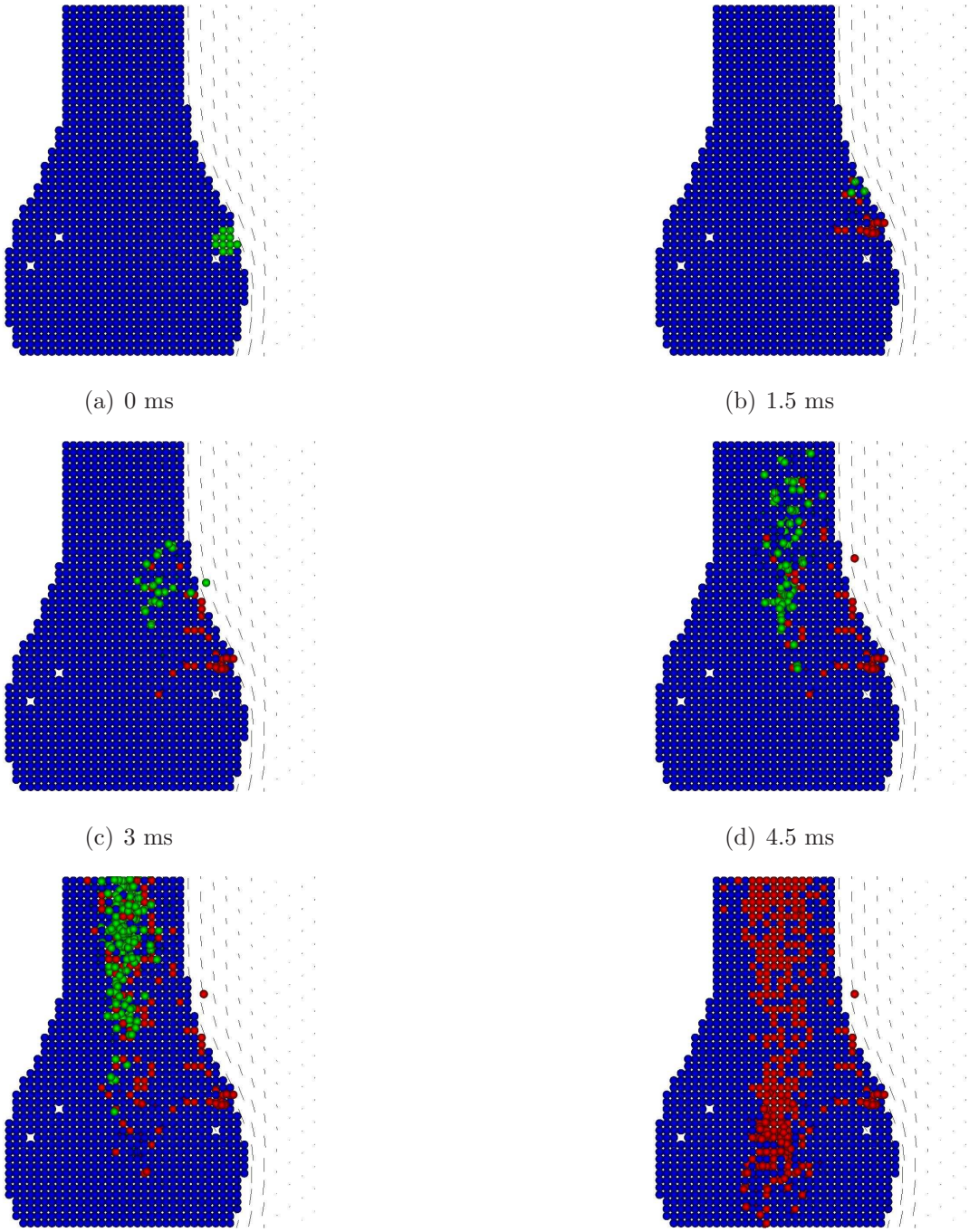

(a) 0 ms

(b) 1.5 ms

(c) 3 ms

(d) 4.5 ms

(e) 6 ms

(f) 60 ms

Figure 6.9: Evolution of particles for a successful event between t=0 ms and t=60 ms for spark location III. Blue particles represent grid cells that have not ignited. Green particles are those that are in motion. Red particles are those that have $Ka > Ka_{crit}$.

6.4 Counterflow experiment

6.4.1 Numerical setup

In this section, we report results for the fuel-air vs air turbulent counterflow experiment of Ref. [84]. The present cases have a dilution factor of 80% on the fuel side. Instead of using a CFD solution, analytical expressions for the Favre averaged axial velocity $\widetilde{U_z}$ and Favre averaged radial velocity $\widetilde{U_r}$ were used. As in the experiment, U_b is the bulk injection velocity on the air side, U_F is the bulk injection velocity on the fuel side and H is the inner diameter of the injection pipes also equal to the distance between the pipes [84]. The mass fluxes on the air side and the fuel side $\rho_{air}U_b = \rho_F U_F$ are equal. The expression for average velocities at an axial distance $z > H/2$ and a radius $r > 0$ is [38]

$$\widetilde{U_z} = -2U_b(\frac{z}{H} - \frac{1}{2}) \tag{6.28}$$

$$\widetilde{U_r} = U_b\frac{r}{H} \tag{6.29}$$

The expression for velocities at an axial distance $z < H/2$ and a radius $r > 0$ is

$$\widetilde{U_z} = -2U_F(\frac{z}{H} - \frac{1}{2}) \tag{6.30}$$

$$\widetilde{U_r} = U_F\frac{r}{H} \tag{6.31}$$

The Favre averaged mixture fraction and rms of mixture fraction was calculated from the following expressions that matched experimental data for the conditions studied [84]

$$\widetilde{\xi} = \frac{1}{2}\mathrm{erfc}(250(z - 0.0125)) \tag{6.32}$$

$$\sqrt{\widetilde{\xi^2}} = 0.39\exp[-\frac{(z - 0.0125)^2}{2(0.0025)^2}] \tag{6.33}$$

Prior to the calculation, the region with flammability factor $F > 0.1$ based on the local mean values is computed, which can be observed in Fig. 6.10(a). In this zone, grid cells are initialised to the cold state. The mean turbulence intensity and

the turbulent length scale are assumed constant, respectively equal to $0.2U_b$ and $L_{turb} = 3$ mm [84]. The time step is taken as $dt = 0.5$ ms, lower than the mean turbulent timescale $L_{turb}/u' = 7.5$ ms. One event lasts 60 ms. The spark volume is a sphere of 2 mm diameter, in order to reproduce the experiment of Ref. [84]. Spark centres are located every 0.15 mm in axial and radial direction in a 2D cut of the flow, assuming axi-symmetry. Two cases were studied with two different bulk velocities, see Table 6.2. Under those conditions, the CPU time to compute a map of ignition probability was about 4h.

Note that in all cases, the grid spacing is larger than the minimum spacing $2(C_0\epsilon_p dt)^{1/2}dt$, based on mean quantities of the flow, required to resolve the propagation induced by the model. Given the small value of ϵ due to the low level of turbulence, the required resolution is very high. This would imply a high computational cost. However, for this problem, the flame spread is not controlled by the bulk and the turbulence convection as in the bluff-body experiment, but by edge flame propagation [84]. Therefore, even a grid spacing smaller than $2(C_0\epsilon_p dt)^{1/2}dt$ would not have reproduced the actual flame propagation since molecular diffusion of the flame is not included in the model. The performance of the model for this configuration is discussed in the next section.

The main findings of the counterflow experiment that the present results intend to reproduce can be summarised as follows. First, a higher bulk velocity resulted in a lower ignition probability. This was attributed both to the higher turbulence intensity, detrimental to edge flame propagation, and to a higher convection velocity against which the edge flame had to propagate to stabilise [84]. Secondly, the ignition probability could be finite on the main axis at location where the flammability factor was virtually zero $F = 0$, see Fig. 6.10a. This was attributed to the finite size of the spark and to the convection of the hot gas towards the flammable region [84]. Note that in our model, there are no grid cells in a region with $F = 0$. This would not lead to different results since particles that switch to the burned state with $F = 0$ sample non-flammable mixture fraction and immediately extinguish. Such particles

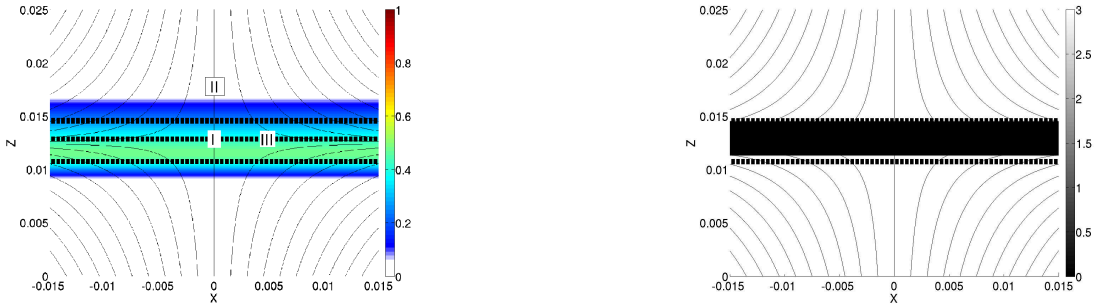

(a) (b)

Figure 6.10: (a) Flammability factor with spark locations I, II and III, (b) Karlovitz number based on averaged quantities. The three lines denote the locations where $\widetilde{\xi} = \xi_R$, ξ_{st}, ξ_L from bottom to top.

do not contribute to the flame spread. Hence, in our model, the far reaching effect of a spark can only be attributed to its size but not to the convection of hot gas from regions with $F = 0$. Thirdly, the ignition probability became low at large radii. This was attributed to the large radial velocity against which the edge flame had to propagate and which made ignition more difficult [84].

6.4.2 Results

In this section, data are presented based on case A, unless stated otherwise. Figures 6.11a, b and c show the time evolution of π_{ign} for all spark events for spark locations I, II and III (see Fig. 6.10), respectively. For spark location I, located in the flammable zone, near the stagnation point, a large variability can be observed. This can be attributed to the large rms of mixture fraction in the flammable region, and to the turbulent motion of the particles. For some events, the particles ignited may have flammable mixture fraction ($Ka_p \leq Ka_{crit}$) and ignite further cells while in other events, particles may experience non-flammable mixture fraction and immediately extinguish ($Ka_p > Ka_{crit}$). Note that the variability of Ka_p comes only from the mixture fraction since both u' and L_{turb} are constant for all particles and events. In

Table 6.2: Cases studied for the experiment of Ref. [84]. The value of $(C_0\epsilon_p dt)$ is estimated from the mean turbulence intensity $u' = 0.2U_b$ and the assumed turbulent length scale $L_{turb} = 3$ mm [84].

Case	U_b	Number of grid cells	Grid spacing
A	2	1,204	$11 \times 2(C_0\epsilon_p dt)^{1/2}dt$=2 mm
B	1.5	1,204	$17 \times 2(C_0\epsilon_p dt)^{1/2}dt$=2 mm

Case	$\pi_{ign,crit}$	Ka_{crit}	Number of events
A	0.30	1.5	50
B	0.30	1.5	50

Fig. 6.11b, the evolution of π_{ign} for spark location II shows again a large variability. Interestingly, π_{ign} increases to relatively high values in some events, implying that much material has been ignited although the spark is in a zone with $F = 0$. Figure 6.11c shows that for spark location III, π_{ign} remains small through the simulation for almost all events.

Figure 6.12a and b show that for case A, the average of π_{ign} over all events is high near centre line, in the mean flammable region. Its value decreases if the spark is moved away from the stagnation point. Note also that it remains finite near the centreline in locations with $F = 0$. The rms of π_{ign} has a similar trend. However, we can notice that on the centre line, the rms is larger near the rich and lean flammability limits than at the stagnation point. This implies that ignition is more probabilistic there. Furthermore, Fig. 6.12c and d show that for case B, with a lower bulk velocity, the same trends are followed but the average of π_{ign} and the rms of π_{ign} are slightly lower.

Figure 6.13 shows the computed ignition probability map and the experimental ignition probability map. First, it can be noticed that the model reproduces well the region of high P_{ign} for case A with $U_b = 2$m/s. As in the experiment, P_{ign} is null

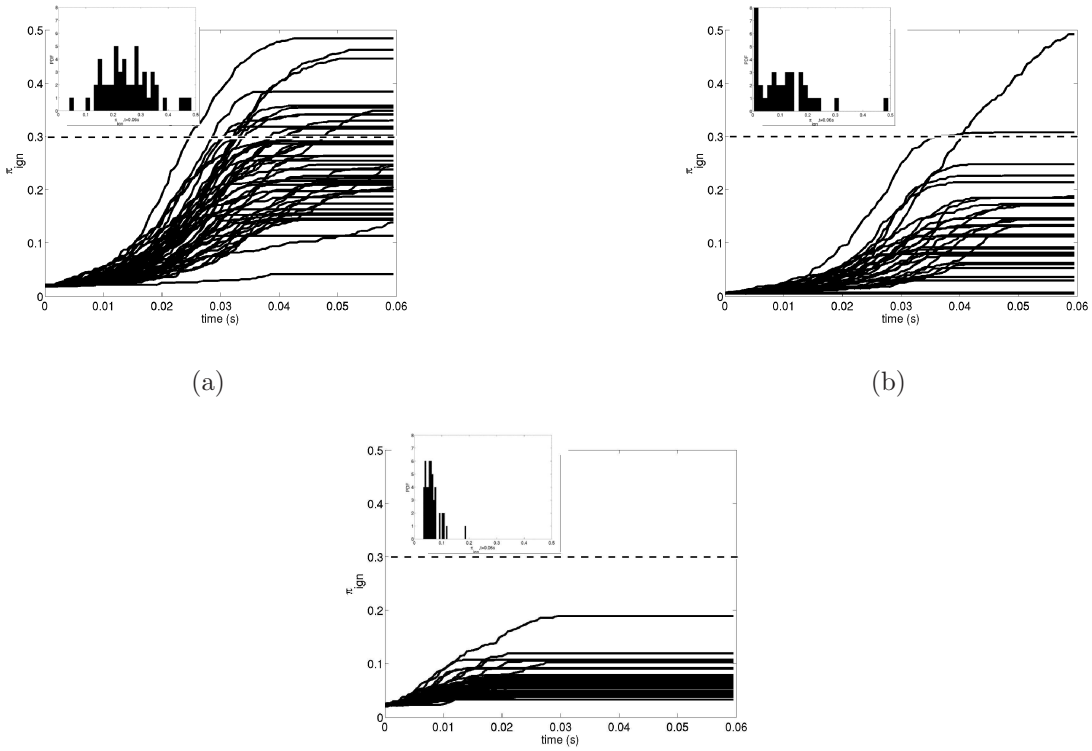

(a)

(b)

(c)

Figure 6.11: Time evolution of π_{ign} of each event for (a) spark I, (b) spark II, (c) spark III. The dashed line show $\pi_{ign} = 0.3$. On the top left of the figure is the PDF of π_{ign} at the end of the simulation.

for radii larger than 10 mm, it is high near the centreline in the mean flammable region and finite probability is found along the centreline where $F = 0$. However, by comparing Fig. 6.13a and b, we do not observe a net increase of the ignition probability as U_b is reduced from 2m/s (case A) to 1.5m/s (case B), as in the experiment. On the contrary, the present simulations result in P_{ign} slightly lower in case B than in case A. This is due to the lower value of π_{ign} observed earlier in case B.

The effect of the bulk velocity on the ignition progress factor π_{ign} demands discussion. In a pure laminar configuration, the particles would have the exact same path with a larger bulk velocity U_b and would ignite the same number of cells. In a

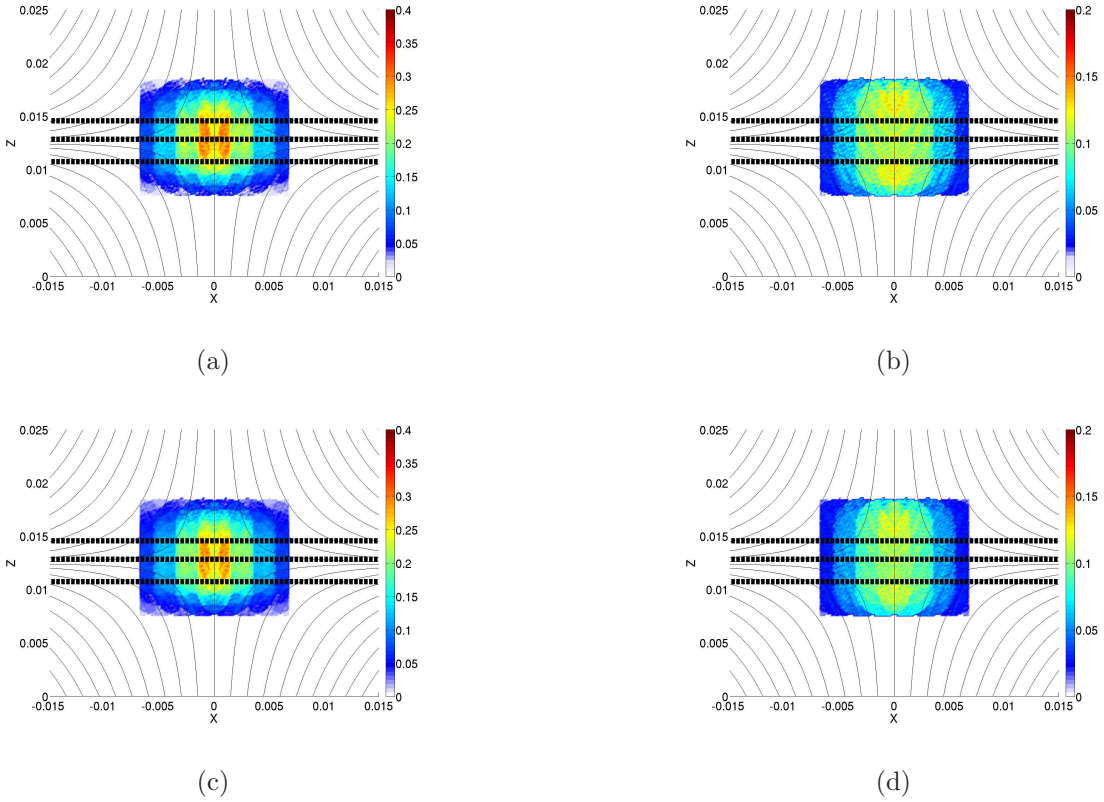

(a) (b)

(c) (d)

Figure 6.12: Statistics over 50 events at each spark location at $t = 60$ ms (a) average of π_{ign} for case A, (b) rms of π_{ign} for case A, (c) average of π_{ign} for case B, (d) rms of π_{ign} for case B. The three lines denote the locations where $\widetilde{\xi} = \xi_R$, ξ_{st}, ξ_L from bottom to top.

turbulent flow, the number of cells ignited, and in turn π_{ign}, can be higher thanks to the turbulent motion. Since a higher bulk velocity also induces a higher turbulence intensity, the random motion of the particles is more important which can lead to more ignited grid cells. Hence, it is expected that at low levels of turbulence that do not lead to extinction ($Ka < Ka_{crit}$), the present model can result in a higher π_{ign} with a higher turbulence intensity. This is the case in the present counterflow configuration since the turbulent intensity is relatively low. In cases A and B, it was observed that particles having $\xi_L < \xi_p < \xi_R$ had Ka_p of the order of 0.1, much lower than Ka_{crit}. Hence, in the simulations, the higher turbulence intensity associated

with the higher U_b will have a beneficial effect on particle spread and virtually no detrimental effect through Ka_p. This is contrary to the experiments that showed that the flame spread is done through edge flame propagation, for which a higher turbulence strain rate and a higher bulk velocity are detrimental [84].

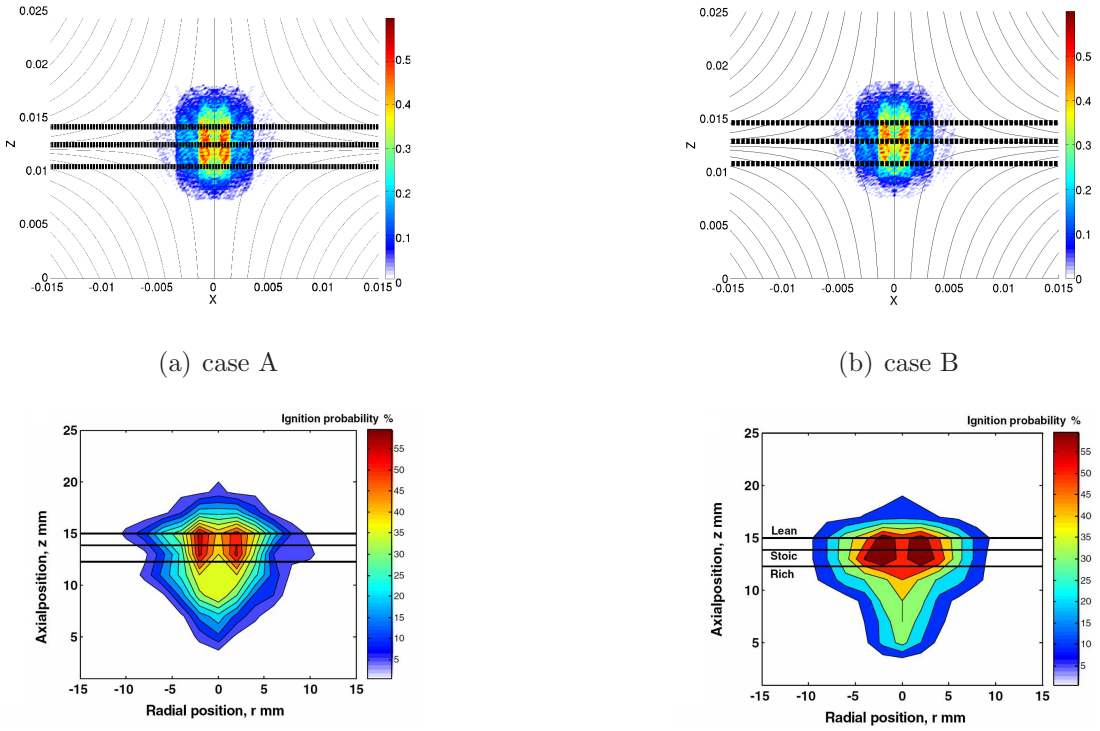

(a) case A

(b) case B

(c) Experiment, case A

(d) Experiment, case B

Figure 6.13: Ignition probability maps for (a) case A, (b) case B, (c) Experimental results for case A [84], (d) Experimental results for case B [84]. The three lines denote the locations where $\widetilde{\xi} = \xi_R$, ξ_{st}, ξ_L from bottom to top.

Figures 6.14, 6.15 and 6.16 show the time evolution of the computed particles for different spark events at locations I, II and III. In Fig. 6.14, particles initially switch to the burned state near the stagnation point and then are convected away by the mean flow. Thanks to their turbulent motion, they can ignite many grid cells on their path. The fact that the spark is initially in a flammable region and at a radius equal to zero results in a relatively high π_{ign}.

Figure 6.15 shows a successful event for spark location II. In that case, some particles are ignited by the spark, located in a region with $F = 0$. Then, they start spreading and ignite further grid cells. The success of ignition is due to the spark size that reaches flammable region and to the fact that ignited cells sample flammable mixture fractions. As mentioned in Section 6.4.1, there are no grid cells in $F < 0.1$ and the far reaching effect of the spark is only due to its size.

Spark location III results in little flame propagation, see Fig. 6.16. In that case, the flame particles are generated in a location where the mean radial flow is high. They are quickly convected to large radii and cannot ignite many grid cells on their path. The detrimental effect of the radial velocity from the experiment is thus reproduced [84].

The present simulation reproduces some physical aspects reported in the experiment [84]. The ignition probability is low at large radii because flame particles are rapidly convected away and do not have time to ignite a large amount of grid cells. In addition, flame spread could occur even if the spark was located in a region with $F = 0$. However, the model reproduces only the effect of the spark size that can overlap with flammable material, not the effect of convection of hot gas from a region with $F = 0$. The model could be modified in order to allow particles to survive even if $Ka_p > Ka_{crit}$ (e.g. quenching after a time delay associated with L_{turb}/u'). Finally, the simulation did not reproduce the decrease probability at higher U_b. This is because the model does not include the propagation of the flame through molecular diffusion that is important in this configuration. Note that it was expected that the model would not perform well when the flame speed is comparable to the flow convection speed and turbulence intensity.

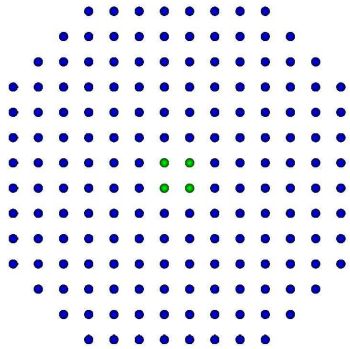

(a) 0 ms

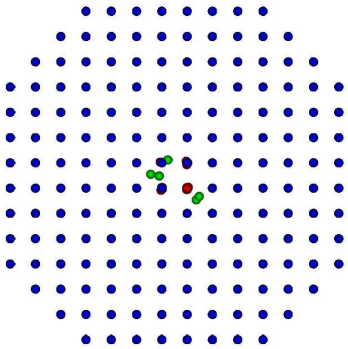

(b) 5 ms

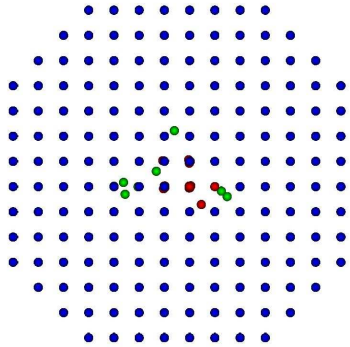

(c) 10 ms

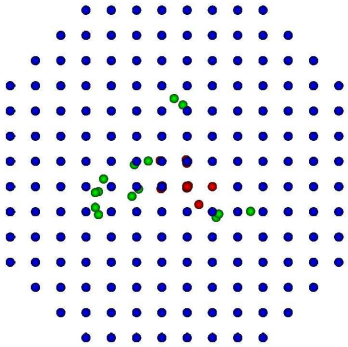

(d) 15 ms

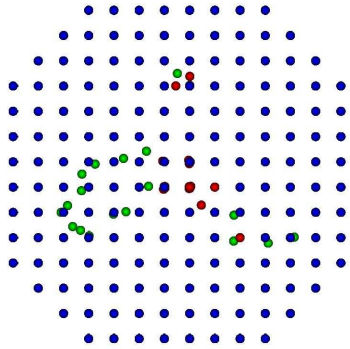

(e) 20 ms

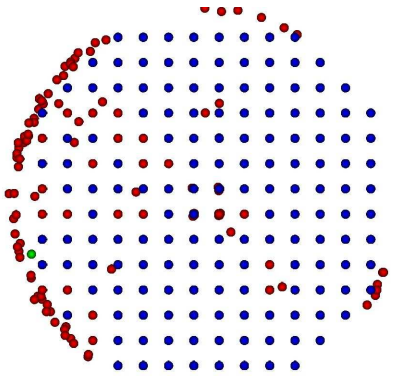

(f) 60 ms

Figure 6.14: Top view of the evolution of particles for a successful event between t=0 ms and t=60 ms for spark location I. Blue particles represent grid cells that have not ignited. Green particles are those that are in motion. Red particles are those that have $Ka > Ka_{crit}$.

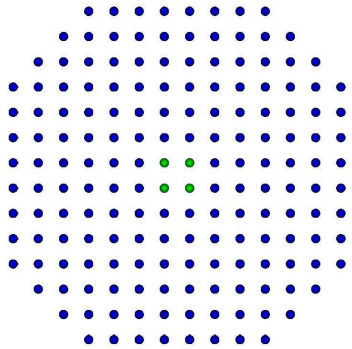

(a) 0 ms

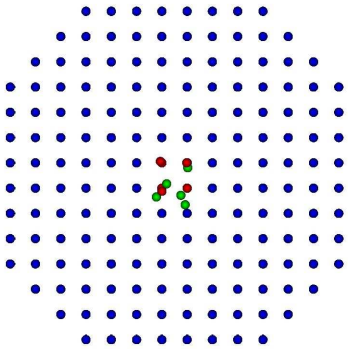

(b) 5 ms

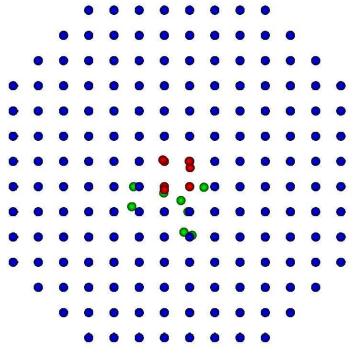

(c) 10 ms

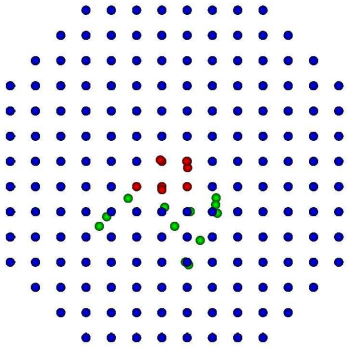

(d) 15 ms

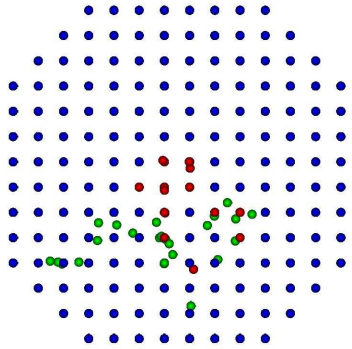

(e) 20 ms

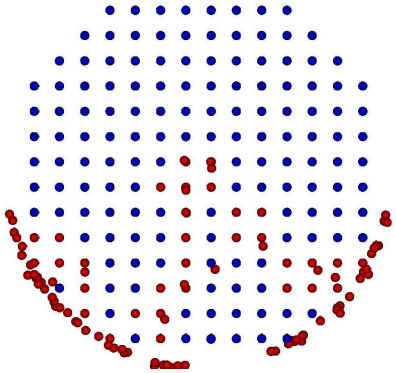

(f) 60 ms

Figure 6.15: Top view of the evolution of particles for a successful event between t=0 ms and t=60 ms for spark location II. Blue particles represent grid cells that have not ignited. Green particles are those that are in motion. Red particles are those that have $Ka > Ka_{crit}$.

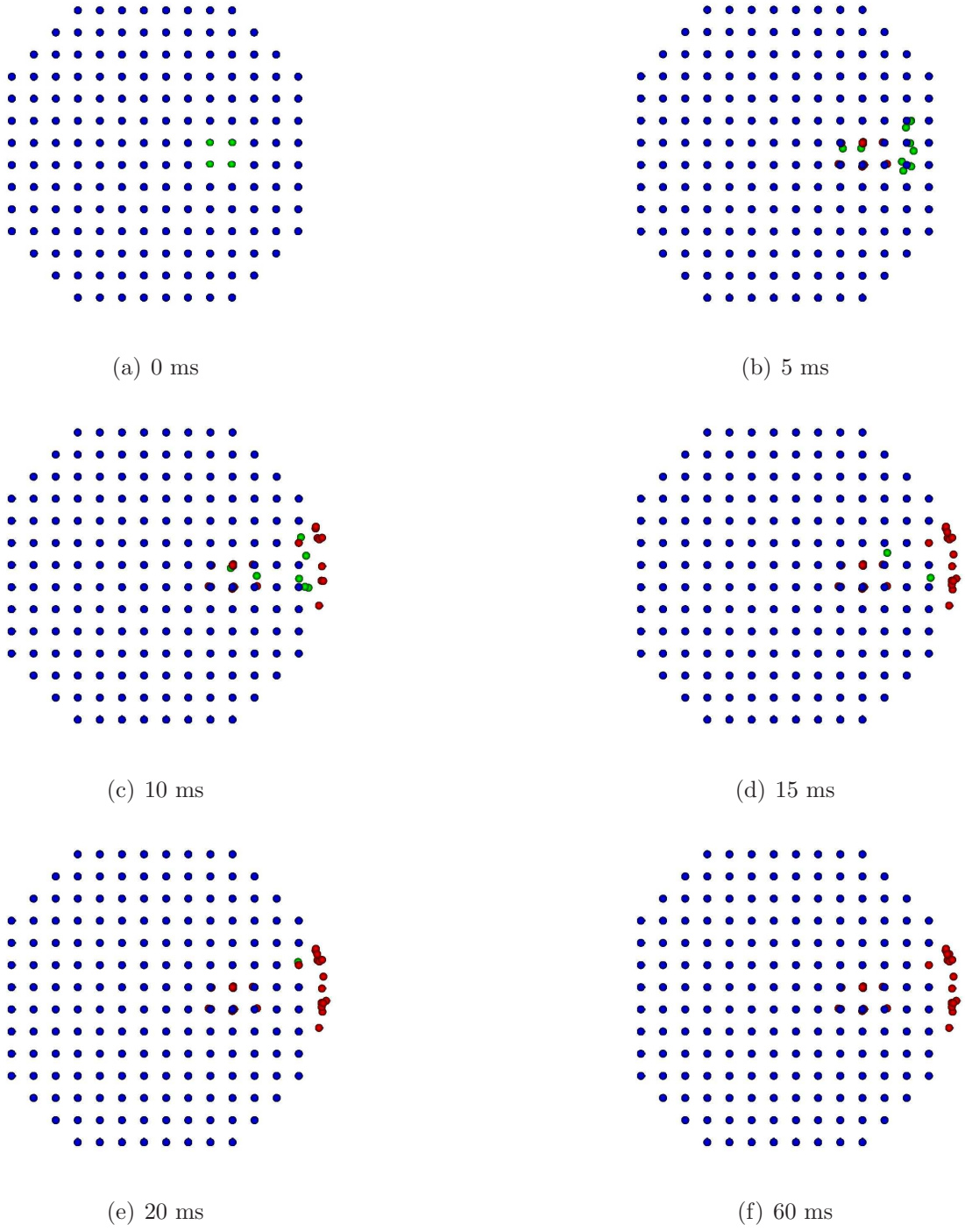

(a) 0 ms

(b) 5 ms

(c) 10 ms

(d) 15 ms

(e) 20 ms

(f) 60 ms

Figure 6.16: Top view of the evolution of particles for a failed event between t=0ms and t=60 ms for spark location III. Blue particles represent grid cells that have not ignited. Green particles are those that are in motion. Red particles are those that have $Ka > Ka_{crit}$.

6.5 Industrial combustor

6.5.1 Numerical setup

In this section, we consider an industrial geometry that was studied numerically [160] and experimentally [112, 164] in EU Project No. AST5-CT-2006-030828. The combustion chamber is shown in Fig. 6.17. The downstream direction aligns with the x-axis. The high-altitude test rig is a two-sector rig, one sector (the left-hand sector when looking downstream) being fitted with a lean-burn injector (Rolls-Royce Deutschland Ltd & Co KG), and the other having an unfuelled dummy injector. The fuel injected is liquid kerosene. A RANS solution of a cold flow field of this geometry was provided by Dr S. Stow from Rolls-Royce plc [160]. The operating conditions chosen for modelling in the CFD calculations are given in Table 6.3.

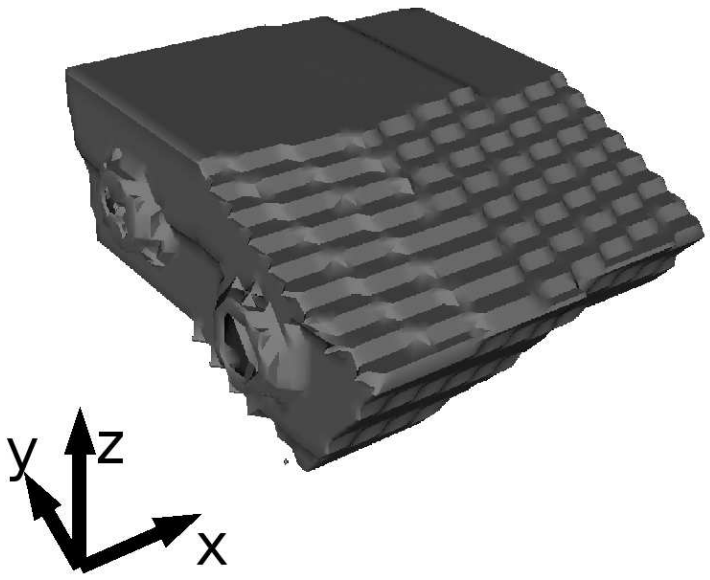

Figure 6.17: Geometry of the industrial combustor [160].

In the previous test cases, where fuel was purely gaseous, grid cells were initialised

Table 6.3: Operating conditions used in the CFD RANS simulation.

Air pressure (bar)	0.552
Air temperature (K)	278
Fuel temperature (K)	288
Normalized air mass flow	0.38
Normalized fuelair ratio	0.56

in the region $F > 0.1$, in order to reduce the number of cells to compute. F could be calculated assuming a beta pdf for the mixture fraction, and the known lean and rich limits, ξ_L and ξ_R, for methane. However, with a spray, the flammability depends on the gaseous mixture fraction, the liquid mixture fraction and the SMD of the droplets. The computation of F would require the knowledge of the joint PDF of those variables. Since in a spray, simple functions cannot be applied, we choose instead to initialise grid cells in all the domain. The RANS solution provides the turbulence kinetic energy and the turbulent dissipation rate at every grid cell. The time step is $dt = 0.5$ ms, lower than the estimated turbulent timescale $L_{turb}/u' = 2$ ms in the flow. One event lasts 60 ms.

The flame speed $S_{L,p}$ at a flame particle is computed using the correlation for decane at atmospheric conditions, presented in section 6.2.4. It is expected that the flame speed at atmospheric conditions can be used since the flame speed of a spray was shown to be similar at low pressure and low temperature in Chapter 3.

A single case was studied, and parameters are summarised in Table 6.4. Under those conditions, the CPU time to compute a single event was about 30 min. Note that the grid spacing is equal to half of the minimum spacing $2(C_0\epsilon_p dt)^{1/2}dt$, based on mean quantities of the flow.

Finally, the spark was initialised in the zone $0.035 < x < 0.06$, $-0.0125 < y < 0.0125$, $0.345 < z < 0.3729$ (in meters). This corresponds to the burned

Table 6.4: Parameters used in the simulations. The value of $(C_0\epsilon_p dt)$ is estimated from the mean turbulent dissipation rate $\epsilon = 19000$.

Number of grid cells	Grid spacing	Ka_{crit}	Number of events
672,287	$0.5 \times 2(C_0\epsilon_p dt)^{1/2} dt$=2 mm	1.5	50

volume initialised in an LES simulation of ignition of this burner [160]. This spark is referred to as spark I. In order to study the effect of the spark location, another burned volume, spark II, was initialised in $0.115 < x < 0.14$, $-0.0125 < y < 0.0125$, $0.345 < z < 0.3729$ (in meters). Spark I and II have the same volume but spark II is located downstream of spark I, closer to the outlet. In the next section, we present results for those two locations only. We report the evolution of π_{ign} and visualisations of the spark events, but we do not compute the ignition probability, since this quantity depends on $\pi_{ign,crit}$ and there are no experimental values to compare with. We also compare our results with findings of interest from the experiment [164]: ignition has a probabilistic nature, the delay between ignition and flame stabilisation varies between 30 ms and 50 ms and successful ignition is associated with a kernel that moved upstream. The two last findings were also reported in the LES simulation mentioned above [160] and in Ref. [111].

6.5.2 Results

Figures 6.18a and b show the time evolution of π_{ign} for all events for spark I and II, respectively. The simulations reproduce the stochasticity of ignition since each event results in different values of π_{ign}. However, the rms of π_{ign} for those two sparks is relatively low. With spark I, all events result in relatively high values of π_{ign} at the end of the simulation, which implies that many grid cells have been ignited. In addition, the timescale over which the increase of π_{ign} occurs is about 50 ms. This is of the order of the ignition timescale reported by the experiment [164] and the

LES simulation of Ref. [160]. In addition, π_{ign} reaches much lower values in spark II than in spark I. This suggest that spark II is less likely to lead to successful ignition than spark I.

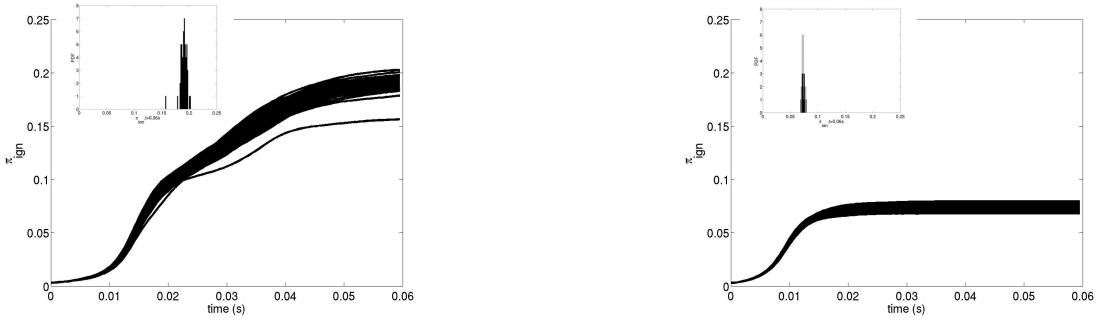

(a) (b)

Figure 6.18: Time evolution of π_{ign} of each event for (a) spark I, (b) spark II. On the top left of the figure is the PDF of π_{ign} at the end of the simulation.

Figures 6.19 and 6.20 show the evolution of the computed particles for spark I and II respectively. In Fig. 6.19, some particles are convected downstream just after ignition. On their path out of the combustor, they ignite many particles. Moreover, some particles from the spark are brought towards the recirculation zone where they also ignite grid cells. Interestingly, the spatial and temporal evolution of the flame is very similar to the LES simulation of Ref. [160]. On the other hand, Fig. 6.20 shows that with spark II, all particles are convected downstream. They ignite only grid cells on their path away from the injector, which leads to low values of π_{ign}.

Hence, the two present simulations show that π_{ign} is high when flame particles are convected upstream by the recirculating turbulent flow. This is consistent with the finding that ignition with this combustor is successful when the kernel moves upstream [164]. This also agrees with previous findings with realistic combustors where ignition occurred when the spark kernel was convected by the gas towards the fuel injector, see Section 2.4.2.

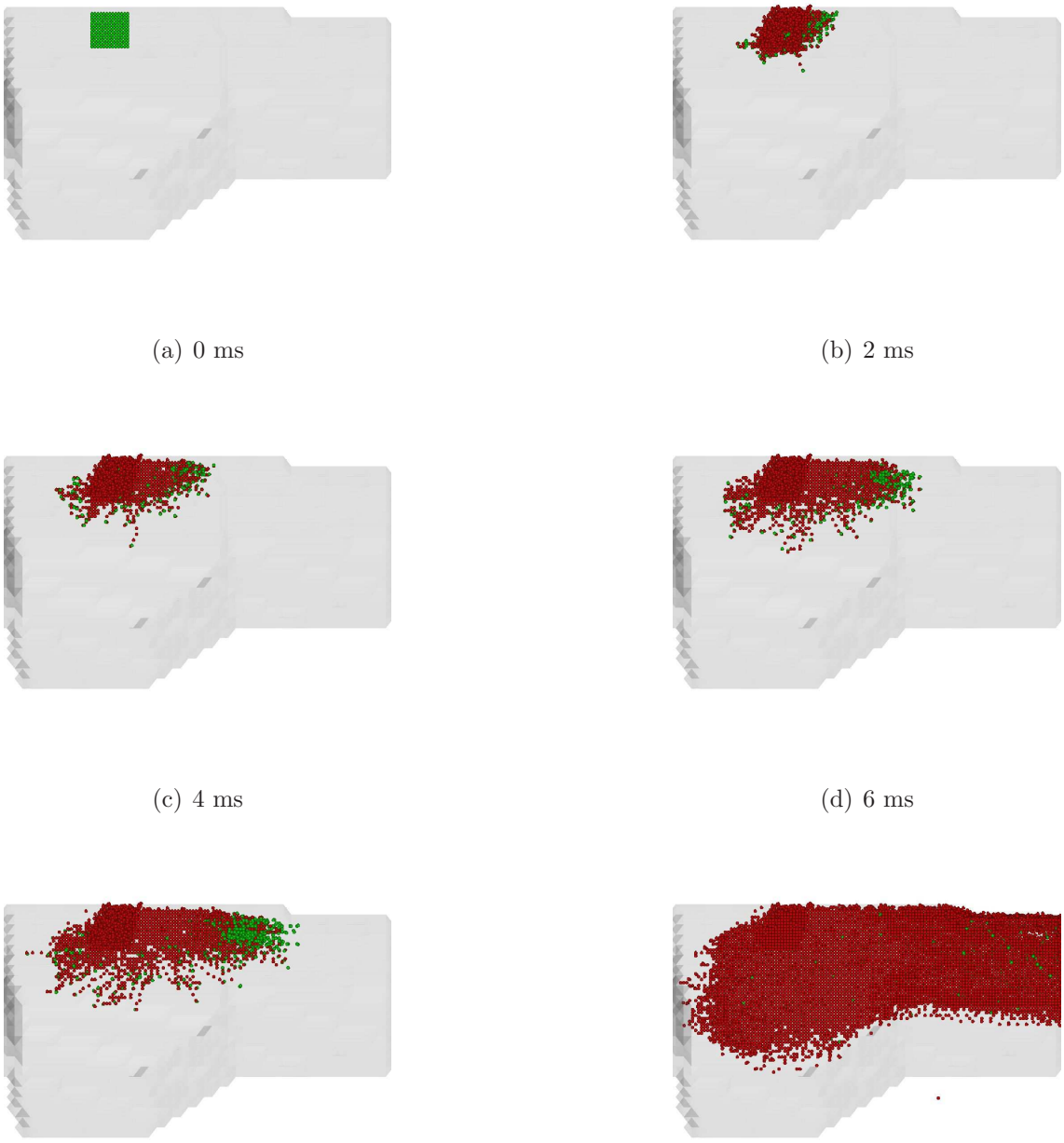

(a) 0 ms

(b) 2 ms

(c) 4 ms

(d) 6 ms

(e) 8 ms

(f) 60 ms

Figure 6.19: Evolution of particles with Spark I between t=0 ms and t=60 ms. Green particles are those that are in motion. Red particles are those that have $Ka > Ka_{crit}$.

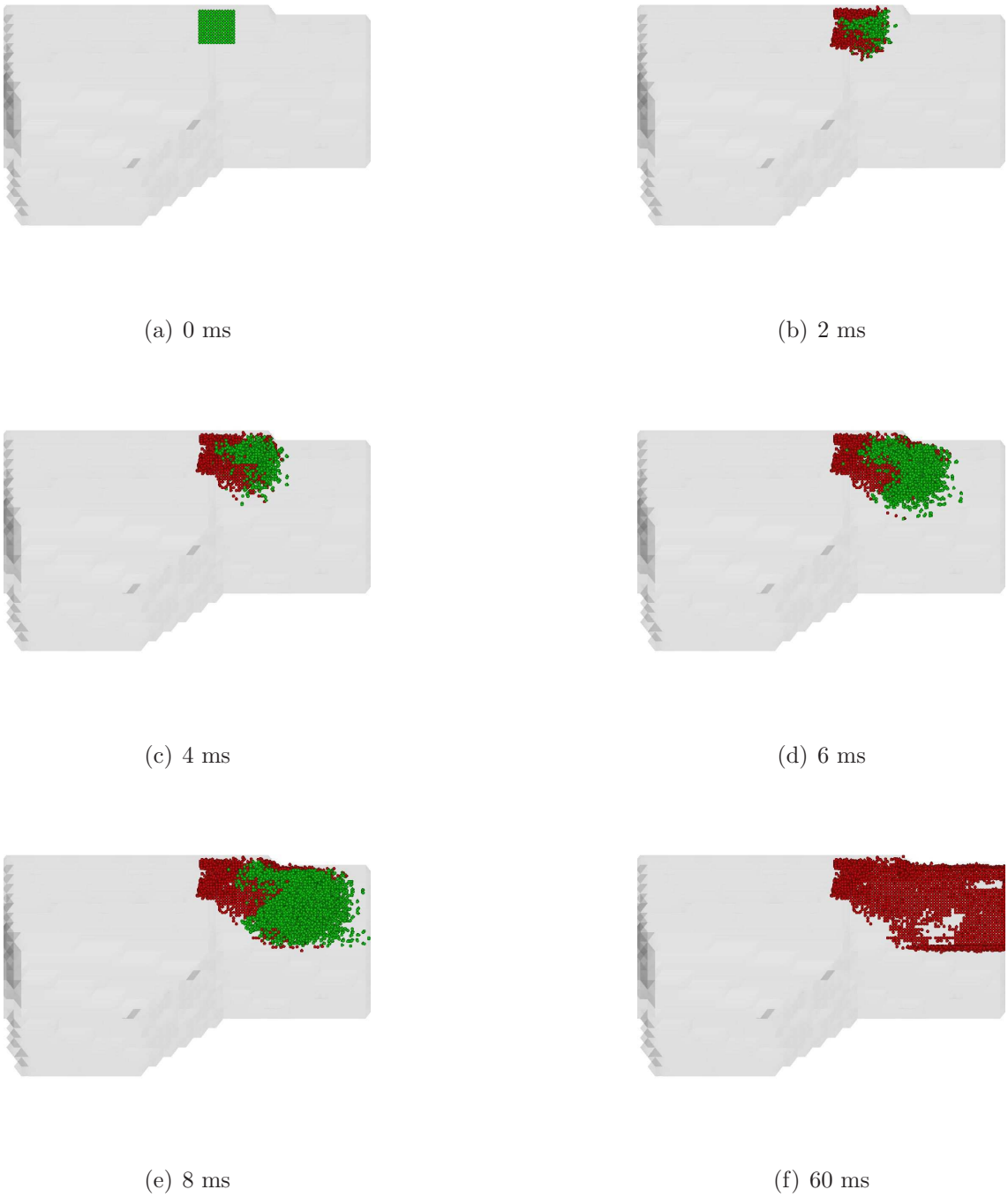

(a) 0 ms

(b) 2 ms

(c) 4 ms

(d) 6 ms

(e) 8 ms

(f) 60 ms

Figure 6.20: Evolution of particles with Spark II between t=0 ms and t=60 ms. Green particles are those that are in motion. Red particles are those that have $Ka > Ka_{crit}$.

6.6 Summary of main findings

A model has been developed to calculate the flame spread following the generation of a kernel, given a cold CFD solution. The mean convection and the turbulent dispersion of flame particles are implemented but the propagation by molecular diffusion is not included. Hence, the model is valid only for limited configurations where the flame propagation speed is a fraction of the turbulence intensity and the mean flow, but such conditions are relevant for industrial applications. In addition, the quenching of the flame particles based on a Karlovitz number criterion was included. Quenching of a particle depended on the parameter Ka_{crit}.

From the simulations, the temporal evolution of the ignition progress factor π_{ign}, equal to the fraction of material ignited, was determined. The model reproduced the probabilistic evolution of π_{ign} and an ignition probability P_{ign} could be calculated. P_{ign} depended on the parameter $\pi_{ign,crit}$.

Simulations were performed for a bluff-body experiment [103], a turbulent non-premixed counterflow experiment [84] and an industrial combustion chamber [164]. Results with the bluff-body experiment showed that the region of high ignition probability was consistent for different values of Ka_{crit} and $\pi_{ign,crit}$. In addition, the model reproduced the effects of the phenomena that control successful ignition and gave reasonable shapes of the P_{ign} contour. Results with the turbulent non-premixed counterflow [84] captured well the zone of high ignition probability. As in the experiment, finite P_{ign} could occur in regions that are not flammable. In the simulations, this was only due to the overlap of the spark with flammable material. The convection of hot burned gas from non-flammable to flammable region was not reproduced. This is because non-flammable flame particles were immediately extinguished. The model could be improved on this side. Moreover, the results did not reproduce the variation of ignition probability with the injection velocity. This was attributed to the fact that flame propagation by molecular diffusion was important in this problem and this mechanism was not included in the model. Hence, improve-

ments on this aspect are necessary if the model is to be applied to configurations where the flame speed is not negligible compared to the flow mean velocity and turbulence intensity.

Finally, simulations done with an industrial combustion chamber reproduced the stochastic nature of ignition and the timescale for the flame spread [164]. Furthermore, high values of π_{ign} were associated with flame particles moving towards the injector, consistent with the experiments [164] and previous work, see section 2.4.2. This suggests that the model is relevant to study the ignition process in such configurations. Since simulations are relatively cheap, the model can also be used to carry out parametric investigations of ignition, e.g. with different spark positions, air flow rate or fuel-air ratio.

Chapter 7

Conclusions

In the present work, numerical simulations were performed in order to progress further in our understanding of spark ignition in sprays and in order to evaluate the ignition probability of realistic burners. In the literature review of Chapter 2, we identified different fundamental areas worth investigating. In this thesis, we focused on: the laminar flame propagation in a uniform spray, the kernel growth in a turbulent spray-air mixing layer with small droplet diameter and the kernel growth in a turbulent premixed spray with moderate diameter. Furthermore, the thesis provides a model of ignitability that aims at reproducing the forced ignition behaviour in realistic recirculating flow combustors. The model generates ignition probability maps. In this chapter, we give a summary of the main findings and provide guidelines for future research.

7.1 Laminar flame propagation in a uniform spray

In Chapter 3, a one dimensional code with skeletal chemical schemes was used to perform a parametric study of the laminar flame propagation in a premixed spray.

- The laminar flame speed was partially correlated with the effective equivalence ratio ϕ_{eff}, defined as the gaseous equivalence ratio at the peak of heat release.

The flame speed tended to be higher for ϕ_{eff} closer to 1.

- The structure of the flame had an important impact on the flame speed. Three structures were identified.

  - With small droplets, the flame structure and the flame speed were similar to the corresponding gaseous flame.

  - With large droplets that led to low ϕ_{eff} (< 0.6), the oxidiser was not entirely consumed at the flame front and fuel burned as soon as it evaporated in the post flame region. This provided additional heat release and in turn resulted in moderate to high flame speeds despite a low ϕ_{eff}.

  - With rich sprays and large droplets that led to $0.6 < \phi_{eff} \leq 1$, the oxidiser was almost entirely consumed at the flame front but droplets still existed behind it. There, the fuel evaporated was pyrolysed with substantial generation of reactive species in the burned region, such as H_2, C_2H_2 and C_2H_4. Those species enhanced the flame speed above the maximum gaseous flame speed due to diffusion.

- The main difference between a volatile and a non-volatile spray was that the volatile spray evaporated faster. This resulted in a higher ϕ_{eff}.

- The flame speed of a spray at atmospheric condition was close to that at high altitude conditions. This was attributed to the competitive effect of low temperature that decreased the flame speed and the evaporation rate and the low pressure that had the opposite effect.

- The results offer insight in the structure and the propagation speed of a spray flame for a large range of spray parameters.

7.2 Spark ignition in a turbulent spray-air mixing layer

In Chapter 4, a DNS code with a classical and a modified single step chemistry was used to perform a parametric study of the spark ignition in a turbulent mixing layer between fine droplets and pure air.

- Rapid kernel growth occurred if fuel was readily available in the spark. This was the case when sparking at the mixing layer interface.

- A spark located on the air side, with initially no droplets in the spark volume, resulted in successful ignition with volatile fuel but failed ignition with non-volatile fuel. This was attributed to the heat diffusing from the spark that could evaporate and ignite the fuel in the spray, provided evaporation was fast.

- The flame propagating along the spray-air mixing layer had a triple flame structure.

- The density weighted displacement speed of the edge flame had a PDF similar to that found in experiments of gaseous turbulent edge flames. At long times after the spark, the displacement speed had a mean value in the range 0.55-0.75$S_{L,0}$, which is similar in magnitude to the mean turbulent edge flame displacement speed in gaseous mixing layers.

- The curvature of the propagating triple flame had a negative impact on the displacement speed. The curvature was reduced with a large kernel and a thick gaseous mixing layer.

  - The curvature was high when sparking on the air side because the kernel was small.

- Slower evaporation, due to larger diameter or non-volatile droplets resulted in a wider gaseous mixing layer.

- An initially wider spray mixing layer led to a thicker gaseous mixing layer. But this effect did not last because turbulence increased the mixing layer width and wiped out the initial difference.

- A higher turbulence level widened the mixing layer on one hand but distorted the flame on the other hand, which could lead to high values of curvature.

- The results demonstrate the long range effect of the spark with fine sprays and that the resulting edge flame speed is relatively low.

7.3 Spark ignition in a turbulent premixed spray

In Chapter 5, a DNS investigation with a skeletal chemical scheme of the kernel development in a uniform spray with moderate droplet size was carried out.

- The difference between a kernel in a premixed gas and in a spray was demonstrated. In a spray, heat release occurred over a large range of mixture fractions due to the stratified field created by the droplets.

- Heat release was high within the nominal flammability limits but could also occur at very lean values. This was attributed to the initial spark effect and to the diffusion of heat and reactive species from vigorously burning regions.

- Two structures of spray kernel were identified.

  - Firstly, a dispersed spray resulted in very localised flammable mixtures and heat release near the droplets. Diffusion flames near individual droplets or group of droplets were observed. It was shown that droplets ignited earlier if they were closer to the spark and that flame spread occurred when droplets were close to each other. This kernel structure was named “droplet ignition mode”.

- Secondly, a dense spray resulted in substantial evaporation between the cold and the hot gas. Consequently, the interdroplet spacing was within the flammability limit and heat release occurred over a large region. The flame looked like the gaseous kernel but with extra-wrinkling due to the stratified mixture. Moreover, the mixture was lean in the cold gas and rich in the hot gas, resulting in a non-premixed character between the cold and the burned regions. This flame had a structure very similar to that described in Chapter 1 with a rich spray and large droplets. Most of the features of this flame were observed from one-dimensional radial averages. This kernel structure was named "interdroplet ignition mode".

- The curvature of the reactions zones were measured. The curvature was positive and high with the droplet ignition mode because of the small droplet-scale flames. It was low and took both positive and negative values with the interdroplet ignition mode because of the wrinkled reaction zone.

- The results offered insight in the kernel structure of a spray with moderate droplet sizes. They are consistent with the Group Combustion Theory and the laminar flame propagation in a uniform spray.

7.4 Numerical model for the computation of ignition probability

In Chapter 6, a model for the computation of the turbulent flame expansion following a spark was presented. The model took a cold CFD solution as an input.

- The model aimed to reproduce the process by which grid cells (i.e. discrete volume elements of the combustor) switched from the unburned state to the burned state because of a propagating flame.

- Flame particles were tracked with a Langevin model. Every time a particle entered a grid cell, the cell switched to the burned state and released a new particle. The main drawback of the model was that a grid cell cell in a burned state did not switch back to the cold state.

- Quenching of flame particles was included based on the local flame speed and turbulence intensity.

- The model was restricted to flows where turbulence and convection dominate the flame propagation, such as realistic non-premixed burners and gas turbines. Propagation by molecular diffusion was not included.

- The model could be applied to gaseous and spray configurations. An expression for the flame speed of a spray based on the results of Chapter 3 was proposed.

- The model was applied to two academic experimental cases with methane: a turbulent bluff-body and a turbulent non-premixed counterflow. The ignition probability map compared reasonably well with experiments for both problems. Moreover, the physics that controlled ignition was captured with the bluff-body but not with the counterflow. In the former problem, flow convection and turbulence dominated the flame spread, while in the latter flame propagation by molecular diffusion was important. In addition, the convection of burned gas from non-flammable region to flammable region was not captured because particles that sampled non-flammable mixture fraction immediately extinguished.

- The model was also applied to an industrial combustion chamber. The results showed that experimental trends (ignition time scale, stochasticity, successful ignition when the kernel moves upstream) were reproduced.

- The model had the potential of helping the analysis of forced ignition in practical non-premixed flows, where the flame speed is a fraction of the mean

velocity and the turbulence intensity.

7.5 Guidelines for future studies

The present work has explored three fundamental areas and has presented a model of spark ignition, where substantial improvement can be done. With the development of numerical capabilities, it is expected that three dimensional simulations with complex chemistry and on larger scale than current simulations will be performed. In this section, we suggest areas of investigations that could extend the present findings:

- A parametric DNS of the uni-directional propagation of a turbulent flame in a spray. This problem of reference has been very little studied with DNS and a wide range of parameters can be explored. Data can be compared with the results of Chapter 3 and Chapter 5.

- Repeat the simulations of Chapter 5 over a longer time and with higher turbulence levels to explore the effect of turbulence on the kernel development.

- DNS of spark ignition in a spray air-mixing layer with moderate droplet sizes with respect to the reaction zone thickness. The long range effect of a spark should be explored and it is expected that the flame structure will be different from that observed with fine droplets in the simulations of Chapter 4.

- The model of Chapter 6 could be improved. The grid cells should be able to switch back to the cold state. If they ignite again, they should release a new flame particle. This must be done whilst keeping the computational cost low. Moreover, the flame particles should be able to survive for a certain time even if they are subjected to quenching conditions (e.g. time delay associated with the turbulent timescale). This would enable the convection of burned gas from non-flammable to flammable region. Finally, if the model is to be

applied to configurations where the flame speed is not negligible compared to the mean flow velocity and the turbulence intensity, flame propagation by molecular diffusion must be included.

Appendix A

Modified single step chemistry

In Appendix A, we present the classical and modified single-step chemistry used in Chapter 4. First, the formulation of the modified chemistry is introduced. Then, a comparison between flame speed profiles calculated with each model and experimental data is presented.

A single-step irreversible chemical reaction following an Arrhenius law was assumed

$$\text{Fuel} + \text{sOxygen} \quad \rightarrow \quad (1+\text{s})\text{Products} \tag{A.1}$$

where s is the mass of oxygen consumed per unit mass of fuel with the stoichiometric fuel mass fraction being $Y_{F_{st}}$=0.062. The modified 1-step chemistry was developed by Richardson [7] with the method of Fernandez-Tarrazo et al. [139] and was tuned to fit the heptane $S_{L,0}$ vs. ϕ curve, where ϕ is the gaseous equivalence ratio.

$$\omega_F \quad = \quad -B\hat{\rho}Y_F Y_{O_2} \exp\left[-\frac{\beta}{\tau}\frac{(1+\tau)^2}{1+\tau\hat{T}}\right] \tag{A.2}$$

with B equal to 6×10^7. The non-dimensional activation energy is

$$\phi \leq 0.74 \quad : \quad \beta = \beta_0(1 + 1.16948(\phi - 0.74)^2) \tag{A.3}$$

$$0.74 < \phi \leq 1.13 \quad : \quad \beta = \beta_0 \tag{A.4}$$

$$\phi > 1.13 \quad : \quad \beta = \beta_0(1 + 0.0092(\phi - 1) + 0.9423(\phi - 1.13)^2) \tag{A.5}$$

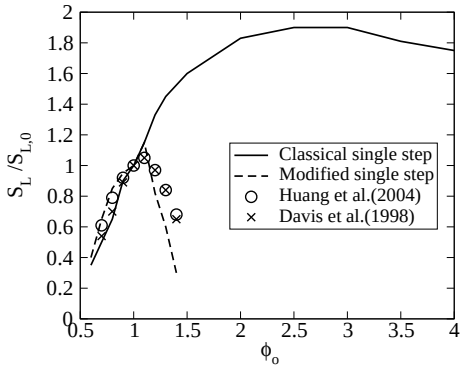

Figure A.1: Comparison of normalised flame speed profiles between the classical single-step chemistry, the modified single step chemistry and experimental data from Huang et al. ($S_{L,0} = 0.38m/s$) [165] and experimental data from Davis et al. ($S_{L,0} = 0.37m/s$) [166].

and the local heat release parameter is

$$\phi \leq 1 \quad : \quad \tau = \tau_0 \tag{A.6}$$

$$1 < \phi \leq \frac{\alpha + 1}{\alpha} \quad : \quad \tau = \tau_0(1 - \alpha(\phi - 1)) \tag{A.7}$$

$$\phi > \frac{\alpha + 1}{\alpha} \quad : \quad \tau = 0 \tag{A.8}$$

where the chemical parameters used are

$$\beta_0 = \frac{E_a(T_{ad} - T_0)}{RT_{ad}^2}, \alpha = \frac{T_{ad} - T_0}{T_{ad}} = \frac{\tau_0}{1 + \tau_0} \tag{A.9}$$

where E_a is the activation energy, R is the universal gas constant, $\tau_0 = 6.68$, and $\beta_0 = 6$. In Fig. A.1, flame speed as a function of equivalence ratio calculated with single step chemistry and modified chemistry are compared with experimental data.

Appendix B

Implementation of spray in SENGA2

In Appendix B, the implementation of the spray subroutines in the DNS code SENGA2 used in Chapter 5 is presented. First, the droplet equations are recalled. Second, the handling of the parallel communication of the particles is explained. Third, test cases with cold evaporation are presented for validation. Finally, the input files necessary to run the code are presented for future users of the program.

B.1 Liquid phase equations

For each droplet d, equations for its position $\mathbf{x}_d$, velocity $\mathbf{v}_d$, diameter a_d and temperature T_d are

$$\frac{d\mathbf{x}_d}{dt} = \mathbf{v}_d \tag{B.1}$$

$$\frac{d\mathbf{v}_d}{dt} = \frac{\mathbf{U}(\mathbf{x}_d,t)-\mathbf{v}_d}{\tau_d^v} \tag{B.2}$$

$$\frac{da_d^2}{dt} = -\frac{a_d^2}{\tau_d^p} \tag{B.3}$$

$$\frac{dT_d}{dt} = \frac{1}{\tau_d^T}\left[T(\mathbf{x}_d,t)-T_d-B_{T,d}\frac{L_v}{W_F C_{P_f}}\left(\frac{T_{crit}-T_d}{T_{crit}-T_{ref}}\right)^{0.38}\right] \tag{B.4}$$

U and T are the local gas velocity and temperature. T_{ref} is the boiling temperature at the reference pressure P_{ref}, T_{crit} the critical temperature, L_v the molar latent heat of evaporation and W_F the molecular mass of fuel. Note that the equation for the temperature evolution derives from the equation governing the time evolution of liquid enthalpy

$$\frac{d(m_d h_L)}{dt} = Q_c^L + \frac{dm_d}{dt} h_L(T_d) \tag{B.5}$$

where the first term Q_c^L is the heat conduction to the droplet at the droplet surface and the second term is the liquid enthalpy change due to mass transfer. For energy balance to hold at the droplet surface, these two terms must be balanced by the heat conduction to the gas at the droplet surface Q_c^g (modeled as a convective heat transfer in Eq. B.4 using the thin film assumption [116]) and the vapour enthalpy change due to mass transfer $-\frac{dm_d}{dt} h_F(T_d)$

$$Q_c^L + \frac{dm_d}{dt} h_L(T_d) + Q_c^g - \frac{dm_d}{dt} h_F(T_d) = 0 \tag{B.6}$$

When rearranging Eq. B.5 into Eq. B.4, the latent heat of evaporation appears as the difference between the fuel vapour enthalpy and the liquid enthalpy at temperature T_d.

The relaxation times appearing above are [116]:

$$\tau_d^v = \frac{\rho_L a_d^2}{18\mu_f(1 + \frac{1}{6}\mathrm{Re_d}^{2/3})} \tag{B.7}$$

$$\tau_d^p = \frac{\rho_L a_d^2}{4\mathrm{Sh_c}} \frac{\mathrm{PrLe_F}}{\mu_f} \frac{1}{\ln(1 + B_{M,d})} \tag{B.8}$$

$$\tau_d^T = \frac{\rho_L a_d^2}{6\mathrm{Sh_c}} \frac{\mathrm{PrLe_F}}{\mu_f} \frac{B_{T,d}}{\ln(1 + B_{M,d})} \frac{C_P^L}{C_{P_f}} \tag{B.9}$$

with $\mathrm{Re_d}$ the droplet Reynolds number, ρ_L the liquid droplet density, C_P^L is the heat capacity of the liquid and $\mathrm{Le_F}$ the fuel Lewis number, taken as 2.89. The mass and the temperature Spalding numbers, $B_{M,d}$ and $B_{T,d}$, are given by $B_{M,d} = (Y_{F,d}^s - Y_F(\mathbf{x}_d, t))/(1 - Y_{F,d}^s)$ and $B_{T,d} = (1 + B_{M,d})^{(C_P^F \mathrm{Sh_c})/(C_{P_f} \mathrm{Nu_c Le_F})} - 1$. C_P^F is the

fuel vapour heat capacity in the film while Sh_c and Nu_c are corrected Sherwood and Nusselt numbers [116]. We consider properties of the volatile fuel n-heptane.

Finally, it is pointed out that, instead of a_d^2, the cube of the droplet diameter a_d^3 is computed with an equation derived from Eq. B.3. This ensures better accuracy for the conservation of mass (proportional to a_d^3) during the integration.

B.2 Parallel communication of the particles and source terms

In SENGA2, the problem is decomposed over a cubical array of processors. The processor number locates the processor relatively to its neighbours. Let $X_{L,proc}$ and $X_{R,proc}$ be respectively the location of the first and the last grid node of the processor. Note that the first grid node of the next processor is at $X_{R,proc} + \Delta x$. Δx is the grid spacing.

In order to track particles (or droplets) over the different processors, the following procedure has been chosen. Each processor has an array of NTPART particles. This is the total number of particles in the global domain. Each particle of the NTPART array has a state PTIN that can be 0 or 1, depending on the presence of the particle in the processor. A processor contains a particle (PTIN=1) if its coordinate x_p (same for y_p and z_p) satisfies $X_{L,proc} \leq x_p < X_{R,proc} + \Delta x$. At the beginning of the simulation, particles are randomly initialised in the global domain and each processor allocates the particles that belongs to it. NPT is the number of particles in the processor and NPT$\leq$NTPART. The first NPT particles of the array have PTIN=1 and the other (NTPART-NPT) particles have PTIN=0. A particle leaves the global domain if it exceeds the global boundaries and its state becomes PTIN=0.

In order to advance a particle in time, gas phase values at the particle location are needed. As explained in Section 5.2.3, interpolation of the scalars from the Eulerian grid onto the particle is performed (subroutine ptinte.f). A particle in the

global domain is always in a small cubic volume formed of 8 Eulerian grid nodes and a weighted interpolation from those grid nodes is performed. If the particle is in an area $X_{R,proc} \leq x_p < X_{R,proc} + \Delta x$, the processor can still provide those 8 values. This is done thanks to the halo layer of the processor that contains the 5 next grid values of the adjacent processor thanks to parallel communication. The halo layer is designed to enable the calculation of the derivative of Eulerian scalars at the processor boundaries.

Once the particle is advanced in time, one must ensure that the particle belongs to the right processor. Therefore, the processor must send and receive particles to adjacent processors using parallel communications. First, if a particle leaves a processor $x_p < X_{L,proc}$ or $x_p > X_{R,proc} + \Delta x$, its status PTIN is switched to 0. The processor locates the appropriate neighbour and performs a parallel transfer of the particle position and of all its properties (subroutine ptparf.f). The receiving neighbour has its own array NTPART. In this array, a particle with status PTIN=0 is switched to PTIN=1. When all the particles have been transferred, the number NPT of each processor is updated. Moreover, the array of size NTPART is arranged so that the first NPT particles have status PTIN=1 and the rest PTIN=0.

Furthermore, source terms must be calculated for each droplet and extrapolated to its 8 surrounding nodes. The source terms are treated as the droplets. Each processor has an array NTPART of source terms. The number of source terms NSRC$\leq$NTPART in the processor is computed at each time step. Source terms have the same position x_p as the corresponding droplet at the beginning of the timestep. A processor contains a source term if $X_{L,proc} - \Delta x \leq x_p < X_{R,proc} + \Delta x$. As with droplets, a source term can be sent to an adjacent processor. A parallel transfer of a source term to an adjacent processor is done if $x_p < X_{L,proc}$ or $x_p > X_{R,proc}$ (subroutine srcpar.f). Note that 2 processors can have the same source term if for one of the processors $X_{R,proc} \leq x_p < X_{R,proc} + \Delta x$. When all source terms have been transferred, the number of source terms NSRC is updated. Then, in every processor, the source terms are extrapolated on the Eulerian grid (subroutines ptextr.f and

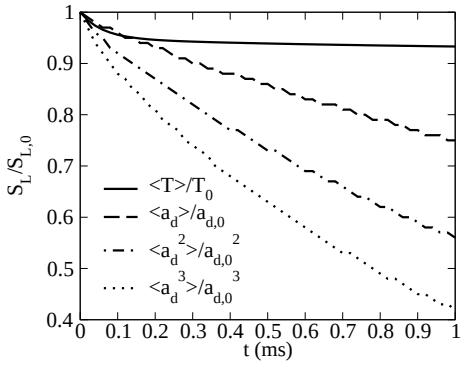

Figure B.1: Evolution of $< T > /T_0$, $< a_d > /a_{d,0}$, $< a_d^2 > /a_{d,0}^2$, $< a_d^3 > /a_{d,0}^3$.

srctrm.f).

B.3 Validation of evaporation cases

Non-reacting evaporating cases have been computed for testing. In a first case, a 32x32x32 domain decomposed over 8 processors was considered with a size and a spray slab similar as that described in Section 5.2.3. However, in this configuration, all the boundaries were periodic so that the domain was closed. With this grid, $\Delta x = 96.8$ μm. A n-heptane spray with $a_{d,0} = 5\mu m$ and $\phi_0 = 1$ (more than 20,000 droplets) and initial droplet temperature $T_{d,0} = 300K$ was initialised in stagnant air with $T_0 = 300K$. The simulation was run for 1ms with a time step 5×10^{-8} s. The total mass (gas and liquid) was conserved within 0.1%, which is a good accuracy given the large number of droplets. Figure B.1 shows the evolution of different quantities averaged over all the droplets (denoted by the symbol $< . >$).

In a second case, a single evaporating droplet in stagnant hot air (P=1 bar, T = 741 K) was computed and compared with experimental data [167]. In the simulation, the initial droplet diameter was $a_d = 20\mu m$ and the time step was 1×10^{-8} s. The effect of the grid size on the evolution of the droplet diameter is shown in Fig. B.2. From the graph, it is evident that the experimental decay rate of the diameter is better captured with a grid size $\Delta x = 7a_d$ than with a grid size

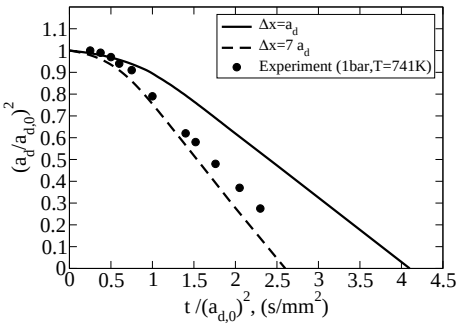

Figure B.2: Evolution of a_d^2 for a single evaporating n-heptane droplet in ambient air (P=1 bar, $T = 741$ K). Numerical simulations with two different grid sizes and $a_d = 20\mu$m are compared with experimental data [167]

$\Delta x = a_d$.

If one wants to capture the evaporation of droplets in a uniform stagnant gas, Δx should be much higher than a_d. However, this limits the range of problems to study. DNS simulations presented in Chapter 5 were performed with $\Delta x = 23.6\mu$m slightly higher than $a_d = 20\mu$m. The low value of Δx was dictated by the fine resolution of the reaction zone and the Kolmogorov length scale. In order to explore realistic conditions, a_d was of the order of Δx. Nevertheless, in the simulations performed, reaction zones near droplets and around group of droplets in presence of turbulence were observed. The point source approximation and the d^2 law have not been proved valid in this situation [36]. Hence, it was considered that the grid size of the DNS would be prescribed by primarily addressing the resolution of the reaction zone and the Kolmogorov length scale rather than by satisfying the point source model. Note also that many DNS studies have considered the droplet diameter to be of the order of the grid size [100, 141, 152, 168].

B.4 User guide to set up a simulation

In order to initialise a new simulation, a file part.dat must be used. Different user parameters must be input and are detailed in the file. Note that the global

equivalence ratio PHIGLBL and the radius of the spray slab (half width of the slab divided by domain length) must be consistent with the number of droplets in the file com_senga2.h.

Appendix C

Implementation of detailed chemistry in SENGA2

In Appendix C, the implementation of the skeletal chemistry in the DNS code SENGA2 used in Chapter 5 is presented. First, the files and the settings used are introduced. Then, validation of the code for autoignition cases and laminar flame speeds are presented.

The procedure for the splitting between transport and chemistry was explained in section 5.2.3. For the chemistry, the implicit solver VODPK [147] was used. At each node, an array YT is advanced in time by VODPK (subroutine impvod.f). YT contains the nodal values of the mass fractions and the energy at the end of the time advancement by the transport equations. In the simulations of Chapter 5, the energy has no source term and thus does not change in the subroutine. It was implemented should users want to implement source terms such as radiation or a spark. The tolerances used in VODPK are ATOL=1×10^{-14} for species and ATOL=1×10^{-6} for the energy while RTOL=1×10^{-6}. In next paragraph, it is shown that these values could be relaxed. However, they were kept low in the DNS simulations, giving confidence in the results.

Two autoignition cases in a laminar premixed gas are presented for testing with

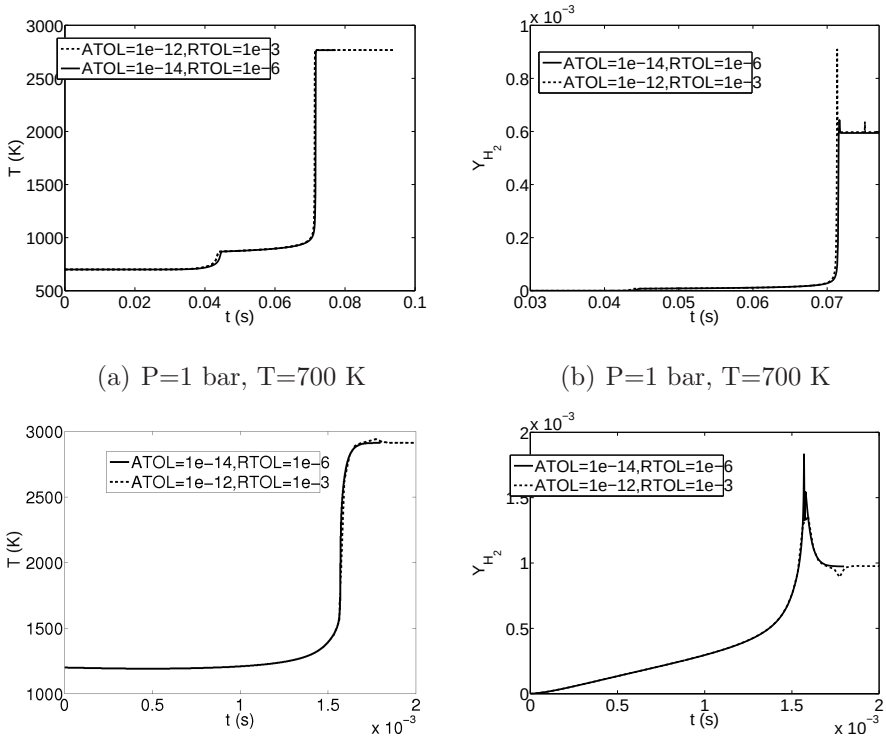

(a) P=1 bar, T=700 K

(b) P=1 bar, T=700 K

(c) P=1 bar, T=1200 K

(d) P=1 bar, T=1200 K

Figure C.1: Computed time evolution of Temperature and Y_{H_2} for different autoignition conditions and different tolerances ATOL and RTOL.

the n-heptane chemistry of Ref. [148], used in Chapter 5. In the first one, $T_0 = 700K$ while in the second one $T_0 = 1200K$. In both simulations, $P_0 = 1bar$. Figure C.1 shows the evolution of temperature and H_2 mass fraction with time. The profiles are presented for two different values of ATOL and RTOL. It can be seen that the effect of ATOL and RTOL is small.

In Fig. C.2, we show the laminar unstrained premixed flame speed profile calculated with a 1D version of SENGA2 and compared with experimental data. In the graph, profiles are normalised by $S_{L,0} = 0.7$ m/s. This value agrees with $S_{L,0} = 0.67$ m/s calculated by Pitsch with the code FlameMaster [169]. In Fig. C.2, the agreement with experimental data is relatively good. The difference with the experimental $S_{L,0}$ is not expected to change the trends of the results but rather to modify quantitatively the chemical timescale. Hence, the 1D version of SENGA2 with op-

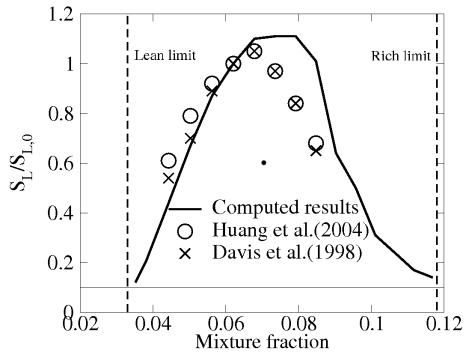

Figure C.2: Comparison of normalised flame speed profiles computed with SENGA2 and the n-heptane chemistry of Ref. [148] ($S_{L,0} = 0.70m/s$), experimental data from Huang et al. ($S_{L,0} = 0.38m/s$) [165] and experimental data from Davis et al. ($S_{L,0} = 0.37m/s$) [166]. The horizontal line shows $S_L/S_{L,0} = 0.1$. The vertical lines denote the nominal lean ($\xi_L = 0.035$) and rich ($\xi_R = 0.116$) flammability limits that are used in Chapter 5.

erator splitting reproduces the laminar flame speed (convection-diffusion-reaction) problem.

Bibliography

[1] A. H. Lefebvre. *Gas Turbine Combustion*. Taylor and Francis, 2nd edition, 1998.

[2] B. Lewis and G. von Elbe. *Combustion, Flames and Explosions of Gases*. Academic Press, 3rd edition, 1987.

[3] S. K. Aggarwal. *Prog. Energy Combust. Sci.*, 24:565–600, 1998.

[4] E. Mastorakos. *Prog. Energy Combust. Sci.*, 35:57–97, 2009.

[5] W. A. Sirignano. *Fluid Dynamics and Transport of Droplets and Sprays*. Cambridge University Press, 1999.

[6] T. Poinsot and D. Veynante. *Theoretical and Numerical Combustion*. Edwards, 2nd edition, 2001.

[7] E. S. Richardson. *Ignition Modelling for Turbulent Non-Premixed Flows*. PhD thesis, Cambridge University, 2007.

[8] R. Maly and M. Vogel. *Proc. Combust. Inst.*, 17:821–831, 1979.

[9] C. C. Swett. Spark ignition of flowing gases. *NACA Report No. 1287*, 1956.

[10] T. Kravchik and E. Sher. *Combust. Flame*, 99:635–643, 1994.

[11] M. Thiele, J. Warnatz, A. Dreizler, S. Lindenmaier, R. Schießl, U. Maas, A. Grant, and P. Ewart. *Combust. Flame*, 128:74–87, 2002.

[12] P. S. Tromans and R. M. Furzeland. *Proc. Combust. Inst.*, 21:1891–1897, 1988.

[13] D. Thevenin. *Proc. Combust. Inst.*, 30:629–637, 2005.

[14] N. Chakraborty, E. Mastorakos, and R. S. Cant. *Combust. Sci. Technol.*, 179:293–317, 2007.

[15] D. Bradley and F. K-K. Lung. *Combust. Flame*, 69:71–93, 1987.

[16] H. L. Olsen, R. B. Edmonson, and E. L. Gayhart. *J. Appl. Phys.*, 23:1157–1162, 1952.

[17] O. O. Akindele, D. Bradley, P. W. Mak, and M. McMahon. *Combust. Flame*, 47:129–155, 1982.

[18] G. F. W. Ziegler, E. P. Wagner, and R. R. Maly. *Proc. Combust. Inst.*, 20:1817–1824, 1985.

[19] Y. Ko, R. W. Anderson, and V. S. Arpaci. *Combust. Flame*, 83:75–87, 1991.

[20] J. L. Beduneau and Y. Ikeda. *Exp. Fluids*, 36:108–113, 2004.

[21] D. R. Ballal and A. H. Lefebvre. *Combust. Flame*, 24:99–108, 1975.

[22] M. Champion, B. Deshaies, G. Joulin, and K. Kinoshita. *Combust. Flame*, 65:319–337, 1986.

[23] M. Mansour, N. Peters, and L. U. Schrader. *Exp. Therm. Fluid Sci.*, 32:1396–1404, 2008.

[24] G. G. de Soete. *Proc. Combust. Inst.*, 13:735–743, 1971.

[25] K. Ishii, O. Aoki, Y. Ujiie, and M. Kono. *Proc. Combust. Inst.*, 24:1793–1798, 1992.

[26] D. Thévenin, O. Gicquel, J. De Charentenay, R. Hilbert, and D. Veynante. *Proc. Combust. Inst.*, 29:2031–2039, 2002.

[27] S. Gashi, J. Hult, K. W. Jenkins, N. Chakraborty, S. Cant, and C. F. Kaminski. *Proc. Combust. Inst.*, 30:809–817, 2005.

[28] H. F. Calcote, C. A. Gregory, C. M. Barnett, and R. B. Gilmer. *Ind. Eng. Chem.*, 44:2656–2662, 1952.

[29] H. E. Rose and T. Priede. *Proc. Combust. Inst.*, 7:436–445, 1958.

[30] D. R. Ballal and A. H. Lefebvre. *Proc. Combust. Inst.*, 15:1473–1481, 1975.

[31] D. R. Ballal and A. H. Lefebvre. *Proc. Roy. Soc. Lond.*, 357:163–181, 1977.

[32] M. Kono, K. Hatori, and K. Ilnuma. *Proc. Combust. Inst.*, 20:133–140, 1985.

[33] C.F. Kaminski, J. Hult, M. Aldén, S. Lindenmaier, A. Dreizler, U. Maas, and M. Baum. *Proc. Combust. Inst.*, 2000:399–405, 28.

[34] A. Dreizler, S. Lindenmaier, U. Maas, J. Hult, M. Aldén, and C. F. Kaminski. *Applied Physics B: Lasers and Optics*, 70:287–294, 2000.

[35] C. C. Huang, S. S. Shy, C. C. Liu, and Y. Y. Yan. *Proc. Combust. Inst.*, 31:1401–1409, 2007.

[36] I. Glassman. *Combustion*. Academic Press, 3rd edition, 1996.

[37] C. K. Law. *Combustion Physics*. Cambridge University Press, 2006.

[38] K. K. Kuo. *Principles of Combustion*. John Wiley and Sons, 2nd edition, 2005.

[39] H. H. Chiu and T. M. Liu. *Combust. Sci. Technol.*, 17:127–142, 1977.

[40] J. Bellan and K. Harstad. *Combust. Sci. Technol.*, 53:75–87, 1987.

[41] M. Lawes, Y. Lee, A. S. Mokhtar, and R. Woolley. *Combust. Sci. Technol.*, 180:296–313, 2008.

[42] A. P. Wandel, N. Chakraborty, and E. Mastorakos. *Proc. Combust. Inst.*, 32:2283–2290, 2009.

[43] F. A. Williams. *Combustion Theory.* Westview Press, 2nd edition, 1994.

[44] J. H. Burgoyne and L. Cohen. *Proc. Roy. Soc. Lond.*, 225:375–392, 1954.

[45] J. A. Browning, T. L. Tyler, and W. G. Krall. *J. Ind. Eng. Chem.*, 49:142–147, 1957.

[46] C. E. Polymeropoulos. *Combust. Sci. Technol.*, 9:197–207, 1974.

[47] D. R. Ballal and A. H. Lefebvre. *Proc. Combust. Inst.*, 18:321–328, 1981.

[48] G. D. Myers and A. H. Lefebvre. *Combust. Flame*, 66:193–210, 1986.

[49] I. Silverman, J. B. Greenberg, and Y. Tambour. *Combust. Flame*, 93:97–118, 1993.

[50] F. Atzler and M. Lawes. Burning Velocities in Droplet Suspensions. *In: ILASS-Europe 98, Manchester, UK, 6 - 8 July*, 1998.

[51] Y. Nunome, S. Kato, K. Maruta, H. Kobayashi, and T. Niioka. *Proc. Combust. Inst.*, 29:2621–2626, 2002.

[52] M. Labowski. *Combust. Sci. Technol.*, 22:217–226, 1980.

[53] A. Umemura, S. Ogawa, and N. Oshima. *Combust. Flame*, 41:45–55, 1981.

[54] M. Mikami, H. Oyagi, N. Kojima, Y. Wakashima, M. Kikuchi, and S. Yoda. *Combust. Flame*, 146:391–406, 2006.

[55] M. Kikuchi, Y. Wakashima, S. Yoda, and M. Mikami. *Proc. Combust. Inst.*, 30:2001–2009, 2005.

[56] H. Oyagi, H. Shigeno, M. Mikami, and N. Kojima. *Combust. Flame*, 156:763–770, 2009.

[57] S. Hayashi, S. Kumagai, and T. Sakai. *Combust. Sci. Technol.*, 15:169–177, 1977.

[58] K. K. Chan and C. S. Jou. *Fuel*, 67:1223–1227, 1988.

[59] Y. Mizutani and T. Nishjmoto. *Combust. Sci. Technol.*, 6:1–10, 1972.

[60] C. E. Polymeropoulos and S. Das. *Combust. Flame*, 25:247–257, 1975.

[61] H. Nomura, M. Koyama, H. Miyamoto, Y. Ujiie, J. Sato, M. Kono, and S. Yoda. *Proc. Combust. Inst.*, 28:999–1005, 2000.

[62] J. B. Greenberg, I. Silverman, and Y. Tambour. *Combust. Flame*, 113:271–273, 1998.

[63] S. K. Aggarwal and W. A. Sirignano. *Combust. Flame*, 62:69–84, 1985.

[64] C. E. Polymeropoulos. *Combust. Sci. Technol.*, 40:217–232, 1984.

[65] M. Zhu and B. Rogg. *Meccanica*, 31:177–193, 1996.

[66] K. V. L. Rao and A. H. Lefebvre. *Combust. Flame*, 27:1–20, 1976.

[67] D. R. Ballal and A. H. Lefebvre. *Proc. Roy. Soc. Lond.*, 364:277–294, 1978.

[68] D. R. Ballal and A. H. Lefebvre. *Combust. Flame*, 35:155–168, 1979.

[69] D. R. Ballal and A. H. Lefebvre. *Proc. Combust. Inst.*, 18:1737–1746, 1981.

[70] A. M. Danis, I. Namer, and N. P. Cernansky. *Combust. Flame*, 74:285–294, 1988.

[71] A. K. Singh and C. E. Polymeropoulos. *Proc. Combust. Inst.*, 21:513–519, 1988.

[72] D. L. Dietrich, N. P. Cernansky, M. B. Somashekara, and I. Namer. *Proc. Combust. Inst.*, 23:1383–1389, 1991.

[73] D. R. Ballal and A. H. Lefebvre. *Combust. Flame*, 31:115–126, 1978.

[74] J. E. Peters and A. M. Mellor. *Combust. Flame*, 38:65–74, 1980.

[75] S. K. Aggarwal and W. A. Sirignano. *Proc. Combust. Inst.*, 20:1773–1780, 1985.

[76] S.A. Rashkovoksky. Spark ignition of ill-mixed gases. *In: First Mediterranean Combustion Symposium, Antaly, Turkey, June*, 1999.

[77] E. S. Richardson and E. Mastorakos. *Combust. Sci. Technol.*, 179:21–37, 2007.

[78] R. Owston and J. Abraham. *Int. J. Hydrogen Energy*, 34:6532–6544, 2009.

[79] X. Qin, C. W. Choi, A. Mukhopadhyay, I. K. Puri, S. K. Aggarwal, and V. R. Katta. *Combust. Theory Model.*, 8:293–314, 2004.

[80] A. D. Birch, D. R. Brown, and M. G. Dodson. *Proc. Combust. Inst.*, 18:1775–1780, 1981.

[81] M. T. E. Smith, A. D. Birch, D. R. Brown, and M. Fairweather. *Proc. Combust. Inst.*, 21:1403–1408, 1988.

[82] S. F. Ahmed and E. Mastorakos. *Combust. Flame*, 146:215–231, 2006.

[83] J. L. McCraw, N. J. Moore, and K. M. Lyons. *Flow Turbul. Combust.*, 79:83–97, 2007.

[84] S. F. Ahmed, R. Balachandran, and E. Mastorakos. *Proc. Combust. Inst.*, 31:1507–1513, 2007.

[85] N. Chakraborty and E. Mastorakos. *Flow Turbul. Combust.*, 80:155–186, 2008.

[86] R. W. Bilger, S. B. Pope, K. N. C. Bray, and J. F. Driscoll. *Proc. Combust. Inst.*, 30:21–42, 2005.

[87] J. Buckmaster. *Proc. Combust. Inst.*, 28:435–475, 2002.

[88] H. Phillips. *Proc. Combust. Inst.*, 10:1277–1283, 1965.

[89] J. W. Dold. *Combust. Flame*, 76:71–88, 1989.

[90] P. N. Kioni, B. Rogg, K. N. C. Bray, and A. Liñán. *Combust. Flame*, 95:276–290, 1993.

[91] G. Ruetsch, L. Vervisch, and A. Liñán. *Phys. Fluids*, 7:1447–1454, 1995.

[92] M. S. Cha and P. D. Ronney. *Combust. Flame*, 146:312–328, 2006.

[93] S. H. Chung. *Proc. Combust. Inst.*, 31:877–892, 2007.

[94] H. G. Im and J. H. Chen. *Combust. Flame*, 119:436–454, 1999.

[95] K. M. Lyons. *Prog. Energy Combust. Sci.*, 33:211–231, 2007.

[96] A. Upatnieks, J. F. Driscoll, C. C. Rasmussen, and S. L. Ceccio. *Combust. Flame*, 138:259–272, 2004.

[97] C. Heeger, B. Bohm, S. F. Ahmed, R. Gordon, I. Boxx, W. Meier, A. Dreizler, and E. Mastorakos. *Proc. Combust. Inst.*, 32:2957–2964, 2009.

[98] J. Ray, H. N. Najm, and R. B. McCoy. Ignition Front Structure in a Methane-Air Jet. *In: 2nd Joint Meeting of the US Sections of the Combustion Institute, Oakland, California, 25 - 28 March*, 2001.

[99] N. Chakraborty and E. Mastorakos. *Phys. Fluids*, 18:105103, 2006.

[100] J. Reveillon and L. Vervisch. *J. Fluid Mech.*, 537:317–347, 2005.

[101] S. K. Marley, E. J. Welle, K. M. Lyons, and W. L. Roberts. *Exp. Thermal Fluid Sci.*, 29:23–31, 2004.

[102] P. Domingo, L. Vervisch, and J. Reveillon. *Combust. Flame*, 140:172–195, 2005.

[103] S. F. Ahmed, R. Balachandran, T. Marchione, and E. Mastorakos. *Combust. Flame*, 151:366–385, 2007.

[104] L. Zimmer, K. Okai, and Y. Kurosawa. Laser Ignition and Plasma Spectroscopy in Non Premixed Hydrogen-Air Burner. *In: ICDERS, Poitiers, July*, 2007.

[105] A. Triantafyllidis, E. Mastorakos, and R. L. G. M. Eggels. *Combust. Flame*, 156:2328–2345, 2009.

[106] V. Subramanian, P. Domingo, and L. Vervisch. *Combust. Flame*, 157:579–601, 2010.

[107] T. Marchione, S. F. Ahmed, and E. Mastorakos. *Combust. Flame*, 156:166–180, 2009.

[108] H. H. Foster and D.M. Straight. Effect of Fuel Volatility Characteristics on Ignition-Energy Requirements in a Turbojet Combustor. *NACA Report No. RM-E52J21*, 1953.

[109] N. Ouarti, G. Lavergne, and R. Lecourt. Modelling of the Ignition Inside a Turbojet Combustor. Application to In-Flight Relight. *In: ILASS-Europe, Nottingham, 6 - 8 September*, 2004.

[110] M. Boileau, G. Staffelbach, B. Cuenot, T. Poinsot, and C. Berat. *Combust. Flame*, 154:2–22, 2008.

[111] R. W. Read, J. W. Rogerson, and S. Hochgreb. Relight Imaging at Low Temperature, Low Pressure Conditions. *In: 46th AIAA Aerospace Sciences Meeting, Reno, Nevada, 7 - 10 January*, 2008.

[112] T. Mosbach, R. Sadanandan, W. Meier, and R. L. G. M. Eggels. Experimental Analysis of Altitude Relight Under Realistic Conditions Using Laser and High-

Speed Video Techniques. *In: Proc. ASME Turbo Expo 2010, Glasgow, UK, 14 - 18 June*, 2010.

[113] P. Dagaut and M. Cathonnet. *Prog. Energy Combust. Sci.*, 32:48–92, 2006.

[114] Rotexo-Softpredict-Cosilab. *GmbH and Co. KG Bad Zwischenahn (Germany), Cosilab Collection, Version 3.0*. www.SoftPredict.com, 2010.

[115] N.-H. Chen, B. Rogg, and K. N. C. Bray. *Proc. Combust. Inst.*, 24:1513–1521, 1992.

[116] B. Abramzon and W. A. Sirignano. *Int. J. Heat Mass Transfer*, 32:1605–1618, 1989.

[117] W. A. Sirignano. *Prog. Energy Combust. Sci.*, 9:291–322, 1983.

[118] M. Chaos, A. Kazakov, Z. Zhao, and F. L. Dryer. *Int. J. Chem. Kinet.*, 39:399–414, 2007.

[119] Z. Zhao, J. Li, A. Kazakov, F. L. Dryer, and S. P. Zeppieri. *Combust. Sci. Technol.*, 177:89–106, 2004.

[120] K. Kumar and C.-J. Sung. *Combust. Flame*, 151:209–224, 2007.

[121] S. R. Turns. *An Introduction to Combustion: Concepts and Applications*. McGraw-Hill, New York, 2nd edition, 2000.

[122] J. Gottgens, F. Mauss, and N. Peters. *Proc. Combust. Inst.*, 24:129–135, 1992.

[123] T. H. Lin, C. K. Law, and S. H. Chung. *Int. J. Heat Mass Transfer*, 31:1023–1034, 1988.

[124] P. H. Paul and H. N. Najm. *Proc. Combust. Inst.*, 27:43–50, 1998.

[125] N. Chakraborty and R. S. Cant. *Combust. Flame*, 137:129–147, 2004.

[126] M. Klein, N. Chakraborty, and R. S. Cant. *Flow Turbul. Combust.*, 81:583–607, 2008.

[127] H. Hesse, N. Chakraborty, and E. Mastorakos. *Proc. Combust. Inst.*, 32:1399–1407, 2009.

[128] R. S. Miller and J. Bellan. *J. Fluid Mech.*, 384:293–338, 1999.

[129] K. W. Jenkins and R. S. Cant. *Proc. 2nd AFOSR Conf. DNS LES, Kluwer Academic Publishers.*, 1999.

[130] R. S. Miller and J. Bellan. *Proc. Combust. Inst.*, 27:1065–1072, 1998.

[131] O. Colin and A. Benkenida. *Combust. Flame*, 134:207–227, 2003.

[132] J. Reveillon and F. X. Demoulin. *Proc. Combust. Inst.*, 31:2319–2326, 2007.

[133] O. Desjardins and H. Pitsch. Modeling Effect of Spray Evaporation on Turbulent Combustion. Number Paper ICLASS06-084, Kyoto, Japan, Aug. 27 - Sept. 1 2006. ICLASS-2006.

[134] H.-W. Ge and E. Gutheil. *Combust. Flame*, 153:173–185, 2008.

[135] M. Mortensen and R. W. Bilger. *Combust. Flame*, 156:62–72, 2009.

[136] T. Echekki and J. H. Chen. *Combust. Flame*, 114:231–245, 1998.

[137] Y. S. Ko and S. H. Chung. *Combust. Flame*, 118:151–163, 1999.

[138] T. D. Dunstan and K. W. Jenkins. *Int. J. Hydrogen Energy*, 34:8389–8404, 2009.

[139] E. Fernández-Tarrazo, A. L. Sánchez, A. Linán, and F. A. Williams. *Combust. Flame*, 147:32–38, 2006.

[140] M. Thiele, S. Selle, U. Riedel, J. Warnatz, and U. Maas. *Proc. Combust. Inst.*, 28:1177–1185, 2000.

[141] Y. Wang and C. J. Rutland. *Proc. Combust. Inst.*, 30:893–900, 2005.

[142] M. D. Smooke and V. Giovangigli. *Lect. Notes Phys.*, Springer-Verlag (1991), 384:1-28.

[143] G. Karaiskakis and D. Gavril. *J. Chromatogr. A*, 1037:147–189, 2004.

[144] H. N. Najm, P. S. Wyckoff, and O. M. Knio. *J. Comput. Phys.*, 143:381–402, 1998.

[145] O. M. Knio, H. N. Najm, and P. S. Wyckoff. *J. Comput. Phys.*, 154:428–467, 1999.

[146] C. A. Kennedy, M. H. Carpenter, and R. M. Lewis. *Appl. Numer. Math.*, 35:177–219, 2000.

[147] P. N. Brown and A. C. Hindmarsh. *J. Appl. Math. Comput.*, 31:40–91, 1989.

[148] S. Liu, J.C. Hewson, J.H. Chen, and H. Pitsch. *Combust. Flame*, 137:320–339, 2004.

[149] G. K. Batchelor and A. A. Townsend. *Proc. Roy. Soc. Lond. Ser. A*, 194:527–543, 1948.

[150] J. C. Sutherland, P. J. Smith, and J. H. Chen. *Combust. Theory Model.*, 9:365–383, 2005.

[151] T. M. Sloane. *Combust. Sci. Technol.*, 86:121–133, 1992.

[152] M. Nakamura, F. Akamatsu, R. Kurose, and M. Katsuki. *Phys. Fluids*, 17:123301, 2005.

[153] R. W. Read. *Experimental Investigations into High-Altitude Relight of a Gas Turbine*. PhD thesis, Cambridge University, 2008.

[154] H. Shalaby and D. Thevenin. *Flow Turbul. Combust.*, 84:357–367, 2010.

[155] A. Williams. *Combust. Flame*, 21:1–31, 1973.

[156] G. Lacaze, E. Richardson, and T. Poinsot. *Combust. Flame*, 156:1993–2009, 2009.

[157] Weckering J., Sadiki A., Janicka J., and Mastorakos E. Investigations of Ignition Probability of a Forced Ignited Turbulent Methane Jet Based on LES. *In: 5th European Conference on Computational Fluid Dynamics, ECCOMAS CFD, Lisbon, Portugal, 14 - 17 June*, 2010.

[158] C. W. Wilson, C. G. W. Sheppard, and H. C. Low. A Novel Technique for Predicting the Ignition Performance of an Aero Gas Turbine Combustion Chamber. *In: Applied Vehicle Technology Panel Symposium, Lisbon, Portugal*, 1999.

[159] R. Said and R. Borghi. *Proc. Combust. Inst.*, 22:569–577, 1989.

[160] S. Stow, S. Sadig, E. Aurifeille, and M. Zedda. Report on Altitude Relight Calculation. *Deliverable D4.1.7, EU Project No. AST5-CT-2006-030828*, 2010.

[161] S. B. Pope. *Turbulent Flows*. Cambridge University Press, London, 2000.

[162] R. G. Abdel-Gayed and D. Bradley. *Combust. Flame*, 62:61–68, 1985.

[163] Vagelopoulos C. M. and Egolfopoulos F. N. *Proc. Combust. Inst.*, 27:513–519, 1998.

[164] T. Mosbach, R. Sadanandan, and W. Meier. Report on the Results of Measurement Campaigns at RR-Rig. *Deliverable D2.2.3a, EU Project No. AST5-CT-2006-030828*, 2009.

[165] Y. Huang, C. J. Sung, and J. A. Eng. *Combust. Flame*, 139:239–251, 2004.

[166] S. G. Davis and C. K. Law. *Proc. Combust. Inst.*, 27:521–527, 1998.

[167] H. Nomura, Y. Ujiie, H. J. Rath, J. Sato, and M. Kono. *Proc. Combust. Inst.*, 26:1267–1273, 1996.

[168] Y. Wang and C. J. Rutland. *Combust. Flame*, 149:353–365, 2007.

[169] H. Pitsch. *Private communication*, August, 2009.